Higher Order Electroweak and QCD Corrections in $e^+e^-\mu^+\mu^-$ production at LHC

Dissertation

zur Erlangung des mathematisch-naturwissenschaftlichen Doktorgrades
"Doctor of Philosophy" Ph.D. Division of Mathematics and Natural Sciences
der Georg-August-Universität Göttingen

im Promotionsprogramm Physik
der Georg-August University School of Science (GAUSS)

vorgelegt von

Simon Luca Villani

aus
Serra de' Conti, Italien

Göttingen 2022

Betreuungsausschuss:

Prof. Dr. Steffen Schumann
Institut für Theoretische Physik, Georg-August-Universität Göttingen

Prof. Dr. Stan Lai
II. Physikalisches Institut, Georg-August-Universität Göttingen

Prof. Dr. Laura Covi
Institut für Theoretische Physik, Georg-August-Universität Göttingen

Mitglieder der Prüfungskommission:

Referent:	Prof. Dr. Steffen Schumann Institut für Theoretische Physik, Georg-August-Universität Göttingen
Koreferent:	Prof. Dr. Stan Lai II. Physikalisches Institut, Georg-August-Universität Göttingen

Weitere Mitglieder der Prüfungskommission:

Prof. Dr. Laura Covi
Institut für Theoretische Physik, Georg-August-Universität Göttingen

Prof. Dr. Arnulf Quadt
II. Physikalisches Institut, Georg-August-Universität Göttingen

Prof. Dr. Karl-Henning Rehren
Institut für Theoretische Physik, Georg-August-Universität Göttingen

Prof. Dr. Ansgar Reiner
Institut für Astrophysik, Georg-August-Universität Göttingen

Tag der mündlichen Prüfung: 02.09.2022

Abstract

This thesis focuses on improving the theoretical modelling of the process $pp \rightarrow e^+e^-\mu^+\mu^-$ at LHC by including both EW and QCD higher-order perturbative corrections. The EW corrections are studied at NLO fixed order and in a multijet-merged parton-shower simulation. The NLO EW fixed order correction is studied for the $e^+e^-\mu^+\mu^-$ final state and, for the first time, for $e^+e^-\mu^+\mu^-$ associated with a jet. In the multijet-merged calculation, EW effects are included only via the NLO virtual and NLL Sudakov approximations. To this end, the fixed order calculation is used as a benchmark for these approximations. In both calculations, the resummation of Sudakov logarithms is discussed, especially the matching to the EW NLO fixed order calculation. For what concerns the higher order QCD corrections, this is the NLO QCD of loop-induced $e^+e^-\mu^+\mu^-$ production. Specifically, the study conducted in this thesis focuses on loop-induced NLO parton-shower matching. This calculation is compared to the fixed order NLO QCD and the 0+1-jet merged matrix elements at leading order to highlight non-trivial effects due to the NLO parton-shower matching. Due to the slow evaluation of the two-loop virtual matrix elements, I have studied the possibility of improving the evaluation time using a multi-dimensional interpolation method. Both these corrections have been studied and implemented in the MC generator SHERPA.

Contents

Introduction

The production of two Electroweak (EW) bosons is a fundamental process for testing the gauge invariance of the Standard Model (SM). An example of their importance is given by the independent discovery of the Higgs boson by the Large Hadron Collider (LHC) [1] experiments A Toroidal LHC ApparatuS (ATLAS) [2] and Compact Muon Solenoid (CMS) [3] in 2012. In these experiments, the Higgs boson was observed as a scalar resonance at an energy of about $125\,\mathrm{GeV}$ in the invariant mass spectrum of four-lepton final states. This discovery sets a milestone in the understanding of the SM gauge invariance. The di-boson production also gives a direct way for testing the EW boson self-couplings. This makes the di-boson production very suitable for some Beyond Standard Model (BSM) searches that modify such couplings *e.g.* , the triple gauge boson coupling between three neutral vector bosons [4] that is not allowed by the gauge invariance of the SM.

With the very successful data-taking from LHC Run I, Run II, and the upcoming Run III, which is going to have an even higher luminosity, reaching $300\,\mathrm{fb}^{-1}$ in 2028, high-energy hadron-collider physics has entered its precision era. With the data collected during the Run II of the LHC, between 2015 and 2018, the measured total cross-section for a four-lepton final state with two same-flavor oppositely charged leptons pair has reached the experimental accuracy of about 3% [5]. This uncertainty is expected to be significantly reduced with the future high-luminosity upgrade of the LHC, that plans to deliver a luminosity of up to $3000\,\mathrm{fb}^{-1}$, and improvements on the particle detectors.

Theoretical predictions must match the experimental precision level with at least the same level of accuracy. A recent calculation of the total cross-section of the four-lepton production with two same-flavor oppositely charged leptons pairs [5] has shown a theoretical uncertainty of about 3%, i.e. comparable with the experimental uncertainty. The calculation was performed evaluating the process at the Quantum Chromo-Dynamics (QCD) next-to-next-to-leading order (NNLO), with higher order electroweak (EW) contributions included as a reweighting factor, depending on the four-lepton invariant mass. The uncertainty in the theoretical predictions comes from the renormalisation and factorisation scale dependence of an observable evaluated in perturbation theory. The scale uncertainty gives an "estimate" of higher-order corrections not included in a calculation. For this reason, it is vital to include higher-order contributions to reduce the uncertainty of theoretical

predictions evaluated in perturbation theory.

In this thesis are studied two types of higher order corrections to the $e^+e^-\mu^+\mu^-$ production in proton-proton collision, the next-to-leading order (NLO) EW [6] and the NLO QCD correction to the loop-induced $e^+e^-\mu^+\mu^-$ final state. Despite QCD effects being usually dominant, NLO EW corrections are significantly enhanced in high-energetic regions of the phase space becoming comparable to higher QCD multiplicity contributions. Including EW corrections is therefore essential for the correct interpretation of actual measurements. A loop-induced process contributes formally to the QCD NNLO correction. However, they can be studied separately from the quark-initiated $e^+e^-\mu^+\mu^-$ production, since they form an ultraviolet (UV) and infrared (IR) finite gauge invariant subset of processes. The importance to include loop-induced processes in a calculation comes from the fact that they contribute to half of the NNLO correction and increase the NLO QCD total cross-section by about 10% [7].

The thesis is structured as follows. Chap. 1 gives a brief introduction to the SM paying particular attention to its gauge invariance and how this dictates the form of the interacting Lagrangian. QCD and EW theories are then discussed, pointing out how these are built by just requiring gauge invariance. The EW spontaneous gauge symmetry breaking, due to the masses of the EW gauge bosons Z and $W^\pm$, is also discussed, describing in particular how gauge invariance can be restored by the Higgs mechanism. Finally, it is given a general overview of the regularisation of the ultraviolet (UV) and infrared (IR) singularity arising from perturbation theory.

In Chap. 2 tools and numerical methods used throughout the thesis to make predictions are discussed. These are based on Monte Carlo simulations to produce events for experimental data comparison. Particular focus is put on the methods available in the MC generator SHERPA, which is this thesis's generator of reference.

Then, in Chap. 3 is presented the phenomenological motivation of this thesis. Specifically, it discusses the state-of-the-art theoretical predictions and the latest total cross-section measurements of the $e^+e^-\mu^+\mu^-$ production.

Finally, in Chap. 4 and Chap. 5 the original results of this thesis are discussed. Higher order EW corrections to the $e^+e^-\mu^+\mu^-$ final state are discussed in Chap. 4. This Chapter first introduces the EW logarithms that cause the large EW enhancement at high energies and then the EW approximations used to include these logarithms in a general multiple QCD emissions simulation. The approximations are validated against the full fixed order NLO EW calculation for producing the $e^+e^-\mu^+\mu^-$ final state associated with 0- and 1-jet. The fixed order NLO EW Z-boson pair production associated with a jet is discussed for the first time in the work presented in Ref. [6] done in collaboration with E. Bothmann, D. Napoletano, M. Schönherr and S. Schumann. Finally, the EW approximations are included in a general QCD simulation to study their phenomenology. Loop-induced processes are discussed in Chap. 5. This Chapter gives firstly a general overview of loop-induced processes discussing their main characteristics. It is then presented the implementation of the NLO correction to the loop-induced process $gg \to e^+e^-\mu^+\mu^-$ in the

MC generator SHERPA. The virtual part of the NLO correction if evaluated using the public code `ggvvamp` [8]. Due to the very expensive numerical evaluation of the virtual matrix elements, an interpolation framework has been developed to improve its evaluation time. Finally, it is discussed the phenomenology of the NLO correction to the loop-induced $e^+e^-\mu^+\mu^-$ production for both, a fixed order calculation and matched to parton-shower.

Chapter 1

Introduction to the Standard Model

The Standard Model (SM) is the theory built to describe the quantum dynamics of the so far known elementary particles. These are twelve particles of matter, with their respective anti-particles, and four mediators of elementary forces. The particles of matter are in turn divided into two subgroups, quarks and leptons, which are respectively strongly- and non-strongly-interacting particles. In each subgroup there are six fermions. The first contains the up (u), down (d), charm (c), strange (s), top (t) and bottom (b) quarks, while the second the electron e^-, muon μ^-, tauon τ^-, with corresponding neutrinos (ν_e, ν_μ and ν_τ). The SM also includes the dynamics of all the elementary forces but gravity (there still are no traces of quantum gravity effects), plus the Higgs field. The coupling with the latter gives rise to particle masses.

This model is the result of a world-wide effort that lasted almost the entire 20th century. Its final theoretical formulation was achieved only in the mid-seventies after the discovery of quarks from the deep inelastic scattering experiments done at the Stanford Linear Accelerator in 1968 [9, 10] that proved the existence of hadron constituents and opened the way to complete a theory for the strong interaction that is, generally speaking, consistent with the formulation of QED and electroweak Lagrangians. All these Lagrangians put together form a Lorentz and U(1)×SU(2)×SU(3) invariant theory able to describe almost all particle phenomena observed so far.

An important confirmation of this model came in 2012 with the discovery of the Higgs boson made by the LHC experiments ATLAS [2] and CMS [3]. This boson was theorized in 1964 by R. Brout, F. Englert [11], P. Higgs [12, 13], G. Guralnik, C. R. Hagen and T. Kibble [14] and its discovery played a crucial confirmation of the SM since it ensures the gauge invariance of the model. This property is going to be discussed later in this chapter.

The three theoretical milestones that led to the formulation of the SM as it is known today were Dirac's quantum formulation of QED which posed the basis for the

mathematical structure of a relativistic quantum field theory, Fermi's "tentativo" of a theory for the β-decay that opened the road to build the general theory of weak interactions later formulated by S. Weinberg [15] and A. Salam [16] and the classifications of the observed hadrons according to the singlet states of the SU(3) group proposed by M. Gell-Mann [17] and Y. Ne'eman [18].

In this chapter I am going to introduce the basics of the Standard Model of electroweak and strong interactions starting by describing how interacting theories can be built just by the requirement of gauge invariance. The theories for the strong and weak forces are then built according to that procedure in order to highlight the significant role gauge invariance plays in the SM. The reason to highlight this aspect is that many experimental analyses focus on verifying the gauge invariance of the SM by measuring the vector boson self couplings. Deviations from the theory prediction may suggest the presence of new fundamental particles that modify those couplings. I will then conclude giving an overview of the particles that are part of the SM.

1.1   Gauge Invariant Field Theories

Symmetries have always played a central role in physics, specially after E. A. Noether's theorem that relates conserved physical quantities to the symmetries of a system. This theorem is applicable to any theory including the quantum field theory the SM is based upon.

Besides the geometrical symmetries of the SM which are related to well known conserved physical quantities such as *e.g.* angular momentum and total energy, there is also the very important invariance under the special unitary symmetry group U(1)×SU(2)×SU(3) which is related to the SM conservation of charged currents.

The interesting fact about this symmetry group is that it implies a theory to be interacting. Indeed, a free field theory would not be invariant under the action of a local unitary gauge group.

The close relation between local gauge invariance and interacting quantum field theories was first proposed by C. N. Yang and R. L. Mills [19]. Their idea came by realizing that the two most studied and most predictive theories of fundamental forces, *i.e.* electromagnetism and gravitation, are both locally gauge invariant. Electromagnetism, specially, keeps this invariance at both classical and quantum level. The aim of Yang and Mills was to give a general prescription to build gauge invariant theories, for a general special unitary group SU(N), similarly as Dirac's QED.

To give an idea of how gauge invariance and interacting theories are related, it is often useful to look at the simpler case of QED. Local gauge transformation in QED is generated by the special unitary group U(1). The fundamental representation of this group is realized on the spinor field space as a complex local phase shift while the adjoint representation is realized on the space of four-dimensional rank-one tensor fields as a $C^{(1)}$ functional shift of the tensor of the adjoint representation. The

gauge transformations of these objects then read

$$\psi(x) \mapsto \psi'(x) = e^{i\alpha(x)}\,\psi(x),$$
$$\overline{\psi}(x) \mapsto \overline{\psi}'(x) = e^{-i\alpha(x)}\,\overline{\psi}(x),$$
$$A_\mu(x) \mapsto A'_\mu(x) = A_\mu(x) + \frac{1}{e}\partial_\mu\alpha(x), \tag{1.1.1}$$

where $\psi(x)$ and $\overline{\psi}(x)$ represent respectively the fermionic spinorial field and its Dirac adjoint $\left(\overline{\psi}(x) = \psi^\dagger\gamma^0\right)$ carrying an electric charge e, while $A_\mu(x)$ is the neutral electromagnetic vector boson field mediated by the photon. The QED Lagrangian density invariant under the action of the transformations (1.1.1) is

$$\mathcal{L}_{\text{QED}} = \overline{\psi}(x)\left(i\slashed{D} - m\right)\psi(x) - \frac{1}{4}F_{\mu\nu}(x)F^{\mu\nu}(x) = \mathcal{L}_{\text{Dirac}} + \mathcal{L}_{\text{EM}}, \tag{1.1.2}$$

where $\slashed{D}$ is the so called covariant derivative written in Feynman slashed notation $(\slashed{D} = \gamma^\mu D_\mu)$ defined as

$$D_\mu = \partial_\mu - ieA_\mu(x). \tag{1.1.3}$$

In Eq. (1.1.2), $\mathcal{L}_{\text{QED}}$ has been divided into two Lagrangian densities, $\mathcal{L}_{\text{Dirac}}$ and $\mathcal{L}_{\text{EM}}$. This separation is chosen in order to have two gauge invariant Lagrangians that describe the dynamics of the spinor field and of the gauge vector boson field, respectively. The gauge invariance of $\mathcal{L}_{\text{Dirac}}$ is simply given by the covariant derivative that is built in order to have $D_\mu\psi(x)$ transforming according to the fundamental representation of U(1). In this way the complex phases of the covariant derivative of $\psi(x)$ and its Dirac adjoint cancel, leaving the Lagrangian U(1) invariant. Moreover, the second term in (1.1.3) accounts for the interaction between the fermionic $\psi(x)$ and the bosonic $A^\mu(x)$ fields. This already shows how a free theory can not be locally gauge invariant. If we expand the covariant derivative, it is easy to see the form of the interaction part of the Lagrangian (1.1.2),

$$\mathcal{L}_{\text{int}} = e\,\overline{\psi}(x)\gamma^\mu\,\psi(x)\,A_\mu(x). \tag{1.1.4}$$

In Eq. (1.1.2), $\mathcal{L}_{\text{EM}}$ accounts for the kinematics of the photon field where $F^{\mu\nu}(x)$ is the anti-symmetric stress-energy tensor defined as

$$F^{\mu\nu}(x) = \partial^\mu A^\nu(x) - \partial^\nu A^\mu(x). \tag{1.1.5}$$

The gauge invariance of $\mathcal{L}_{\text{EM}}$ can be easily read off the following equivalence:

$$F^{\mu\nu}(x)\psi(x) = ie\left(\partial^\mu A^\nu(x) - \partial^\nu A^\mu(x)\right)\psi(x)$$
$$= ie\left[D^\mu, D^\nu\right]\psi(x). \tag{1.1.6}$$

The second line of Eq. (1.1.6) proves the gauge invariance of $F^{\mu\nu}(x)$ since the application of the commutator of the covariant derivatives onto the spinor field is a covariant object itself, therefore

$$\left(F^{\mu\nu}(x)\psi(x)\right)' = e^{i\alpha(x)}F^{\mu\nu}(x)\psi(x) = F^{\mu\nu}(x)\psi'(x). \tag{1.1.7}$$

The gauge invariance of the field strength tensor can be proved in many ways, however the procedure used in this case, Eq. (1.1.6), is particularly useful for building a general gauge invariant field theory since it gives a direct relation between the covariant derivative and the strength tensor field.

Yang and Mills generalized the gauge invariance of QED to any arbitrary local special unitary group SU(N) that act on an N-dimensional vector space spanned by a linear combination of spinor objects. The elements of this N-dimensional space can be written as $\Psi(x) = (\psi_1(x), \ldots, \psi_N(x))$ with $\psi_i(x)$ being linearly independent spinor fields. The gauge group acting on this vector space is realized as an $N \times N$ unitary matrix. The fundamental representation of this group is given by,

$$\Psi(x) \mapsto \Psi'(x) = e^{i\alpha^A(x)t^A}\Psi(x) = U(x)\Psi(x), \tag{1.1.8}$$

where t^A, $A = 1, \ldots, N^2 - 1$ are the generators of the group and $\alpha^A(x)$ is the continuous real phase associated with each generator. Moreover, the index A is euclidean-like, so we make no distinction between upper and lower indices. Also, Einstein notation for repeated indices, $\alpha^A(x)t^A = \sum_{A=1}^{N^2-1}\alpha^A(x)t^A$, is adopted.

The choice of the group generators is completely arbitrary as long as they satisfy the following normalization trace condition,

$$\mathrm{Tr}\left[t^A t^B\right] = T_F\delta^{AB}, \tag{1.1.9}$$

with T_F being an algebra constant of the fundamental representation.

The algebra formed by the SU(N) generators in the fundamental representation is given by the following commutative relation,

$$\left[t^A, t^B\right] = if^{ABC}t^C, \tag{1.1.10}$$

where f^{ABC} are the completely antisymmetric structure constants of this algebra.

In order to build a gauge invariant Lagrangian for an N-dimensional spinor multiplet $\Psi(x)$, it is necessary to define a covariant derivative similar to the QED one, *i.e.* Eq. (1.1.3). In this case it is defined as

$$D_\mu = \partial_\mu \mathbb{I} - ig A_\mu^A(x) t^A, \qquad (1.1.11)$$

where $\mathbb{I}$ is the $N \times N$ identity matrix and $A_\mu^A(x)$ is the vector boson associated with the group generator t^A. The covariance of D_μ is assured by defining the gauge transformation for the vector boson field according to

$$A_\mu^A(x) t^A \mapsto A_\mu'^A(x) t^A = U(x) A_\mu^A t^A U^\dagger(x) + \frac{i}{g} U(x) \partial_\mu U^\dagger(x). \qquad (1.1.12)$$

This transformation is the adjoint representation of the SU(N) group realized on the vector field space. Eq. (1.1.12) ensures that the action of the derivative (1.1.11) on $\Psi(x)$ transforms like

$$D^\mu \Psi(x) \mapsto D'^\mu \Psi'(x) = U(x) D^\mu \Psi(x). \qquad (1.1.13)$$

Using this definition of the covariant derivative it is possible to write down the gauge invariant Lagrangian for the dynamics of an N-dimensional spinor multiplet,

$$\mathcal{L}_\Psi = \overline{\Psi}(x) \left(i\slashed{D} - M \right) \Psi(x). \qquad (1.1.14)$$

Here M is a diagonal $N \times N$ matrix containing the mass terms of the components of $\Psi(x)$.

The last part to add is the Lagrangian for the vector field. The main ingredient is a field strength tensor $F^{\mu\nu}(x)$ that contains first derivatives of the vector potentials. This can be built accordingly to the QED one as shown in Eq. (1.1.6). Using the covariant derivative defined in Eq. (1.1.11) we can derive the expression for the $N^2 - 1$ field strength tensors,

$$\begin{aligned} F_{\mu\nu}^A(x) t^A \Psi(x) &= ig \left[D_\mu, D_\nu \right] \Psi(x) \\ &= ig \left(\partial_\mu A_\nu^A(x) - \partial_\nu A_\mu^A(x) + g f^{ABC} A_\mu^B(x) A_\nu^C(x) \right) t^A \Psi(x). \end{aligned} \qquad (1.1.15)$$

It is then possible to write down the gauge invariant Lagrangian density for the vector boson dynamics,

$$\mathcal{L}_F = -\frac{1}{4} F_{\mu\nu}^A(x) F^{A,\mu\nu}(x). \qquad (1.1.16)$$

Combining Eq. (1.1.14) and Eq. (1.1.16) it is possible to write the famous Yang-Mills Lagrangian density for an N-dimensional spinor multiplet $\Psi(x)$ invariant under the action of the special unitary group SU(N):

$$\mathcal{L}_{\text{YM}} = \overline{\Psi}(x) \left(i\slashed{D} - m\mathbb{I} \right) \Psi(x) - \frac{1}{4} F^A_{\mu\nu}(x) F^{A,\mu\nu}(x). \tag{1.1.17}$$

Actually, the theory as just written is also renormalizable making this the most general four-dimensional renormalizable gauge invariant relativistic field theory. The renormalization of a theory is going to be discussed in Sec. 1.2, but it is important to highlight that other gauge invariant terms exist but are non-renormalizable.

A major new aspect of a Yang-Mills theory compared to QED is that in this case cubic and quartic vector potential terms, arising from the non-commutativity of the SU(N) group, are present. These are interpreted as self-interaction of the theory's vector bosons and have the following form:

$$\begin{aligned}
\mathcal{L}_{\text{self-int}} = &- g_s f^{ABC} \partial_\mu A_{A,\nu}(x) A^\mu_B(x) A^\nu_C(x) \\
&- \frac{1}{4} f^{ABC} f^{ADE} A_{B,\mu}(x) A_{C,\nu}(x) A^\mu_D(x) A^\nu_E(x).
\end{aligned} \tag{1.1.18}$$

Here the first line gives a three body interaction vertex and the second line gives a four body interaction vertex.

Finally, in order to make predictions with this theory, it is necessary to choose a gauge in which to compute observables. Without this choice it would not be possible to define the Green's function of the vector boson fields. The gauge fixing works by simply including terms in the Lagrangian that break its gauge invariance. A very common choice is the *covariant gauge*. This is a generalization of the Lorenz gauge of classical electrodynamics, and it is defined as

$$\mathcal{L}_{\text{gauge}} = -\frac{1}{2\lambda} \partial^\mu A^A_\mu(x) \partial^\nu A^A_\nu(x). \tag{1.1.19}$$

This choice then needs to be backed up by introducing a non-observable ghost field needed to cancel unphysical degrees of freedom introduced by the gauge symmetry breaking. For the covariant gauge the Lagrangian density for the ghost field is

$$\mathcal{L}_{\text{ghost}} = \partial^\mu \eta^{A\dagger}(x) D^\mu_{AB} \eta^B(x). \tag{1.1.20}$$

Gauge invariant theories only allow for massless vector boson fields. A massive term, such as $m^2 A^A_\mu(x) A^{\mu,B}(x) t^A t^B$ would break the gauge invariance of the theory. In-

deed, the gauge transformation of a possible mass term for the vector boson field would be,

$$
\begin{aligned}
m^2 A_\mu'^A(x) A'^{B,\mu}(x) t^A t^B =& m^2 \Big[A_\mu^A(x) A^{B,\mu}(x) + A_\mu^A(x) \partial^\mu \alpha^B(x) + \\
& A_\mu^B(x) \partial^\mu \alpha^A(x) + \partial_\mu \alpha^A(x) \partial^\mu \alpha^B(x) \Big] \times \\
& \times U(x) t^A t^B U^\dagger(x) \neq m^2 U(x) A_\mu^A(x) A^{B,\mu}(x) t^A t^B U^\dagger(x),
\end{aligned}
$$
(1.1.21)

hence, $m^2 A_\mu'^A(x) A'^{\mu,B}(x) t^A t^B \neq m^2 A_\mu^A(x) A^{\mu,B}(x) t^A t^B$. However, methods to recover gauge invariance of theories with massive vector bosons have been developed, where the mass of the vector field comes from the coupling with a scalar field. This mechanism, also known as the Englert–Brout–Higgs–Guralnik–Hagen–Kibble mechanism [11, 12, 13, 14], will be discussed later in this chapter, when introducing the weak interacting Lagrangian where the weak force mediators, bosons Z and W, are massive.

1.2   Renormalization of UV divergences

The non-linearity of the interacting Lagrangians discussed in the previous Sec. 1.1 makes it difficult to find general exact solutions of their equations of motion. Consequently, these theories are usually studied either perturbatively or numerically by computation on a grid or lattice. The latter is usually the standard method to treat low-energy quantum systems.

High energy quantum field theory is mainly studied perturbatively. The approach used is taking the initial/incoming and final/outgoing state of an interacting system as asymptotic states, *i.e.* solutions of the free theory. The initial state is evolved using the theory's interacting potential. This can be read from the second term in the covariant derivative, Eq. (1.1.11). To give an example, the amplitude of a generic QED observable is,

$$
\begin{aligned}
{}_\infty\langle \Psi_{\text{out}} | \, e^{ig \int \mathrm{d}x \, \hat{\bar{\Psi}} \hat{\slashed{A}} \hat{\Psi}} \, | \Psi_{\text{in}} \rangle_\infty =& \ {}_\infty\langle \Psi_{\text{out}} | \, \sum_n \frac{1}{n!} \left(ig \int \mathrm{d}x \, \hat{\bar{\Psi}} \hat{\slashed{A}} \hat{\Psi} \right)^n | \Psi_{\text{in}} \rangle_\infty \\
=& \ {}_\infty\langle \Psi_{\text{out}} | \Psi_{\text{in}} \rangle_\infty + {}_\infty\langle \Psi_{\text{out}} | \, ig \int \mathrm{d}x \, \hat{\bar{\Psi}} \hat{\slashed{A}} \hat{\Psi} \, | \Psi_{\text{in}} \rangle_\infty + \mathcal{O}(g^2) \\
=& \ {}_\infty\langle \Psi_{\text{out}} | \Psi_{\text{in}} \rangle_\infty + S(\Psi_{\text{in}}, \Psi_{\text{out}}, g),
\end{aligned}
$$
(1.2.1)

where the interaction potential used is the one given in Eq. (1.1.4). In the last line, the second term is the Scattering matrix that represents the interacting ampli-

tude treated perturbatively, while the first term accounts for the possibility of an interaction-free evolution from the initial to the final state.

Even if perturbing a free high energy quantum system, as just described, is a very useful approach, it also has some drawback. The perturbative expansion contains non-finite terms that make an observable expectation value divergent. This is obviously not the result one would expect and it is of course not shown by experimental observations. Renormalization is the method used to get rid of these infinities by redefining the quantities of a theory such as the fields, their masses and the coupling constants that before being renormalized are called *bare*.

These infinities come from the ultraviolet (UV) sector of loop integrals. When the set of singular loop integrals can be reduced to a finite set of divergent master integrals a theory is said to be *renormalizable*, otherwise it is a *non-renormalizable* theory [20]. The request that a renormalizable theory has to have a finite set of divergent master integrals comes from the fact that these happen to be the same at every perturbative order. Therefore, it is possible to resum them into a singular multiplicative prefactor used to renormalize the quantities of a theory. Alternatively, if this condition is not met, it would mean that there is an infinite number of these singular factors making the renormalization of the theory's objects impossible.

In order to regularize these divergent integrals, many techniques have been developed which isolate the singular terms from the finite result of a loop correction. The most commonly used technique is Dimensional Regularization (DR). This technique consists of an analytical continuation of the four physical dimensions into a $4 - \epsilon$ dimensional space, with ϵ being an arbitrary small constant. Changing the dimensions of the space forces to introduce a scaling parameter μ to recover the physical dimension of an amplitude. This is then expressed as a Laurent series in terms of the infinitesimal variable ϵ depending on the unphysical regularization scale μ. For completeness, it is important to mention that the use of unphysical scales is made also in other regularization techniques like Pauli-Villars regularization [21] which uses a UV cut-off to regularize a loop integral. It is clear that any physical result can not depend directly on such a parameter. This is achieved by renormalizing the theory. Using DR a theory is renormalized by rescaling its parameters with a function of ϵ, usually called $Z(\epsilon)$, divergent for infinitesimal values of ϵ.

Using this procedure, a renormalized theory will still depend on the unphysical regularization scale μ. Since an arbitrary observable cannot directly depend on this variable one has to require it to satisfy the following differential equation,

$$\mu^2 \frac{d}{d\mu^2} \, G\left(\frac{Q^2}{\mu^2}, \alpha\right) = 0. \tag{1.2.2}$$

where $G(\cdot, \cdot)$ is for simplicity a dimensionless observable, α the fine structure constant, *e.g.* $g^2/4\pi$, and Q^2 the energy scale at which we evaluate the observable. The direct consequence of Eq. (1.2.2) is that the coupling constant, and similarly all the other parameters of the theory, can be substituted with new functions that depend

on the system's energy. These parameters are called *running* parameters and encode the entire dependence over Q^2 of $G(\cdot,\cdot)$. This is easily shown by expressing the total derivative in (1.2.2) as sum of partial derivatives. The expression then becomes,

$$\left[\mu^2\frac{\partial}{\partial\mu^2} + \mu^2\frac{\partial\alpha}{\partial\mu^2}\frac{\partial}{\partial\alpha}\right] G\left(\frac{Q^2}{\mu^2},\alpha\right) = 0. \tag{1.2.3}$$

This differential equation can be solved by introducing the *running coupling* $\alpha(Q^2)$ defined as follows:

$$\log\left(\frac{Q^2}{\mu^2}\right) = \int_\alpha^{\alpha(Q^2)}\frac{dx}{\beta(x)}, \qquad \alpha(\mu^2)\equiv\alpha. \tag{1.2.4}$$

Here $\beta(x)$ is the *beta function* defined as

$$\beta(x) = \mu^2\frac{\partial x}{\partial\mu^2}. \tag{1.2.5}$$

By taking the derivative of Eq. (1.2.4) it is clear that the running coupling evaluated at Q^2 is also a solution of Eq. (1.2.2). Indeed,

$$\mu^2\frac{\partial\alpha(Q^2)}{\partial\mu^2} = -\beta(\alpha(Q^2)), \qquad \beta(\alpha)\frac{\partial\alpha(Q^2)}{\partial\alpha} = \beta(\alpha(Q^2))\,. \tag{1.2.6}$$

The running of the coupling constant is nowadays a well established fact that has been extensively studied. An example of the good agreement between the theoretical prediction and data is shown for the strong coupling in Figure 1.1. Data is taken from the experiments CMS [22, 23, 24], DØ[25, 26], H1 [27] and ZEUS [28] and compared to the running of $\alpha_s(Q^2)$ evaluated at two-loop accuracy with five active flavors.

1.3   Quantum Chromodynamics

The strong force is the binding force between the hadron constituents, quarks and gluons, together called partons. Quarks are fermions with fractional electric charge, which can be either -1/3 or 2/3, and are the only fermions in the SM that can interact through every known fundamental force. The strong charge carried by the quarks exists in three different types named after the three colours red, blue and green. Consequently, the strong charge is also called *colour charge*.

The existence of quarks was proposed in the prime 1960s by two independent works made by M. Gell-Mann [30] and G. Zweig [31, 32]. These were follow-ups of the hadron classification proposed in the previous years by M. Gell-Mann [17] and Y. Ne'eman [18], in independent works. They showed that hadrons can be classified
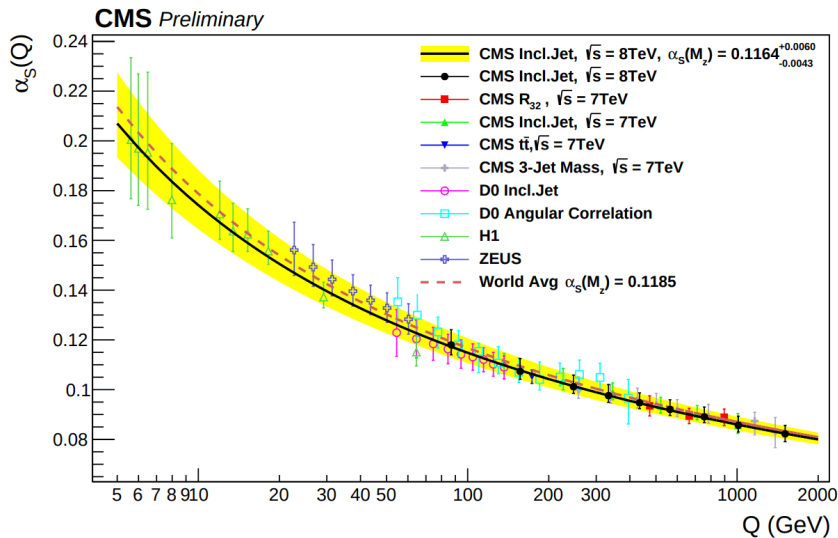
Figure 1.1: The figure represents the comparison between the data collected in various experiments such as CMS [22, 23, 24], DØ[25, 26], H1 [27] and ZEUS [28], at a center-of-mass energy of $\sqrt{s} = 8$TeV, and the theoretical running coupling. The theoretical result is obtained by evolving $\alpha_s(M_Z^2)$ using a beta function evaluated at two-loop order with five active flavor quarks. This plot has been taken from the article [29] licensed with Creative Common License 3.0

as singlets of the SU(3) symmetry group. This classification was called by M. Gell-Mann the *eightfold way*. The singlet states, according to the colour naming, are called *white* states, meaning that the quarks inside a hadron are organized in order to have a neutral total colour charge. In these works it was also postulated that quarks cannot be observed as free but only as bound states with neutral colour charge. This property of QCD is called *colour confinement*. A very important confirmation of this classification model came from the discovery of the Ω^- baryon [33] that was first predicted by this classification model and only later discovered. These studies on the hadrons classification helped to understand that a theory describing a strongly interacting system has to be SU(3) invariant and feature colour confinement.

The first request fits well in the general gauge field theory described in the previous section. A SU(3) invariant Lagrangian is nothing but Eq. (1.1.17), where the spinor multiplet $\Psi(x)$ contains the three differently coloured fermions,

$$\Psi(x) = \begin{pmatrix} \psi_r(x) \\ \psi_g(x) \\ \psi_b(x) \end{pmatrix}, \tag{1.3.1}$$

where $\psi_c(x)$, with $c \in \{r, g, b\}$, is the spinor carrying the colour charge c. The group SU(3) has in total eight generators ($N^2 - 1$ with $N = 3$ gives a total of eight

independent generators). The strong force is therefore mediated by eight vector bosons called *gluons*.

A common choice for the generators t^A are the Gell-Mann matrices divided by two,

$$t^A = \frac{1}{2}\lambda^A, \tag{1.3.2}$$

where,

$$\lambda^1 = \begin{pmatrix} 0 & 1 & 0 \\ 1 & 0 & 0 \\ 0 & 0 & 0 \end{pmatrix}, \lambda^2 = \begin{pmatrix} 0 & -i & 0 \\ i & 0 & 0 \\ 0 & 0 & 0 \end{pmatrix}, \lambda^3 = \begin{pmatrix} 1 & 0 & 0 \\ 0 & -1 & 0 \\ 0 & 0 & 0 \end{pmatrix},$$

$$\lambda^4 = \begin{pmatrix} 0 & 0 & 1 \\ 0 & 0 & 0 \\ 1 & 0 & 0 \end{pmatrix}, \lambda^5 = \begin{pmatrix} 0 & 0 & -i \\ 0 & 0 & 0 \\ i & 0 & 0 \end{pmatrix}, \lambda^6 = \begin{pmatrix} 0 & 0 & 0 \\ 0 & 0 & 1 \\ 0 & 1 & 0 \end{pmatrix},$$

$$\lambda^7 = \begin{pmatrix} 0 & 0 & 0 \\ 0 & 0 & -i \\ 0 & i & 0 \end{pmatrix}, \lambda^8 = \frac{1}{\sqrt{3}}\begin{pmatrix} 1 & 0 & 0 \\ 0 & 1 & 0 \\ 0 & 0 & -2 \end{pmatrix}. \tag{1.3.3}$$

The trace property of these matrices then reads

$$\mathrm{Tr}\left[t^A t^B\right] = \frac{1}{2}\delta^{AB}, \tag{1.3.4}$$

with $T_F = 1/2$. Finally the structure constants of the group generators are

$$f^{123} = 1, \qquad f^{257} = f^{147} = f^{246} = f^{345} = \frac{1}{2},$$

$$f^{156} = f^{367} = -\frac{1}{2}, \qquad f^{485} = f^{678} = \frac{\sqrt{3}}{2}, \tag{1.3.5}$$

with all the other components being zero.

Making use of the general Yang-Mills Lagrangian, Eq. (1.1.17), we can write down the Lagrangian density to describe the dynamics of coloured particles as fol-

lows,

$$\mathcal{L}_{\text{QCD}} = \sum_c \overline{\psi}_c(x) \left(i \partial\!\!\!/_\mu - m \right) \psi_c(x) + g_s \sum_{c_1,c_2} \overline{\Psi}_{c_1}(x) A\!\!\!/^A(x) t^A_{c_1 c_2 A} \Psi_{c1}(x)$$

$$- \frac{1}{4} \sum_{A=1}^{8} F^A_{\mu\nu}(x) F^{A,\mu\nu}(x), \tag{1.3.6}$$

where c, c_1 and c_2 are colour indices.

colour confinement is more complicated to prove analytically since there still is no general exact solution for QCD. However it can be shown that QCD is an *asymptotically free* theory. This means that at very high energies quarks do not interact with each other and the theory is essentially free, while at low energies (about the typical hadronic scale of 200 MeV) the theory becomes very strongly interacting pushing the parton towards the inner part of a hadron which is at a lower potential energy. Even though this is not a direct proof of colour confinement it is a very good indicator that coloured particles tend to stay very close together forming colourless states to minimize their total energy. This effect is a consequence of running couplings where in QCD it decreases increasing the energy of a system, see Fig. 1.1. This behavior was studied and explained in 1973 by David Gross, Frank Wilczek [34] and David Politzer [35]. The different behavior between QCD and QED is due to the different sign taken by the beta function in the two cases. At the lowest perturbative order of Eq. (1.2.5), where the beta function is usually written as,

$$\beta(x) = x \sum_{n=0}^{\infty} b_n x^{n+1} = b_0 x^2 + \mathcal{O}(x^3), \tag{1.3.7}$$

the solution of the differential equation (1.2.5) is

$$x(\mu^2) = \frac{x(\mu_0^2)}{1 + x(\mu_0^2) b_0 \log(\mu^2/\mu_0^2)}. \tag{1.3.8}$$

If b_0 is negative (that is the case in QCD as shown in [34, 35]), $x(\mu^2)$ is a monotone decreasing function, otherwise, for positive b_0, it is a monotone increasing function (QED case). The asymptotic freedom is not just a feature of QCD, but it is a consequence of the gauge vector boson self interaction. This means that this property is entirely dictated by the gauge invariance of the theory and its non-commutativity. The same thing would happen for the weak interaction, but in that case the force mediators are so massive that they decay before showing any sign of confinement.

The parton model

Due to colour confinement the only way to test QCD is by looking at processes involving hadrons, *e.g.* probing a hadron with a sufficiently energetic electron to

resolve its structure. In this way it is possible to study how the electron interacts with the hadron's constituents. This specific process is called deep inelastic scattering (DIS).

The parton model was originally proposed by R. P. Feynman in Ref. [36]. He argued that at high energies, scattering processes involving hadrons are actually the result of the interaction with their constituents, which he named partons. At high energies these are distributed inside a hadron according to their *parton distribution function* (PDF) $f_p(x)$. These functions can be visualized as an instantaneous picture of a parton's distribution at the time of the collision. This assumption holds whenever the partons' interaction time is much shorter than the partons' change of momentum and composition inside the hadron. With this assumption, scattering processes involving hadrons can be treated as QCD processes weighted by the PDFs of the partons involved in the scattering process carrying the momentum fraction,

$$p_{\mathrm{q}}^{\mu} = x\, P_{\mathrm{H}}^{\mu}. \tag{1.3.9}$$

Here P_{H}^{μ} is the hadron four-momentum, p_{q}^{μ} the partonic four-momentum and x its momentum fraction.

Generally, a total hadronic cross section, taking the DIS as example, can be written as

$$\sigma = \int d\Phi \int_0^1 dx \sum_p f_p(x)\, \tilde{\sigma}_p(x, \Phi), \tag{1.3.10}$$

where p runs over the partons taking part in the process, $\tilde{\sigma}(x, \Phi)$ is the partonic differential cross section and Φ the phase space of the particles involved in the partonic collision process.

1.4 Electroweak Theory

The weak force is the elementary force responsible for the β-decay. A theory for the weak interaction can be built similarly to how it is done for QCD, *i.e.* finding a spinor multiplet the force act upon and building a gauge invariant theory starting from that. The spinor multiplet in this case was understood thanks to the extension of Fermi's β-decay theory [37] the V-A theory proposed by Feynman and Gell-Mann [38], Marshak-Sudarshan [39] and Sakurai [40]. In this theory the Hamiltonian density for the weak interaction is

$$\mathcal{H} = \frac{G_F}{\sqrt{2}} J_\mu(x) J^\mu(x) + \text{h.c.}, \tag{1.4.1}$$

where G_F is Fermi's constant and $J_\mu(x)$ is the sum of the leptonic and hadronic currents $J^\mu(x) = j_l^\mu(x) + j_h^\mu(x)$ that are

$$j_l^\mu(x) = \bar{\nu}_e(x)\gamma^\mu \left(1 - \gamma^5\right) e(x),$$
$$j_h^\mu(x) = \bar{u}(x)\gamma^\mu \left(1 - \gamma^5\right) \left[\cos\theta_c\, d(x) + \sin\theta_c\, s(x)\right]. \tag{1.4.2}$$

Here $\nu_e(x)$, $e(x)$, $u(x)$, $d(x)$ and $s(x)$ are the spinors representing respectively the electron neutrino, electron, up, down and strange quark. The angle θ_c is the Cabibbo angle, see Ref. [41]. From the current (1.4.2) it is easy to identify the spinor multiplet we are looking for, i.e.

$$\begin{pmatrix} \nu_e^L(x) \\ e^L(x) \end{pmatrix}, \tag{1.4.3}$$

where L stands for the left helicity of the spinors $e(x)$ and $\nu_e(x)$. This comes directly from the use in Eq. (1.4.2) of the projection operator $1 - \gamma^5$. It is then clear that the weak interaction can be built as a SU(2) invariant relativistic quantum field theory.

This is a very well-known group since it is the same group used to represent spinor spin states. The generators of this group are given by the Pauli matrices

$$\tau_1 = \begin{pmatrix} 0 & 1 \\ 1 & 0 \end{pmatrix}, \qquad \tau_2 = \begin{pmatrix} 0 & i \\ -i & 0 \end{pmatrix}, \qquad \tau_3 = \begin{pmatrix} 1 & 0 \\ 0 & -1 \end{pmatrix}. \tag{1.4.4}$$

The first two can be combined into the operators $\tau^+ = (\tau_1 + i\tau_2)/2$ and $\tau^- = (\tau_1 - i\tau_2)/2$. Then, $\tau^\pm$ and τ^3 form a closed algebra with respect to the commutator

$$\left[\tau^+, \tau^-\right] = \tau_3, \qquad \left[\tau_3, \tau^\pm\right] = \pm 2\tau^\pm. \tag{1.4.5}$$

The generators τ^+ and τ^- are associated with two electrically charged gauge vector bosons called $W^\pm$ (bosons), while the generator τ_3 is associated to a neutral gauge vector boson called W_3. At the time of the development of the weak interaction theory it was thought that this neutral vector boson could be identified with the photon, however, despite being neutral, the W_3 vector boson was soon realized not to be the photon. There are two reasons for that, first this neutral vector boson can also be emitted by neutrinos, which are electrically neutral, and second the electromagnetic current does not distinguish between left- and right-handed spinor helicities, while in this case the neutral vector boson couples only to left-handed spinors. This was very strongly motivated by experimental evidence. Hence, right-handed fermions are assigned to the scalar representation of the SU(2) group. At this point a theory invariant under the action of the SU(2) group can be built as shown in Sec. 1.1.

Thanks to the works of Glashow [42], Weinberg [15] and Salam [43] it was possible to unify the weak and electromagnetic forces into one single theory called Electroweak (EW) theory (or Glashow-Weinberg-Salam model). The unification of

these two theories requires the Lagrangian to be invariant under the U(1)×SU(2) group. This invariance can be assured by requiring that each chiral fermionic field transforms according to,

$$\psi(x) \mapsto \psi'(x) = e^{ig'\alpha(x)\frac{Y(\psi)}{2}}\psi(x), \tag{1.4.6}$$

where g' is the coupling associated to U(1) and $Y(\psi)$ is a quantum number called *weak hypercharge* specific for each $\psi(x)$. The weak hypercharge is also the same for all the components of the SU(2) multiplet since it has to commute with the generators of the group SU(2). A new vector boson associated with the group U(1) needs to be added to the three weak-force mediators bosons, $W^{\pm}$ and W^3. This boson is canonically called $B^{\mu}(x)$.

With these ingredients it is possible to write down the covariant derivative for the theory,

$$D^{\mu} = \partial^{\mu} - i\frac{g}{2}W^{\pm,\mu}(x)\tau^{\pm} - i\frac{g}{2}W_3^{\mu}(x)\tau_3 - i\frac{g'Y}{2}B^{\mu}(x), \tag{1.4.7}$$

where Y is a diagonal matrix with $Y(\psi)$ as its diagonal entries.

The theory now provides four massless gauge bosons, of which two are electrically charged, $W^{\pm,\mu}$, and two electrically neutral, W_3^{μ} and B^{μ}. However, the theory as it is, still does not represent the experimental observations. Only one massless EW boson has so far been observed (the photon), but, as shown in Eq. (1.1.21), mass terms for gauge bosons break the Lagrangian's gauge invariance. A solution to recover the gauge invariance for a theory involving massive bosons was proposed, almost at the same time, by three different groups, *i.e.* R. Brout, F. Englert [11], P. Higgs [12, 13], G. Guralnik, C. R. Hagen and T. Kibble [14]. Their work was later implemented in the modern theory of weak interaction made by S. Weinberg [15] and A. Salam [16]. They have shown how it is possible to build a U(1)×SU(2) invariant theory where three bosons can acquire mass and one is left massless.

The mechanism presented by P. Higgs on how a vector boson can acquire mass coupling to a scalar field works as follows. The Lagrangian density for a doublet of electrically charged scalar fields and invariant under U(1)×SU(2) is,

$$\mathcal{L} = D_{\mu}\Phi^{\dagger}(x)D^{\mu}\Phi(x) - \mathcal{V}(\Phi^{\dagger}(x)\Phi(x)), \tag{1.4.8}$$

where D_{μ} is the covariant derivative defined in Eq. (1.4.7). The scalar doublet $\Phi(x) = (\phi^+(x), \phi^0(x))$ is taken to have the first component positively electrically charged and the second one electrically neutral. The potential $\mathcal{V}(\Phi^{\dagger}(x)\Phi(x))$ is instead defined as follows:

$$\mathcal{V}(\Phi^{\dagger}(x)\Phi(x)) = \lambda(\Phi^{\dagger}(x)\Phi(x))^2 + \mu^2\Phi^{\dagger}(x)\Phi(x). \tag{1.4.9}$$

This potential has a minimum different from zero, $\Phi(x) = 0$. This is responsible for the spontaneous gauge symmetry breaking, since the vacuum of the Higgs field can still couple to a vector boson leaving it with a mass term in its Lagrangian. The minimum of the potential is reached for $\Phi^\dagger(x)\Phi(x) = \mu^2/(2\lambda)$, where μ and λ are general parameters, and the scalar doublet vacuum expectation value is,

$$\langle\Phi\rangle_0 = \frac{1}{\sqrt{2}} \begin{pmatrix} 0 \\ v \end{pmatrix}, \tag{1.4.10}$$

with $v = \sqrt{\mu^2/\lambda}$. The weak hypercharge is set in order to make the Higgs vacuum state invariant under the action of the U(1) group so that the photon field does not couple to it, and consequently it does not acquire mass. The Higgs vacuum state then has to satisfy,

$$e^{i\alpha(x)(\tau_3+Y)/2}\langle\phi(x)\rangle_0 = \langle\phi(x)\rangle_0. \tag{1.4.11}$$

For the gauge transformation, the sum of τ_3 and Y generators is used because the massless vector boson has to be electrically neutral, therefore a combination of the generators associated with electrically neutral vector bosons has to be used. The only unbroken generator then is

$$Q = \frac{\tau_3 + Y}{2} = \begin{pmatrix} 1 & 0 \\ 0 & 0 \end{pmatrix}, \tag{1.4.12}$$

which we identify as the U(1) group generator.

It is possible now to evaluate the Lagrangian density (1.4.8) inserting the vacuum state of $\Phi(x)$. By doing this procedure one gets the following mass terms for the vector bosons:

$$\mathcal{L}_{\mathrm{M}} = \frac{v^2}{8} \left[\left(gW_3^\mu(x) - g'YB^\mu(x)\right) \left(gW_{3,\mu}(x) - g'YB_\mu(x)\right) + 2g^2 W_\mu^-(x)W^{+,\mu}(x)\right]. \tag{1.4.13}$$

The mass term involving $W_3^\mu(x)$ and $B^\mu(x)$ can be diagonalized performing a rotation by an angle θ_W (called either Weinberg angle or electroweak mixing angle),

$$\begin{pmatrix} Z^\mu(x) \\ A^\mu(x) \end{pmatrix} = \begin{pmatrix} \cos\theta_W & -\sin\theta_W \\ \sin\theta_W & \cos\theta_W \end{pmatrix} \begin{pmatrix} W_3^\mu(x) \\ B^\mu(x) \end{pmatrix}. \tag{1.4.14}$$

The angle is fixed such that the masses of the two new vector bosons (Z^μ and $A\mu$) are

$$M_Z^2 = \frac{(g^2 + g'^2)v^2}{4}, \qquad M_A^2 = 0. \tag{1.4.15}$$

The Weinberg angle is then set by the relative strengths of the coupling constants $\sin^2 \theta_W = g'^2/(g^2 + g'^2)$ and amounts to $\theta_W \simeq 28.2°$ (value taken from the Particle Data Group tables from 2020 [44]).

This choice gives the following Lagrangian density for the vector bosons mass terms,

$$\mathcal{L}_{\mathrm{M}} = \frac{g^2 v^2}{4} W_\mu^-(x) W^{+,\mu}(x) + \frac{(g^2 + g'^2)v^2}{8} Z_\mu(x) Z^\mu(x), \tag{1.4.16}$$

where only three of the four EW gauge bosons are massive.

The Lagrangian density for the field $\Phi(x)$ can be reformulated in order to have the vacuum state explicit. This is done by simply perturbing the vacuum state using a general function $H(x)$,

$$\Phi(x) = e^{it_A \frac{\alpha_A(x)}{v}} \begin{pmatrix} 0 \\ \frac{H(x)+v}{\sqrt{2}} \end{pmatrix}. \tag{1.4.17}$$

The function $H(x)$ is the Higgs scalar field and t_A the generators of SU(2) group representing the three degrees of freedom (Goldstone modes [45, 46, 47]) that are cancelled by the three massive gauge vector bosons, $W^\pm$ and Z. In this way the only remaining dynamical scalar field is the Higgs field whose Lagrangian density is,

$$\mathcal{L}_{\mathrm{H}} = \frac{1}{2}|\partial_\mu H(x)|^2 - \mathcal{V}\left(H^2(x)\right), \tag{1.4.18}$$

with

$$\mathcal{V}\left(H^2(x)\right) = \frac{1}{2}M_H^2 H^2(x) + \frac{M_H^2}{2v}H^3(x) + \frac{M_H^2}{8v^2}H^4(x). \tag{1.4.19}$$

The same symmetry breaking mechanism has to be applied to the masses of fermions which are not SU(2) invariant. This is true only for the weak force since it acts differently on the left- and right-handed fermions. These are mixed in the Dirac mass term:

$$m\,\overline{\psi}(x)\psi(x) = m\,\left(\overline{\psi}_L(x)\psi_R(x) + \overline{\psi}_R(x)\psi_L(x)\right). \tag{1.4.20}$$

In this case the mass term of a fermion can be rewritten including its coupling to the Higgs field,

$$\mathcal{L}_{\mathrm{m}_f} = \left(1 + \frac{H(x)}{v}\right) m_f \overline{\psi}_f(x)\psi_f(x). \tag{1.4.21}$$

Including the Higgs field it is then possible to write up the U(1)×SU(2) invariant Lagrangian density for the electroweak theory:

$$
\begin{aligned}
\mathcal{L}_{\mathrm{EW}} = &\sum_f \overline{\psi}_f(x)\left(i\slashed{\partial} - m_f - g\frac{m_f H(x)}{2M_W}\right)\psi_f(x) \\
&- \sum_f \overline{\psi}_f(x)\left[\frac{g}{2\sqrt{2}}\slashed{W}^+(x)(1-\gamma^5)\tau^+ + \slashed{W}^-(x)(1-\gamma^5)\tau^- \right. \\
&\left. + eQ_f\slashed{A}(x) + \frac{g}{2\cos\theta_W}\slashed{Z}(x)(v_f - a_f\gamma^5)\right]\psi_f(x) \\
&+ \left(M_W^2 W_\mu^-(x)W^{+,\mu}(x) + \frac{M_Z^2}{2}Z_\mu(x)Z^\mu(x)\right)\cdot\left(1 + g\frac{H(x)}{M_W} + g^2\frac{H^2(x)}{4M_W^2}\right) \\
&+ \mathcal{L}_{\mathrm{H}},
\end{aligned}
\tag{1.4.22}
$$

where $v = 2M_W^2/g$ according to Eq. (1.4.16) and f runs over the leptonic flavors.

In the case of quarks the situation is analogous but a bit more involved. The weak interaction acts differently on quarks than on leptons, as shown in Eq. (1.4.2). In this case it is necessary to take into account the quark flavor mixing given by the *Cabibbo-Kobayashi-Maskawa* (CKM) [41, 48] matrix,

$$
\begin{pmatrix} d'(x) \\ s'(x) \\ b'(x) \end{pmatrix} = \begin{pmatrix} V_{ud} & V_{us} & V_{ub} \\ V_{cd} & V_{cs} & V_{cb} \\ V_{td} & V_{ts} & V_{tb} \end{pmatrix} \begin{pmatrix} d(x) \\ s(x) \\ b(x) \end{pmatrix}. \tag{1.4.23}
$$

In terms of the new spinor vector on the r.h.s. of Eq. (1.4.23), the weak interaction takes the same form as it does for the leptons. Alternatively, the weak interaction current could be written as

$$j_q \propto V_{ij}\bar{u}_i(x)\gamma^\mu\left(1-\gamma^5\right)d_j(x), \tag{1.4.24}$$

where $u_i(x)$ and $d_j(x)$ distinguish respectively quarks with electric charge 2/3 and -1/3 of the positron electric charge. The complete U(1)×SU(2) gauge invariant Lagrangian can be written as done for the fermions by keeping the quark mixing matrix into account.

1.5   The Standard Model

Adding the QCD Lagrangian in Eq. (1.3.6) to the electroweak and Higgs Lagrangian in Eq. (1.4.22), one gets the famous U(1)×SU(2)×SU(3) invariant SM Lagrangian.

In total the SM describes the dynamics of 61 elementary particles of which 48 are fermions and 13 bosons. The fermionic matter is divided into coloured and colourless particles called, respectively, *quarks* and *leptons*. Each of these two groups is further split into three fermion generations made by electroweak isospin doublets, e.g. (e, ν_e) or (u, d). The mediators of the fundamental forces described by the SM are the photon (γ), gluon (g), Z boson, W boson and the Higgs (H) boson. This organization is summarized in Tab. 1.1.

The theories described so far impose limitations only on the mathematical form of the interaction between elementary particles. However, the number of different fermions does not have any theoretical constraint. So far they have been limited only by experimental evidence. The number of lepton generations is constrained by the very accurate measurement of the Z boson decay width into neutrinos [49], which is perfectly fitted only by a three lepton generations theory. The number of quarks is instead somewhat constrained by the observed CP violation in K^0 decay [50]. This can happen only with at least three generations of quarks. The observed CP-violation constrains the dimension of the quark mixing unitary CKM matrix, given in Eq. (1.4.23). Its unitarity requires the CKM matrix to have $n(n-1)/2$ independent parameters representing the mixing angles and $n(n+1)/2$ parameters that are complex phases. Of these parameters, $2n-1$ are not physically significant and can be reabsorbed into the quark fields. The total independent number of complex phases then are $1/2\,(n-1)(n-2)$. These are the cause of the observed CP-violation. It is straightforward to see then that only for at least three generations of quarks there can be CP-violation in K^0 decay. Even if more than three generations of quarks are in principle possible, there still haven't been any experimental observation indicating that this is the case.

1.6   Factorisation and Resummation of IR divergences

As discussed in Sec. 1.2, the UV divergences from loop diagrams are removed by renormalizing the theory. However, an observable can also suffer from infrared (IR) singularities. These come from the soft and/or collinear region of the phase space of either virtual or real emission diagrams involving massless particles. The procedure to treat these singularities is completely different from the regularization method used for the UV ones. At fixed order in perturbative theory the IR divergence is cancelled simply by taking into account both the squared amplitudes of the virtual and real emission. These two pieces, indeed, can be shown to have the exact same IR singularity but with opposite sign. This is discussed in many textbooks like in Ref. [51].

The cancellation of the IR singularities leaves the real emission contribution with

Flavor	Mass [GeV]	Charge	Isospin [L,R]	Spin
e^-	0.51×10^{-3}	-1	-1/2, 0	1/2
μ^-	0.106	-1	-1/2, 0	1/2
τ^-	1.78 ± 0.12	-1	-1/2, 0	1/2
ν_e	$< 1.1 \times 10^{-9}$	0	+1/2, $\cdot$	1/2
ν_μ	$< 0.19 \times 10^{-3}$	0	+1/2, $\cdot$	1/2
μ_τ	$< 18.2 \times 10^{-3}$	0	+1/2, $\cdot$	1/2
u	$2.16^{+0.49}_{-0.26} \times 10^{-3}$	2/3	+1/2, 0	1/2
d	$4.67^{+0.48}_{-0.17} \times 10^{-3}$	-1/3	-1/2, 0	1/2
c	1.27 ± 0.2	2/3	+1/2, 0	1/2
s	$93.4^{+8.6}_{-3.4} \times 10^{-3}$	-1/3	-1/2, 0	1/2
t	$4.18^{+0.03}_{-0.02}$	2/3	+1/2, 0	1/2
b	172.7 ± 0.3	-1/3	-1/2, 0	1/2
γ	$< 1 \times 10^{-27}$	0	0	1
g	0	0	0	1
$W^\pm$	80.377 ± 0.012	± 1	± 1	1
Z	91.1876 ± 0.0021	0	0	1
H	125.25 ± 0.17	0	1/2	0

Table 1.1: Physical values of the particles included in the standard model. The value for the particle masses are taken from the 2020 Particle Data Group tables reported in ref. [44].

a logarithmic enhancement in the soft and/or collinear region of the real emission phase space. In Fig. 1.2 it is shown, for a calculation at QCD NLO accuracy (red line), how observables sensible to real emission configurations fail to reproduce the data in the collinear region. The observables shown are the transverse momentum p_{T}^{ll} and the angular variable ϕ_η^*, defined in Ref. [52], of a lepton pair produced in a proton-proton collision (Drell-Yan process), $pp \to l\bar{l}$ with $l = e^-, \mu^-$, and a center of mass energy of $\sqrt{s} = 13\,\mathrm{TeV}$. The discrepancy with data in that region of the phase space comes from the IR logarithmic enhancement caused by logarithms of the type,

$$\alpha_s^n \log^{2n}(x) \quad \text{and} \quad \alpha_s^n \log^{2n-1}(x), \tag{1.6.1}$$

where x is a function of the kinematic variables of the process that approaches 0 in the soft and/or collinear region of the phase space. The terms proportional to
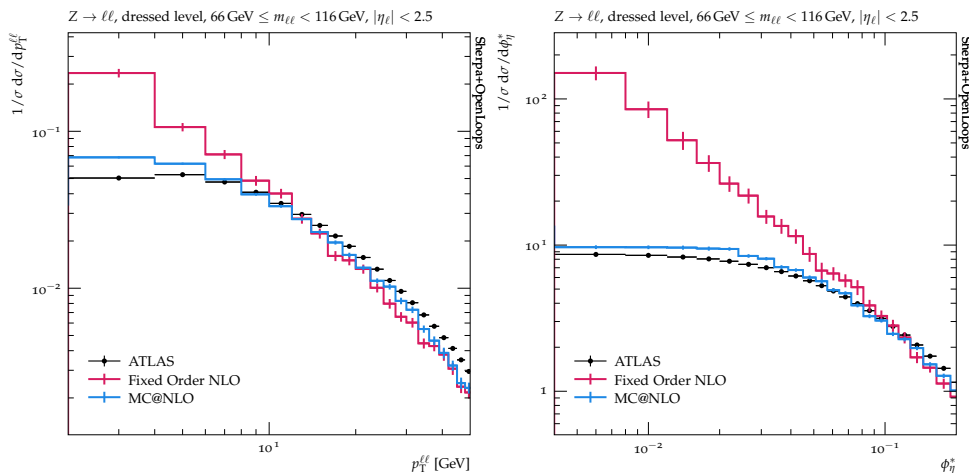
Figure 1.2: In the figures are shown the transverse momentum p_{T}^{ll} and the angular variable ϕ_η^* of the lepton pair in proton-proton collisions at $\sqrt{s} = 13\,\mathrm{TeV}$. The plots show the comparison of the QCD NLO calculation at fixed order and matched to the parton shower using the MC@NLO method compared against experimental data ATLAS data from the 2019 analysis of Ref. [53].

$\alpha^n \log^{2n}(x)$ are the leading logarithmic accuracy (LL) while the terms proportional to $\alpha^n \log^{2n-1}(x)$ are the next-to-leading logarithmic accuracy (NLL).

Nonetheless, these logarithms can be factorized from a real emission squared matrix element at every perturbative order. The factorisation of the IR singular pieces can be shown by taking the soft-collinear approximation of a generic real emission process. To give an example it is enough to look at the emission of a photon with momentum k off the incoming particles with momenta p_1 and p_2. The matrix element for this process is,

$$- ie\, \bar{u}(p_1) \not{\varepsilon}(k) \frac{\not{p}_1 - \not{k}}{(p_1 - k)^2} \mathcal{M}(p_1 - k, p_2; P_f) + (p_1 \leftrightarrow p_2)$$
$$= ie\, \frac{\varepsilon(k) \cdot p_1}{p_1 \cdot k} \bar{u}(p_1) \mathcal{M}(p_1 - k) + (p_1 \leftrightarrow p_2) + \text{reg. terms.} \qquad (1.6.2)$$

In the limit of a soft emission, $k^\mu \to 0$, it can be further simplified and we get

$$i\, e\, \varepsilon_\mu(k) \left[\frac{p_1^\mu}{p_1 \cdot k} + \frac{p_2^\mu}{p_2 \cdot k} \right] \mathcal{M}_0(p_1, p_2; P_f). \qquad (1.6.3)$$

Here $\mathcal{M}(p_1, p_2; P_f)$ includes also the incoming spinor $\bar{u}(\cdot)$, and it now represents the matrix element of the leading order. P_f, indicates all the external final state momenta. Squaring Eq. (1.6.3) and summing over the photon helicities, we get the

well known Eikonal term of the soft-collinear emissions,

$$\left[e^2 \frac{p_1 \cdot p_2}{(p_1 \cdot k)(p_2 \cdot k)} \right] |\mathcal{M}_0(p_1, p_2; P_f)|^2 = J(p_1, p_2, k) |\mathcal{M}_0(p_1, p_2; P_f)|^2 . \qquad (1.6.4)$$

As expected, the function $J(p_1, p_2, k)$ is singular when the emitted particle is either collinear to the incoming particles, $(p_1 \cdot k)(p_2 \cdot k) \to 0$, or soft, $k \to 0$. This same approximation can be repeated for an arbitrary number of sequential soft-collinear emissions. For a generic number of emissions, Eq. (1.6.4) becomes,

$$\frac{1}{n!} \left[J(p_1, p_2, k) \right]^n |\mathcal{M}_0(p_1, p_2; P_f)|^2 , \qquad (1.6.5)$$

where $n!$ accounts for the over counting of identical emissions.

The sum of any possible number of soft/collinear emissions opens the possibility to exponentiate IR divergent logarithms making the fixed order result finite. In Fig 1.2 the NLO QCD fixed order accurate calculation is compared against the NLO QCD calculation matched to the parton-shower, which is a numerical technique to resum soft and/or collinear QCD emissions. From the plots it is clear that the effects of including multiple QCD emissions is to dampen the logarithmic enhancement of the fixed order calculation improving the agreement with the experimental data.

The resummation of these logarithms can be done either analytically or numerically. However, in this work we will focus on the numerical method using the so-called parton-shower technique.

Chapter 2

Event Generation using Monte Carlo methods

In the previous chapter the theory to model the quantum dynamics of the elementary particles discovered so far has been introduced. In order to make predictions with it, a direct mapping from a SM prediction to experimental signatures is needed. High energy experiments, such as ATLAS and CMS at LHC, SLAC at Stanford, and CDF and D0 at Fermilab, are collision experiments where the subject of study are the scattering processes in either hadron-hadron, electron-hadron, or electron-positron collisions. Monte Carlo (MC) event generators are the theoretical tools explicitly built to fill this gap.

MC event generators are used to simulate every step of a two-body collision process. They start by evaluating the hard scattering process that is modelled using the S-matrix elements Eq. (1.2.1) in perturbation theory. In this step we have the direct link to the SM fixed perturbative order predictions used to study many of its features. The incoming and outgoing particles of the scattering process are then let to radiate both QCD and QED particles until the typical hadronic energy scale is reached. At this point the event generator starts the hadronisation process. In this step, the newly produced final states are organized into hadrons, followed by the hadronic decay chain into more stable particles detected in experiments. The conversion from MC generated events and the signals recorded by detectors, or vice versa, are usually done on the experimental side. The simulation of the detector response is usually done using the software GEANT4 [54, 55, 56]. The most common general purpose Monte Carlo event generators are SHERPA [57], HERWIG [58, 59], PYTHIA [60]

The aim of this thesis is to improve the predictions of a general MC simulation, performed with the computer program SHERPA, by including higher order perturbative corrections. Therefore, in this Chapter, are given general concepts behind the techniques used in this specific general-purpose event generator. Particular attention is given to the techniques used for producing an arbitrary number of QCD final state particles, using the parton-shower approach, and on the calculation of QCD

perturbative corrections. On the other hand, EW corrections are not discussed here in order to help the reader following better the main results of this thesis. These corrections will be discussed in Chap. 4.

2.1 Multiple QCD Emissions Simulation using a Parton Shower

A large part of the detected signal in collision experiments comes from hadronic jets, resulting from QCD jets hadronisation. This makes the modelling of jets a crucial part of an MC simulation. As anticipated in Sec. 1.6 it is possible to use numerical methods to include an arbitrary number of soft and/or collinear QCD emissions using the method called *parton-shower*, that is based on the factorisation property discussed in Sec. 1.6. This method treats multiple QCD emissions as a Markov chain, meaning that they are modelled as iterative random events where each one depends only on the the state of the previous event. This technique is based on the Sudakov form factor [61], $\Delta_a(t_0, t)$, that gives the probability of no emission in the energy range $[t_0, t]$,

$$\Delta_a(t_0, t) = \exp\left\{ -\sum_b \int_{t_0}^{t} \frac{dt'}{t'} \int dz \frac{\alpha_s}{2\pi} \hat{P}_{ba}(z) \right\}, \tag{2.1.1}$$

where t is the virtuality of the emitting parton p_a and z the emitting parton energy fraction $z = E_b/E_a = 1 - E_c/E_a$ (the subscripts b and c refer to the products of the branching) and $\hat{P}_{ab}(t', z)$ is the non-regularized Altarelli-Parisi (AP) splitting function [62] for the partons a and b. Non-regularized here means that they are still IR divergent. In the context of the parton-shower, this IR divergence is removed by simply applying a cut-off to the z variable, $\epsilon(t, t_0) < z < 1 - \epsilon(t, t_0)$ in the integral of (2.1.1). The cut-off, which is to some extent arbitrary, can be interpreted as a separation between *resolvable* and *unresolvable* splittings.

The AP splitting functions come from the factorisation of singular collinear terms of a QCD real emission squared matrix element. The collinear limit of a partonic emission is reached for small parton branching opening angles, *i.e.*

$$\theta \to 0 \quad \Rightarrow \quad t = p_{T,a}^2 \to 0. \tag{2.1.2}$$

In this limit the squared real emission matrix element factorizes as

$$|M_{n+1}|^2 \underset{\text{coll. lim.}}{\simeq} |M_n|^2 \frac{\alpha_s}{2\pi} \hat{P}_{ab}(z), \tag{2.1.3}$$

where ab are the emitter and emitted partons. In Eq. (2.1.3), the integration over the azimuth angle and the summation over the spin and polarisation of the external

particles is understood.

The probabilistic interpretation of the Sudakov form factor can be understood from the *Dokshitzer-Gribov-Lipatov-Altarelli-Parisi* (DGLAP) equation [62, 63, 64]. This equation describes the energy evolution of PDFs that is given by

$$t\frac{\partial}{\partial t}\left(\frac{f_a(x,t)}{\Delta_a(t_0,t)}\right) = \frac{1}{\Delta_a(t_0,t)}\sum_b \int \frac{dz}{z}\frac{\alpha_s(t)}{2\pi}\hat{P}_{ab}(z)f_b(x/z,t). \qquad (2.1.4)$$

Its integrated form gives the easily interpretable equation,

$$f_a(x,t) = \Delta_a(t_0,t)f_a(x,t_0) + \sum_b \int_{t_0}^t \frac{dt'}{t'}\frac{\Delta_a(t_0,t)}{\Delta_a(t_0,t')}\int \frac{dz}{z}\frac{\alpha_s(t')}{2\pi}\hat{P}_{ab}(z)f_b(x/z,t').$$
$$(2.1.5)$$

It is possible to visualize that a branching has happened at a certain energy t by looking at the PDFs $f_a(x,t)$ energy fraction x. A change in x clearly means that a splitting has happened since a parton's energy fraction has changed. Then, the first term in the equation keeps the energy fraction x unchanged. Therefore, it represents the PDF's evolution from t_0 to t where no branching has happened. The initial PDF $f_a(x,t_0)$ gets just scaled by the Sudakov form factor $\Delta_a(t_0,t)$, meaning that it gives the probability of no-branching between the energies $[t_0,t]$. The second term, instead, has the PDF multiplied by the differential weight,

$$\sum_b \frac{dt}{t}\frac{dz}{z}\frac{\alpha_s(t)}{2\pi}\hat{P}_{ab}(z). \qquad (2.1.6)$$

This is interpreted as the differential splitting probability of the incoming parton a with virtuality t and energy fraction z after the emission.

The factor $\Delta_a(t_0,t)/\Delta_a(t_0,t') = \Delta_a(t,t')$, instead, gives the probability of no-branching between t' and t. These two pieces combined give the probability that a parton with virtuality t has split exactly once.

What a parton-shower does is to evolve any on-shell parton taking part in the hard scattering process using a *forward* evolution for final-state partons and a *backward* evolution for the initial-state partons. The main difference between these two evolutions is that in the forward evolution the probability of having just one soft and/or collinear emission is as for Eq. (2.1.5), *i.e.* $\Delta_a(t)/\Delta_a(t')$, while in the backward evolution the single emission form factor is modified by including also the parton's density function as $(f_a(x,t')\Delta(t_0,t))\,/\,(f_a(x,t)\Delta_a(t_0,t'))$ [65, 66].

What a parton-shower does is to evolve any on-shell parton in a hard scattering process according to Eq. (2.1.5), where the factor $\Delta_a(t)/\Delta_a(t')$ is randomly generated by a uniform distribution over the interval $[0,1]$. After a branching has occurred the new particle is added to the ensemble of the final state particles and the procedure is repeated iteratively until a target energy is reached.

Following Eq. (2.1.5) the parton-shower can be easily applied to a leading order calculation. For an n-particle final state the leading order differential cross-section matched to the parton-shower reads

$$d\sigma^{\mathrm{LO+PS}} = \mathrm{d}\Phi_n B(\Phi_n) \sum_{ab} \left[\Delta_a(t_0, t) + \int_{t_0}^{t} \frac{dt'}{t'} \Delta_a(t, t') \int \frac{dz}{z} \frac{\alpha_s}{2\pi} \hat{P}_{ab}(z) \right], \quad (2.1.7)$$

where $t = t(\Phi_n)$ and the indices a and b run over all the final state partons. $B(\Phi_n)$ also contains the process' luminosity, flux factor and the symmetry factor.

2.2 Matching NLO Accurate Matrix Elements to a Parton Shower

Before discussing how next-to-leading order (NLO) accurate calculations can be matched to a parton-shower it is important to discuss how an observable at the NLO accuracy is numerically evaluated.

Following the discussion in Sec. 1.6, IR divergences can only be cancelled including both the virtual and real emission corrections to a process. Numerically, this is not so straightforward since the virtual and real corrections have different phase spaces and a Monte Carlo event generator is designed to produce fully differential events. This means that virtual events are generated separately from the real emission one leading to possible events with infinite weight. In order to make both contributions IR finite during the event generation phase, NLO accurate calculations are performed implementing subtraction terms that cancel the IR divergence of each piece without affecting the NLO accuracy of the combined result.

The subtraction terms are IR-singular functions of the real emission phase space that are subtracted from the real emission correction and added to the virtual correction, integrating them over the one-emission phase space. They are labelled as $D^S(\Phi_B, \Phi_1)$, and the integrated ones as $I(\Phi_B) = \int d\Phi_1 D^S(\Phi_B, \Phi_1)$. The choice of these functions is completely arbitrary as long as they are able to exactly cancel the IR divergences of a process.

An NLO accurate calculation is then done by producing events according to

$$\begin{aligned} d\sigma^{\mathrm{NLO}} = d\Phi_n \Big[B(\Phi_n) + V(\Phi_n) + I(\Phi_n) \Big] \\ + d\Phi_{n+1} \Big[R(\Phi_{n+1}) - D^S(\Phi_n, \Phi_1) \Big]. \end{aligned} \quad (2.2.1)$$

Here $V(\Phi_n)$ is the virtual correction that also includes the mass-factorisation terms of the PDFs and $R(\Phi_{n+1})$ the real emission correction. Events generated according to the first term of the r.h.s. of Eq. (2.2.1) are called S-type events, and those generated from the second term are called H-type events. Generating events using

this approach assures that inclusive observables are NLO accurate and IR-finite. However, the result still suffers from large logarithms in the soft/collinear region of the real emission phase space, as discussed in Sec. 1.6.

Some NLO QCD subtraction methods developed so far include the antenna subtraction [67, 68], the FKS subtraction scheme [69] and the Catani-Seymour dipole subtraction [70, 71]. The latter is implemented in SHERPA [72]. Therefore, we are going to briefly discuss this subtraction method specifically.

The Catani-Seymour subtraction method is based on the *dipole factorisation formula* [70, 71] presented in 1997 by S. Catani and M. H. Seymour in Ref. [70]. This formula reproduces exactly the IR singularities of an $n+1$ final state squared matrix element. In the singular regions of the phase space, collinear singularities happen for pairs of partons, called emitter and emitted, with the following singular structure,

$$D_{ik,j} \propto -\frac{1}{2p_i p_k} \quad \text{and} \quad D_{jk,i} \propto -\frac{1}{2p_j p_k}. \tag{2.2.2}$$

Dipoles for the soft singularities, instead, also need a spectator. This is due to the fact that soft singular terms factorize only as colour dipoles, and therefore the singularity is given by terms of the following form,

$$D_{ik,j} \propto -\frac{1}{(p_i p_k)(p_j p_k)}. \tag{2.2.3}$$

As an example, the complete expression of a massless soft/collinear singular dipole where the emitter and emitted partons are both final states particles is given by the following expression,

$$D_{ik,j} = -\frac{1}{2p_i p_k}\, {}_m\langle 1,\ldots,\tilde{ik},\ldots,\tilde{j},\ldots,m+1| \frac{T_j \cdot T_{ik}}{T_{ik}^2} V_{ik,j} |1,\ldots,\tilde{ik},\ldots,\tilde{j},\ldots,m+1\rangle_m. \tag{2.2.4}$$

Here T_j and T_{ik} are the colour charges of the spectator and emitter, while $V_{ik,j}$ is a dimensionless non-singular matrix in the emitter's spin and colour space. From the m-parton final state the partons i and k are combined into the "mother" particle (the emitter) $\tilde{ik}$. The spectator j is instead mapped into $\tilde{j}$ with a momentum different from the initial j-th parton momentum. The momentum of $\tilde{ik}$ and $\tilde{j}$ are defined in order to grant all partons to be on-shell and to fulfill the momentum conservation $\tilde{p}_{ik} + \tilde{p}_j = p_i + p_j + p_k$. An example of this splitting is given in Fig. 2.1 The cases of initial state emitter with final state spectator and both initial state emitter and spectator are left out for clarity.

The parton-shower matching to a NLO accurate calculation is done very similarly to the LO case. The main difference is that in this case we have to be careful with double counting between the parton-shower single emission off S-type events and the actual hard real emission, especially in the soft and/or collinear region of the

phase space. The two main approaches to avoid double counting when matching NLO accurate matrix elements to a parton-shower are the POWHEG method [73, 74] and the MC@NLO method [75].
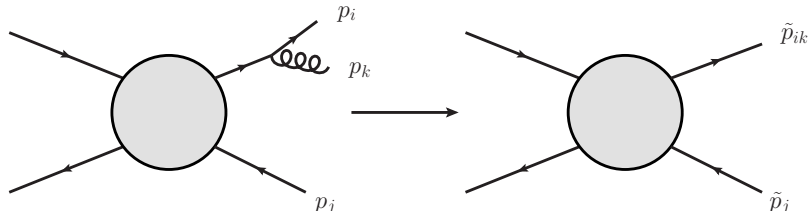

Figure 2.1: Examples of a final state dipole splitting and how momenta are reorganized.

2.2.1   MC@NLO Method

In order for this method to be as general as possible, it uses a modified NLO subtraction scheme to avoid the double counting of soft and/or collinear single-emissions. This modified subtraction works by splitting the real emission contribution into its infrared-singular $D^A(\Phi_n, \Phi_1)$ and infrared-finite $H(\Phi_{n+1})$ pieces, $R(\Phi_{n+1}) = H(\Phi_{n+1}) + D^A(\Phi_n, \Phi_1)$ [76]. The virtual correction is instead still regularized by the integrated CS dipoles $I(\Phi_n)$, as discussed previously. The singular part of the real emission is then integrated over and added to the S-type events as follows,

$$\bar{B}(\Phi_n) = B(\Phi_n) + V(\Phi_n) + I(\Phi_n) + \int d\Phi_1 \left(D^A(\Phi_n, \Phi_1) - D^S(\Phi_n, \Phi_1) \right). \quad (2.2.5)$$

Generating the first parton-shower emission using the new splitting functions $D^A(\Phi_n, \Phi_1)$ ensures the NLO accuracy of the method and avoids double counting of soft and/or collinear emissions. Consequently, in the MC@NLO method events up to the first real emission are generated according to

$$d\sigma^{\mathrm{MC@NLO}} = d\Phi_n \bar{B}(\Phi_n) \left[\bar{\Delta}(t_0) + \int_{t_0} d\Phi_1 \bar{\Delta}(t) \frac{D^A(\Phi_n, \Phi_1)}{B(\Phi_n)} \right]$$
$$+ d\Phi_{n+1} H(\Phi_{n+1}), \quad (2.2.6)$$

where $\bar{\Delta}(t)$ is the Sudakov form factor with splitting kernels given by $D^A(\Phi_n, \Phi_1)/B(\Phi_n)$. After the first emission, the parton-shower is let to radiate using its standard definition given in eq. (2.1.7).

The original MC@NLO method used the AP parton-shower splitting kernels to subtract the IR singularities of the real emission squared matrix elements. With this

choice it is possible to resum all the logarithms at the leading-logarithmic accuracy (1.6.1) in the large-N_c limit. However, this might still lead to infinite results since the modified subtraction of the real emission contribution has not cancelled the singular sub-leading colour configurations. One can solve this by making a different choice for $D^A(\Phi_n, \Phi_1)$ to better match the colour structure of the real emission. The MC@NLO method implemented in SHERPA uses the Catani-Seymour dipoles [77] for the parton-shower first emission. This is called the S-MC@NLO method [78]. This choice guarantees that the first parton-shower emission reproduces the right soft and/or collinear limit of the real emission matrix element.

2.2.2   POWHEG Method

In this method the choice for $D^A(\Phi_n, \Phi_1)$ is the squared real matrix element itself. This choice helps to simplify the parton-shower matching since it is done like in Eq. (2.1.7), by substituting

$$B(\Phi_n) \rightarrow \bar{B}(\Phi_n) = B(\Phi_n) + V(\Phi_n) + I(\Phi_n) + \int d\Phi_1 \big(R(\Phi_{n+1}) - D(\Phi_n, \Phi_1)\big). \quad (2.2.7)$$

Therefore, the parton-shower matching with an NLO accurate calculation in the POWHEG method is done according to,

$$d\sigma^{\text{POWHEG}} = d\sigma^{\text{NLO}} \left[\bar{\Delta}(t_0) + \int_{t_0} d\Phi_1 \bar{\Delta}(t) \frac{R(\Phi_{n+1})}{B(\Phi_n)} \right], \quad (2.2.8)$$

where,

$$\bar{\Delta}(t) = \exp \left\{ -\int_{t_0} d\Phi_1 \frac{R(\Phi_{n+1})}{B(\Phi_n)} \right\}. \quad (2.2.9)$$

A major drawback of this approach is that in the Sudakov form factors there are exponentiated terms that do not factorize at every perturbative order. This usually leads to a harder radiation spectrum compared to the MC@NLO method and generally may lead to unexpected results. However, since its first proposal this method has been improved by limiting the region of activity of the parton-shower. This helps to improve the agreement between the two methods and with the fixed order calculation's hard emission spectrum. A detailed comparison of the POWHEG and MC@NLO methods has been presented in [78].

2.3   Merging Multi-Jet Matrix Elements

Despite the parton-shower being able to reproduce the soft and collinear behavior of an arbitrary number of QCD emissions, its validity is restricted to a specific region of

the phase space. Consequently, the parton-shower is not able to accurately describe multiple hard jets or wide angle parton splittings. To have a more accurate description of the hard emission energy spectrum, the actual matrix elements for higher multiplicities are needed. Moreover, these have to be carefully included in order to avoid overlapping in phase space regions populated by both hard and parton-shower emissions. This phase-space overlapping is avoided by multi-jet merging techniques, that generally consist in separating *resolvable* and *non-resolvable* emissions using a jet resolution scale, Q_{cut}. The phase space region below Q_{cut} is populated by a truncated parton-shower while the region above Q_{cut} is populated by the hard emission matrix elements. Some algorithms developed to merge multi-jet matrix elements into one event are the CKKW [79, 80], CKKW-L [81, 82] and MLM [83] methods and their extensions to NLO matrix elements [84, 85, 86].

In the SHERPA event generator, the multi-jet merging algorithm implemented is a generalisation of the CKKW approach presented in [87] for LO merging and [84, 85] for NLO QCD merging. SHERPA performs a backward-clustering using the k_T-algorithm to calculate the corresponding separation scale Q_{n+m}, where n indicates the core process multiplicity and m the additional number of jets. This scale is then compared with the user defined Q_{cut}. The jet multiplicity that survives the merging cut is then evaluated, and sets the starting conditions for the truncated parton-shower. A direct benefit of this method is that the renormalisation and factorisation scales are dynamically set for the additional multiplicities. This accommodates the multiscale nature of multiple real emissions.

When the multi-jet matrix elements used in the calculation are all at LO, events are generated according to the following formula,

$$\sigma^{\text{MEPS@LO}} = \sum_n \int d\Phi_n B_n(\Phi_n) \mathcal{F}_n(\mu_Q^2; Q_{\text{cut}}). \tag{2.3.1}$$

Here $\mathcal{F}_n(\mu_Q^2; Q_{\text{cut}})$ is the truncated parton-shower functional that reads

$$\mathcal{F}_n(\mu_Q^2; Q_{\text{cut}}) = \Delta(t_c, t) + \int_{t_c}^t d\Phi_1' K_n(\Phi_1') \Theta\left(Q_{\text{cut}} - Q_{n+1}(t')\right) \Delta(t', t) \mathcal{F}_{n+1}(t'), \tag{2.3.2}$$

where $\mathcal{F}_n(t)$ is the truncated parton-shower generator. The scale $Q_{n+1}(t')$ used in the truncated parton-shower is the smallest reconstructed emission scale for the $n+1$ new particle ensemble. For NLO accurate matrix elements included in the calculation it is necessary to distinguish also between configurations of the real emission correction of the NLO matrix elements and higher multiplicities present in the calculation. Since in SHERPA NLO accurate processes are matched to the parton-shower using the MC@NLO method, the multi-jet merged calculation modifies the H-type events in order to avoid populating the same phase space of higher multiplicities. Therefore,

H-type events are constrained to populate only the phase space region below Q_{cut}. In this way inclusive observables are evaluated at the right NLO accuracy while higher multiplicities matrix elements are let to populate the hard-emission's phase space. The constraint on the H-type events is done by simply applying the cut $\Theta(Q_{\text{cut}} - Q_{n+1})$ to the H-type events of the Mc@Nlo method. A qualitative representation of S- and H-type events in the multijet-merging method is given in Fig. 2.2.
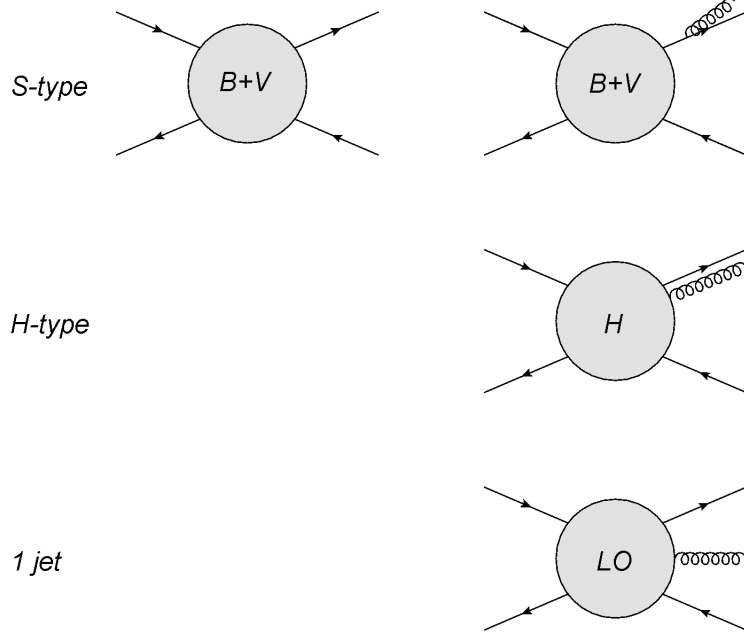
Figure 2.2: Examples of emissions contribution in S-, H-type and 1-jet events. S-type events contain contributions from the core process and its first parton-shower emission, while the real emission of the NLO correction, *i.e.* an H-type event, is constrained to be in a more soft and/or collinear emission region. The hard emission is instead given by the correct full 1-jet matrix element.

The NLO accurate part of the multi-jet merged calculation is then evaluated according to

$$\sigma^{\text{MEPS@NLO}} = \int d\Phi_n \bar{B}_n \times$$
$$\times \left[\bar{\Delta}(t_c, \mu_Q^2) + \int_{t_c}^{\mu_Q^2} d\Phi_1' \bar{K}(\Phi_1') \Theta(Q_{\text{cut}} - Q_{n+1}) \bar{\Delta}(t', \mu_Q^2) \mathcal{F}_{n+1}(t') \right]$$
$$+ \int d\Phi_{n+1} H(\Phi_{n+1}) \Theta(Q_{\text{cut}} - Q_{n+1}) \mathcal{F}_{n+1}(\mu_Q^2, Q_{\text{cut}}),$$
$$(2.3.3)$$

where $\bar{\Delta}(t_c, \mu_Q^2)$ and $\bar{K}(\Phi_1')$ are respectively the modified Sudakov form factor and

the modified splitting kernels used in the MC@NLO method (2.2.6) in order to reproduce exactly the soft and collinear structure of NLO QCD matrix elements. Moreover, higher LO multiplicities are supplemented with a local k-factor that depends on the phase space of the highest multiplicity evaluated at NLO. This k-factor has the following differential form,

$$k_n(\Phi_n, \Phi_{n+1}) = \frac{\bar{B}_n(\Phi_n)}{B_n(\Phi_n)} \left(1 - \frac{H_n(\Phi_{n+1})}{B_{n+1}(\Phi_{n+1})}\right) + \frac{H_n(\Phi_{n+1})}{B_{n+1}(\Phi_{n+1})}. \qquad (2.3.4)$$

with n the multiplicity of the highest NLO-multiplicity.

2.4   State-of-the-art of NNLO Accurate Predictions

In recent years many processes have been calculated at the QCD NNLO accuracy, both at fixed order and matched to a parton-shower. An example is the Drell-Yan di-lepton production. This is known at QCD NNLO accuracy for both single boson production [88, 89, 90] and the boson production associated with a jet [91, 92]. The NNLO correction of this process, for example, helps to reduce significantly the theoretical uncertainty on the Z boson transverse momentum as shown in Ref. [93]. Such improvement in the theoretical prediction is crucial for the upcoming high precision measurements at LHC experiments. Other processes known at NNLO are, for example, di-photon production [94, 95], top-pair production [96], off-shell di-boson production [97, 98, 99] and Higgs production [100].

Technically a completely automated method to generate and evaluate NNLO corrections has not yet been developed. All the calculations mentioned above are specific analytical solutions implemented in matrix element providers such as MA-TRIX [101] and MCFM [102, 103, 104]. The difficulties to automate the evaluation of NNLO corrections is due to the presence of two-loop integrals. These are not yet possible to be automatically generated and evaluated due to the very complicated two-loop structure, including the multiscale nature of the integrals and reduction to master integrals. However, the development of general IR-subtraction schemes has been recently very active. Some developed methods are the Antenna subtraction [105], nested soft-collinear [106], geometric subtraction [107] and local analytic sector subtraction [108]. These subtraction schemes are also very useful in the development of NNLO accurate calculations matched to a parton-shower. Nonetheless, in this case the parton-shower matching has not yet been completely generalized, which is true also for the dipole shower used in SHERPA. Some available methods are *reweighted* MiNLO [109, 110], UNNLOPS [111] and MINNLOPS [112, 113, 114]. The reweighted MiNLO and MiNNLOPS approach are both based on merging NLO+PS matrix elements for colourless final states up to 1-jet with the 0-jet multiplicity evaluated at NNLO. Differently from the multi-jet merging presented in Sec. 2.3 this method does not require any user-defined merging scale, but instead the merging is done according to information from the p_T-resummation. The UNNLOPS, instead,

uses a modification of the unitarized CKKW algorithm UNLOPS [115]. Here, the NNLO accurate calculation is regularized with a q_T-subtraction where the *zero-q_T* has the exclusive NNLO calculation and q_T values above it are at the right NLO QCD accuracy.

2.5 The SHERPA Event Generator

SHERPA is a modular `C++` code that simulates every step of a high energy collision process where either the incoming particles are hadrons or leptons. The modular structure of the code allows for easy improvements and modifications of the various modules [57, 116, 117, 118, 119, 120]. Moreover, it gives to the user the possibility to easily add plugins of their own such as new parton-showers, physical models or external matrix element generators.

At the moment SHERPA has an explicit implementation of the SM and some of its extensions, such as the Minimal Supersymmetric Standard Model (MSSM), the ADD model for large extra dimensions and a set of operators used to parametrize anomalous triple and quartic EW gauge boson self couplings. SHERPA's modular structure also allows the user to implement other BSM models by defining the BSM model parameters and the new Feynman rules.

SHERPA starts by handling the incoming beams with the module `BEAMS`. Here if there are initial state hadrons, SHERPA can use either internal PDFs or the external code LHAPDF [121] which offers a very large set of PDFs.

The hard scattering matrix elements can be generated by both the `AMEGIC` [122] and `COMIX` codes. These are in-house tree-level matrix-element generators. `AMEGIC` is the original matrix-element supplier of SHERPA. It generates helicity amplitudes from Feynman diagrams using the methods presented in Refs. [123, 124]. `COMIX` is the newer fully automated tree-level matrix-element generator based on the colour-dressed Berends-Giele recursion relations [125]. This method uses a recursive colour sampling which makes it very suitable for high multiplicity QCD matrix elements calculations. For this reason `COMIX` is used as the default generator for QCD high-multiplicity calculations while `AMEGIC` is mostly used for lower QCD multiplicity processes. Both these generators come with their own phase-space integrators [122] based on multi-channel MC algorithms with VEGAS optimisation [126]. With the future release of SHERPA (version 3.0.0) a new module will be included, `EXTAMP`, which is a general interface to external matrix-element providers. This module is particularly useful for processes that can not be generated with the default matrix-element generators, such as for example loop-induced processes where the lowest order contribution already contains a loop. This module can also be interfaced to analytical matrix element providers such as MCFM, which can give faster semi-analytic matrix element evaluation compared to the internal numerically evaluated ones. The phase space integration is however not part of the module, and therefore it has to rely on other phase space integration libraries included in SHERPA, such as RAMBO [127]. Another possibility is to generate phase space integration libraries

using `AMEGIC`. This generates the phase space integration libraries for a generic final state, optimized for the tree-like processes it knows. These libraries can be loaded at run-time as external libraries making them available to the matrix element generator used by the `EXTAMP` module. Part of this thesis' work has been to validate and update this module for the future release of SHERPA.

After the evaluation of the hard scattering process SHERPA performs the parton showering of both final and initial states. The QCD radiation in this phase is handled by the `CSSHOWER++` and `MCATNLO` modules [77]. These implement the dipole shower discussed in Sec. 2.1 for both LO and NLO parton-shower matching. The QED radiation, instead, is handled by the `PHOTONS++` module which applies the D. R. Yennie, S. C. Frautschi and H. Suura (YFS) resummation [128] on the leptonic final states [129, 130]. This method will be discussed in more details in Sec. 4.3. Besides the hard scattering process and its matching to the parton-shower, SHERPA also account for multiple particle interactions (MPI), which are semi-hard collisions, and uses an independent parton-shower on these events as well. This part is taken care from the `AMISIC++` module [131].

Finally, when the parton-shower has reached the hadronic scale, SHERPA performs the hadronisation of the particles produced by the parton-shower. This is done by the module `AHADIC++` [132], using the cluster-fragmentation model presented in Ref. [133, 134]. Consequently, the identified hadrons, and tauons, are let to decay into more stable particles by the module `HADRONS++`. The hadron decay chain is performed using form factors from heavy-quark effective theory and light-cone sum rules [135, 136], while τ-decays are modelled using the Kühn-Santamaria model [137] and the form-factor parametrisation from Resonance Chiral Theory [138].

Chapter 3

Diboson production at the Large Hadron Collider

Processes involving the production of two electroweak bosons constitute a very important test bed of the EW sector of the SM and BSM searches. These processes are a direct way to test the EW spontaneous symmetry breaking, and its gauge invariance. This is due to the fact that EW gauge boson self-coupling diagrams and their interaction with the Higgs boson are directly accessible. Some examples of these self-coupling diagrams are the Z-boson decay into W^+W^- or the four-body interaction vertices like $W^+W^- \to ZZ$ or $W^+W^- \to W^+W^-$. In Fig. 3.1 two examples for di-boson production diagrams in a parton-parton scattering that involve EW gauge boson self-couplings are shown. The diagram on the left shows the decay of an intermediate Z boson into a pair of W bosons in a gluon fusion process. This diagram is part of the NNLO QCD correction of the $pp \to W^+W^-$ process. The diagram on the right, instead, gives access to the quartic EW self coupling in the production of two Z bosons associated with two jets. This process is part of the NLO EW correction to the $pp \to ZZjj$ process. For completeness, the same quartic EW coupling could be accessed from the ZZ production in gluon fusion as virtual EW correction to the $gg \to ZZ$ process. In any case, this diagram has not yet been calculated due to the complications of treating massive two-loop integrals as explained in Sec. 2.4. The importance of testing the EW gauge bosons self-coupling terms in the SM Lagrangian is highlighted in Chap. 1

Access to gauge boson self coupling diagrams makes the production of two EW bosons a very useful tool also to test BSM theories. An example of this is the triple gauge boson coupling between three neutral vector bosons [4]. This interaction vertex is not allowed by the SM, but it could be explained by modifications of it, as described in [139]. Also many experimental analyses focus on the di-boson production to find signs of any anomalies [140, 141, 142, 143].

The di-boson final state is also the main channel to study Higgs bosons, and it constitutes a major background in Higgs boson measurements [144, 145, 146, 147]. Moreover, direct Higgs boson production diagrams have a sizeable destructive inter-
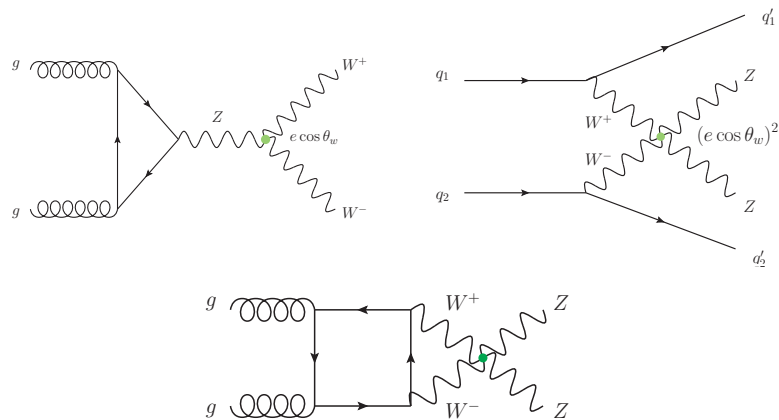
Figure 3.1: Examples of di-boson production in proton-proton collision with triple and quartic EW couplings. The diagram on the left shows the decay of an off-shell Z boson into a pair of W bosons through gluon fusion at $\mathcal{O}\left(\alpha_s^2\alpha^2\right)$. The right and lower diagrams give an example of quartic gauge boson self coupling in the production of two Z bosons both at the order at $\mathcal{O}\left(\alpha_s^2\alpha^3\right)$. The first shows the di-boson production associated with two jets, while the second shows the EW virtual correction to the ZZ production in gluon fusion.

ference with the continuous di-boson production [7]. Accurate modelling of di-boson production is therefore necessary for high precision Higgs physics measurements, *e.g.* evaluating its decay width [148, 149].

All these aspects together with the next LHC upgrade, which is expected to increase the current luminosity of about $300\,\mathrm{fb}^{-1}$ to $3000\,\mathrm{fb}^{-1}$ in the decade $2028-2038$ [150], make an accurate and complete modelling of the di-boson production channels fundamental for future studies.

In this thesis the focus is put on just one specific four-lepton final state for the di-boson production. This is the $e^+e^-\mu^+\mu^-$ four-lepton final state. Since this final state also contains intermediate virtual photons, $Z\gamma^*$ and $\gamma^*\gamma^*$, when referring to ZZ production also virtual photons are included. This specific process has been chosen because it provides the cleanest experimental signal in studying di-boson production. This is due to the fact that there are no neutrinos or degenerate leptons flavor in the final states.

In this chapter an overview of the state-of-the-art of the theoretical modelling of the ZZ production is given, together with the latest measurement of the total cross-section. Moreover, some BSM models that would particularly benefit from improving the theoretical modeling of this process are also briefly discussed.

3.1   State-of-the-art of the Theoretical Modelling

The production of two EW gauge vector bosons in a proton-proton collision has been computed so far at the NNLO QCD and NLO EW fixed-order accuracy for

both on- and off-shell production. The LO and NLO QCD calculations are by now known both analytically and numerically. The analytical NLO QCD computation of the Z boson pair production was done thirty years ago for both on-shell [151] and off-shell [152] final states. The numerical evaluation, instead, is by now fully automated and included in general-purpose MC event generators such as SHERPA, POWHEG, MATRIX [101], MADGRAPH5_AMC@NLO [153] and more. In SHERPA the evaluation of the virtual corrections for the ZZ production is done using external loop matrix-element provider like OPENLOOPS [154], RECOLA [119, 155], MCFM[102, 103, 104], GOSAM [156] or MADLOOP [157].

Similarly to the NLO QCD corrections, the NLO EW correction to the LO QCD ZZ production is well known both analytically [158, 159, 160, 161] and numerically from the same tools used to calculate the NLO QCD correction. The combination of the NLO QCD and NLO EW corrections was first done in Ref. [162] to study the anomalous triple gauge coupling (aTGC) BSM model.

The NNLO QCD correction, instead, has so far been computed only analytically, due to the limitations explained in Sec. 2.4. The analytical correction to the quark-initiated off-shell ZZ production (*i.e.* not including any $gg \rightarrow 4l$ diagram) was recently calculated in Ref. [163] and implemented in the MATRIX event generator [98, 164]. The LO accurate loop-induced gluon initiated di-boson production, part of the NNLO QCD correction, is known analytically since 2013 [165], and can be numerically evaluated using standard loop matrix-element generators. The virtual QCD correction to this process is known analytically for both the ZZ and the four-lepton final state with massless quarks running inside the loop [166, 8] and very recently only for on-shell ZZ production including the full top-quark mass dependence [167]. This is one of the first known N³LO virtual correction piece for the inclusive four-lepton production. This correction has been implemented in the MC event generators POWHEG [168], MATRIX [169] and SHERPA (as part of the main results of this thesis).

The parton-shower matching of these calculations has not yet reached a final stage, and its development is still very active. Recently the NLO QCD+EW accurate calculation has been matched with a QCD+EW parton-shower using the POWHEG method presented in Ref. [170]. However, the method used in this reference is still not complete since it lacks mixed QCD×EW parts of the correction. A general and consistent inclusion of the NLO EW corrections in a full particle-level simulation is still not available due to the high complexity of defining the parton-shower initial conditions and history for mixed EW corrections. The parton-shower matching is even more complicated in multijet-merging calculations due to the fact that it requires a mix evolution of QCD and QED parton-shower emissions. Nonetheless, it is possible to include approximate virtual EW corrections in a multijet-merged calculation, using soft photons resummation methods to include also approximate QED real emission kinematics. These corrections are one of the main results of this thesis, and are going to be discussed in Chap. 4.

NNLO QCD accurate calculations have recently been matched to a parton shower

[171]. The methods used for the NNLO QCD parton-shower matching are the same as discussed in Sec. 2.4.

In SHERPA, the state-of-the-art of the $e^+e^-\mu^+\mu^-$ calculation in a general multiple QCD emission simulation includes a multi-jet merging calculation where the 0- and 1-jet multiplicity evaluated at NLO QCD are merged with up to three jets at LO. The lower 0- and 1-jet multiplicities also include the approximated NLO EW correction (see Chap. 4). Moreover, the loop-induced gluon initiated diagram is also included at its NLO QCD accuracy matched to a parton-shower using the MC@NLO method.

3.2   Cross Section Measurements

To give an idea of the physical region covered by a detector the fiducial phase space of the ATLAS detector [172] is briefly discussed as an example. This detector has a cylindrical geometry covering almost a 4π solid angle, an inner particle tracking detector surrounded by a thin superconducting solenoid providing a 2 Tesla axial symmetric magnetic field, an electromagnetic and hadronic calorimeter, and a muon spectrometer. The inner tracking detector covers a pseudorapidity region of $|\eta| <$ 2.5, while the electromagnetic and hadronic calorimeters cover respectively a region of $|\eta| < 3.2$ and $|\eta| < 1.7$ with a total coverage of the two calorimeters combined of at most $|\eta| = 4.9$. Finally, the muon spectrometer has a total coverage of $|\eta| < 2.7$.

In ATLAS analyses prompt electrons are also "dressed", meaning that the momenta of photons in a radius of $\Delta R = 0.1$ around them are summed to the electron's momentum. This is necessary due to the resolution of the electromagnetic calorimeter that detects also the EM energy around an electron. On the other hand, muons are not dressed. This is because in their detection EM radiation is not included. The isolation of leptons is done by summing the transverse momentum of all detected charged particles around the lepton, within a cone of $\Delta R = 0.3$. Moreover, it is required that the ratio of the transverse momenta of the sum of all the particles around the main lepton and the main lepton itself is higher than 0.16.

An example of fiducial selection cuts used in experimental analyses [5, 53] is that the identified leptons (either electrons or muons) are required to have a transverse momentum greater than $7\,\mathrm{GeV}$ and a pseudorapidity of $|\eta| < 2.47$ for an electron and a $p_T > 5\,\mathrm{GeV}$ and $|\eta| < 2.7$ for a muon. Additional particles are also allowed including possible BSM particles. Moreover, the leading and sub-leading leptons are required to have respectively a transverse momentum of $p_T > 20\,\mathrm{GeV}$ and $p_T > 10\,\mathrm{GeV}$, and any same-flavor oppositely charged lepton pair must have an invariant mass of at least $5\,\mathrm{GeV}$.

The experimental value for the total cross-section of $pp \to 4l$ $(l = e, \mu)$ with a center of mass energy $\sqrt{s} = 13\,\mathrm{TeV}$ in the ATLAS fiducial phase space is shown in Table 3.1. Here the experimental cross-section is compared against two theoretical estimations from SHERPA and POWHEG +PYTHIA 8. Both theoretical results are in very good agreement with the experimental value, within the theoretical and experimental uncertainties. The uncertainty of the measured total cross-section

is expected to reach an accuracy of 1% with the next LHC and ATLAS detector upgrades.

	ATLAS	SHERPA	POWHEG +PYTHIA 8
Total cross-section [fb]	89 ± 3	86 ± 5	83 ± 5

Table 3.1: This data show the result of the ATLAS analysis from Ref. [5].

SHERPA's result has been obtained merging up to three jets multiplicities where the 0- and 1-jet multiplicities are evaluated at NLO while the multiplicities from two to three jets are evaluated at LO. The multi-jet merging method used is described in Sec. 2.3. Additionally, loop-induced $gg \to 4l + 0, 1$ samples are generated in an independent simulation merging the 0- and 1-jet multiplicity matrix elements at LO. POWHEG +PYTHIA 8's result, instead, calculates the $pp \to 4l + X$ process first at NLO and this is later rescaled by the NNLO calculation obtained with MATRIX [173, 101] as a function of m_{4l}. The loop-induced process has been added to this result too by using SHERPA's calculation. Both cases have applied EW effects as a reweighting of the virtual NLO EW correction as a function of m_{4l}. A comparison between predicted and measured total cross-sections for each four-lepton final state with same-flavor opposite charged (SVO) leptons, *i.e.* $e^+e^-\mu^+\mu^-$, $e^+e^-e^+e^-$ and $\mu^+\mu^-\mu^+\mu^-$ is shown in Ref. [174]. Again, all of these channels show a good agreement with the theoretical prediction within the estimated uncertainties.

3.3   Beyond Standard Model Effects

As briefly discussed at the beginning of this chapter, the production of two EW gauge bosons gives the possibility to study some very interesting BSM models. One of these is the anomalous triple gauge coupling [139]. This model describes the existence of a neutral triple gauge coupling which is not allowed by the gauge invariance of the EW Lagrangian, Eq. (1.4.22). The interesting aspect of this model is that it gives an indirect way to test gauge invariance of the EW sector of the SM. This BSM model introduces four new couplings, two for the Z boson and two for the photon. Both the Z boson and the photon have one CP-violating and one CP-conserving coupling to a new electrically neutral vector boson. If this model is true it would increase the production rate for high energetic final states. Therefore, signs of aTGC should be visible in the high energy region of observables like di-boson invariant mass or Z boson transverse momentum. A good modelling of the SM is crucial to improve the limits set for this BSM theory. Examples of theoretical prediction for aTCG model against ATLAS data for ZZ production in proton-proton collisions at a center-of-mass energy of $\sqrt{s} = 8$ TeV is given in Ref. [175]. In this work the constraints on the new couplings introduced by the aTGC model are set to about $\pm 3.5 \times 10^{-3}$ with a 95% confidence level. Despite these values being very small they still do not

entirely disprove the model requiring more accurate analysis from both theory and the experimental side.

Another important BSM model that affects the production of two off-shell EW bosons is the global baryon-number-minus-lepton-number $(B-L)$ model [176] where $B-L$ is treated as a local gauge symmetry of the SM. The consequence of breaking this symmetry is the non-conservation of the baryon and lepton numbers individually which would have important consequences in the lepto- and baryogenesis in early Universe models. Proton decay is a consequence of the $B-L$ symmetry breaking. However, this is very hard to observe since its lifetime is expected to be between 10^{32} and 10^{36} years [177], which is much longer than the age of the Universe.

The request of having a $B-L$ invariant Lagrangian let us introduce a new EW neutral vector boson, called Z'. Similar to the Higgs mechanism, the spontaneous breaking of the $B-L$ symmetry introduces a new "Higgs"-like particle (h_2) which mixes with the observed Higgs boson. A direct consequence of this symmetry is the shifting of the W boson mass due to new loop contributions involving the two Higgs bosons and their mixing angle [178, 179]. However, there is still no experimental sign of either these new bosons.

Chapter 4

Electroweak Corrections to $e^+e^-\mu^+\mu^-$

The combination of EW and QCD NLO corrections has recently seen a very active development. However, they have not yet been fully integrated in general multiple QCD emissions simulations. This Chapter shows a method to include approximated EW corrections in a QCD simulation in SHERPA. These approximations are based on the high energy behavior of EW loop matrix elements, *i.e.* at scales much larger than the typical EW energy scale. In this high energy limit the EW virtual matrix-elements are dominated by Sudakov logarithms [61]. Moreover, in Refs. [180, 181], it was shown the factorisation of these logarithms at leading-logarithm (LL) and next-to-leading logarithm (NLL) accuracy at every perturbative order.

The EW approximations discussed in this chapter are based on the high-energy limit of the full NLO EW correction.

To validate the accuracy of the approximations, these are compared against the fixed order NLO EW calculations for the $e^+e^-\mu^+\mu^-$ production and the production associated with a jet. These calculations allow to study both the EW approximations accuracy and the effect of one extra QCD radiation on the EW corrections. The $e^+e^-\mu^+\mu^-j$ final state at the NLO EW fixed order accuracy has been studied for the first time in this thesis, and published in [6] in collaboration with E. Bothmann, D. Napoletano, M. Schönherr, S. Schumann. In the context of the fixed order EW correction, it is also studied the possibility to resum the high energy EW Sudakov logarithms to all orders and their matching to the fixed order NLO EW calculation. Finally, it is discussed the phenomenology of the EW approximations in a general QCD simulation in SHERPA.

4.1 High Energy Behavior of Electroweak Virtual Corrections

The EW Sudakov logarithms are enhanced in phase space configurations where all kinematic invariants are significantly larger than the typical EW energy scale. These are classified into double logarithms (DL), that are leading EW Sudakov logarithms, and single logarithms (SL), that instead are sub-leading logarithms arising from the collinear virtual emission of a weak gauge boson. These two classes are made up by terms of the form,

$$L(|r_{ij}|, M) = \frac{\alpha}{4\pi} \log^2 \frac{|r_{ij}|}{M^2}, \qquad l(r_{ij}, M) = \frac{\alpha}{4\pi} \log \frac{r_{ij}}{M^2}, \qquad (4.1.1)$$

where $r_{ij} = (p_i + p_j)^2$ is a kinematic invariant of the calculation.

DLs were first studied by V. V. Sudakov in 1956 [61] and later generalized to all DL and SL by A. Denner and S. Pozzorini [181, 180] for both one- and two-loop EW corrections at LL and NLL accuracy. They have also shown the universal factorisation of these logarithms at every perturbative order. It is important to point out that this high-energy approximation can not yet be applied to QCD loop diagrams since new type of high-energy logarithms may arise from EW boson exchange inside the quark-loop.

The fully automated evaluation of the EW logarithms has been implemented in SHERPA in Ref. [182]. This implementation uses the COMIX matrix element generator to evaluate all the necessary tree-like matrix elements needed by the EW Sudakov approximation, in a fully differential way. This method allows for the evaluation of EW Sudakov logarithms in any possible final state multiplicity as long as the computational resources allow it.

Even though nowadays the NLO EW corrections have been calculated for a variety of processes, and are now becoming a standard in MC simulations, a full EW NLO fixed order calculation is still limited to low multiplicity final states. On the other hand the high energy approximation of EW loop corrections allow to study EW effects for processes with a high final-state multiplicity, thanks to the fact that this approximation has a tree-like computational complexity.

In order to give a general idea of how the EW Sudakov logarithms look like, it is useful to briefly discuss the two classes of logarithms, DL and SL. These are usually split into four subclasses, Leading Soft-Collinear (LSC), Sub-leading Soft-Collinear (SSC) and Collinear (C). In terms of these logarithms the approximated loop matrix element can be written as,

$$\mathcal{M}_{\text{virt}}^{i_1...i_n}(p_1, \ldots, p_n) \simeq \mathcal{M}_0^{i_1...i_k'...i_l'...i_n} \delta_{i_k' i_k i_l' i_l}, \qquad (4.1.2)$$

where the i_k run over final state flavor. The $\delta_{i_k' i_k i_l' i_l}$ is the sum of all the logarithmic contributions coming from the four subclasses, and it satisfies the U(1)×SU(2) alge-

bra. This tensor structure is due to the factorisation property of these logarithms. However, the factorized Born matrix element is not the same for each logarithm subclass since the $\delta_{i'_k i_k i'_l i_l}$ changes the final state signature.

Leading Soft-Collinear Logarithms

The first subclass of Sudakov logarithms discussed here is the leading soft-collinear logarithms. These arise from the soft and collinear virtual emission of the W, Z or γ boson for which the δ tensor reads,

$$\delta^{\text{LSC}}_{i'_k i_k} = -\frac{1}{2}\left[C^{\text{EW}}_{i'_k i_k}L(s) - 2\left(I^Z_{i'_k i_k}\right)^2 \log\frac{M_Z^2}{M_W^2}l(s)\right], \tag{4.1.3}$$

where C^{EW} is the EW Casimir operator, $I^Z_{i'_k i_k}$ the Z gauge coupling and finally, $L(s)$ and $l(s)$ are the logarithms in Eq. (4.1.1) for which $M = M_W$. The δ tensor in this case is always diagonal except for the cases of transversally polarized neutral gauge boson. In this case there is a mixing between amplitudes involving a Z boson and those involving a photon.
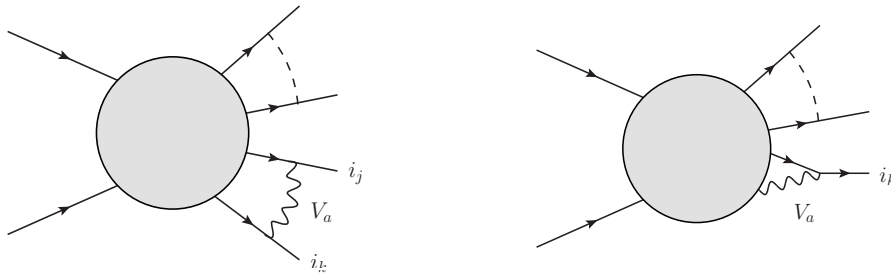
Figure 4.1: Example of diagrams showing the configurations that give rise to leading soft-collinear logarithms, sub-leading soft-collinear logarithms (left) and collinear/soft single logarithms (right).

Sub-leading Soft-Collinear Logarithms

Sub-leading logarithms carry the angular dependency of the soft-collinear approximation. In this case the δ is,

$$\delta^{V_a,\text{SCC}}_{i'_k i_k i'_l i_l} = 2I^{V_a}_{i'_k i_k}I^{\bar{V}_a}_{i'_l i_l}\log\frac{|r_{kl}|}{s}l(s). \tag{4.1.4}$$

Different from the LSC logarithms, here the δ tensor depends on the type of the vector gauge boson exchanged ($V_a = \{\gamma, Z, W^\pm\}$) and on the final state lepton pair. So it does no longer depend on just one single final-state.

Collinear/Soft Single Logarithms

These logarithms arise from both the running of the field renormalisation constants and the splitting of a final state particle into two internal lines with one of these being an EW vector boson. In Fig. 4.1 are shown example diagrams for these logarithms. The δ for these terms act on chiral fermions as,

$$\delta_{i_k i'_k}^{\mathrm{C}} = \delta_{\sigma_k \sigma'_k} \left[\frac{3}{2} C_{\lambda_k}^{\mathrm{EW}} - \frac{1}{8s_W^2} \left((1 + \delta_{\lambda_k R}) \frac{m_{\lambda_k \sigma_k}^2}{M_W^2} + \delta_{\lambda_k L} \frac{m_{\lambda_k \bar{\sigma}_k}^2}{M_W^2} \right) \right] l(s). \qquad (4.1.5)$$

In this expression λ_k and σ_k refer respectively to the fermion chirality and its isospin. The subscript $\bar{\sigma}_k$ stands for the opposite of σ_k, $i.e.$ $\bar{\sigma}_k = -\sigma_k$. The term s_W is, instead, the Weinberg angle. If an external particle is a transversally polarized W boson, the logarithmic behavior of Eq. (4.1.5) remains the same, with the only difference being in the squared brackets. Now, in the square brackets there is a combination of Dynkin operators [183] proportional to the one-loop coefficient of the β-function. Longitudinally polarized final state W bosons, instead, are substituted by Goldstone bosons for which the δ reads,

$$\delta_{\phi_k^\pm \phi_k^\pm}^{C} = \left[2C_{i_k}^{\mathrm{EW}} - \frac{N_C}{4s_W} \frac{m_t^2}{M_W^2} \right] l(s). \qquad (4.1.6)$$

To give an idea of how each of these logarithms affects a leading order calculation, in Fig. 4.2 is shown, the ZZ production at leading order comparing each class of logarithm separately and with the full $\mathrm{EW_{sud}}$ correction. The observables shown are the Z-boson pair invariant mass and leading lepton transverse momentum. The large negative EW correction is driven by the LSC logarithms, while the SSC and C give a positive correction, yet not as large as the LSC, leaving the full $\mathrm{EW_{sud}}$ correction negative.

4.2   Electroweak Approximations: $\mathrm{EW_{virt}}$ and $\mathrm{EW_{sud}}$

Besides the high-energy EW approximation described in the previous Section, now dubbed $\mathrm{EW_{sud}}$, The other EW approximation studied in this thesis is called $\mathrm{EW_{virt}}$. Also this approximation, like the $\mathrm{EW_{sud}}$ approximation, is based on enhanced high energy EW Sudakov logarithms. The $\mathrm{EW_{virt}}$ approximation consists in simplifying the full NLO EW correction by keeping only the virtual part and the integrated soft-collinear subtracted terms of the NLO EW fixed order calculation. This integrated subtraction term is needed to regularize the virtual matrix element. In SHERPA the IR cancellation for NLO EW calculations is done using the same methods for NLO QCD calculations [184].

The use of the complete virtual matrix element makes the $\mathrm{EW_{virt}}$ approximation more expensive than the $\mathrm{EW_{sud}}$, especially for higher final state multiplicity. Moreover, the EW virtual matrix elements are not yet known for any arbitrary process. Its
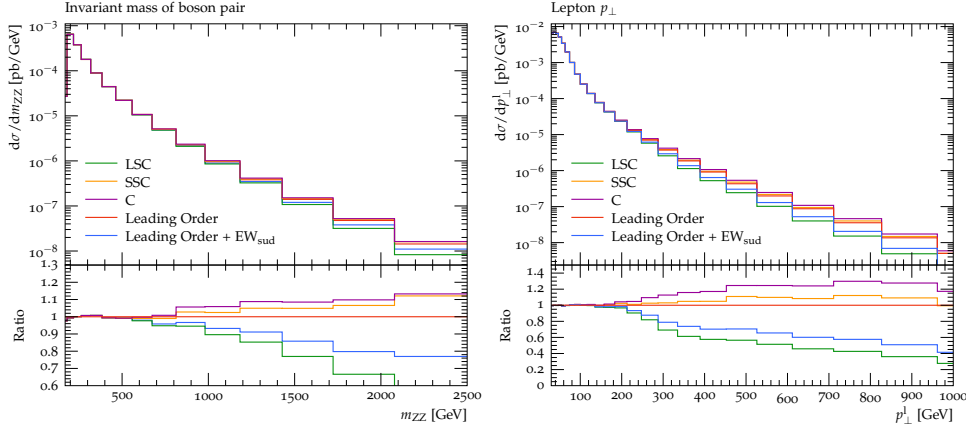
Figure 4.2: Effects of the EW Sudakov LSC, SSC and C logarithms on the leading order of the $pp \to e^+e^-\mu^+\mu^-$ process. The differential observable shown are the di-boson invariant mass and the leading lepton transverse momentum.

use is therefore limited to low final-state multiplicity processes. In multi-jet merged calculations, however, EW effects in the EW$_{\mathrm{virt}}$ approximation, can be propagated to higher QCD multiplicities modifying the local k-factor of a MENLOPS calculation as given in Eq. (2.3.4).

In a leading order calculation both approximations are applied as a differential k-factor to the Born piece, *i.e.*

$$d\sigma^{\mathrm{LO+EW}} = d\Phi B(\Phi)\Big(1 + \delta^{\mathrm{EW}}(\Phi)\Big), \qquad (4.2.1)$$

where the δ^{EW} function respectively for the EW$_{\mathrm{virt}}$ and the EW$_{\mathrm{sud}}$, reads

$$\delta^{\mathrm{EW}}_{\mathrm{virt}}(\Phi) = \frac{V^{\mathrm{EW}}(\Phi) + I^{\mathrm{EW}}(\Phi)}{B(\Phi)}, \qquad \delta^{\mathrm{EW}}_{\mathrm{sud}}(\Phi) = \frac{V^{\mathrm{EW}}_{\mathrm{NLL}}(\Phi) + I^{\mathrm{EW}}_{\mathrm{NLL}}(\Phi)}{B(\Phi)} = K^{\mathrm{NLL}}_{\mathrm{sud}}(\Phi).$$
$$(4.2.2)$$

The $I^{\mathrm{EW}}_{\mathrm{NLL}}$ term is the integrated real photon emission in the soft-collinear approximation at the same logarithmic accuracy as the $V^{\mathrm{EW}}_{\mathrm{NLL}}(\Phi)$.

The strict high-energy limit of the EW$_{\mathrm{sud}}$ approximation, which requires that all the kinematic invariants of a calculation are simultaneously much larger than the EW energy scale, would set to zero all the EW Sudakov logarithms for processes with intermediate electroweak bosons (either Z or W). This is due to the Breit-Wigner distribution that imposes the decay product of an intermediate EW boson to be in the EW energy region. Here this problem is addressed by clustering pairs of leptons (k, l) whose masses are close to the intermediate weak boson mass M_V $(V = Z, W)$ and share the same quantum numbers. The clustering is done according to the following criterion,

$$\Delta_{kl} = \frac{|m_{kl} - M_V|}{\Gamma_V} < \Delta_{\text{thr}}, \qquad (4.2.3)$$

with Γ_V being the resonant EW boson width. The new phase space of the clustered amplitude is built by assigning the lepton pair four-momenta to the new external EW vector boson, $p_{V,kl} = p_k + p_l$. Afterwards, the momenta of the new clustered amplitude are reshuffled in order to bring the new external EW vector bosons on-shell, *i.e.* $p^2_{V,kl} = M^2_V$. The EW correction $\delta^{\text{EW}_{\text{sud}}}(\Phi_m)$ is therefore evaluated in this new phase space. The threshold value adopted in this work is $\Delta_{\text{thr}} = 10$. This value has been varied by a factor of 2, upward and downward, without noticing any difference in differential observables, such as the leading lepton transverse momentum and leading Z-boson transverse momentum.

4.3   Soft-photons Resummation

The EW approximation studied in this chapter account only for corrections from EW virtual boson exchange. The real emission kinematics is instead taken into account using the YFS soft photon resummation in SHERPA. The soft photon resummation is only applied to final state leptons in order not to interfere with the strongly ordered resummation of QCD radiations generated by the parton-shower.

The YFS resummation works by clustering the final state leptons into intermediate pseudo-resonant weak bosons, similarly to what is done in the EW_{sud} approximation, and correcting their leading-order decay width with the all-order resummation of soft real and virtual emitted photons. The general differential expression for the resummed decay width Γ^{YFS} is,

$$\text{d}\Gamma^{\text{YFS}} = \text{d}\Gamma_0\, e^{\alpha Y(\omega_{\text{cut}})} \sum_{n_\gamma} \frac{1}{n_\gamma!} \left[\prod_{i=1}^{n_\gamma} \text{d}\Phi_{k_i} \alpha \tilde{S}(k_i) \Theta(k_i^0 - \omega_{\text{cut}}) \right] \mathcal{C}. \qquad (4.3.1)$$

Here the function $\exp\{\alpha Y(\omega_{\text{cut}})\}$ is the resummed form factor that exponentiate all the logarithms of the unresolved real and virtual soft-photons, while the rest of the expression account for a number n_γ of resolved emitted photons with four momentum k_i which are distributed according to the eikonal factor $\tilde{S}(k_i)$. The parameter ω_{cut} is used to distinguish between resolved and unresolved photons phase space regions. The default value of this cut variable used in SHERPA is $\omega_{\text{cut}} = 1\,\text{MeV}$. Finally, the factor $\mathcal{C}$ contains exact higher order corrections, that in our case are up to the NLO EW accuracy. The explicit expressions for $Y(\omega_{\text{cut}})$, $\tilde{S}(k_i)$ and $\mathcal{C}$ are given in [129]. Recently this method has been extended to a lager set of processes, specially with initial state leptons, in Ref. [185].

It is important to point out that the phase space region populated by the EW_{virt} and EW_{sud} approximations overlaps with the unresolved resummed soft photons from YFS. Nonetheless, during this study we found out that the overlapping is non-

logarithmic in the high-energy limit, and therefore it does not spoil the logarithmic accuracy of the EW approximations.

4.4   Resummation of High-Energy Electroweak Sudakov Logarithms

The factorisation property of the high energy EW Sudakov logarithms allows for their exponentiation [186, 187, 188, 189, 190, 191, 192, 193, 194]. This property allows us to improve predictions at very high energy since the large EW Sudakov logarithms are included at all perturbative orders. The resummation of these logarithms is simply done by the exponentiation of the $\mathrm{EW_{sud}}$ correction, *i.e.* $\delta_{\mathrm{sud}}^{\mathrm{EW}} \to \exp\left\{\delta_{\mathrm{sud}}^{\mathrm{EW}}\right\}$. The $\mathrm{EW_{virt}}$ approximation contains also non-logarithmic terms that do not exponentiate, making this EW approximation not suitable for exponentiating the EW Sudakov logarithms. For a LO accurate calculation the exponentiation is simply done as follow,

$$\mathrm{d}\sigma^{\mathrm{LO+EW_{sud}^{exp}}} = \mathrm{d}\Phi\, B(\Phi)\exp\left(\delta_{\mathrm{sud}}^{\mathrm{EW}}(\Phi)\right). \tag{4.4.1}$$

An example of the effect of the $\mathrm{EW_{sud}}$ exponentiation is given in Fig. 4.3. Here, it is shown the comparison between $\mathrm{EW_{sud}}$ and the exponentiated $\mathrm{EW_{sud}}$ for the transverse momentum of the hardest Z boson in the $pp \to e^+e^-\mu^+\mu^-$ process at LO with a center of mass energy $\sqrt{s} = 13\,\mathrm{TeV}$. The plot in Fig. 4.3 shows clearly that exponentiating higher order the high energy EW Sudakov logarithms at NLL logarithmic accuracy produces a harder spectrum in the high energy range.

Finally, the exponentiation of the $\mathrm{EW_{sud}}$ logarithms can also be matched to the full NLO EW calculation improving its high energy description of the result. In the next calculations the NLO EW matching has been done as follows,

$$\mathrm{d}\sigma^{\mathrm{NLO\ EW\ +\ NLL\ EW_{sud}^{exp}}} = \mathrm{d}\Phi\ \mathrm{B}(\Phi)\ \left[\exp\left(\delta_{\mathrm{sud}}^{\mathrm{EW}}(\Phi)\right) - \delta_{\mathrm{sud}}^{\mathrm{EW}}(\Phi) + \delta^{\mathrm{EW}}(\Phi)\right]\ . \tag{4.4.2}$$

Here the first correction $\mathcal{O}(\alpha)$ of the exponentiated $\mathrm{EW_{sud}}$ is removed and the full NLO EW calculation is used instead. The differential $\delta^{\mathrm{EW}}(\Phi)$ is the full NLO EW local k-factor

$$\delta^{\mathrm{EW}}(\Phi) = \frac{V^{\mathrm{EW}}(\Phi)}{B(\Phi)} + \mathrm{d}\Phi_1\frac{R^{\mathrm{EW}}(\Phi\cdot\Phi_1)}{B(\Phi)}. \tag{4.4.3}$$

The theoretical scale uncertainty in the NLO EW matched calculation is not affected by the EW Sudakov logarithms resummation since scheme depending terms are not included beyond the fixed order accuracy of the calculation. In any case,
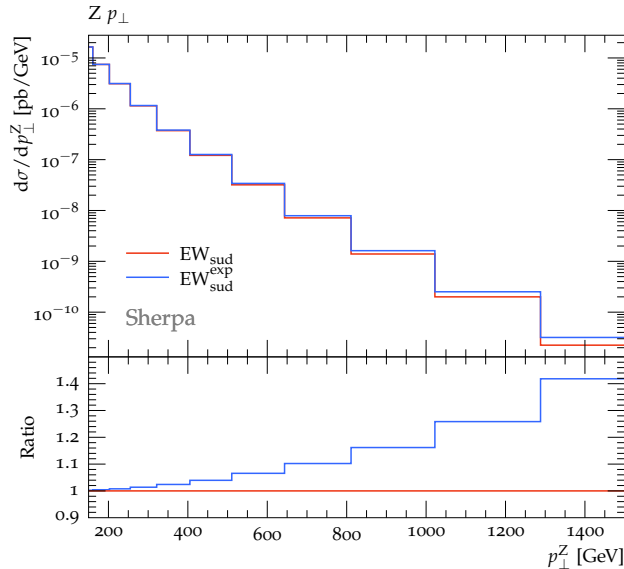
Figure 4.3: Comparison of the EW_{sud} approximation and its exponentiation applied to the on-shell production of two Z bosons at leading order accuracy. Off-shell dynamics is taken into account by letting them decay according to the Breit-Wigner distribution.

scheme dependence enters the resummed factor through the running coupling α of the Sudakov logarithms. For this reason the uncertainty estimation is more reliable in the fixed-order regime. A discussion on the scheme dependence is given in the following Section.

4.5 Event Production at NLO EW Fixed Order Accuracy

In order to validate the accuracy of the EW approximations, these are compared against the NLO EW correction to the $e^+e^-\mu^+\mu^-$ final state for both the 0- and 1-jet multiplicity. Both these processes are evaluated at leading-order QCD in order to keep the comparison as simple as possible. The $e^+e^-\mu^+\mu^-$ final state plus one jet is also useful for understanding the impact of extra QCD radiations on the EW corrections before applying the EW_{virt} and EW_{sud} approximations to a multiple QCD emission simulation.

Numerical Setup

The following calculations have been performed using the fully automated SHERPA +OPENLOOPS/RECOLA framework that will be available in next major release of SHERPA (v3.0.0). The interface to the matrix element generator RECOLA to this version of SHERPA is part of the technical contributions of this thesis. In Appendix

[A](#) are shown some validation plots for this implementation. RECOLA is used to evaluate all the virtual matrix elements of the $4l + j$ process in both NLO EW fixed order calculation and EW_{virt} approximation. All the other loop matrix elements are evaluated using OPENLOOPS. The reason why RECOLA is used for the four-lepton production associated with a jet is purely technical since OPENLOOPS, at the time of writing the work published in Ref. [6], did not have the EW virtual correction library of the process $e^+e^-\mu^+\mu^-j$ publicly available. Both these programs, OPENLOOPS and RECOLA, use the tensor-reduction library COLLIER in order to write the loop matrix elements in terms of known 1-loop diagrams' master integrals. Moreover, OPENLOOPS uses the program CUTTOOLS to compute 1-loop amplitudes at the integrand level. All the other parts of the simulation are taken care of by SHERPA using its internal matrix element generators AMEGIC and COMIX.

The proton-proton collision is simulated with a center of mass energy $\sqrt{s} = 13\,\text{TeV}$ and the SM masses and widths of the Z, W, H bosons and top-quark are set to the following values,

$$
\begin{aligned}
M_W^{\text{OS}} &= 80.385\,\text{GeV} & \Gamma_W^{\text{OS}} &= 2.085\,\text{GeV} \\
M_Z^{\text{OS}} &= 91.1876\,\text{GeV} & \Gamma_Z^{\text{OS}} &= 2.4952\,\text{GeV} \\
M_h &= 125.0\,\text{GeV} & \Gamma_h &= 0.00407\,\text{GeV} \\
m_t &= 173.2\,\text{GeV} & \Gamma_t &= 0\,.
\end{aligned}
$$

The other particles are treated as massless. Consequently, a five flavor scheme for the SM parameters running is used throughout this Chapter. The weak boson masses and the weak mixing angle are evaluated in the complex-mass scheme,

$$
\mu_V^2 = M_V^2 - \mathrm{i}M_V\Gamma_V, \qquad \sin^2\theta_w = 1 - \frac{\mu_W^2}{\mu_Z^2}, \tag{4.5.1}
$$

where the pole masses and widths are obtained from the on-shell ones according to [195],

$$
M_V = \frac{M_V^{\text{OS}}}{\sqrt{1 + \left(\Gamma_V^{\text{OS}}/M_V^{\text{OS}}\right)^2}}, \qquad \Gamma_V = \frac{\Gamma_V^{\text{OS}}}{\sqrt{1 + \left(\Gamma_V^{\text{OS}}/M_V^{\text{OS}}\right)^2}}. \tag{4.5.2}
$$

The default scheme chosen to evaluate the renormalized EW coupling constant is the G_μ scheme with the Fermi's constant G_F set to,

$$
G_F = 1.16637 \times 10^{-5}\,\text{GeV}^{-2}, \tag{4.5.3}
$$

according to [44]. The EW coupling constant is then evaluated as,

$$\alpha_{G_\mu} = \frac{\sqrt{2}}{\pi} G_F M_W^2 \left(1 - \frac{M_W^2}{M_Z^2}\right) = 1/132.294 \,. \tag{4.5.4}$$

In order to understand the non-trivial EW scheme dependence of the fixed order NLO EW correction, and how well this is captured by the EW approximations, the fixed order results and the EW approximated ones have also been computed in the $\alpha(M_Z^2)$ scheme,

$$\alpha(M_Z^2) = 1/128.802. \tag{4.5.5}$$

The main difference in these two schemes is that the G_μ-scheme includes also higher order operators, reducing the size of the NLO EW correction compared to the $\alpha(M_Z^2)$ scheme. This is explained in detail in Sec. 4.5.2. An automated EW scheme variation, as for the strong coupling constant α_s, is not yet available due to the fact that different EW schemes would also affect other EW parameters, such as gauge vector boson masses and EW mixing angle.

The PDF set used is NNPDF31_nlo_as_0118_luxqed from LHAPDF, through its interface with SHERPA. The strong coupling constant is set accordingly to,

$$\alpha_s(M_Z^2) = 0.118 \,. \tag{4.5.6}$$

Finally, the renormalisation and factorisation scales are set to

$$\mu_R = \mu_F = \tfrac{1}{2}\left(E_{T,2e} + E_{T,2\mu}\right) \,,$$

where the transverse energies of the two vector bosons given by

$$E_{T,2\ell} = \sqrt{m_{2\ell}^2 + p_{T,2\ell}^2} \,.$$

Event Selection

The analysis used in the following calculations covers the fiducial phase space of the ATLAS detector. Similarly to the discussion in Sec. 3.2, photons collinear to a final state lepton, in a cone of radius $R = 0.1$, are combined together. This combination is also essential to regularize the IR singularity of real emitted photons, both from the fixed order real photon emission correction and the resummed collinear-soft photons. On the dressed leptons are applied cuts on their transverse momentum, rapidity and distance with other leptons,

$$p_{T,\ell} > 20\,\text{GeV}, \qquad |y_\ell| < 2.5, \qquad \Delta R_{\ell\ell'} > 0.1 \,. \tag{4.5.7}$$

Final state jets, in both the $e^+e^-\mu^+\mu^-j$ NLO EW fixed-order and the multi-jet merged calculation, are defined using the anti-k_t algorithm [196] with the standard $R = 0.4$ cone radius. On the identified jets are applied cuts on their transverse momentum, rapidity and distance with the leptons,

$$p_{\mathrm{T},j} > 30\,\mathrm{GeV}, \qquad |y_j| < 4.5, \qquad \Delta R_{\ell j} > 0.4\,. \qquad (4.5.8)$$

4.5.1   Contributions at Leading- and Next-to-leading EW Order

In this section are discussed the contributions to the LO and NLO EW correction for the $e^+e^-\mu^+\mu^-$ and $e^+e^-\mu^+\mu^-j$ final states. Moreover, in order to be as general as possible, also diagrams with external photons, are included in the calculation, whether they are initial or final states. The EW approximations, $\mathrm{EW}_{\mathrm{virt}}$ and $\mathrm{EW}_{\mathrm{sud}}$, are benchmarked against the full NLO EW keeping as reference also the $e^+e^-\mu^+\mu^-$ at LO. The YFS soft photon resummation is included only in the EW approximated samples in order to keep the comparison with the fixed order NLO EW as simple as possible. Moreover, effects of the all-order EW Sudakov logarithms resummation at the NLL accuracy, are discussed for both leading and next-to-leading order calculation. Finally, the EW scheme dependence is discussed for the total cross-sections and differential distributions. For the latter, specifically, this is displayed as an uncertainty band. It is important to point out that this can not be interpreted as an actual theoretical uncertainty band since it takes into account only two schemes. However, it is still useful to understand the EW renormalisation scheme dependence. As an extra benchmark for the EW approximations, the total cross-sections have been calculated using an additional high-energy cut, *i.e.* $p_{\mathrm{T},2e} > 600\,\mathrm{GeV}$, to study the effects of the EW approximations in their regime of validity.

Inclusive production

At the lowest perturbative order, *i.e.* $\mathcal{O}(\alpha^4)$, the four-lepton inclusive production has two possible initial states, a quark-antiquark or a photon pair (photon induced).

$$q\bar{q} \to e^+e^-\mu^+\mu^-, \qquad \gamma\gamma \to e^+e^-\mu^+\mu^- \qquad (4.5.9)$$

An example of these processes is given in Fig. 4.4a. Despite being numerically small, photon induced production is included for completeness since it contributes at this order of accuracy. In Fig. 4.5 are instead given some example of the contributing EW virtual diagrams. Two of these are the 6-point diagram for both the quark-antiquark and di-photon initial states. These diagrams have two interesting aspects. Firstly, they include the $e^+e^-\mu^+\mu^-$ production with only W boson as virtual intermediate states, and secondly, the photon induced diagram contains triple EW gauge boson coupling through vector boson fusion (VBS) whose phenomenological relevance has

been discussed in Chap. 3.

The real emission, that is at the order $\mathcal{O}(\alpha^5)$, opens up a new initial state channel with a quark and a photon. The contributing partonic processes to the real emission correction are,

$$q\bar{q} \to e^+e^-\mu^+\mu^-\gamma, \quad \gamma\gamma \to e^+e^-\mu^+\mu^-\gamma \quad \text{and} \quad \gamma\bar{q}^{(\!\!\!\!\;)} \to e^+e^-\mu^+\mu^-\bar{q}^{(\!\!\!\!\;)}. \qquad (4.5.10)$$

Examples of these diagrams are shown in Fig. 4.4b. The inclusion of the new channel is very important because it contains collinear singularities that cancel the corresponding ones in both quark- and photon-initiated virtual diagrams.

In Tab. 4.1 are shown the total cross sections for the B and V+R pieces of the fixed order calculation separated by initial state channels. All the total cross sections reported in this table have a statistical uncertainty below permille, it is therefore not reported here. As anticipated, the photon-induced diagrams and the initial states with just one single photon give a very small correction to the total cross sections, but again, they have to be included for completeness and they are needed to cancel all the IR singularities in the calculation. The largest contribution is given by the quark-initiated processes.

	$q\bar{q}$-initiated	$\gamma\gamma$-initiated	$\gamma\bar{q}^{(\!\!\!\!\;)}$-initiated
B	9.805	0.014	-
V+R	-0.788	0.004	0.001

Table 4.1: Total cross sections of the Born and the NLO EW correction to the $e^+e^-\mu^+\mu^-$ production divided by the three available initial-state channels. The total cross-sections are given in femtobarn [fb].

Production in association with a jet

The diagrams that contribute at the Born level to the $e^+e^-\mu^+\mu^-j$ final state at the perturbative order $\mathcal{O}(\alpha_s\alpha^4)$, are

$$q\,\bar{q} \to e^+e^-\mu^+\mu^-\,g \quad \text{and} \quad g\,\bar{q}^{(\!\!\!\!\;)} \to e^+e^-\mu^+\mu^-\,\bar{q}^{(\!\!\!\!\;)}.$$

These diagrams can be visualized by attaching an external gluon to the Born-level quark-initiated diagrams of the four-lepton production shown in Fig. 4.4a. Since we also include final state photons, the virtual correction for the four lepton production associated with a jet has two new channels compared to the leading-order. These are,

$$q\,\bar{q} \to e^+e^-\mu^+\mu^-\,\gamma \quad \text{and} \quad \gamma\,\bar{q}^{(\!\!\!\!\;)} \to e^+e^-\mu^+\mu^-\,\bar{q}^{(\!\!\!\!\;)}.$$
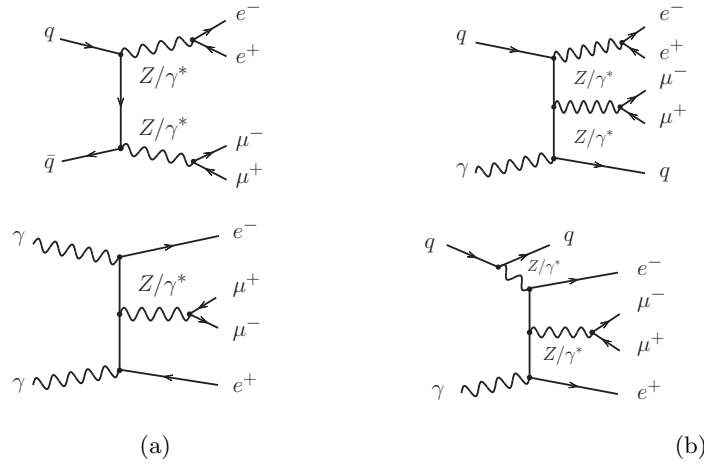
Figure 4.4: Example Born-level (a) and real-emissions diagrams (b) contributing to $pp \rightarrow e^+e^-\mu^+\mu^- + X$ at $\mathcal{O}(\alpha^4)$ and $\mathcal{O}(\alpha^5)$, respectively.
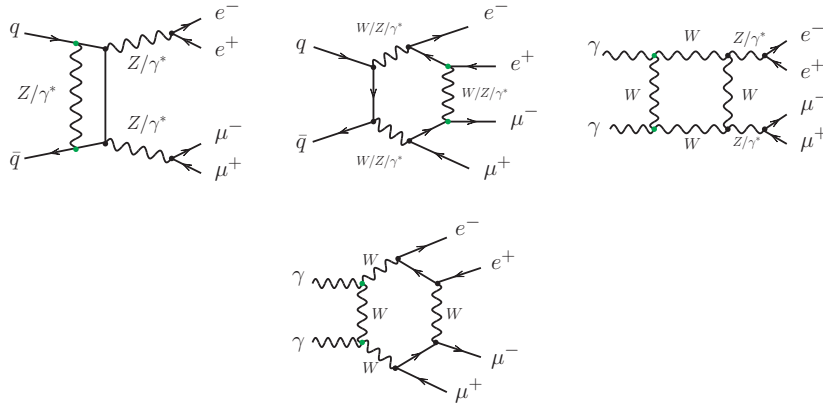
Figure 4.5: Example one-loop diagrams contributing to $pp \rightarrow e^+e^-\mu^+\mu^-$ at $\mathcal{O}(\alpha^5)$.

These two new channels are actually QCD-loops coming from the QCD virtual correction to the EW real emission diagrams of the 0-jet case. The rest of the virtual diagrams are pure EW loops. Examples of these diagrams are given in Fig. 4.6.

The real emission diagrams are

$$q\,\bar{q} \rightarrow e^+e^-\mu^+\mu^-\,g\,\gamma\,, \quad g\,\overset{(-)}{q} \rightarrow e^+e^-\mu^+\mu^-\,\gamma\,\overset{(-)}{q}\,,$$
$$\gamma\,\overset{(-)}{q} \rightarrow e^+e^-\mu^+\mu^-\,g\,\overset{(-)}{q}\,, \quad \gamma\,g \rightarrow e^+e^-\mu^+\mu^-\,q\,\bar{q} \quad \text{and} \quad \overset{(-)}{q}\,\overset{(-)}{q} \rightarrow e^+e^-\mu^+\mu^-\,\overset{(-)}{q}\,\overset{(-)}{q}\,.$$
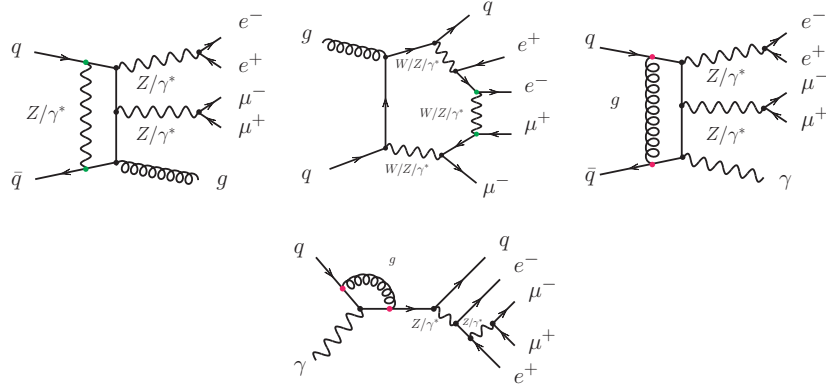
Figure 4.6: Example one-loop diagrams contributing to $pp \to e^+e^-\mu^+\mu^- j$ at $\mathcal{O}(\alpha_s\alpha^5)$.
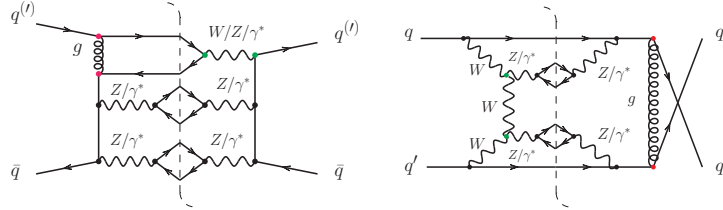
Figure 4.7: Example real-emission QCD–EW interference contributions in $\bar{q}^{(\prime)}\bar{q}^{(\prime)} \to e^+e^-\mu^+\mu^-\bar{q}^{(\prime)}\bar{q}^{(\prime)}$.

The first four processes are real emissions that account only for either one EW or QCD radiation at $\mathcal{O}(\alpha_s\alpha^5)$. These processes are responsible for the cancellation of IR singularities from the virtual emission contributions needed to make the NLO calculation IR finite. The latter process needs a separate discussion. This process is an interference between $\mathcal{O}(e^6)$ and $\mathcal{O}(g_s e^5)$ diagrams that are respectively EW and QCD real emission diagrams. To help visualize the interfering diagrams, in Fig. 4.7 are shown two examples. Due to the colour algebra, the interference can happen only between $s-$ and $t-$channels or $t-$ and $u-$channels. Usually, interference terms are relatively small for inclusive observables, but since in this case this is the only process with two initial state valence quarks, *i.e.* uu, ud, or dd, a sizeable contribution may be expected.

4.5.2 Electroweak Scheme Dependence

There are three main choices for the EW coupling constant when working with processes involving EW interactions, $\alpha(0)$, $\alpha(M_Z^2)$ and G_μ. The choice of the scheme strongly depends on the process under consideration. In the $\alpha(0)$ scheme, the renormalisation is done in the Thompson limit, *i.e.* $Q^2 = 0$. When this scheme is used for processes at the EW energy scale $Q^2 \sim M_Z^2$ the coupling constant needs to be

evolved from $\alpha(0)$ to $\alpha(M_Z^2)$ using the running coupling equation,

$$\alpha(M_Z^2) = \frac{\alpha(0)}{1 - \Delta\alpha(M_Z^2)}. \tag{4.5.11}$$

The term in the denominator $\Delta\alpha(M_Z^2)$ [197, 198] comes from the resummation of the UV logarithms from the renormalisation procedure. In this term, logarithms from the charge renormalisation constant are also included. These produce logarithms like $\alpha \log(M_Z^2/m_f^2)$, where m_f is the mass of all the light fermions. At the one-loop accuracy, $\Delta\alpha(M_Z^2)$ reads,

$$\Delta\alpha(M_Z^2) = \frac{\alpha(0)}{3\pi} \sum_{f\neq t} N_C^f Q_f^2 \left[\log \frac{M_Z^2}{m_f^2} - \frac{5}{3}\right]. \tag{4.5.12}$$

This logarithms are instead not present in the $\alpha(M_Z^2)$ scheme where the renormalisation is done directly at $Q^2 = M_Z^2$. In this case the $\Delta\alpha(M_Z^2)$ terms are cancelled by the renormalisation of the coupling constant removing every light fermion logarithm. These makes the $\alpha(M_Z^2)$ scheme a better choice over the $\alpha(0)$ scheme for calculations involving massive EW bosons. On the other hand, the $\alpha(0)$ scheme is more suitable for calculations involving external photons, since the renormalisation of their on-shell propagator cancels exactly the light-fermion logarithms. An optimal choice would be a mixed scheme where external photons couple according to the $\alpha(0)$ scheme and internal EW bosons according to $\alpha(M_Z^2)$. Finally, the G_μ scheme is derived from Fermi's constant G_F setting the value of α to Eq. (4.5.4). This scheme is related to the $\alpha(0)$ scheme by the following relation at the NLO EW accuracy [199, 200],

$$\alpha_{G_\mu} = \alpha(0) \left(1 + \Delta\alpha(M_Z^2) - \Delta\rho \frac{\cos^2\theta_w}{\sin^2\theta_w}\right) + \mathcal{O}(\alpha^3), \tag{4.5.13}$$

where,

$$\Delta\rho = \frac{3\alpha(0)m_t^2}{16\pi \sin^2\theta_w M_W^2}. \tag{4.5.14}$$

From Eq. (4.5.13) it is clear that in the G_μ scheme α is renormalized at a similar scale as the $\alpha(M_Z^2)$ scheme due to the presence of $\Delta\alpha(M_Z^2)$. This makes also this scheme preferable over the $\alpha(0)$ scheme for processes involving massive EW bosons. For what concern the difference with the $\alpha(M_Z^2)$ scheme, these lay in the extra term, $\Delta\rho$. This term is the same to the one arising from the renormalisation of the weak mixing angle θ_w, that is $\sin^2\theta_w \to \sin^2\theta_w + \Delta\rho \cos^2\theta_w$. Therefore, the combination of $\alpha_{G_\mu}/\sin^2\theta_w$ cancels universal terms coming from the renormalisation of the theory parameters [201]. This can also be seen as if the renormalisation correction of α_{G_μ}

is absorbed into the weak mixing angle renormalisation. This property makes the G_μ scheme more suitable for processes involving W bosons, since the coupling has exactly the form $\alpha_{G_\mu}/\sin^2\theta_w$. The G_μ scheme, is therefore a better choice over the $\alpha(M_Z^2)$ scheme for processes involving W bosons. In the case Z bosons are present in the process, the G_μ scheme is still a better choice because at least a part of $\Delta\rho$ is absorbed from the weak mixing angle renormalisation.

4.5.3   Phenomenology of ZZ Production

It is now discussed the phenomenology of the $pp \to e^+e^-\mu^+\mu^- + X$ process. In Tab. 4.2 are reported the relative corrections to the leading order of the NLO EW fixed order, EW_virt, EW_sud and the exponentiated EW_sud matched to the LO and NLO EW calculations. The first interesting observation from these total cross sections is the difference between the two EW schemes in the leading order and NLO EW. At leading order, $i.e.$ $\mathcal{O}(\alpha^4)$, the change of the EW scheme result in a simple rescaling factor due to the different values of α. Indeed the fourth power of α in the two EW schemes, using the values given in Eq. (4.5.4) and Eq. (4.5.5), is exactly 11.3%. At NLO EW, the scheme dependence is instead no longer trivial. The mass factorisation and real emission terms still have the EW scheme dependence as a simple rescale of the coupling constant α. The EW correction, instead, has a non-trivial scheme dependence that differs very much both in magnitude and structure as can be appreciated by the two very different sizes of the NLO EW correction in the two EW schemes of -6.8% for the G_μ and -19.4% for the $\alpha(M_Z^2)$ scheme. The smaller impact of the NLO EW correction on the leading order calculation in the G_μ-scheme shows how this is more adequate for calculations involving massive EW bosons, as anticipated in Sec. 4.5.2.

Looking at the two EW approximations, the EW_virt is the one that better captures the non-trivial EW scheme dependence of the full NLO EW correction. This is due to the fact that it uses the full virtual matrix-elements responsible for the non-trivial scheme-dependence. On the other hand the EW_sud has a leading-order-like scheme dependence due to the fact that the scheme dependence enters only via the tree-like matrix-elements that multiply the Sudakov logarithms. The NLO EW matched result, dubbed in the table NLO EW + NLL $\text{EW}_\text{sud}^\text{exp}$, does not show any significant difference in the scheme dependence compared to the NLO EW fixed order result since the effect of the resummed EW Sudakov logarithms is very small in fully inclusive observables.

Each approximation under consideration can reproduce quite well the NLO EW fixed order result with an extra reduction of the leading order total cross section up to 1%. The small discrepancy between the NLO EW fixed order result and the EW approximations is due to the use in the latter of the YFS soft photon resummation. On the NLO EW + NLL $\text{EW}_\text{sud}^\text{exp}$ result, instead, the impact of the resummed EW_sud logarithms is rather negligible. This is due to the fact that the resummed higher order logarithms contribute only at very high energy where the dominant correction

to the total cross-section is already given by the Sudakov logarithms of the NLO EW correction. In order to have a better comparison between the NLO EW fixed order calculation and the EW approximations, in Tab. 4.2 the EW corrections are shown also with an additional high-energy cut. In this case the full fixed order correction is responsible for a negative correction of -42% which is in very good agreement with both the EW_{virt} and EW_{sud} approximations with a correction respectively of -45% and -39%. In this case the effect of the EW_{sud} resummation on the NLO EW calculation is, as expected, more sizeable reducing the negative impact of the NLO EW fixed order calculation to -36%. It is clear then that higher order Sudakov logarithms increase the production rate at very high energies.

$pp \to e^+e^-\mu^+\mu^-$		fiducial cross section	corrections to LO				
Scheme	Region	LO	NLO EW	LO + EW_{virt} + YFS	LO + EW_{sud} + YFS	LO + $\text{EW}_{\text{sud}}^{\text{exp}}$ + YFS	NLO EW + NLL $\text{EW}_{\text{sud}}^{\text{exp}}$
G_μ	inclusive	**9.819 fb**	-6.8%	-7.9%	-7.3%	-7.2%	-6.7%
$\alpha(M_Z^2)$		10.928 fb	-19.4%	-20.2%	-7.7%	-7.6%	-19.3%
$\delta_{G_\mu}^{\alpha(M_Z^2)}$		11.3\%	-3.8%	-3.6%	10.8\%	10.8\%	-3.7%
G_μ	high energy	$4.27 \cdot 10^{-3}$ fb	-42%	-45%	-39%	-33%	-36%

Table 4.2: Inclusive fiducial cross sections for $pp \to e^+e^-\mu^+\mu^-$ at $\sqrt{s} = 13$ TeV at LO along with the relative corrections for NLO EW, NLO EW + NLL $\text{EW}_{\text{sud}}^{\text{exp}}$ and the EW_{sud} and EW_{virt} approximations in both G_μ and $\alpha(M_Z^2)$ scheme. The table also gives results for the "high-energy" region, which requires $p_{\text{T},2e} > 600\,\text{GeV}$ in addition to the fiducial cuts.

The differential observables studied are shown in Fig. 4.8. These are the invariant mass of the four-lepton system m_{4l}, transverse momentum of the electron pair $p_{\text{T},2e}$, Z-boson distance $\Delta R_{2e,2\mu}$ and electron rapidity y_{e^-}. Moreover, the NLO EW fixed order calculation is reported in both the G_μ and the $\alpha(M_Z^2)$ schemes as a "scheme uncertainty" band taking as reference the calculations obtained in the G_μ-scheme.

From the differential observables is immediately clear the very good agreement between the EW approximations and the full NLO EW fixed order calculation. The Z-boson distance is the only observable to display a noticeable difference for values smaller than π. This is due to the fact that this region is dominated by real-photon radiation that for the EW approximations is entirely populated by the YFS soft-photon resummation. From this observable, it is also clear the role played by the non-trivial EW scheme dependence of the virtual correction. The region below π, being populated only by the real emission events, has a tree-like scheme dependence of about 14\%, exactly the ratio of the α to the power of 5 in the two EW schemes under consideration. While in the region above π the uncertainty band changes sign due to the fact that this region is also populated by the virtual correction.

The effects of the EW corrections can be discussed by separating the observables into two classes, energy-dependent and energy-independent. In the former class there are the four-lepton invariant mass and the electron pair transverse momentum, while the latter there are the Z-boson distance and the electron rapidity. The energy-independent observables do not show any particular EW effect besides in the
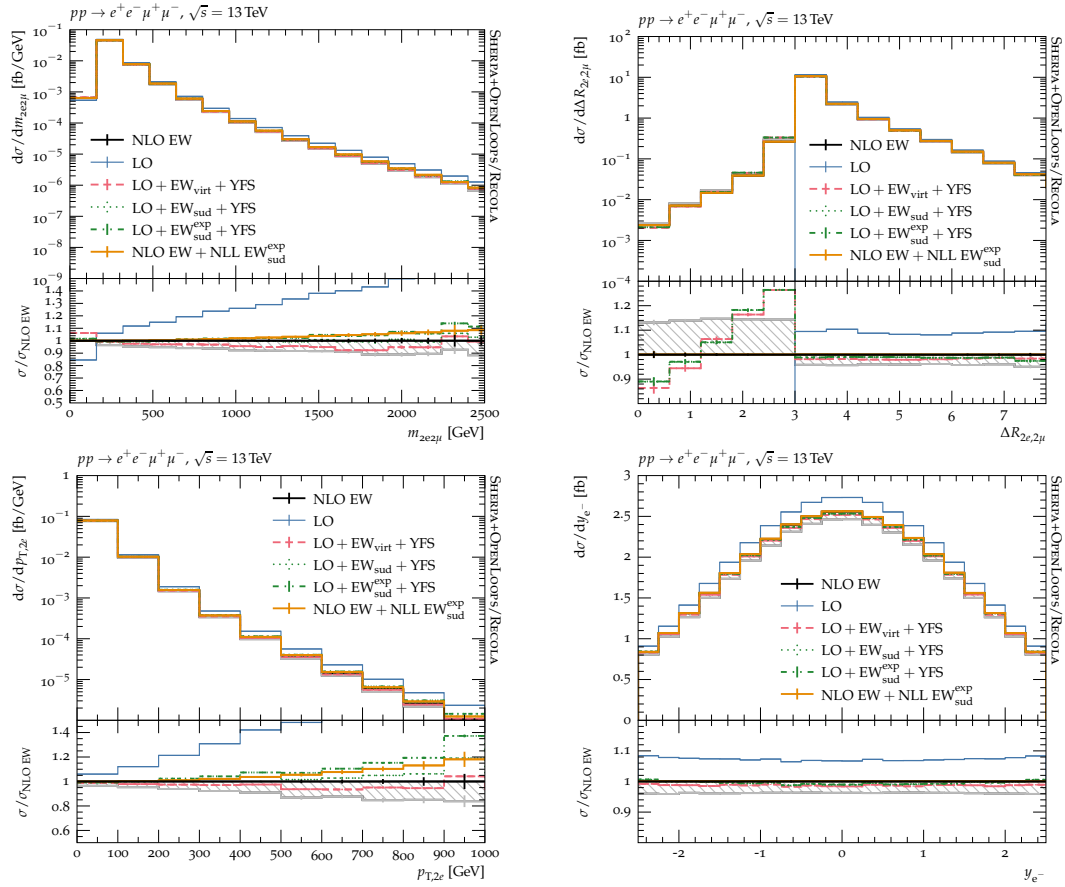
Figure 4.8: Observable distributions for the $pp \to e^+e^-\mu^+\mu^-$ process. From top left to bottom right it is shown the four-lepton invariant mass $m_{2e2\mu}$, the Z-boson distance $\Delta R_{2e,2\mu}$, the transverse momentum of the di-electron pair $p_{T,2e}$, and the rapidity of the electron y_{e^-}. Results are given at LO and NLO EW. These are compared to approximative EW calculations. The NLO EW is given for the G_μ and $\alpha(M_Z^2)$ renormalisation schemes All predictions are calculated using SHERPA+OPENLOOPS/RECOLA.

$\Delta R_{2e,2\mu}$, as discussed before. In the single electron rapidity distribution the EW corrections act as constant k-factors. The energy-dependent observables, instead, show a large suppression in the tail of the distributions. The only difference between the two is that the electron pair transverse momentum displays a stronger suppression. This happens because single EW bosons are more directly affected by virtual boson exchanges than the full $e^+e^-\mu^+\mu^-$ final state. Finally, for these observables both approximations fall within 5-10% from the fixed order NLO EW result in the last displayed bin. In accordance with the observations in the total cross sections with the additional high energy cut, the NLO EW calculation matched to the resummed EW$_{sud}$ has a smaller suppression at high energies of about 5-10% in the last displayed bin of the energy-dependent plots.

4.5.4 Phenomenology of ZZ Production in Association with One Jet

The calculation presented in this section is the first public study of the full NLO EW effects for the $e^+e^-\mu^+\mu^-$ production associated with a jet. Differently from the previous case, checking the EW approximations here requires more care due to the presence of QCD-EW interference diagrams that are not included in the approximated calculations. However, contributions from interference diagrams are typically small in inclusive observables but can be sizeable in one-jet exclusive observables.

$pp \to e^+e^-\mu^+\mu^- j$		fiducial cross section	corrections to LO				
Scheme	Region	LO	NLO EW	$\text{LO} + \text{EW}_{\text{virt}} + \text{YFS}$	$\text{LO} + \text{EW}_{\text{sud}} + \text{YFS}$	$\text{LO} + \text{EW}^{\text{exp}}_{\text{sud}} + \text{YFS}$	$\text{NLO EW} + \text{NLL EW}^{\text{exp}}_{\text{sud}}$
G_μ	inclusive	**5.170 fb**	$-6.6\,\%$	$-8.5\,\%$	$-6.9\,\%$	$-6.7\,\%$	$-6.4\,\%$
$\alpha(M_Z^2)$		5.754 fb	$-19.2\,\%$	$-20.6\,\%$	$-6.9\,\%$	$-6.7\,\%$	$-19.0\,\%$
$\delta^{\alpha(M_Z^2)}_{G_\mu}$		11.29 %	$-3.7\,\%$	$-3.4\,\%$	11.3 %	11.3 %	$-3.7\,\%$
G_μ	high energy	$6.64 \cdot 10^{-3}$ fb	$-33\,\%$	$-37\,\%$	$-30\,\%$	$-25\,\%$	$-29\,\%$

Table 4.3: Inclusive fiducial cross sections for $pp \to e^+e^-\mu^+\mu^- j$ at $\sqrt{s} = 13$ TeV at LO along with the relative corrections for NLO EW, NLO EW + NLL EW$^{\text{exp}}_{\text{sud}}$ and the EW$_{\text{sud}}$ and EW$_{\text{virt}}$ approximations in both G_μ and $\alpha(M_Z^2)$ scheme. The table also gives results for the "high-energy" region, which requires $p_{\text{T},2e} > 600$ GeV in addition to the fiducial cuts.

In Tab. 4.3 are given the total cross-sections for the same calculation setups used in the previous section. The results obtained in this case follow very closely what was observed in the four-lepton production.

The full NLO EW calculation corrects the leading order by a -6.6% and -19.2%, respectively for the G_μ and $\alpha(M_Z^2)$ schemes. This suggests that one additional QCD real emission does not affect significantly EW effects. Moreover, the similarity between this case and the inclusive four lepton production also shows that the non-trivial NLO contributions present in this case, such as QCD loop matrix elements and QCD-EW interference, are small for more inclusive calculations. To give an example, if we exclude QCD loops and the QCD-EW interference, the correction to the LO becomes -7.2%, which is just 0.4% bigger than the full NLO EW correction.

The EW$_{\text{virt}}$ in this case shows a worse agreement with the full NLO EW result, due to the missing QCD loop matrix elements and QCD-EW interference terms. Indeed, comparing the EW$_{\text{virt}}$ approximation to the NLO EW fixed order without these contributions increase the level of agreement of the two calculations, reducing it to 1.3% from 2%. The EW$_{\text{sud}}$, on the other hand, shows a better agreement with the full NLO EW calculation. This is in part accidental since this approximation neglects important terms in the inclusive total cross section calculation. However, it is important to highlight the overall good agrement in the G_μ scheme for the EW approximations and the full NLO EW fixed order calculation. Finally, like for the inclusive four-lepton production, the resummation of the Sudakov logarithms has a small impact on the total cross section.
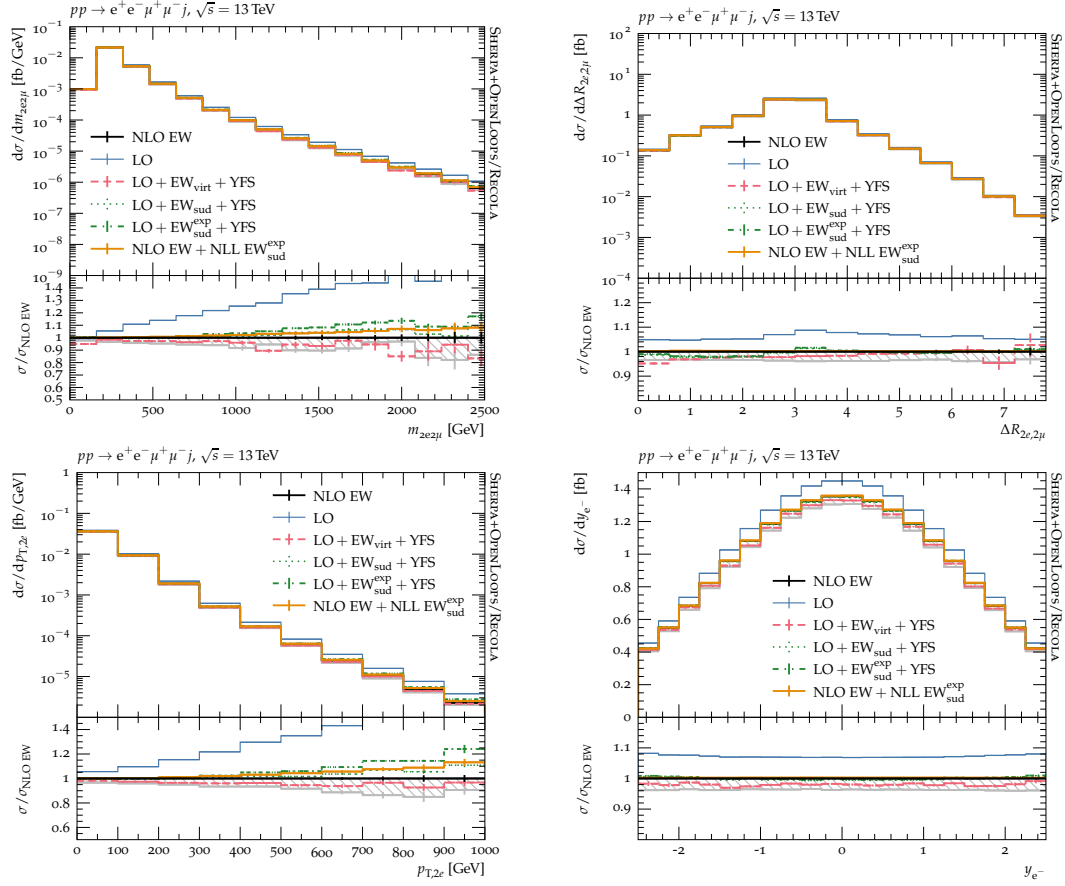
Figure 4.9: Leptonic observable distributions as shown in Fig. 4.8 but for the $pp \rightarrow e^+e^-\mu^+\mu^- j$ process.

The observables studied in the previous case are repeated here and are shown in Fig. 4.9. The EW effects are again comparable to the observation of the previous case. The only difference is in the EW scheme dependence, and the size of the NLO EW corrections that are just slightly reduced. This again suggests that the EW Sudakov logarithms factorize with respect to at least one additional QCD emission. Therefore, the final state distribution of EW charges is not affected by QCD corrections, that is also discussed in Ref. [202].

A major difference from the 0-jet case is in the Z-boson distance observable. In this case the region below π is already populated at leading order by the extra final state jet included in the calculation. This means that also this region gets the large EW virtual correction, resulting in a smaller EW scheme dependence and no jump between the regions below and above π for the EW approximated calculations. This observable displays now an almost flat NLO EW correction of about 5-10%.

Finally, for this process two one-jet observables have been studied in order to check the behavior of the EW corrections and the effects of the QCD-EW interference

diagrams. The jet observables under study are the hardest jet transverse momentum $p_{\mathrm{T},j}$ and the angular separation between the hardest jet and the four-lepton system $\Delta\phi_{4l,j}$. Both observables are shown in Fig. 4.10.

In order to check the effects of the interference between QCD and EW diagrams a new line labelled "NLO EW (no interf.)" is included. This refers to the full NLO EW calculation excluding only the interfering diagrams. It is important to stress again that this contribution is not included in neither EW approximations since they are simply applied to the Born-level matrix elements. Moreover, these diagrams are IR finite, meaning that they are not even approximated by the YFS soft-photon resummation.

In order to make a more fair comparison between the two EW approximations and the NLO EW fixed order result, these have been compared to the "NLO EW (no interf.)" line. This comparison is shown in the lower ratio panel in Fig. 4.10. The upper panel, instead, compare the full NLO EW fixed order calculation to the one where the QCD-EW interference terms are excluded. In the azimuthal angle separation between the four-lepton system and the hardest jet, real emissions populate the angular range $0° \leq \Delta\phi_{4l,j} \leq 180°$, while the back-to-back final state configuration, *i.e.* $\Delta\phi_{4l,j} = 180°$, is also populated by Born kinematics. This means that for non-back-to-back configurations the EW approximated results are entirely modelled by the YFS resummation. From the lower panel we can see that the YFS modelling of multiple soft-photon emission is able to reproduce quite well the NLO EW fixed order spectrum specially in the range $0° < \Delta\phi_{4l,j} < 90°$. The region $90° < \Delta\phi_{4l,j} < 180°$, instead, shows an offset of about $20 - 30\%$. This was also observed in the $\Delta R_{2e2\mu}$ observable from the 0-jet calculation for $\Delta R_{2e2\mu} < \pi$. From the upper ratio panel we can see that the effect of the QCD-EW interference diagrams is a bump at high $\Delta\phi_{4l,j}$ peaked around $120°$ with a difference of roughly 30%. The two lines, instead, converge for smaller angle separations. In this observable it is possible to appreciate the effects of the non-trivial scheme dependence in the renormalisation factors of the EW virtual correction looking at the rightmost bin. This bin gets populated also by virtual emission diagrams that are responsible for the jump displayed in the EW approximated calculations. Also for the hardest jet transverse momentum the impact of the QCD-EW interference diagrams is quite sizeable, specially at energies above $300\,\mathrm{GeV}$. Still the EW approximations agree very well with the "NLO EW (no interf.)" result. In particular in this case an excellent agreement for the EW$_{\mathrm{virt}}$ approximation is displayed. These observations suggest that limiting the jet activity using a jet veto can improve the agreement between the EW approximations and the full NLO EW fixed order calculation, without the need of excluding pieces of the calculation. This possibility was studied in Ref. [202] for the WW and WWj production using only the EW$_{\mathrm{virt}}$ approximation to approximate EW effects. In this work was observed a very good agreement between the two calculations proving that a jet veto is a good way for improving the accuracy of EW approximations. However, it has to be noted that a jet veto has to be carefully added to the calculation since it introduces logarithms of the jet-veto
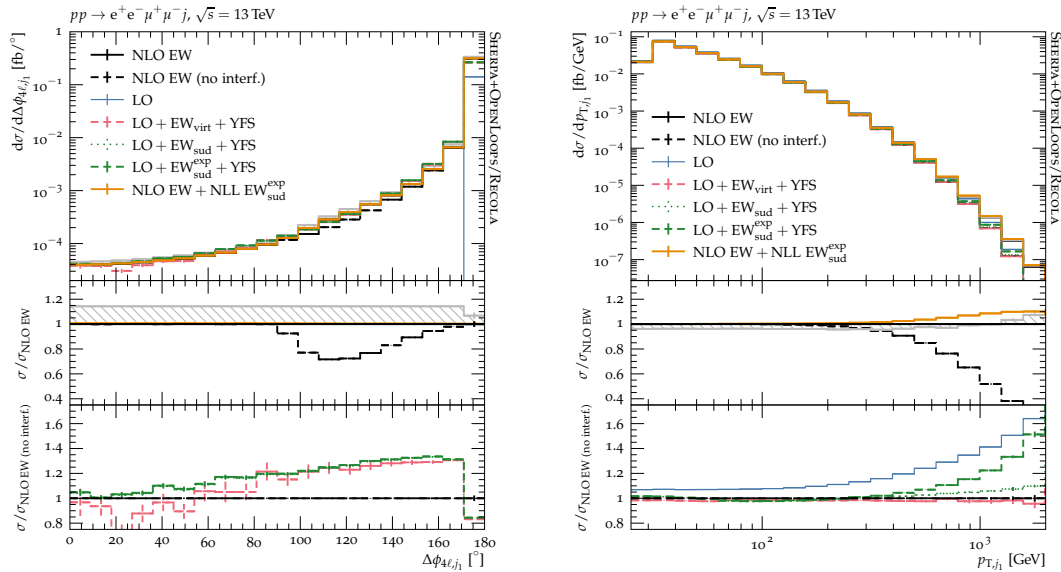
Figure 4.10: Distributions for the azimuthal distance between the four-lepton system and the leading jet $\Delta\phi_{4\ell,j_1}$ (left), and the leading-jet transverse momentum p_{T,j_1} (right) for the $pp \rightarrow e^+e^-\mu^+\mu^-j$ process. They are given at LO and at NLO EW and compared to approximative EW calculations. The NLO EW is given for the G_μ (black line) and $\alpha(M_Z^2)$ (grey line) renormalisation schemes, and the span between the two is marked by a hatched band. In addition, the NLO EW is plotted without interference terms ("no interf."). All predictions are calculated using SHERPA+OPENLOOPS/RECOLA.

scale that would need to be resummed.

Finally, it is also important to note that even in the absence of jet vetoes, the inclusion of QCD real emission corrections would size the impact of the QCD-EW interference diagrams since it is well known that NLO QCD corrections are of the order of 100% at high energies [203]. Moreover, in a multi-jet merged calculation, the merging cut would limit even more the activity of such process. In order to give a clear idea of the effects of higher QCD multiplicities on the size of the four-quark diagram, in Fig. 4.11 is added to the NLO EW calculation the NLO QCD correction which include diagrams of the order $\mathcal{O}(\alpha_s^2\alpha^4)$ with both virtual and real emissions. Particular care was taken in order to avoid including the same diagrams twice. Only coloured initial- and final-states have therefore been allowed.

In both observables the effect of the QCD-EW interference diagrams has been reduced by the dominating extra QCD radiation. Specially for the angular separation between the four-lepton system and the hardest jet. In the hardest-jet transverse momentum their effect is still visible but it is now reduced to a correction of about 20% at $p_{T,j_1} = 1.5$ TeV compared to the only NLO EW case where the correction was more than 70% at this transverse momentum.
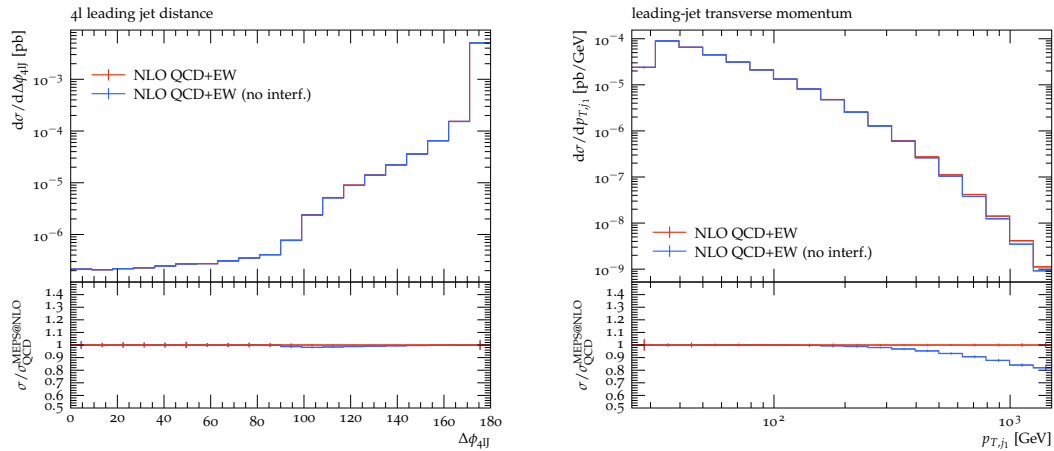
Figure 4.11: Distributions for the azimuthal distance between the four-lepton system and the leading jet $\Delta\phi_{4\ell,j_1}$ (left), and the leading-jet transverse momentum p_{T,j_1} (right) for the $pp \to e^+e^-\mu^+\mu^- j$ process. The reference sample (red line) is evaluated at NLO EW + QCD including multiplicative terms. This is compared with the same calculation excluding the QCD-EW interference diagrams. All predictions are calculated using SHERPA+OPENLOOPS.

4.6   Electroweak Effects in a General QCD Simulation

Finally, the results for EW effects in a general QCD simulation for the production of the four-lepton final state $e^+e^-\mu^+\mu^-$ are discussed. Firstly, is given a general analysis of how EW approximations are implemented in SHERPA's multi-jet merged framework together with a validation of the implementation. In the validation step, it is checked that the choices made for the inclusion of the EW approximations, do not spoil the claimed accuracy of the calculation and do not introduce any spurious effect. To conclude the chapter, it is going to be discussed the phenomenology for the production of two off-shell Z bosons in a multi-jet merged setup with EW corrections.

4.6.1   Electroweak Approximation in Multi-jet Merged Samples

The purpose of a multijet-merged calculation is to describe the effects of multiple real QCD radiations relying on the actual matrix elements instead of considering solely the soft-collinear approximation used in a parton-shower. This method is particularly important for an accurate modelling of high-energetic QCD radiations. This very same region is also sensible to EW corrections as discussed so far. It is thus important to have a consistent and detailed treatment of EW effects alongside a multiple QCD hard emission simulation.

The multijet-merging method implemented in SHERPA has already been introduced in Sec. 2.3. The combination of EW corrections with this method requires particular care in order to not interfere with the ordering of the QCD emissions either hard or soft. In this case all the results include soft-photons real emission off the final state leptons according to the YFS method.

In the multijet-merging method EW approximations are applied as a local k-factor to the pieces of the calculation. For leading order matrix elements, evaluated according to Eq. (2.3.1), EW corrections enter as,

$$B_n \to B_n \left(1 + \delta_n^{\mathrm{EW}}\right), \tag{4.6.1}$$

while in NLO accurate calculations EW corrections are applied to both S- and H-type events, see Eq. (2.3.3), as

$$\overline{B}_n \to \overline{B}_n \left(1 + \delta_{n,S}^{\mathrm{EW}}\right), \qquad H_n \to H_n \left(1 + \delta_{n,H}^{\mathrm{EW}}\right). \tag{4.6.2}$$

Special care has also to be taken when dealing with leading order matrix elements merged on top of NLO QCD accurate matrix elements. In this case EW corrections enter the calculation also through the local k-factor of Eq. (2.3.4), applying the transformations in Eq. (4.6.1) and Eq. (4.6.2) to Born, S- and H-type bits in the local k-factor. This allows to propagate EW effects to higher multiplicities, specially for the $\mathrm{EW}_{\mathrm{virt}}$ approximation since EW virtual matrix elements may not be available or just computationally too expensive.

To deal with the computational cost of the actual EW virtual matrix elements used in the $\mathrm{EW}_{\mathrm{virt}}$ approximation, this is applied only to S-type events of the multiplicities evaluated at NLO, $i.e.$

$$\delta_{n,S}^{\mathrm{EW}}\left(\Phi_n\right) = \frac{\mathrm{V}_n^{\mathrm{EW}}\left(\Phi_n\right) + \mathrm{I}_n^{\mathrm{EW}}\left(\Phi_n\right)}{\mathrm{B}_n\left(\Phi_n\right)},$$
$$\delta_{n,H}^{\mathrm{EW}}\left(\Phi_{n+1}\right) = 0, \qquad \text{and} \qquad \delta_{\mathrm{virt},n,\mathrm{B}}^{\mathrm{EW}}\left(\Phi_n\right) = 0. \tag{4.6.3}$$

There is also another possibility to define $\delta_{n,S}^{\mathrm{EW}}$ that is,

$$\delta_{n,S}^{\mathrm{EW}}\left(\Phi_n\right) = \frac{\mathrm{V}_n^{\mathrm{EW}}\left(\Phi_n\right) + \mathrm{I}_n^{\mathrm{EW}}\left(\Phi_n\right)}{\overline{\mathrm{B}}_n\left(\Phi_n\right)}. \tag{4.6.4}$$

These two choices differ by terms of relative accuracy $\mathcal{O}(\alpha_s\alpha)$ and are referred to respectively as multiplicative and additive method. The multiplicative and additive nature of these two $\delta_{n,S}^{\mathrm{EW}}$ follows the fact that in the expression $\overline{B}_n\left(1 + \delta_{n,S}^{\mathrm{EW}}\right)$ when using the $\delta_{n,S}^{\mathrm{EW}}$ from Eq. (4.6.4), the $\bar{B}_n(\Phi_n)$ in the denominator leave the EW corrections just as additive terms, while when using the definition from Eq. (4.6.3) the $\mathrm{V}_n^{\mathrm{QCD}}\left(\Phi_n\right) + \mathrm{I}_n^{\mathrm{QCD}}\left(\Phi_n\right)$ gets multiplied by $\mathrm{V}_n^{\mathrm{EW}}\left(\Phi_n\right) + \mathrm{I}_n^{\mathrm{EW}}\left(\Phi_n\right)$ accounting for approximate mixed QCD-EW corrections. Their effects are studied in the following validation step. The practical choice to set to zero the $\mathrm{EW}_{\mathrm{virt}}$ for Born and H-type events requires a careful validation of the $\mathrm{EW}_{\mathrm{virt}}$ approximation in order to be sure that no important contribution is left out the calculation.

The $\mathrm{EW}_{\mathrm{virt}}$ approximation enters the local k-factor of higher multiplicities as

follows,

$$k_{\text{virt},m}^{\text{EW}}\left(\Phi_m, \Phi_{m+1}\right) = \frac{\overline{\text{B}}_m\left(\Phi_m\right)\left(1 + \delta_{\text{virt},m,\mathbb{S}}^{\text{EW}}(\Phi_m)\right)}{\text{B}_m\left(\Phi_m\right)}\left(1 - \frac{\text{H}_m\left(\Phi_{m+1}\right)}{\text{B}_{m+1}\left(\Phi_{m+1}\right)}\right)$$
$$+ \frac{\text{H}_m\left(\Phi_{m+1}\right)}{\text{B}_{m+1}\left(\Phi_{m+1}\right)}\,, \qquad (4.6.5)$$

where $m = n_{\max}^{\text{NLO}}$. The local k-factor is built in such a way that in $(n_{\max}^{\text{NLO}} + l)$-jet events the underlying $n_{\max}^{\text{NLO}}$-jet topology receives the right EW approximate correction at the claimed accuracy.

The EW_{sud} approximation, not having the same computational constraints of the EW_{virt}, is applied to every piece of the calculation, thus

$$\delta_{\text{sud},n,\text{B}}^{\text{EW}}\left(\Phi_n\right) = \delta_{\text{sud},n,\mathbb{S}}^{\text{EW}}\left(\Phi_n\right) = \text{K}_{\text{sud},n}^{\text{NLL}}\left(\Phi_n\right) \quad \text{and} \quad \delta_{\text{sud},n,\mathbb{H}}^{\text{EW}}\left(\Phi_{n+1}\right) = \text{K}_{\text{sud},n+1}^{\text{NLL}}\left(\Phi_{n+1}\right)\,.$$
$$(4.6.6)$$

Including the EW_{sud} approximation in this way, let the multi-jet merged calculation to have all the important EW Sudakov logarithms at the NLL logarithmic accuracy for every jet multiplicity. The higher multiplicities evaluated at leading order also receive EW corrections from the local k-factor. However, these get cancelled by the H-type events avoiding any double counting of the higher-order EW effects, resulting in the correct NLL accuracy of the EW Sudakov logarithms. Similarly to the fixed order case, the EW_{sud} correction could be exponentiated using the simple mapping $1 + \delta_{\text{sud}}^{\text{EW}} \to \exp\left\{\delta_{\text{sud}}^{\text{EW}}\right\}$.

Loop-induced gluon initiated contributions both for 0- and 1- jet multiplicities are also taken into account. These are matched in a separate sample using the MEPS@LO method described in Sec. 2.3. The possibility to generate these processes separately comes from the fact that they do not interfere with any of the processes in the MEPS@NLO. For the EW virtual matrix elements instead, these are not yet available for this process. The EW_{virt} approximation is thus not applicable for loop-squared processes. The EW_{sud}, on the other hand, could be used since there is no technical limitation in the algorithm implemented in SHERPA. However, a detailed study of the high energy behavior of EW corrections for loop-squared diagrams has not yet been done and the implemented set of logarithms in the EW_{sud} approximation may be incomplete not representing the right NLL accuracy for the EW Sudakov logarithms. This is due to possible new logarithms arising from virtual EW gauge bosons exchanged between the quarks inside the loop. For this reason also the EW_{sud} is not applied to this sample.

The QCD virtual correction for the $gg \to e^+e^-\mu^+\mu^-$ process has been recently computed [8]. Its implementation in SHERPA is part of the original outcome of this thesis and it is presented in details in Chap. 5. However for the results in this Chapter, loop-induced processes are considered only at leading order, for both the

0- and 1-jet multiplicity. This choice has been made in order to have a clear and clean phenomenological study of EW corrections to processes where they act upon. The loop-induced process has been considered only to check the impact of other large corrections that are part of a general calculation. Some examples of some contributing loop-induced diagrams respectively for the 0- and 1-jet multiplicity are given in Fig. 5.6 and Fig. 5.8.

4.6.2   Validation of the EW Approximations

In this multi-jet merged calculation the processes $pp \rightarrow e^+e^-\mu^+\mu^-$ and $pp \rightarrow e^+e^-\mu^+\mu^- j$ are evaluated at NLO QCD accuracy while the processes $pp \rightarrow e^+e^-\mu^+\mu^- jj$ and $pp \rightarrow e^+e^-\mu^+\mu^- jjj$ are instead evaluated at leading order accuracy. In order to have another reference for the validation of the EW approximations' implementation, the MEPs@Nlo calculation is also compared against the MEPs@Lo with all jet multiplicity evaluated at leading order. In the differential observables the MEPs@Lo sample includes also the EW$_{\text{sud}}$ approximation. The implementation of the EW$_{\text{virt}}$ approximation does not allow to use it in a MEPs@Lo calculation since its $\delta^{\text{EW}}_{\text{virt},n,\text{B}}(\Phi_n)$ is by default set to zero. Moreover, it is not yet possible to apply EW corrections only to some specific Born multiplicity. In the studied observables, the MEPs@Lo has been rescaled by a global QCD factor taken by the ratio of the MEPs@Nlo and MEPs@Lo total cross-section using the values in Tab. 4.4. The reason for rescaling the MEPs@Lo sample is to capture non-trivial higher order kinematical effects.

The CKKW algorithm for the multijet matrix element merging has been used with a merging cut of

$$Q_{\text{cut}} = 30\,\text{GeV}. \tag{4.6.7}$$

All other scales in the calculation, *i.e.* renormalisation, factorisation and resummation scales, are set according to the CKKW scale-setting prescription described in Sec. 2.3. The renormalisation scale $\mu_{\text{R}} = \mu_{\text{CKKW}}$ is then set to

$$\alpha_s^n(\mu^2_{\text{CKKW}}) = \alpha_s(t_1)\ldots\alpha_s(t_n), \tag{4.6.8}$$

where t_i is the scale of the ith-emission reconstructed by the CKKW clustering algorithm. The core process scale, meaning that no emission has happened, is set to the transverse energy defined as

$$\mu_{\text{core}} = \frac{1}{2}\left(E_{\text{T},ee} + E_{\text{T},\mu\mu}\right). \tag{4.6.9}$$

In Tab. 4.4 are reported the total cross-sections evaluated in the fiducial phase space defined in Sec. 4.5. The first noticeable result is that higher order real QCD emissions increase the total cross-section by about 13% compared to the leading

order fixed order total cross-section given in Tab. 4.2. This shows again the large impact of multiple QCD hard emissions also in fully inclusive calculations. Instead, evaluating the 0- and 1-jet multiplicity at NLO increases the MePs@Lo cross-section by a further 20%. In the differential observables discussed below the MePs@Lo is then rescaled by a factor of 1.2 to match the MePs@Nlo total cross-section. The EW effects on the total cross-section of the MePs@Nlo are slightly smaller compared to the fixed order calculations of Sec. 4.5. In this case they amount to a negative correction of about 4% for both EW_{virt} and EW_{sud}. The exponentiated EW_{sud} instead reduce the dampening effect of the EW corrections by a 1%. The reason why the EW corrections in this case are smaller is because the YFS soft photon resummation now is also included in the reference samples.

$pp \to e^+e^-\mu^+\mu^-$ + jets		fiducial cross section		corrections to MePs@Nlo + YFS		
Scheme	Region	MePs@Lo + YFS	MePs@Nlo + YFS	$\times\,EW_{virt}$	$\times\,EW_{sud}$	$\times\,EW_{sud}^{exp}$
G_μ	inclusive	11.10 fb	**13.34 fb**	-4%	-4%	-3%

Table 4.4: Inclusive fiducial cross sections for $pp \to e^+e^-\mu^+\mu^-$ + jets at $\sqrt{s} = 13\,\text{TeV}$ for MePs@Lo and MePs@Nlo in the G_μ scheme including YFS photon emissions. For the MePs@Nlo predictions, relative corrections for the combination with the EW_{virt} and EW_{sud} approximations are also listed.

The observables taken under consideration for the validation of the EW approximation in a multi-jet merged calculation have been separated into two sets. The first includes only lepton exclusive observables, that are four lepton invariant mass $m_{2e2\mu}$, Z-boson separation $\Delta R_{2e2\mu}$, transverse momentum of the electron pair $p_{T,2e}$ and the four lepton transverse momentum $p_{T2e2\mu}$, while the second set only jet observables, that are angular separation between the four-lepton system and the hardest jet, hardest jet transverse momentum p_{T,j_1}, jet multiplicity N_{jet} and subleading jet transverse momentum p_{T,j_2}. All these plots have two lower panels. The upper one shows the EW corrections relative to the MePs@Nlo QCD calculation while the lower shows the size of the contributions that make up the MePs@Nlo sample.

Each observable shows very similar EW effects to those observed in the fixed order calculations. To summarize, in the high energy regime EW corrections produce a large destructive effect, as it is clear from every energy-dependent observable (four-lepton invariant mass and the transverse momentum observables). On the other hand, energy-independent observables receive an almost flat, small and negative correction from both EW_{sud} and EW_{virt} corrections. In particular for the number of jets N_{jet} observable it confirms the behavior discussed in Sec. 4.5.4 that QCD real emissions do not change the qualitative behavior of EW effects. This property can be explained by the fact that QCD emissions are predominantly soft and collinear, meaning that it does not significantly change the final state EW charge distribution nor induce any other additional large scale.

The lower panel in the plots of Fig. 4.12 and Fig. 4.13 shows the S- and H-type events for both 0- and 1-jet multiplicities and the Born events for 2- and 3-jet multiplicities. The contribution of H-type events is very small across all observables, contributing at most 5% in the $\Delta\phi_{4l,j_1}$ observable, only in the low angle separation region. This ensures that there is no significant admixture of H-type events in the observables under consideration, justifying the choice made for the EW_{virt} approximation to turn it off in these events. The small impact of the H-type events is not surprising since they are constrained to be below the merging cut by $\theta(Q_{\text{cut}} - Q_{n+1})$ (See Eq. (2.3.3)). The 2- and 3-jet samples, on the other hand, have a more sizeable contribution with an impact of more that 20% for $\Delta_{2e2\mu} < \pi$, $\Delta\phi_{4l,j_1} < \pi$, $N_{\text{jet}} > 1$ and in the tail of all the transverse-momentum observables. Generally put, 2- and 3-jet samples give a larger contribution for kinematical configurations that require hard and/or widely separated jets. On these events, the EW_{virt} approximation is applied only through the MENLOPS local k-factor. However, no significant difference between the EW_{virt} and EW_{sud} is displayed, meaning that the choice of propagating EW effects in the EW_{virt} approximation to higher multiplicities via the MENLOPS local k-factor does not introduce any spurious effect.

Finally, the rescaled MEPS@LO $+\text{EW}_{\text{sud}}$ does not show any major differences in regions dominated by 0-jet kinematics. Instead, it differs from the MEPS@NLO $+\text{EW}_{\text{virt}}/\text{EW}_{\text{sud}}$ up to 10% in the rest of the phase space. Looking at the impact of the EW_{sud} correction to the MEPS@NLO it is noticeable an almost identical behavior. This follows the fact that H-type events are negligible. This provides a very important validation for the implementation of the EW_{sud} approximation since it means that there is no difference whether the EW_{sud} is applied to leading order or S-type events.

4.6.3 Phenomenology of EW Effects

With the structural analysis of the multi-jet merged sample of the previous Section, it is now possible to safely apply these approximations and discuss their phenomenology. The previous MEPS@NLO sample is now supplemented with a theoretical uncertainty band defined enveloping the 7-point scale variation of the QCD renormalisation and factorisation scale [204],

$$\left\{ (\tfrac{1}{2}\mu_{\text{R}},\ \tfrac{1}{2}\mu_{\text{F}}),\ (\tfrac{1}{2}\mu_{\text{R}},\mu_{\text{F}}),\ (\mu_{\text{R}},\tfrac{1}{2}\mu_{\text{F}}),\ (\mu_{\text{R}},\mu_{\text{F}}),\ (\mu_{\text{R}},2\mu_{\text{F}}),\ (2\mu_{\text{R}},\mu_{\text{F}}),\ (2\mu_{\text{R}},2\mu_{\text{F}}) \right\}.$$

In SHERPA this scale variation is fully automated using an on-the-fly reweighting strategy [205]. The α_s and PDF scales in the parton shower are varied accordingly. The reason why the theoretical scale uncertainty has been evaluated only for the MEPS@NLO calculation is because in this way it is possible to understand the phenomenological relevance of the EW corrections under consideration. In a separate sample, the 0+1-jet loop-induced four-lepton production is added to the MEPS@NLO calculation labelled MEPS@LOOP^2. This is presented as a separate
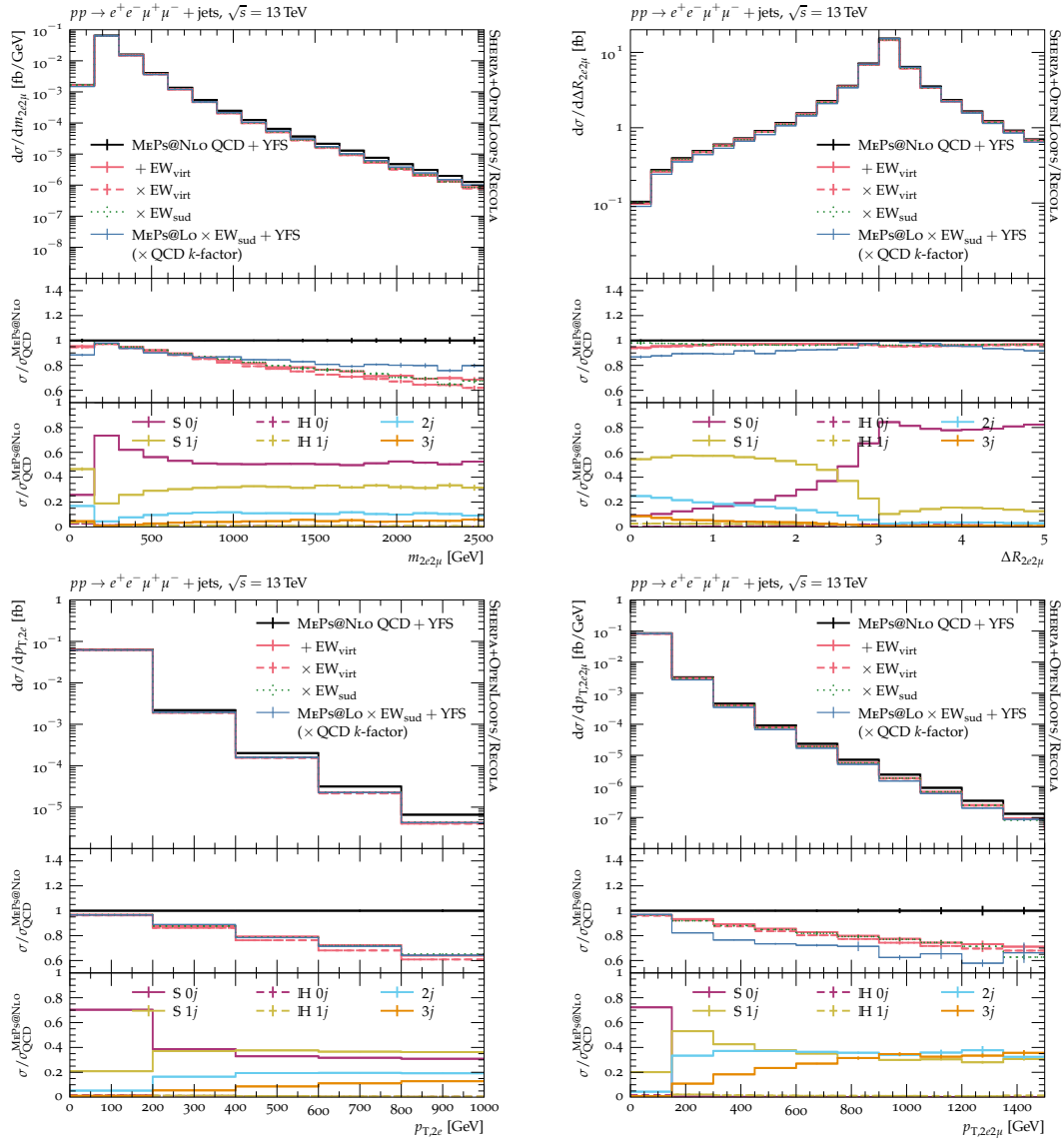
Figure 4.12: Differential leptonic observables for the process $pp \to e^+e^-\mu^+\mu^- +$ jets. The reference calculation is a MePs@Nlo calculation in the G_μ scheme. On top of it, EW$_{\mathrm{virt}}$ and EW$_{\mathrm{sud}}$ approximations are applied. The EW$_{\mathrm{sud}}$ approximation is also shown for a MePs@Lo calculation, rescaled by the total MePs@Nlo rate using the total cross-section QCD k-factor of 1.20. The four observables from top left to bottom right are: the invariant mass of the four-lepton system $m_{2e2\mu}$, the Z-boson distance $\Delta R_{2e,2\mu}$, the transverse momentum of the di-electron pair $p_{\mathrm{T},2e}$, and the transverse momentum of the four-lepton system $p_{\mathrm{T},2e2\mu}$. All predictions are calculated using Sherpa+OpenLoops/Recola. The first ratio plot shows the relative size of the EW corrections, while the second one gives the relative size of the contributions to the MePs@Nlo prediction.
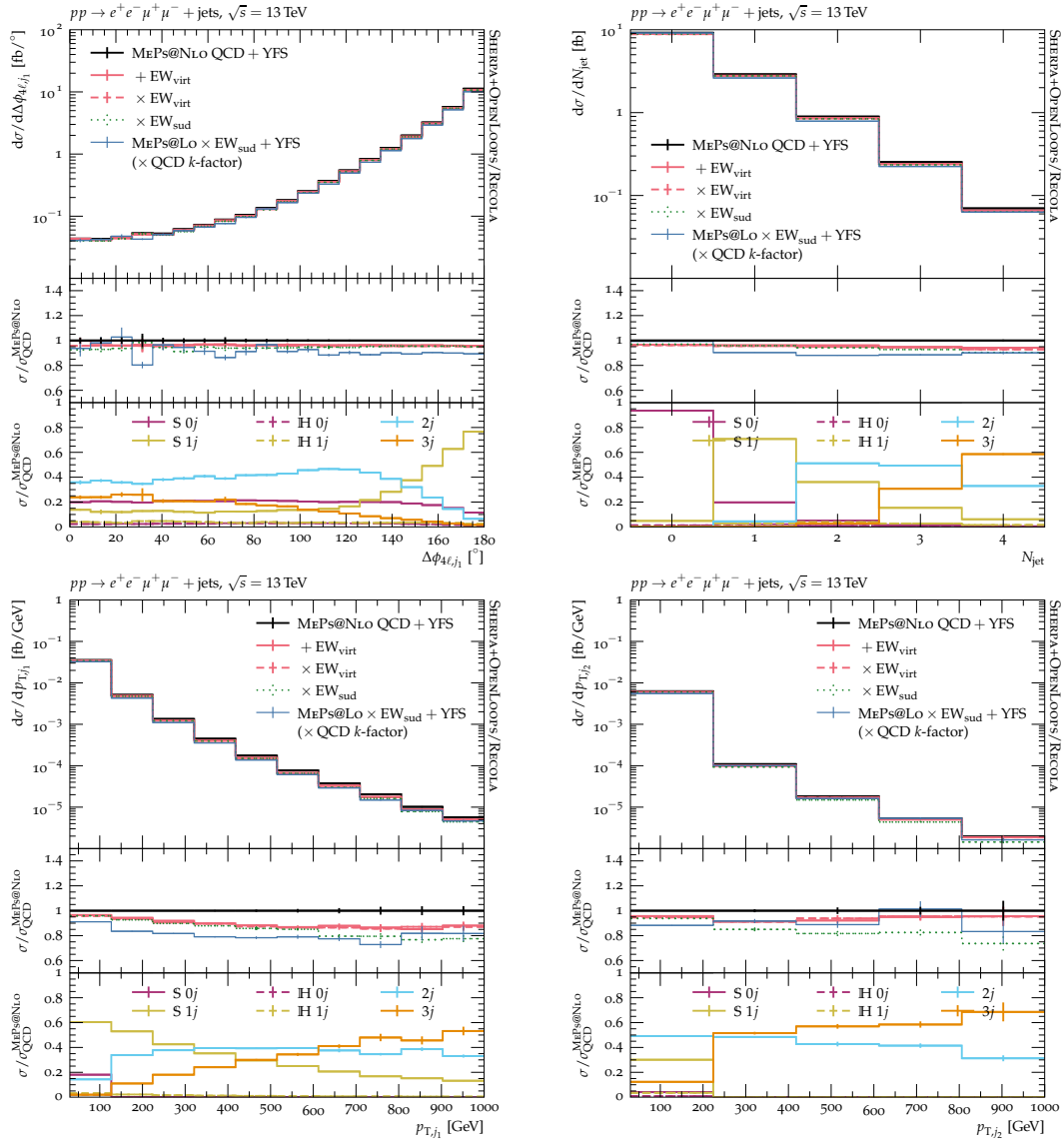
Figure 4.13: As Fig. 4.12 but for jet observables. Shown are from top left to bottom right: the angular separation between the four-lepton system and the hardest jet $\Delta\phi_{4\ell,j_1}$, the number of jets N_{jet}, and the transverse momenta of the hardest jet p_{T,j_1} and second hardest jet p_{T,j_2}.

sample in order to isolate large effects from loop-induced diagrams to give a clear idea of the impact of loop-induced processes on the MEPS@NLO +EW corrections samples without over-complicating the study of EW effects on the processes they are applied to. In this case the additive EW$_{\mathrm{virt}}$ is not shown since in the previous section the two schemes did not display any noticeable difference. The EW$_{\mathrm{sud}}$, instead, is shown also exponentiated.
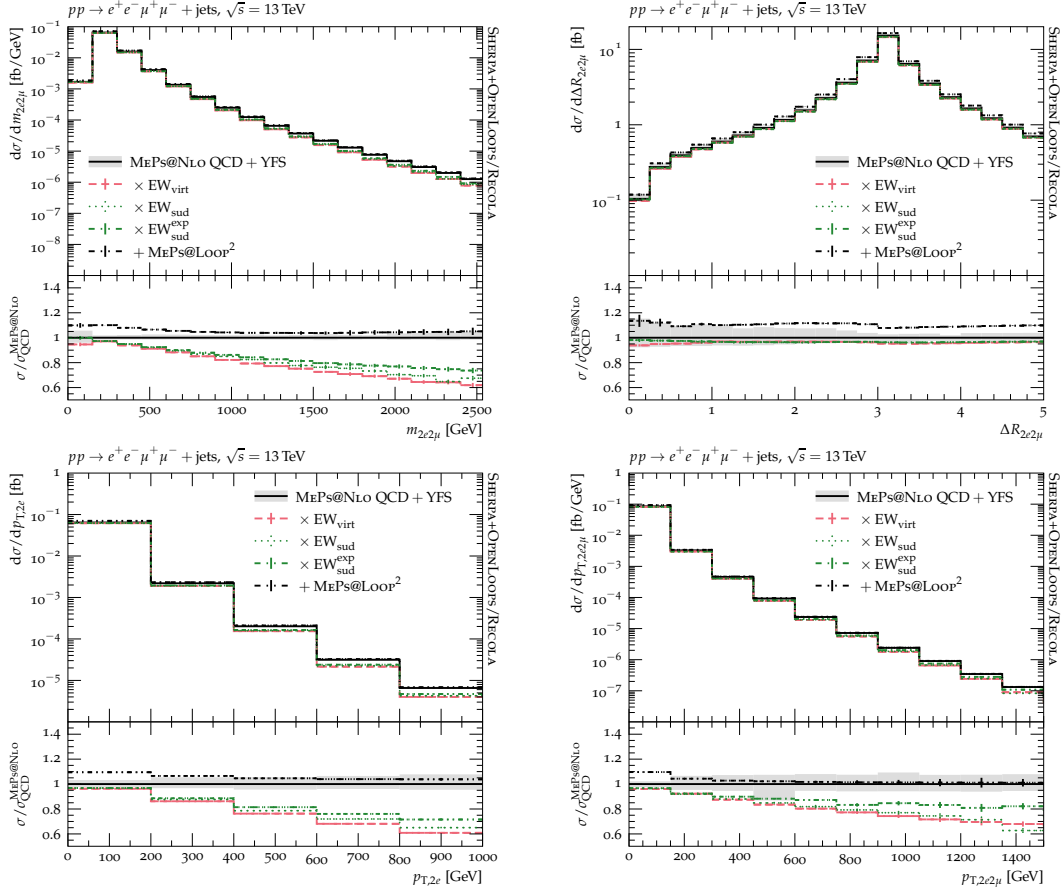
Figure 4.14: Distributions of leptonic observables for $pp \to e^+e^-\mu^+\mu^-$ + jets production. The reference calculation is given by the MEPS@NLO result in the G_μ scheme, with the grey band that indicates the 7-point scale-variation uncertainty. On top of it, loop-induced corrections and $\text{EW}_{\text{virt}}/\text{EW}_{\text{sud}}$ approximations are applied. From top left to bottom right the shown observables the four-lepton invariant mass $m_{2e2\mu}$, the Z-boson distance $\Delta R_{2e,2\mu}$, the di-electron transverse momentum $p_{\text{T},2e}$, and four-lepton transverse momentum $p_{\text{T},2e2\mu}$. All predictions are calculated using SHERPA+OPENLOOPS/RECOLA.

In Fig. 4.14 are shown the same inclusive observables studied in the validation step. These are $m_{2e2\mu}$, $p_{\text{T},2e}$, $\Delta R_{2e,2\mu}$ and $p_{\text{T},2e2\mu}$. The first thing to notice is the larger QCD scale uncertainty in the phase space region where higher multiplicities contributions are more dominant. Particularly, for $\Delta R_{2e,2\mu} < \pi$ and $p_{\text{T},2e2\mu} > 100\,\text{GeV}$, where the four-lepton system recoil against hard QCD emissions. In these regions the QCD scale uncertainty reaches 10%. In both, four-lepton invariant mass and leptons transverse momentum, the scale uncertainty is not able to cover the large effects of the EW corrections, specially for energies above $200\,\text{GeV}$. On the other hand, in scale-less observables the effect of the EW correction is almost entirely covered by the theoretical QCD scale uncertainty band.

The jet observables, $\Delta\phi_{4\ell,j_1}$, N_{jet}, p_{T,j_1} and p_{T,j_2} shown in Fig. 4.15, get large corrections by the 2- and 3-jet multiplicity samples, as shown previously in Fig. 4.13. This is reflected in a much larger scale uncertainty when compared to the inclusive observables given in Fig. 4.14. The magnitude of this theoretical uncertainty is due to the fact that higher order multiplicities are taken at leading order. The uncertainty band goes on average from a -10% to a +20% of the nominal value. The larger scale uncertainty reduces to about ±5% in the region dominated by more inclusive samples, which are evaluated at NLO QCD accuracy. This is particularly visible in the first bin of the number of jet observable N_{jet}. However, this large QCD scale uncertainty does not cover the very large EW correction in energy dependent observables such as p_{T,j_1} and p_{T,j_2}. Specifically, in the leading-jet transverse momentum observable the EW approximations are about -20% at $p_{\text{T},j_1} = 1\,\text{TeV}$.

The impact of the MEPS@LOOP^2 is overall flat and increases the MEPS@NLO calculation by about $5-10\%$. The larger impact from the loop-induced processes comes from low energy regions, *i.e.* roughly below 200 GeV. This means that their inclusion in a complete calculation would not affect much the size of the EW corrections in the high energy region. The smaller impact of the loop-induced processes at high energies is due to the fact that it is evaluated only for 0- and 1-jet multiplicities while that energy region is dominated by higher QCD multiplicities.

Finally, the exponentiated EW$_{\text{sud}}$ gives almost identical results compared to the non-exponentiated one, MEPS@NLO +EW$_{\text{sud}}$, due to the moderate absolute value of the EW$_{\text{sud}}$ correction for the observables under consideration.
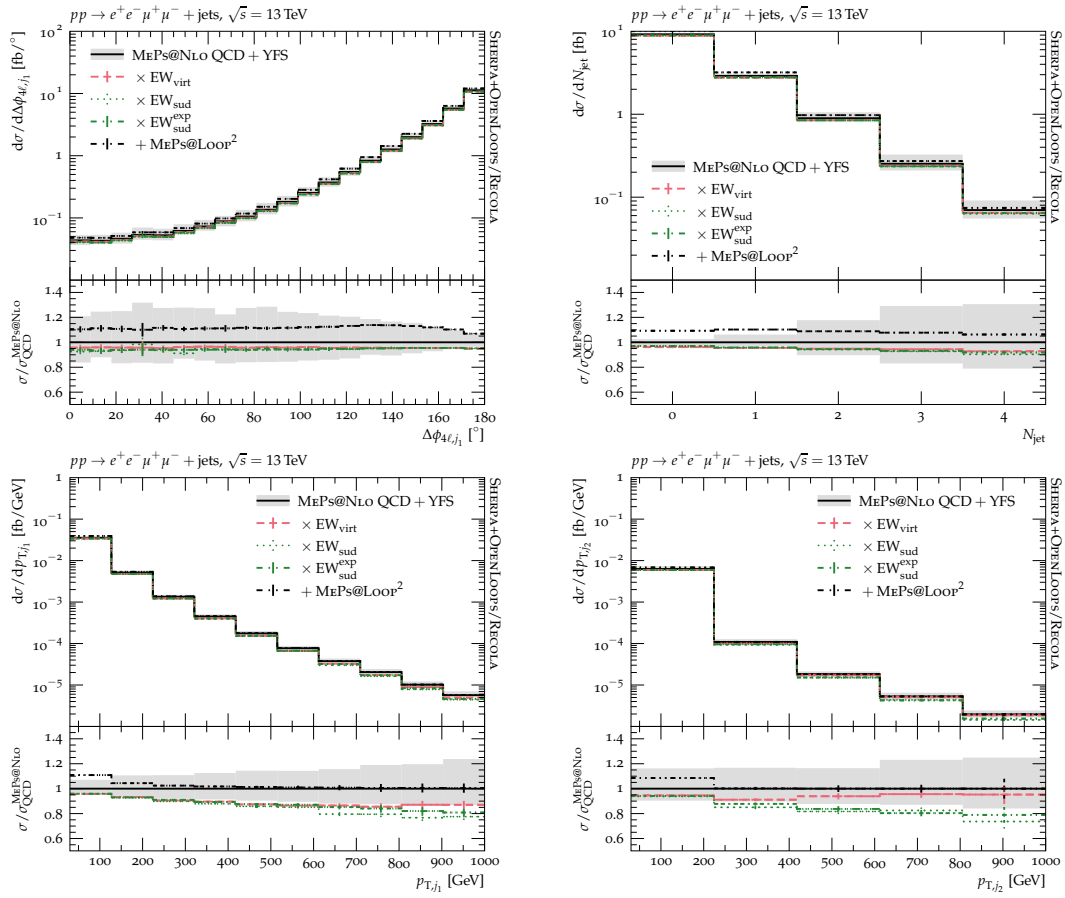
Figure 4.15: As Fig. 4.14 but for jet observables. Shown are from top left to bottom right: the angular separation between the four-lepton system and the hardest jet $\Delta\phi_{4\ell,j_1}$, the number of jets N_{jet}, and the transverse momenta of the hardest jet p_{T,j_1} and second hardest jet p_{T,j_2}.

Chapter 5

QCD Corrections to $e^+e^-\mu^+\mu^-$: Gluon Fusion

This section presents the second set of original outcome from this thesis work. This chapter discusses a particular class of processes called loop-induced gluon-initiated, briefly discussed in previous sections. As for the EW corrections discussed in Chap. 4, this study of the loop-induced processes focuses on the $e^+e^-\mu^+\mu^-$ final state. Beside this final state, another process is discussed in order to highlight common features of loop-induced gluon-initiated processes such as large NLO QCD correction and non-trivial parton-shower matching effects. This is the on-shell production of a Higgs boson associated with a Z boson in gluon fusion. The discussion includes results published in the 2019 Les-Houches proceedings [206], done in collaboration with E. Bothmann, M. Calvetti, P. Francavilla, C. Pandini and E. Re.

Lately, there has been much work on the four-lepton production through gluon fusion due to its phenomenological importance [168, 169, 207]. This chapter focuses on a technical study of the parton-shower matching performed in SHERPA.

5.1 Introduction to Four-lepton Production in Gluon Fusion

Loop squared diagrams are a virtual radiative correction appearing at NNLO. The amplitude of the loop-induced process belongs to this class of diagrams with the main difference that it appears as its first non-trivial contribution, *i.e.* its leading order. The gluon initiated loop induced diagram is a particularly important example due to its phenomenological relevance. Indeed, it has been crucial in the discovery of the Higgs boson [2, 3] since its main production channel is in fact a gluon initiated loop induced process $gg \to H^* \to (Z/\gamma^*)(Z/\gamma^*)$. An example of Higgs production in gluon fusion is given in the second diagram of Fig. 5.6.

The production of the four-lepton final state $e^+e^-\mu^+\mu^-$ in gluon fusion plays a very important role in its theoretical modelling for two main reasons. Firstly, the

gluon-gluon initial state channel is opened for the first time by this process in the NNLO QCD correction of the process $pp \to e^+e^-\mu^+\mu^-$. As such, it is expected to have a sizeable impact on inclusive observables, moreover this is increased even further by the large initial state gluon flux. Secondly, it has an enhanced scale uncertainty due to the fact that it contributes at $\mathcal{O}(\alpha_s^2)$ with a leading order like renormalisation and factorisation scale dependence.

The leading order of loop-induced processes has been known for a long time [208, 209], and their evaluation is nowadays fully automated both numerically and analytically. The numerical evaluation is done with standard loop matrix element providers such as, RECOLA and MADLOOP [210], while the analytical evaluation of loop induced amplitudes at leading order is implemented in the MC generators MA-TRIX or MCFM. The NLO QCD virtual correction to $gg \to e^+e^-\mu^+\mu^-$, which is formally an N^3LO correction, can not yet be automatically computed via numerical methods due to the complicated structure of multi-loop matrix elements as discussed in Sec. 2.4. However, the analytical expression for the off-shell di-boson production is known in the case of massless quark-loops [211, 212, 8], and very recently also with full top-quark mass dependence in the case of on-shell final state Z-boson pair [167, 213]. The massless virtual correction has been implemented in the matrix-element generators POWHEG [168] and MATRIX [169]. Concerning the MC generator SHERPA, the massless virtual two-loop matrix elements have been implemented in this thesis work. The implementation will be part of the next major release of SHERPA v3.0.0. In all these implementations, top-quark effects have been included via approximations. In the MC generators MATRIX and SHERPA these have been taken into account rescaling the massless virtual amplitude with the leading order matrix element with full top-quark mass dependence. This method is described in Sec. 5.3.2. In POWHEG, top-quark mass effects have been taken into account by using the large-m_t expansion as presented in Ref. [212]. Due to these approxima-tions, the evaluation of the gluon-initiated loop-induced $e^+e^-\mu^+\mu^-$ production can be considered accurate only within the range $m_{2e2\mu} < 2m_t$. The top-quark mass de-pendence of the di-boson production through gluon fusion is discussed more in detail in Sec. 5.3.2. The real emission correction, instead, is readily available from the au-tomated one-loop matrix-element generators with full top-quark mass dependence. In principle, also higher multiplicities could be evaluated using RECOLA. However, this possibility has been investigated in this thesis finding that the evaluation time for a single phase space point in a simple MEPs set-up is $\mathcal{O}(s)$. For this reason this contribution is not included in the results discussed below.

The tools already available for parton-shower matching can be applied to this case with no extra modifications. This is due to the fact that, despite being a loop-squared type of contribution, it does not contain any UV or IR singularity. This aspect is discussed in detail in Sec. 5.1.3. The matching to the NLO accurate loop-induced calculation has already been investigated for the four-lepton final state using the POWHEG method [168, 207]. On the other hand an in-depth analysis of the NLO matching uncertainties has never been done for the process under consideration. A

preliminary study on this matter was presented for the di-Higgs production in Ref. [214]. This aspect of the parton-shower matching to the NLO accurate loop-induced process in $e^+e^-\mu^+\mu^-$ is the main focus of this chapter.

5.1.1   Higgs Production in Gluon Fusion

A good example of loop-induced processes is Higgs production via gluon fusion. In Fig. 5.1 the result of a simulation from the ATLAS collaboration [53] is shown highlighting the impact of each sub-process in the four-lepton invariant mass spectrum. This simulation gives a clear idea of the important role played by the gluon-gluon channel in on-shell Higgs production which dominates over the other processes, namely continuous gluon-initiated ZZ production $gg \to ZZ \to 4l$, $q\bar{q} \to 4l$ and other Higgs production channels like vector-boson fusion (VBF) and Higgs-strahlung. Moreover, while Higgs production is usually studied on-shell due to the very small decay-width of about $4\,\mathrm{MeV}$ [44], its off-shell production can become quite sizeable, especially in the four-lepton high invariant mass. This is due to destructive interferences between off-shell Higgs boson production $gg \to H^* \to VV \to 4l$ (signal) and continuous di-boson production $gg \to VV \to 4l$ (background). To give an example of the size of the signal-background interference, here are the total cross-sections for the signal, background and interference contributions in the total cross-section of the $e^+e^-\mu^+\mu^-$ production in gluon fusion

$$
\begin{aligned}
\sigma_{\mathrm{sig}} &= 0.074(1)\,\mathrm{fb} \\
\sigma_{\mathrm{bkg}} &= 2.90(1)\,\mathrm{fb} \\
\sigma_{\mathrm{int}} &= -0.154(1)\,\mathrm{fb}.
\end{aligned}
\tag{5.1.1}
$$

These values are taken from Ref. [207]. The signal-background interference adds a negative correction of about 5.5% to the total $gg \to e^+e^-\mu^+\mu^-$ cross-section, *i.e.* $\sigma_{\mathrm{tot}} = \sigma_{\mathrm{sig}} + \sigma_{\mathrm{bkg}} + \sigma_{\mathrm{int}}$. In Ref. [207] the process under consideration is evaluated with a center-of-mass energy of $\sqrt{s} = 13\,\mathrm{TeV}$, imposing only two selection cuts on the final-state leptons to focus on off-shell Higgs production, *i.e.* a Z-boson of invariant mass $60\,\mathrm{GeV} < m_{ll} < 120\,\mathrm{GeV}$ and four-lepton invariant mass $150\,\mathrm{GeV} < m_{4l} < 340\,\mathrm{GeV}$. Off-shell Higgs production is known to be a fundamental tool to determine its decay width [215, 165]. These examples highlight the need of having a sound modelling of loop induced processes for accurate predictions in Higgs physics analyses.

5.1.2   Impact of $gg \to ZZ$ on the Theoretical Scale Uncertainty

The fact that a loop-induced process has a leading-order-like QCD scale dependence at the $\mathcal{O}(\alpha_s^2)$ perturbative order together with the large PDFs, unsurprisingly makes
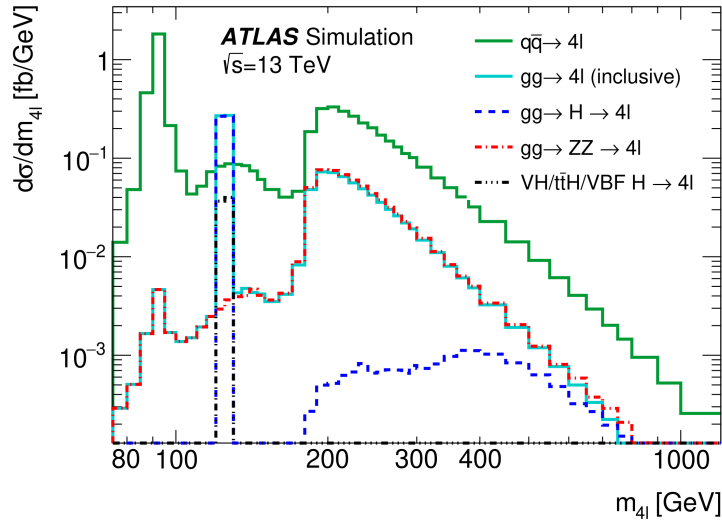
Figure 5.1: Four-lepton final state invariant mass spectrum where is highlighted the contribution of the quark initiated (solid green line), the gluon initiated loop-induced (solid light blue line) and vector boson fusion (dashed black line) production. Moreover, of the loop-induced process are also shown the direct Higgs production in gluon fusion $pp \rightarrow H \rightarrow 4l$ (dashed blue line) and continuous background di-boson production $pp \rightarrow ZZ \rightarrow 4l$ (dashed red line). The Figure is taken from Ref. [53], and it is covered by the Creative Commons Attribution 4.0 International Public License copyright that allows either public or commercial reproduction of the results shown in the work.

its renormalisation and factorisation QCD scale variations particularly large. Considering on-shell ZZ production for simplicity, Tab. 5.1 shows the total cross-sections for the $q\bar{q}$-LO, $q\bar{q}$-NLO, gg-LO and the NLO+ggLO contributions at a center-of-mass energy of $\sqrt{s} = 13$ TeV including their renormalisation and factorisation scale uncertainty evaluated using the standard 7-point scale variation. From the table we see the well known scale uncertainty reduction between the $q\bar{q}$-LO and the $q\bar{q}$-NLO which reduces the uncertainty from $+3.4\%/-4.2\%$ to $+2.2\%/-1.8\%$. The gg-LO total cross-section, as expected, displays a very large scale uncertainty of about 20%, which when combined with the $q\bar{q}$-NLO contribution increases the overall scale uncertainty by about 1%. In Ref. [169, 7] the impact of the gg loop-induced channel scale uncertainty is compared also against the quark initiated processes at NNLO QCD. In these works it has been observed that the loop-induced process contributes to more than half of the total NNLO QCD correction to $pp \rightarrow e^+e^-\mu^+\mu^-$. This large contribution makes the loop-induced process impact on the renormalisation and factorisation scale uncertainty quite sizeable. Indeed, in Ref. [169] it is shown that the quark-initiated process at NNLO, $i.e.$ excluding the gluon-initiated loop induced contribution, reduces the scale uncertainty of the NLO calculation by 1%, while taking into account also the loop induced contribution makes the complete NNLO correction having a scale uncertainty of about 0.5% bigger than the NLO

scale uncertainty.

Processes	Total Cross Section [fb]
$q\bar{q}$-LO	$11.67(4)^{+3.4\%}_{-4.2\%}$
$q\bar{q}$-NLO	$14.73(6)^{+2.2\%}_{-1.8\%}$
gg-LO	$1.095(2)^{+22.8\%}_{-17.8\%}$
$q\bar{q}$-NLO+gg-LO	$15.83(6)^{+3.5\%}_{-2.9\%}$

Table 5.1: Total cross-sections of the process $pp \rightarrow e^+e^-\mu^+\mu^-$ for the quark initiated LO and NLO, the gluon initiated LO and the quark initiated NLO with the LO gluon initiated. The total cross-section values are given in fb.

Since the QCD scale uncertainty increment is due to the fact that the di-boson production through gluon fusion has a leading-order-like QCD scale dependence it is essential to have its NLO correction included for high precision analyses.

5.1.3   Parton Shower Matching Uncertainty

The fact that the available parton-shower matching methods can be applied to loop-induced processes without any modification follows directly from the fact that loop-induced processes do not have any lower order contribution than a loop-squared. Indeed, the universal UV and IR singularities enter the calculation as terms proportional to lower order matrix elements, which in this case there are none. To give a more accurate description of why this happens it is sufficient to look at the general amplitude renormalisation procedure substituting the bare couplings with the running ones. The relation between the bare coupling constant α_0^u and the running coupling $\alpha_s(\mu^2)$ at one-loop order in the standard $\overline{\text{MS}}$ is given by

$$\alpha_s^u \mu_0^{2\epsilon} S_\epsilon = \alpha_s(\mu^2)\mu^{2\epsilon}\left[1 - \frac{\alpha_s(\mu^2)}{2\pi}\frac{\beta_0}{\epsilon} + \mathcal{O}(\alpha_s^2(\mu^2))\right], \qquad (5.1.2)$$

where μ_0 is the regularisation scale, usually set to $\mu_0^2 = s$, β_0 is the first order of the QCD beta function expansion in power of $\alpha_s(\mu^2)$ (1.2.5), μ^2 the scale at which we perform the renormalisation and finally S_ϵ is the spherical factor of the $\overline{\text{MS}}$ scheme which is defined as $S_\epsilon = \exp[\epsilon(\log 4\pi + \gamma_E)]$ with γ_E being Euler's gamma. Using this expression to renormalize a generic amplitude at NLO accuracy, where A_u^0 and A_u^1 are respectively the leading- and next-to-leading order unrenormalized amplitudes, one gets
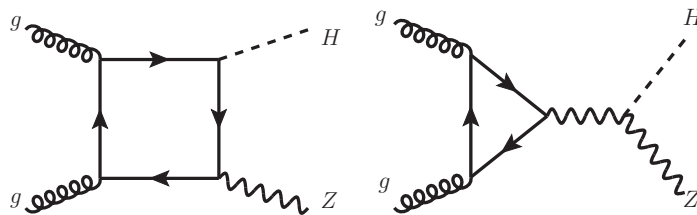
Figure 5.2: Examples of contributing diagrams to the production on the on-shell Z- and Higgs-boson through gluon fusion.

$$A^0 = A^0_u$$
$$A^1 = A^1_u - \frac{\beta_0}{\epsilon}A^0.$$

It is clear from these equations that if a process has no tree-like Born contributions it does not have any UV divergence nor renormalisation scale dependence other than the one coming from the coupling constant. Moreover, as shown in Sec. 1.6 IR divergent terms, in either loop matrix element or the respective real emission matrix element, are proportional to the Born matrix element, and therefore the leading order of a loop-induced processes can not have any IR singularity.

The parton-shower matching for this kind of processes can therefore be done using the already available tools. Nonetheless, unique features of loop-induced processes make NLO parton-shower matching not completely straightforward. This requires particular care when studying the results of a NLO calculation matched to a parton-shower. This aspect is described in detail in Sec. 5.4.

In order to give an extra point of view of the physics of loop-induced processes, it is now discussed the leading order parton-shower matching for the ZH (Higgs-strahlung) on-shell production.

Higgs-strahlung

The *Higgs-strahlung* is a phenomenologically relevant example of loop-induced gluon-initiated process. Its relevance comes from the fact that it is a direct way to study the $H \to ZZ$ interaction vertex, needed to test the EW gauge symmetry breaking mechanism.

Here, the parton-shower matching uncertainty is studied for the on-shell production of a Higgs production associated with a Z-boson. Off-shell effects on the final-state bosons are included using the Breit-Wigner distribution. The Z boson is let to decay into an electron-positron pair, and the Higgs boson to a $b\bar{b}$ pair. The samples were generated using both SHERPA and POWHEG +PYTHIA 8 for the leading order parton-shower matching. The MEPS samples are compared against a

multi-jet merged calculation merging the 0- and 1-jet multiplicity matrix elements at leading order using SHERPA.

The process is simulated in a proton-proton collision at a center-of-mass energy of $\sqrt{s} = 13$ TeV. The PDF set used is the `PDF4LHC15` which uses PDFs at NLO QCD accuracy. The renormalisation and factorisation scale have been set to the transverse energy,

$$\mu_R = \mu_F = H_\perp = \sqrt{M_H^2 + p_{H,\perp}^2} + \sum_i p_\perp^{(i)}, \qquad (5.1.3)$$

while as EW scheme was used the G_μ-scheme.

In SHERPA's samples, the loop-induced matrix element has been evaluated using OPENLOOPS, and it was matched to SHERPA's internal default Catani-Seymour dipole shower. POWHEG, instead, evaluates the loop-induced process using its internal code `ggHZ`, and matching it to the parton-shower in PYTHIA 8.2. The POWHEG parton-shower matching to PYTHIA 8 is done in two ways. The default matching uses the so called *wimpy* shower, which sets the parton-shower starting scale to the invariant mass of the ZH system, while the second setting used is a vetoed power-shower starting at the kinematical limit $p_\perp = \sqrt{\hat{s}}/2$. The analysis used was developed in order to be as close as possible to the ranges probed in experimental analyses. Electrons produced by the Z-boson decay are required to have a transverse momentum higher than 7 GeV, $p_{e,\perp} > 7$ GeV, and a pseudo-rapidity of $|\eta| < 2.7$ within a lepton-pair mass range of 81 GeV $< m_{ll} < 101$ GeV. Jets are reconstructed using the anti-k_T algorithm with jet-radius parameter $R = 0.4$, jet transverse momentum $p_{j,\perp} > 25$ GeV and a pseudo-rapidity of $|\eta| < 4.5$. Jets are also discarded if an electron is produced within a cone $\Delta R < 0.4$ from the jet-axis. For the theoretical uncertainties, SHERPA's samples also include the parton-shower starting scale variation bands varied by a factor of two both upward and downward.

In Fig. 5.3 are reported the four observables under study. These are the ZH system transverse momentum $p_\perp^{ZH}$, the number of jets N_{jets}, the hardest jet transverse momentum $p_\perp^j$ and the angle separation between the Z-boson and the Higgs boson $\Delta\phi(Z, H)$. The transverse momentum observables display a very large matching uncertainty in the energy region dominated by hard real emission configurations, *i.e.* above 200 GeV. This is expected since the parton-shower is outside its region of validity. This is also reflected in the very large difference between SHERPA's and PYTHIA's parton-shower radiation pattern in the ZH high energy transverse momentum. In the parton-shower region of validity there is, instead, a good agreement between the parton-showers, especially between SHERPA and PYTHIA's wimpy shower. A similar behavior is observed for the angular separation of the Z- and Higgs boson for values far from the back-to-back scattering, *i.e.* for an angle separation $\Delta\phi(Z, H) < 2$. However, in this observable the parton-showers under consideration show a very good agreement. The number of jet observable N_{jets}, instead, shows a very different radiation pattern between SHERPA's and PYTHIA's parton-showers.
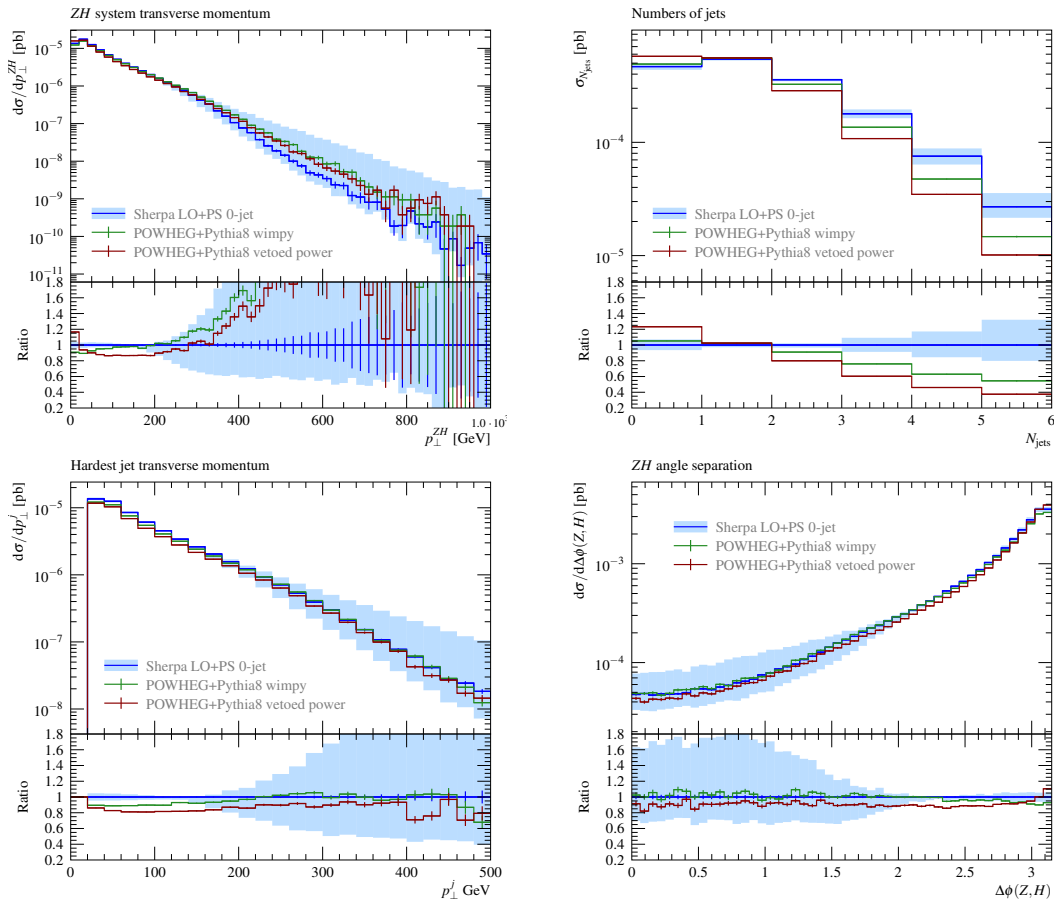
Figure 5.3: Comparison of the 0-jet inclusive distribution for the POWHEG +PYTHIA 8 wimpy and vetoed power shower setups and the SHERPA prediction

This time the difference is not covered by the SHERPA's parton-shower starting scale uncertainty. This shows that the parton-shower starting scale uncertainty can not entirely cover the matching scheme uncertainty.

This large parton-shower matching uncertainty is not characteristic just of loop-induced processes, but it is general for parton-showers. This uncertainty can be reduced including higher multiplicity matrix elements in the calculation. In this case, it is used SHERPA's multijet-merging algorithm to merge the 0- and 1-jet multiplicity at leading order. To this calculation is added a 7-point renormalisation and factorisation scale variation to understand how MEPs calculations compare to actual theoretical uncertainties in observables dominated by real emission configurations.

The comparison of the MEPs and multi-jet merged calculations is shown in Fig. 5.4. The differential observables taken under consideration are the ZH sys-
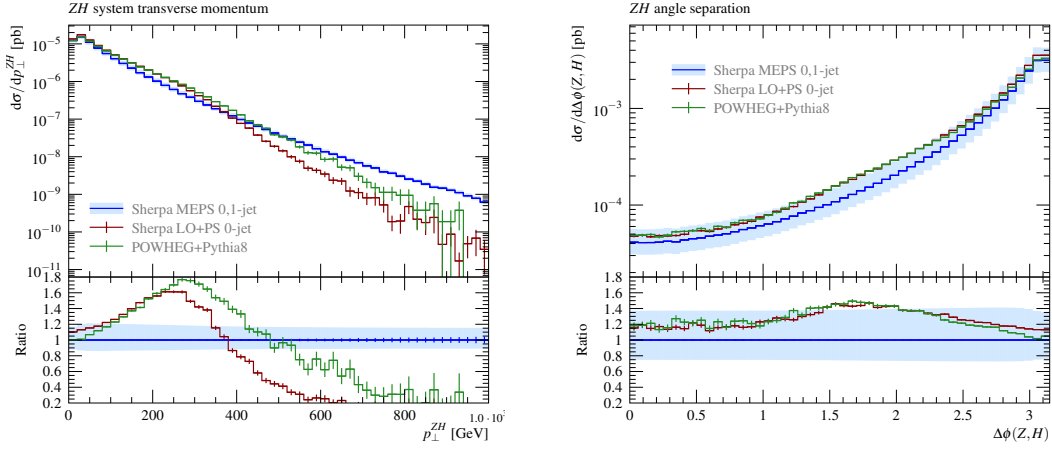
Figure 5.4: Comparison of the 0+1-jet inclusive distribution for the POWHEG+PYTHIA 8 wimpy and vetoed power shower setups and the SHERPA prediction

tem transverse momentum $p_\perp^{ZH}$ and the angular separation between the two bosons $\Delta\phi(Z,H)$. Both observables display large deviations between the MEPs and 0+1-jet merged calculations that exceed the theoretical scale uncertainty of the multi-jet merged result. In the transverse momentum observable, both MEPs calculations have a harder spectrum compared to the 0+1-jet calculation for energies around $p_\perp^{ZH} = 250\,\mathrm{GeV}$, The MEPs calculations, instead, become softer in the hard emission tail, failing to capture the hard emission spectrum of the 0+1-jet calculation. Similarly, in the ZH angle separation the MEPs calculation shows large deviations from the 0+1-jet merged calculations that exceed the scale uncertainty band for azimuthal separation of about $1.5-2$. The large deviations displayed in the transverse momentum region around $250\,\mathrm{GeV}$ can be attributed to the initial state gluon splitting functions together with the fact that gluons have access to the full PDF x-range, in contrast with initial state valence quarks that have the PDF constrained around just one value of x. Indeed, a similar behavior has also been observed for other loop-induced processes like on-shell di-Higgs production [214] and $gg \to e^+e^-\mu^+\mu^-$ shown in Fig. 5.5a for the ZZ and hardest jet transverse momentum. In order to have a direct comparison with a quark-initiated process, in Fig. 5.5b is shown the same calculation as for the samples of Fig 5.5a. The quark-initiated 0-jet calculation largely underestimates the real emission spectrum for energies above $40\,\mathrm{GeV}$ in both the ZZ and hardest jet transverse momentum, on the contrary, the loop-induced calculation has a harder spectrum in the energy region between $40\,\mathrm{GeV}$ and $90\,\mathrm{GeV}$ for both transverse momentum observables. The large impact of the gluon splitting function in the loop-induced parton-shower matching indicates that a particular care is needed when studying the matching to NLO accurate loop-induced calculations.
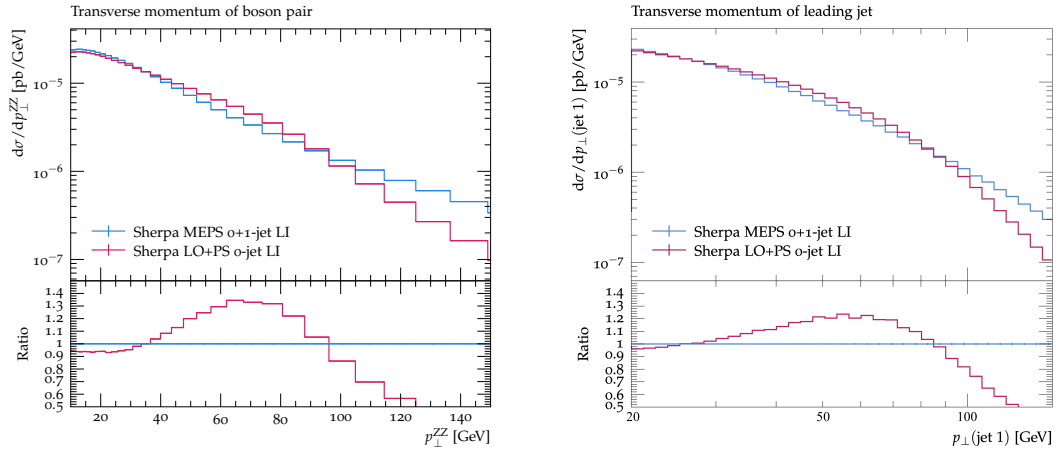
(a) $gg \to e^+e^-\mu^+\mu^-$
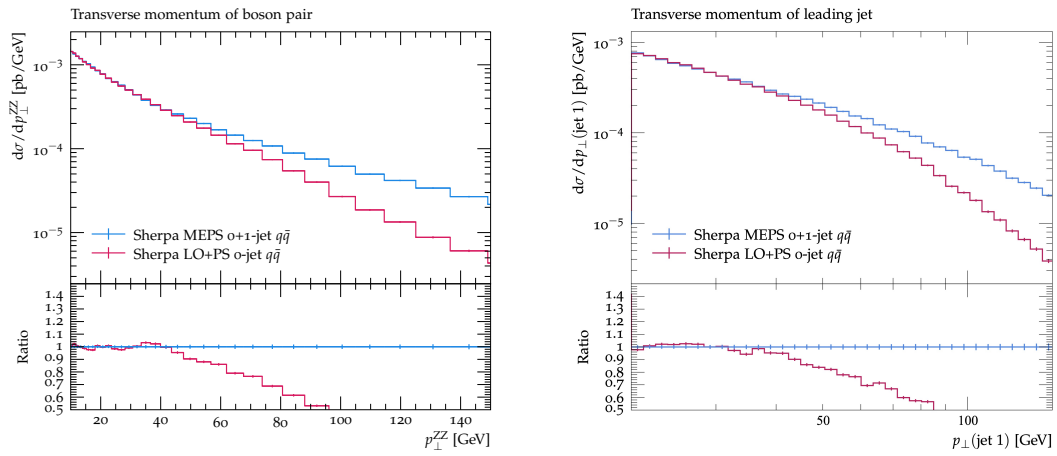
(b) $pp \to e^+e^-\mu^+\mu^-$

Figure 5.5: Comparison of the 0+1-jet inclusive distribution to the 0-jet matched to parton-shower in SHERPA.
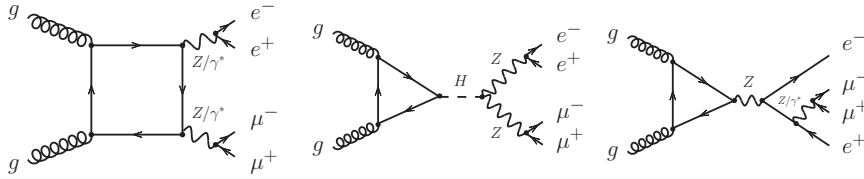
Figure 5.6: Examples of leading order contributing diagrams.

5.2 Anatomy of NLO QCD Di-boson Production in Gluon Fusion

This section presents the diagrams that make up the NLO QCD calculation for the gluon initiated $e^+e^-\mu^+\mu^-$ production. The contributions considered here are such that the intermediate EW bosons can only be emitted by either a loop quark or an external final state lepton. This is an important distinction from the real emission diagrams where one Z boson may be emitted from an initial state quark. This is needed to separate gluon-initiated loop-induced from quark-induced contributions that coexist at higher orders. Although in merging calculations these quark-induced processes are not directly included, they are still approximated by the parton-shower.

5.2.1 Leading Order

At the leading order, *i.e.* $\mathcal{O}\!\left(\alpha_s^2\alpha^4\right)$, the only loop induced process is $gg \to e^+e^-\mu^+\mu^-$. The diagrams of this process have three different topologies, that are: box, Higgs triangle and single Z-boson triangle diagrams. These are shown respectively from left to right in Fig. 5.6.

It is important to note that in the single resonant diagram, the Z-boson couples to the quark loop only via its axial mode. This gives the possibility to directly study the axial coupling mode of the Z-boson, especially because these type of diagrams are dominant in the energy region $m_{2e2\mu} \simeq M_Z$, which is well separated from the double-resonant energy region, *i.e.* $m_{2e2\mu} \simeq 2M_Z$.

5.2.2 Next-to-Leading Order

At the NLO QCD the virtual diagrams do not have any new initial state channel, but there is a new diagram topology, *i.e.* double triangle diagrams. An example is given in the second diagram of Fig. 5.7. In these type of diagrams the external EW bosons are attached to two different triangle quark-loops. Double triangle diagrams give a non-zero contribution only if the quarks running inside the loop are massive. For massless quark-loops the vector mode of the Z-boson coupling is zero due to Furry's theorem, while the axial mode cancels out for degenerate isospin doublets. However, since these double-triangle processes exchange a highly off-shell t-channel gluon, their contribution to the total cross-section is only at few permille [212]. The
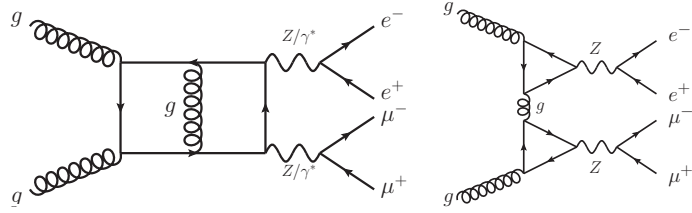
Figure 5.7: Examples of virtual corrections to $gg \to e^+e^-\mu^+\mu^-$.

virtual correction to a box-like diagram is instead simply a new internal virtual gluon line. This is exchanged between either the external gluons, within the quark-loop or an external gluon, or inside the quark-loop. Box diagrams allow for massive and massless quark-loops. In the case of massive loops, the two external bosons can couple with each of their mode, while a massless quark-loop would vanish the vector-axial coupling due to charge parity conservation [209, 216]. Finally, the class of single triangle-like diagrams can only have an axial coupling to the quark-loop, as discussed for leading-order triangle diagrams. This axial coupling mode allows only for non-degenerate isospin doublets in the loop, meaning that only a massive quark-loop would give a non-zero contribution.

In the real emission diagrams, there are two new channels, *i.e.* $q\bar{q}$ and $g\overset{(-)}{q}$. The processes contributing to the real emission correction for the $e^+e^-\mu^+\mu^-$ production in gluon-fusion are,

$$ g\,g \to e^+e^-\mu^+\mu^-\,g\,, \quad \overset{(-)}{q}\,g \to e^+e^-\mu^+\mu^-\,\overset{(-)}{q} \quad \text{and} \quad q\,\bar{q} \to e^+e^-\mu^+\mu^-\,g. $$

Some example diagrams are given in Fig. 5.8. Quark-initiated diagrams ($\overset{(-)}{q}g$ and $q\bar{q}$) can interfere with the NLO QCD real emission amplitudes of the $e^+e^-\mu^+\mu^-$ production. These interferences are part of the NNLO QCD correction to the four-lepton production. In principle the separation between these two contributions is not possible and in some works they have been therefore kept out, see for example Ref. [212, 168]. However, since these contributions come from a gauge invariant subset of diagrams, and their IR singularities are cancelled by the collinear singularities of the PDFs, they can actually be included in our calculations. A more complicated situation happens in a multi-jet merged calculation where both the standard quark initiated and loop-induced four-lepton production are considered. Here higher order contributions in the standard quark initiated processes can, at least, approximate the loop-induced real emission corrections. This problem is solved by including in the loop-induced real emission samples only diagrams where the external EW vector bosons couple either to the closed quark-loop or to the external leptons, as explained in Ref. [217].
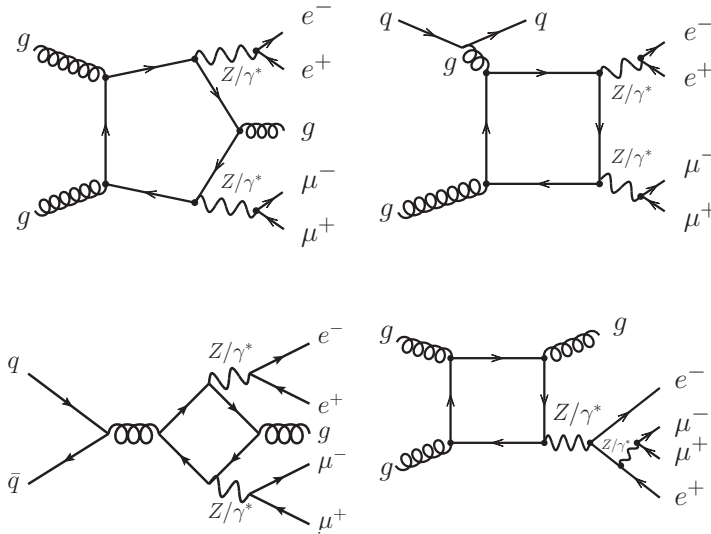
Figure 5.8: Examples of real emission contributions

5.3 Implementation in SHERPA Monte Carlo Event Generator

The simulation of loop-induced gluon-initiated processes at leading order is already fully automated in SHERPA v2 via an extension of AMEGIC that allows to use an external matrix element generator in leading order calculations. However, this implementation can not be easily extended beyond leading order accuracy limiting the use of loop-induced processes to fixed order, MC@NLO or 0+1-jet merging calculations. In the next major release of SHERPA, it will be available a new module called `EXTAMP` that allows to use any external matrix-element provider as general matrix-element generator. The validation and maintenance of this module took a good part of the technical workload needed to produce the main results of this thesis. In particular, now `EXTAMP` can handle MC@NLO and multi-jet merged calculations at NLO. In Appendix A are show some validation plots to confirm the consistency between the updated `EXTAMP` module and internal default frameworks.

With this module it is possible to use the external matrix element generator OPENLOOPS to get the needed loop-squared matrix elements for the leading order and NLO QCD real emission. The virtual amplitude for massless quarks is instead taken from the public C++ code `ggvvamp` [8], which provides the analytical expression for the virtual amplitude's form factors. In order to use this code it has been necessary to develop an interface to `EXTAMP`. Since this is the only available virtual correction to $gg \to e^+e^-\mu^+\mu^-$, an event-wise validation of its implementation was not possible. Therefore, the validation has been done comparing the total cross-section from SHERPA's implementation and the one calculated in [169] using the same C++ library.

5.3.1   The `ggvvamp` Library

The evaluation of the virtual amplitude is based on the decomposition of two loop massless amplitudes into four-point master integrals with massless internal propagators and two external massive legs. These master integrals are already well known and were presented for equal final state masses in Refs. [218, 219] and for different final state masses in Refs. [220, 221, 222, 163].
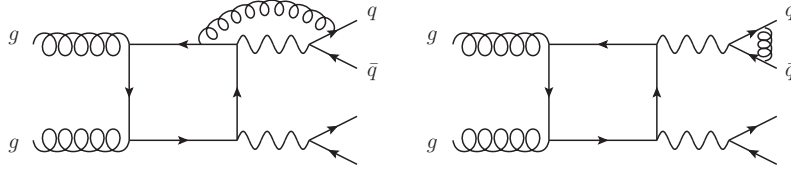
Figure 5.9: Example of QCD virtual corrections to a di-boson production in gluon fusion $\mathcal{O}\left(\alpha_s^3\alpha^2\right)$ with a quark-antiquark pair in the final-state.

The code evaluates the form factors at both leading order and NLO accuracy for the $2 \to 2$ process, $g(p_1) + g(p_2) \to V_1(p_3) + V_2(p_4)$. Here each external vector boson is treated off-shell, and it can be either a Z- or W-boson, or a photon γ^*. The fact that the virtual correction has been calculated only for this $2 \to 2$ process means that it cannot be used for quark final states since it would be missing virtual gluon exchange involving coloured final states, see for example Fig. 5.9. The general form of the amplitude for the $2 \to 2$ process considered here can be written as,

$$M(p_1, p_2; p_3) = \delta^{a_1 a_2} N_{V_1 V_2} \epsilon_1^\rho(p_1) \epsilon_2^\sigma(p_2) M_{\mu\nu\rho\sigma}(p_1, p_2; p_3) \epsilon_3^{*\mu}(p_3) \epsilon_4^{*\nu}(p_4). \qquad (5.3.1)$$

Here the momenta of the incoming gluons are p_1 and p_2, and p_3 and p_4 the momenta of the electroweak final state bosons. The multiplying factors $\delta^{a_1 a_2}$ and $N_{V_1 V_2}$ are respectively the gluons colour factor, which is $1/8$, and the two electroweak bosons couplings to the internal quark-loop. The amplitude is written to depend only on three of the four momenta involved in the process because of the momentum conservation, $p_4 = p_1 + p_2 - p_3$. Since the two electroweak bosons couple to a massless loop the only possible diagram topology they can couple to is the box-like, as explained in Sec. 5.2.2. The EW factor $N_{V_1 V_2}$ for this diagram can take the following forms,

$$N_{\gamma\gamma} = \frac{1}{2} \sum_i \left[\left(L_{q_i q_i}^\gamma\right)^2 + \left(R_{q_i q_i}^\gamma\right)^2 \right], \quad N_{Z\gamma} = \frac{1}{2} \sum_i \left(L_{q_i q_i}^Z L_{q_i q_i}^\gamma + R_{q_i q_i}^Z R_{q_i q_i}^\gamma \right),$$

$$N_{ZZ} = \frac{1}{2} \sum_i \left[\left(L_{q_i q_i}^Z\right)^2 + \left(R_{q_i q_i}^Z\right)^2 \right], \quad N_{WW} = \frac{1}{2} \sum_{i,j} L_{q_i q_j}^W L_{q_j q_i}^W,$$

where

$$
\begin{aligned}
L_{q_iq_j}^{\gamma} &= -e_{q_i}\delta_{q_iq_j}, & R_{q_iq_j}^{\gamma} &= -e_{q_i}\delta_{q_iq_j}, \\
L_{q_iq_j}^{Z} &= \frac{I_3^{q_i}-\sin^2\theta_w e_{q_i}}{\sin\theta_w\cos\theta_w}\delta_{q_iq_j}, & L_{q_iq_j}^{Z} &= -\frac{\sin^2\theta_w e_{q_i}}{\cos\theta_w}\delta_{q_iq_j}, \\
L_{q_iq_j}^{Z} &= \frac{1}{\sqrt{2}\sin\theta_w}\epsilon_{q_iq_j}, & R_{q_iq_j}^{W} &= 0,
\end{aligned}
$$

are the couplings to the left- and right-handed quark helicities. The QCD couplings are instead included in the tensor $M_{\mu\nu\rho\sigma}(p_1,p_2;p_3)$.

Due to Lorentz invariance, the tensor $M_{\mu\nu\rho\sigma}(p_1,p_2;p_3)$ can be decomposed into 138 independent tensors which can be further reduced to 20 since 118 of them are transverse to the external bosons' polarisation vectors that have to satisfy

$$
\begin{aligned}
\epsilon_1\cdot p_1 = \epsilon_1\cdot p_2 &= 0 \\
\epsilon_2\cdot p_1 = \epsilon_2\cdot p_2 &= 0 \\
\epsilon_3\cdot p_3 = \epsilon_4\cdot p_4 &= 0.
\end{aligned}
$$

These relations come from the polarisation sum rules

$$
\sum_\lambda \epsilon_{\lambda,1}^{*\mu}(p_1)\epsilon_{\lambda,1}^{\nu}(p_1) = \sum_\lambda \epsilon_{\lambda,2}^{*\mu}(p_2)\epsilon_{\lambda,2}^{\nu}(p_2) = -g^{\mu\nu} + \frac{p_2^\mu p_1^\nu + p_1^\mu p_2^\nu}{p_1\cdot p_2}
$$

$$
\sum_\lambda \epsilon_{\lambda,j}^{*\mu}(p_j)\epsilon_{\lambda,j}^{\nu}(p_j) = -g^{\mu\nu} + \frac{p_j^\mu p_j^\nu}{p_j^2}.
$$

These relations use the same gauge fixing as in Ref. [8]. The first line is the sum over the incoming gluons' polarisations, while the second sums over the massive final state EW gauge bosons. The index $j = [3,4]$ identifies either the boson with momentum p_3 or p_4.

The amplitude in Eq. (5.3.1) can be written as a sum of 20 linearly independent tensors multiplied by a form factor. In the calculation taken as reference, Ref. [8], the tensors are defined as follows,

$$
\begin{aligned}
M(p_1,p_2;p_3) &= \delta^{a_1a_2}N_{V_1V_2}\epsilon_1^\rho(p_1)\epsilon_2^\sigma(p_2)M_{\mu\nu\rho\sigma}(p_1,p_2;p_3)\epsilon_3^{*\mu}(p_3)\epsilon_4^{*\nu}(p_4) \\
&= \delta^{a_1a_2}N_{V_1V_2}\left[\sum_{j=1}^{20}A_j(p_1,p_2;p_3)T_{j,\mu\nu}(p_1,p_2;p_3)\right]\epsilon_3^{*\mu}(p_3)\epsilon_4^{*\nu}(p_4).
\end{aligned}
$$

$$(5.3.2)$$

The explicit expressions for the kinematic tensors $T_{j,\mu\nu}(p_1,p_2;p_3)$ are given in Ref.

[8]. The `C++` code `ggvvamp` evaluates the leading order and virtual correction of the regularized A_j's form factors in the kinematic variables s, t, p_3^2, p_4^2. In SHERPA is implemented the squared of the amplitude in Eq. (5.3.2) at leading order and for its virtual correction, according to,

$$|\mathcal{M}|^2 = \frac{\alpha^2}{32}\pi^2 T_F N_{V_1 V_2}^2 \left[\left(\frac{\alpha_s}{2\pi}\right)^2 \left|S^{(1)}\right|^2 + 2\left(\frac{\alpha_s}{2\pi}\right)^3 \mathrm{Re}\left(S^{(1)}\bar{S}_{qT}^{(2)}\right)\right]. \qquad (5.3.3)$$

Here $\left|S^{(1)}\right|^2$ and $\mathrm{Re}\left(S^{(1)}\bar{S}_{qT}^{(2)}\right)$ are both averaged over the initial state gluons' polarisation and summed over the final state EW boson polarisation. The amplitudes product is done in matrix form as

$$\mathrm{Re}(S_a S_b) = A_a^i T_{ij} A_b^j, \qquad (5.3.4)$$

where A_a^i are the form factors evaluated by `ggvvamp` with i, j being the form factor number from 1 to 20 and a, b the perturbative order, *i.e.* either (1) or (2). The T^{ij} is instead,

$$T^{ij} = D^{\rho\rho'} D^{\sigma\sigma'} D_3^{\mu\mu'} D_4^{\nu\nu'} T_{\mu\nu\rho\sigma}^i T_{\mu'\nu'\rho'\sigma'}^j. \qquad (5.3.5)$$

The tensors $T_{\mu\nu\rho\sigma}^i$ are the same as in Eq. (5.3.2) but this time they do not include the gluons' polarisation vectors, *i.e.* $T_{\mu\nu}^i = \epsilon_1^\rho(p_1)\epsilon_2^\sigma(p_2)T_{\mu\nu\rho\sigma}^i$. The D's tensors are the sum over the external bosons polarisations. The first two are for the gluons and the other two for the EW bosons,

$$D^{\mu\nu} = \sum_\lambda \epsilon_\lambda^{\mu*}\epsilon_\lambda^\nu = -g^{\mu\nu} + \frac{p_1^\mu p_2^\nu + p_1^\nu p_2^\mu}{p_1 \cdot p_2}, \qquad (5.3.6)$$

$$D_j^{\mu\nu} = \sum_{\lambda_j} \epsilon_{\lambda_j}^{\mu*}\epsilon_{\lambda_j}^\nu = -g^{\mu\nu} + \frac{p_j^\mu p_j^\nu}{p_j^2}. \qquad (5.3.7)$$

All tensor contractions and manipulations have been performed using the Mathematica package `Package-X` [223]. The generated squared form factors have been organized in terms of the functions,

$$\begin{array}{rclcrcl} \beta_3 &=& 1 - \frac{t}{M_3^2}, & \quad & \beta_4 &=& 1 - \frac{t}{M_4^2}, \\ \beta_{3s} &=& 1 - \beta_3 \frac{M_3^2}{s}, & \quad & \beta_{4s} &=& 1 - \beta_4 \frac{M_4^2}{s}, \\ \beta_f &=& \frac{s - M_3^2 - M_4^2}{2}, & & & & \end{array}$$

which helped to reduce the length of the expression allowing for an easy and fast export as a `C++` code. With this implementation of the `ggvvamp` library it is possible

to use SHERPA to evaluate the $gg \to VV$ process at NLO QCD for off-shell EW bosons. The four-lepton final state amplitudes need a separate implementation due to the fact that the `ggvvamp` code supply the four-lepton form factors in the spinor-helicity formalism [224, 225, 226, 227]. However, the form factors for the four-lepton production

$$g(p_1) + g(p_2) \to V_1(p_3) + V_2(p_4) \to l_5(p_5) + \bar{l}_6(p_6) + l_7(p_7) + \bar{l}_8(p_8), \qquad (5.3.8)$$

in the spinor-helicity formalism can be written in terms of the form factors of Eq. (5.3.2). The advantage of using this formalism is that it simplifies the amplitude evaluation and its squaring. In this formalism, spinors are rewritten as a pair of Weyl spinors as

$$\frac{1}{2}\left(1 + \gamma^5\right) u(p_i) = u_+(p_i) \equiv |i\rangle, \qquad \frac{1}{2}\left(1 - \gamma^5\right) u(p_i) = u_-(p_i) \equiv |i]. \qquad (5.3.9)$$

The multiplication between these spinors is then defined as,

$$\bar{u}_-(p_i)u_+(p_j) \equiv \langle ij \rangle = [ij]^*. \qquad (5.3.10)$$

These two objects, $\langle ij \rangle$ and $[ij]$, are directly related to the spinors four-momenta, i.e.

$$\langle ij \rangle = \sqrt{\left(p_i^0 + p_i^3\right)\left(p_j^0 - p_j^3\right)} \left[\frac{p_i^1 + \mathrm{i}\, p_i^2}{\sqrt{\left(p_i^1\right)^2 + \left(p_i^2\right)^2}}\right] - (i \leftrightarrow j). \qquad (5.3.11)$$

On the other hand, in the spinor-helicity notation the two external massless polarisation vectors become,

$$\epsilon_{1,+}^\mu(p_1) = \frac{[2|\gamma^\mu|1\rangle}{\sqrt{2}[12]}, \qquad \epsilon_{1,-}^\mu(p_1) = \frac{\langle 2|\gamma^\mu|1]}{\sqrt{2}\langle 12\rangle},$$

$$\epsilon_{2,+}^\mu(p_2) = \frac{[1|\gamma^\mu|2\rangle}{\sqrt{2}[21]}, \qquad \epsilon_{2,-}^\mu(p_2) = \frac{\langle 1|\gamma^\mu|2]}{\sqrt{2}\langle 21\rangle}, \qquad (5.3.12)$$

where the spinors $|1\rangle$ and $|2\rangle$ carry respectively the momenta p_1 and p_2.
In these terms, the amplitude for the four-lepton final state has in total four independent helicities. Two are for the incoming gluons and two for the final-state lepton pairs. In the spinor-helicity formalism, the latter reads

$$\mathrm{J}_L^\mu(p_i, p_j) = [j|\gamma^\mu|i\rangle = \mathrm{J}_R^{\mu*}(p_i, p_j) = \mathrm{J}_R^\mu(p_j, p_i). \qquad (5.3.13)$$

Each of these can take two values $[R, L]$, or often also defined as $[+, -]$. There is a total of 16 possible helicity configurations that can be reduced to 2 via symmetry relations. From Eq. (5.3.13) it is clear that the two helicities of the lepton currents are equivalent if the momenta of the outgoing leptons are exchanged, while from the definition of the spinor product in Eq. (5.3.9) it is easy to see that $\epsilon^\mu_{i,+}(p_i) = \epsilon^{*\mu}_{i,-}(p_i)$. Thanks to these symmetry relations, the total amount of independent helicity configurations can be reduced to two, $(\lambda_1, \lambda_2, \lambda_3, \lambda_4) = (L, L, L, L)$ and $(\lambda_1, \lambda_2, \lambda_3, \lambda_4) = (L, R, L, L)$. In $(\lambda_1, \lambda_2, \lambda_3, \lambda_4)$ the helicities 1 and 2 are for the incoming gluons while helicities 3 and 4 for the outgoing lepton currents. The two missing initial state gluon helicity configurations $(\lambda_1, \lambda_2) = (R, L)$ and $(\lambda_1, \lambda_2) = (R, R)$ are related to $(\lambda_1, \lambda_2) = (L, L)$ and $(\lambda_1, \lambda_2) = (L, R)$ by a simple complex conjugation,

$$M_{RLLL}(p_1, p_2; p_5, p_6, p_7, p_8) = [M_{LRLL}(p_1, p_2; p_5, p_6, p_7, p_8)]^*,$$
$$M_{RRLL}(p_1, p_2; p_5, p_6, p_7, p_8) = [M_{LLLL}(p_1, p_2; p_5, p_6, p_7, p_8)]^*. \tag{5.3.14}$$

The three missing helicity configurations for the final-state lepton currents, $(\lambda_3, \lambda_4) = (R, L)$, $(\lambda_3, \lambda_4) = (L, R)$, $(\lambda_3, \lambda_4) = (R, R)$ are instead related to $(\lambda_3, \lambda_4) = (L, L)$ by exchanging the final-state momenta of the lepton pairs, *i.e.*

$$M_{\lambda_1\lambda_2 RL}(p_1, p_2; p_5, p_6, p_7, p_8) = M_{\lambda_1\lambda_2 LL}(p_1, p_2; p_6, p_5, p_7, p_8),$$
$$M_{\lambda_1\lambda_2 LR}(p_1, p_2; p_5, p_6, p_7, p_8) = M_{\lambda_1\lambda_2 LL}(p_1, p_2; p_5, p_6, p_8, p_7), \tag{5.3.15}$$
$$M_{\lambda_1\lambda_2 RR}(p_1, p_2; p_5, p_6, p_7, p_8) = M_{\lambda_1\lambda_2 LL}(p_1, p_2; p_6, p_5, p_8, p_7).$$

It is then possible to write down the helicity amplitudes for the production of four final-state leptons in gluon fusion in terms of the identified di-boson amplitude given in Eq. (5.3.2), *i.e.*

$$M_{\lambda_1\lambda_2 LL}(p_1, p_2; p_5, p_6, p_7, p_8) =$$
$$\delta^{a_1 a_2} N_{V_1 V_2} (4\pi\alpha)^2 \frac{L^{V_1}_{f_5 f_6} L^{V_2}_{f_7 f_8}}{D_{V_1}(p_5 + p_6) D_{V_2}(p_7 + p_8)} \times \tag{5.3.16}$$
$$\times \epsilon^\rho_{1\lambda_1}(p_1) \epsilon^\sigma_{2\lambda_2}(p_2) M_{\mu\nu\rho\sigma}(p_1, p_2; p_3) \mathrm{J}^\mu_L(p_5, p_6) \mathrm{J}^\nu_L(p_7, p_8),$$

where the function $D_V(q)$ is the denominator of the intermediate electroweak vector bosons' propagator, that can have the following forms based on the flavor of the EW vector boson,

$$D_{\gamma^*}(q) = q^2, \qquad D_{V=Z,W}(q) = q^2 - M_V^2 + \mathrm{i}\,\Gamma_V M_V. \qquad (5.3.17)$$

The third line of Eq. (5.3.16) can either be computed using the form factors from Eq. (5.3.2) or it can be rewritten in terms of new form factors that depend on the independent helicity configurations, and the $A_i(p_1, p_2; p_3)$'s form factors. The former possibility would make the implementation of the four-lepton final state amplitude more compatible with the implementation of the identified di-boson production amplitude, but it would also make the matrix elements very long and hard to manipulate. On the other hand, the latter option helps to make Eq. (5.3.16) compact and readable. Therefore, the helicity amplitude is implemented in SHERPA using 9 new helicity form factors. The helicity amplitude with this choice reads,

$$M_{\lambda_1\lambda_2 LL}(p_1, p_2; p_5, p_6, p_7, p_8) =$$

$$\delta^{a_1 a_2} N_{V_1 V_2} (4\pi\alpha)^2 \frac{L_{f_5 f_6}^{V_1} L_{f_7 f_8}^{V_2}}{D_{V_1}(p_5 + p_6) D_{V_2}(p_7 + p_8)} \times$$

$$\times C_{\lambda_1\lambda_2} \Big[[2\!\!\not{p}_3 1\rangle \Big(E_1^{\lambda_1\lambda_2} \langle 57\rangle [68] + E_2^{\lambda_1\lambda_2} \langle 15\rangle\langle 17\rangle [16][18]$$

$$+ E_3^{\lambda_1\lambda_2} \langle 15\rangle\langle 27\rangle [16][28] + E_4^{\lambda_1\lambda_2} \langle 25\rangle\langle 17\rangle [26][18]$$

$$+ E_5^{\lambda_1\lambda_2} \langle 25\rangle\langle 27\rangle [26][28] \Big) + E_6^{\lambda_1\lambda_2} \langle 15\rangle\langle 17\rangle [16][28]$$

$$+ E_7^{\lambda_1\lambda_2} \langle 15\rangle\langle 17\rangle [26][18] + E_8^{\lambda_1\lambda_2} \langle 15\rangle\langle 27\rangle [26][28]$$

$$+ E_9^{\lambda_1\lambda_2} \langle 25\rangle\langle 17\rangle [26][28] \Big], \qquad (5.3.18)$$

where the factor $C_{\lambda_1\lambda_2}$ are,

$$C_{LL} = [1\,\not{p}_3 2\rangle \frac{\langle 12\rangle}{[12]}, \quad C_{LR} = [2\,\not{p}_3 1\rangle. \qquad (5.3.19)$$

The ggvvamp code also provides the analytical expressions for these helicity form factors $E_i^{\lambda_1\lambda_2}$ in terms of the A_is. The explicit relations between these two objects are again reported in Ref. [8], therefore they are not repeated here.

The regularisation of the two-loop amplitude is done for the A_i form factors which directly make the $E_i^{\lambda_1\lambda_2}$ functions to be UV and IR finite. The renormalisation is done using the conventional dimensional regularisation in $4 - \epsilon$ dimensions in the $\overline{\text{MS}}$ scheme at the scale $\mu^2 = \hat{s}$, where $\hat{s}$ is the invariant mass squared of the initial partonic system. The technical aspect of the UV renormalisation for these amplitudes follows closely the discussion of Sec. 5.1.3. The IR regularized virtual amplitude is given in ggvvamp in two subtraction schemes, q_T-subtraction [228] and Catani subtraction [229]. In the ggvvamp code the subtraction scheme choice is left

to the user. The IR regularisation is performed as follows,

$$
\begin{aligned}
A_{\text{fin}}^0 &= A_{\text{IR-div}}^0 \\
A_{\text{fin}}^1 &= A_{\text{IR-div}}^1 - I(\epsilon)A_{\text{IR-div}}^0,
\end{aligned}
\tag{5.3.20}
$$

where, for gluon initiated processes, the IR-singular function $I(\epsilon)$ is,

$$
I(\epsilon) = -\frac{e^{\epsilon\gamma}}{\Gamma(1-\epsilon)}\left(\frac{\mu_F^2}{\hat{s}}\right)^{\epsilon}\left(\frac{1}{\epsilon^2} + \frac{i\pi}{\epsilon}\right)C_A - \frac{1}{\epsilon}\beta_0\left(\frac{\mu_F^2}{\hat{s}}\right)^{\epsilon} + \delta,
\tag{5.3.21}
$$

with δ being a constant specific for the regularisation scheme adopted. In the q_T-subtraction scheme this is simply $\delta_{q_T} = 0$ while in the Catani subtraction scheme it is,

$$
\delta_{CS} = -\frac{1}{2}\pi^2 C_A + i\pi\beta_0.
\tag{5.3.22}
$$

In SHERPA, the subtraction scheme is chosen to be the q_T-subtraction despite the fact that the Catani-Seymour subtraction is the default used in SHERPA. This choice was made to simplify the implementation of the virtual amplitudes scale dependent terms from the IR- and UV-regularisation. The implementation is made consistently with SHERPA's default Catani-Seymour subtraction.

5.3.2 Top Quark Mass Approximation

In SHERPA, all the loop-squared amplitudes needed to compute a loop-induced process at NLO are evaluated using external loop matrix-element generators like OPENLOOPS. In these generators the loop-squared amplitudes are computed with full top-quark mass dependence by default, even though they can also be computed in the $N_f = 5$ flavor scheme. The virtual matrix element evaluated by `ggvvamp` account only for massless quark-loops. Therefore, top-quark mass effects have to be added to have a reliable NLO correction, especially for the IR-singularity cancellation between the virtual and real emission diagrams above $2m_t$. In order to give an idea of the top-quark mass effects for a loop-induced process, in Fig. 5.10 are shown the di-boson invariant mass, single Z-boson transverse momentum, pseudorapidity difference of the Z-boson pair and pseudorapidity of the hardest lepton for the $gg \to e^+e^-\mu^+\mu^-$ process at leading order for both full top-quark dependence and in the $N_f = 5$ calculation. The invariant mass distribution shows a flat offset for $m_{ZZ} < 2m_t$ of about 5% between the two calculations, while they start to diverge for energies above $400\,\text{GeV}$. Similarly, the single Z-boson transverse momentum shows the same 5% difference but this time only up to about $100\,\text{GeV}$. The

difference between the scale at which top-quark effects become dominant in these two observables is due to the fact that in the di-boson invariant mass the continuous ZZ production is the dominant contribution [207], and due to the Z boson couplings to the quark-loop, the top-quark starts to contribute more only above its threshold production, *i.e.* $m_{ZZ} \simeq 2m_t$. On the other hand, in transverse momentum observables the direct Higgs boson production is comparable to the continuous ZZ production [207]. For the direct Higgs production top-quark effects become sizeable already at the Higgs mass energy scale, *i.e.* about 125 GeV. The di-boson pseudorapidity difference and single lepton pseudorapidity, instead, show a good agreement between the two calculations displaying only a flat shift of about 5%. From these observables, it is clear that energy-independent observables are not much affected by top-quark effects, while they can be quite sizeable in energy-dependent observables. In the light of what has just been described, the evaluation of the $e^+e^-\mu^+\mu^-$ production in gluon fusion at NLO using the `ggvvamp` library for the virtual amplitude is expected to provide a good approximation at energies below $2m_t$ for invariant mass distributions or below m_H in transverse momentum distributions.

A more detailed discussion about top-quark effects in the virtual amplitude is given in Ref. [167]. Here the authors have compared the large-m_t approximation [230, 231] of the virtual amplitude with their calculation with full top-quark mass dependence. Their results showed that the large-m_t approximation, holds very well for energies below $2m_t$ while it starts to rapidly deteriorate at higher energies. This motivates the use of top-quark approximations to study this process at these energies. However, the large-m_t approximation has not been used in SHERPA's implementation of the `ggvvamp` because the approximated amplitudes are not publicly available. In its place, the full virtual amplitude $\mathcal{A}^{(1)}(\Phi)$ is calculated in the massless approximation where the massless virtual amplitude $\mathcal{A}^{(1)}_{\text{no-top}}(\Phi)$ is reweighted by the one-loop amplitude with full top-quark mass dependence, *i.e.* multiplying it by the factor $\mathcal{A}^{(0)}(\Phi)/\mathcal{A}^{(0)}_{\text{no-top}}(\Phi)$. The virtual correction is therefore evaluated according to,

$$
\begin{aligned}
V(\Phi) = \mathcal{A}^{(0)*}(\Phi)\mathcal{A}^{(1)}(\Phi) &\simeq \mathcal{A}^{(0)*}(\Phi)\frac{\mathcal{A}^{(0)}(\Phi)}{\mathcal{A}^{(0)}_{\text{no-top}}(\Phi)}\mathcal{A}^{(1)}_{\text{no-top}}(\Phi) \\
&= B(\Phi)\frac{\mathcal{A}^{(0)*}_{\text{no-top}}(\Phi)\mathcal{A}^{(1)}_{\text{no-top}}(\Phi)}{\mathcal{A}^{(0)*}_{\text{no-top}}(\Phi)\mathcal{A}^{(0)}_{\text{no-top}}(\Phi)} = B(\Phi)\frac{V_{\text{no-top}}(\Phi)}{B_{\text{no-top}}(\Phi)}.
\end{aligned}
$$
(5.3.23)

The Born piece with full top-quark mass dependence $B(\Phi)$ is the same as the Born piece used in the NLO calculation, while the massless pieces are both taken from the `ggvvamp` library.
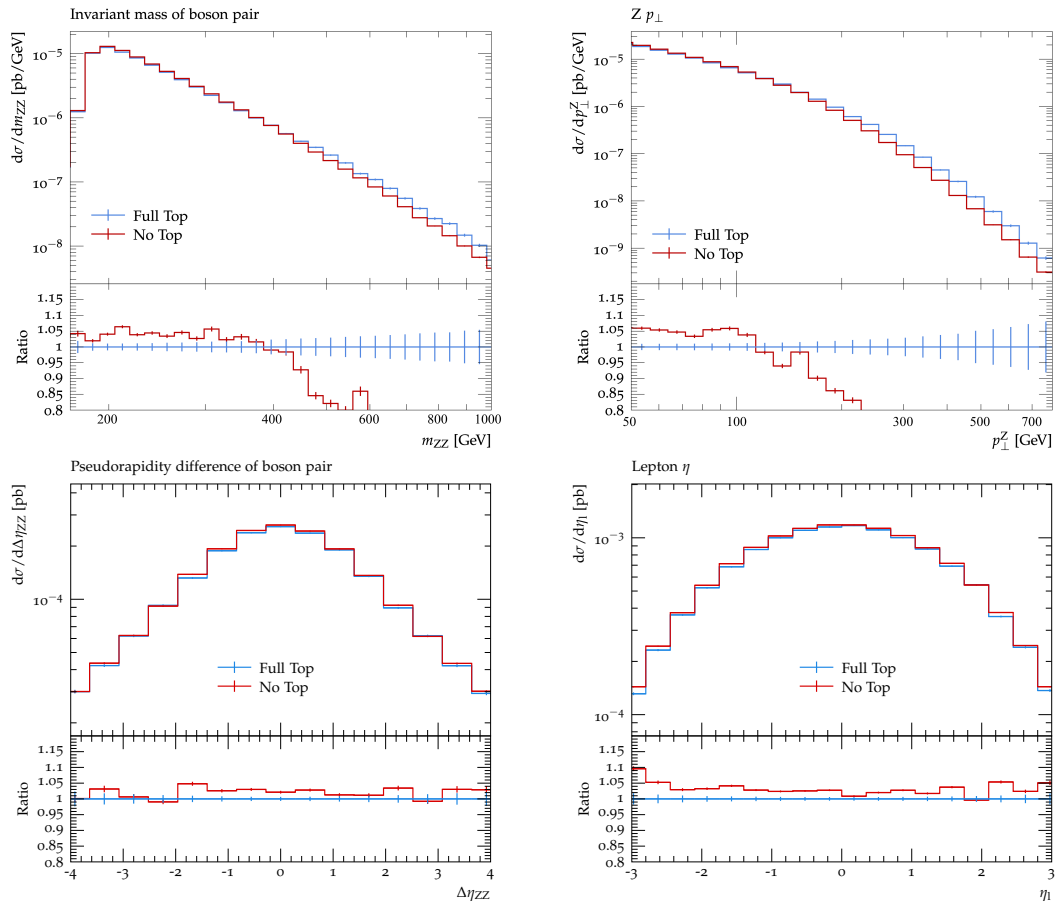
Figure 5.10: Comparison of di-boson production in gluon fusion with and without top-quark mass dependence. The simulation has been performed using SHERPA + OPENLOOPS.

5.3.3   Validation of the Implementation

The implementation of the `ggvvamp` code in the MC generator SHERPA described so far has been validated against the calculation presented in Ref. [169]. In this work the $e^+e^-\mu^+\mu^-$ production in gluon fusion is evaluated at NLO QCD, including all the initial-state real emission channels (see Sec. 5.2.2). In both Ref. [169] and SHERPA's calculation OPENLOOPS is used to evaluate all the one-loop matrix elements and `ggvvamp` to evaluate the virtual matrix element. Top-quark mass effects are included in both calculations using the same approximation, given in Eq. (5.3.23). The leading order and real emission matrix elements are evaluated using the OPENLOOPS libraries `ppllll2` and `pplllj2`, that include full top-quark and Higgs-boson dependence.

Concerning SHERPA's calculation, the numerical evaluation of the real emission matrix elements showed to fluctuate significantly in the soft/collinear emission phase-space regions. To this end, the numerical stability was controlled using two

settings. The first is OPENLOOPS' internal stability check for loop-squared amplitudes `stability_kill2` (a stability threshold evaluated according to a scaling criterion that uses either double or quadruple precision, a detailed description is given in Ref. [154]). This parameter was set to 0.01 and its value was varied by a factor of 10, upward and downward, without noticing any significant difference. The second setting is SHERPA's `DIPOLES: AMIN`. This acts as a low energy cut-off in the evaluation of the H-type events in order to avoid miscancellations in the dipole subtraction for the very soft and collinear region. In SHERPA the default value is set to 10^{-8}. In this case, it is found that a value of at least 10^{-6} is necessary to have a stable evaluation of the real subtracted term. Also, it was noticed that too large values of `AMIN`, *i.e.* above 10^{-4}, have a noticeable impact on the NLO total cross-section at the percent level. For this calculation the `AMIN` value is set to 10^{-6}. It is interesting to note that such numerical instability in the soft/collinear region happens only for a four-lepton final state calculation. It is instead not present, or at least it happens for more remote phase-space regions, for the on-shell di-boson production in gluon fusion.

The validation set-up evaluates the process $gg \to e^+e^-\mu^+\mu^-$ at NLO QCD for a center-of-mass energy of $\sqrt{s} = 13\,\text{TeV}$. The renormalisation and factorisation scales are set to half the four-lepton invariant mass $\mu = m_{4l}/2$, the EW scheme to the G_μ-scheme, with $G_F = 1.16639 \times 10^{-5}\,\text{GeV}^{-2}$ and the α_s is set accordingly to the PDF set `NNPDF30_nnlo_as_0118`. The vector boson masses, the top-quark's mass and width, and the bottom mass have been set according to [169], *i.e.*

$$
\begin{aligned}
M_W^{\text{OS}} &= 80.385\,\text{GeV} & \Gamma_W^{\text{OS}} &= 2.085\,\text{GeV} \\
M_Z^{\text{OS}} &= 91.1876\,\text{GeV} & \Gamma_Z^{\text{OS}} &= 2.4952\,\text{GeV} \\
M_h &= 125.0\,\text{GeV} & \Gamma_h &= 0.00407\,\text{GeV} \\
m_b &= 4.18\,\text{GeV} & \Gamma_b &= 0 \\
m_t &= 173.2\,\text{GeV} & \Gamma_t &= 1.44262\,\text{GeV} \;.
\end{aligned}
$$

The cuts used are taken from an ATLAS analysis in Ref. [175] in order to cover the fiducial phase space of the ATLAS detector described in Sec. 3.2, plus extra phase space cuts specific for the di-boson production, such as constraining the lepton-pair invariant mass to $66\,\text{GeV} \le m_{e^+e^-/\mu^+\mu^-} \le 116\,\text{GeV}$. The cuts used then are,

Cuts
$p_{T,e/\mu} > 7$ GeV,   one electron with $|\eta_e| < 4.9$,   the others $|\eta_e| < 2.5$, $|\eta_\mu| < 2.7$
$\Delta R_{ee/\mu\mu} > 0.2$, $\Delta R_{e\mu} > 0.2$, 66 GeV $\le m_{e^+e^-/\mu^+\mu^-} \le 116$ GeV

In Tab. 5.2 are reported the total cross-sections for the loop-induced $e^+e^-\mu^+\mu^-$

production at both leading order and NLO QCD. The comparison shows perfect agreement between the two calculations within statistical uncertainty.

Order	Reference [fb] [169]	SHERPA [fb]
LO	2.0052(1)	2.003(7)
NLO	3.626(1)	3.631(4)

Table 5.2: Comparison between the implementation of the `ggvvamp` code from Ref. [169] and the implementation done in SHERPA and presented here for the loop-induced $e^+e^-\mu^+\mu^-$ production at $\sqrt{s} = 13\,\mathrm{TeV}$.

Since the computation of these amplitudes is very demanding, it is essential to make sure that the on-the-fly scale variations available in SHERPA [205] can also be applied for this process in order to simplify its theoretical uncertainty estimation. To this end, to make sure that the on-the-fly scale variation implemented in SHERPA works also for this process we did a point-by-point comparison of the on-the-fly scale variation for the same process evaluated at two different central scale values, m_{4l} and $2 \cdot m_{4l}$. In this way the on-the-fly evaluation of the NLO correction at the scales (μ_R, μ_F), $(2\mu_R, \mu_F)$, $(\mu_R, 2\mu_F)$ and $(2\mu_R, 2\mu_F)$ with the central scale set to m_{4l} has to match the on-the-fly evaluation at the scales $(\mu_R/2, \mu_F/2)$, $(\mu_R, \mu_F/2)$, $(\mu_R/2, \mu_F)$ and (μ_R, μ_F) for the calculation with the central scale set to $2m_{4l}$. This test shows perfect agreement between the on-the-fly variation and the explicit scale variation for every phase space point tested. Tab. 5.3 shows an example for one phase space point looking separately at the BVI and RS part of the calculation.

5.3.4   Fast Evaluation of the Two-Loop Amplitudes

The evaluation of the very complex analytical virtual matrix element can be very time-consuming due to the evaluation of many polylogarithmic functions. Moreover, in the `ggvvamp` code the authors have implemented a routine to ensure numerical stability that increases the computational time even further. This routine does a point-wise stability check that consists in evaluating the A_j functions twice, once at `double` precision and once at `quadruple` precision. In case the two results are not in agreement within a user defined accuracy the code switches to higher numerical accuracy repeating the comparison. This procedure is repeated until the user requested accuracy is met. Due to this procedure and the complexity of the amplitude's analytical structure, the evaluation time of the virtual matrix-element's form factors is at the order of seconds. In Fig. 5.11 the distribution of the evaluation time of all form factors A_j at both leading and next-to-leading order is shown. The evaluation of the leading order form factors is also taken into account because

(μ_R, μ_F)	m_{4l}		$2 \cdot m_{4l}$		(μ_R, μ_F)
factors	BVI	RS	BVI	RS	factors
(1,1)	2.79097	1.56608	2.79097	1.56608	(1/2,1/2)
(2,1)	2.4373	1.20853	2.4373	1.20853	(1,1/2)
(1,2)	2.96485	1.46515	2.96485	1.46515	(1/2,1)
(2,2)	2.5606	1.13065	2.5606	1.13065	(1,1)

Table 5.3: Comparison between explicit scale variation and on-the-fly scale variation in SHERPA for the BVI and RS part of the $e^+e^-\mu^+\mu^-$ production in gluon-fusion. The two columns m_{4l} and $2m_{4l}$ represent the user defined renormalisation and factorisation scale at which the BVI and RS pieces are evaluated, while each row represents one on-the-fly scale variation. The on-the-fly scale variations for each central scale are organized in order to ease the comparison between the two on-the-fly scale variation BVI and RS pieces evaluation.

they can not be computed separately since they are needed for the virtual matrix element regularisation. The plot has been generated evaluating 5000 random phase space points covering the entire four-lepton phase space. The evaluation has been performed on an Intel® Xeon® Gold 6126 CPU @ 2.60GHz. From the plot it is possible to read the average computational time for one phase space point, *i.e.* about $2s$ to $3s$. The large computational time makes the use of this library very impractical for phenomenological studies, especially in complex simulations involving many weight variations. However, there are different ways to deal with this problem. For instance, in a fixed order calculation a possibility is to generate the BVI and RS samples separately. The BVI piece converges faster than the RS due to the simpler phase space, therefore it needs fewer events to get to the same statistical accuracy of the RS piece. This can be improved even further by reducing the fraction of evaluated virtual terms in the BVI sample, since the leading contribution in BVI is given by the Born piece, meaning that the virtual correction can be evaluated for fewer events without affecting the accuracy of the result. Evaluating the virtual correction only for a fraction of the generated points can also be used in a MC@NLO calculation where it is not possible to separately generate the BVI and RS samples. However, these methods do not help in every, *e.g.* unweighted event generation.

To this end another method is given by using an interpolation framework. The development and implementation of this method is part of the original results of this thesis. The virtual matrix element interpolation framework developed here is similar to some extent to the one presented in Ref. [232] used to interpolate a pre-evaluated grid for the two-loop form factors of the NNLO QCD W^+W^- production. The interpolation is done by using multidimensional cubic splines [233] that can be accessed from the public code Btwxt [234]. This code employs cubic Hermite splines in a given N-dimensional interval where each polynomial is defined by the interval values and their first derivative on the corners of it. The library has been

Time Distribution of ggvvamp Form Factors
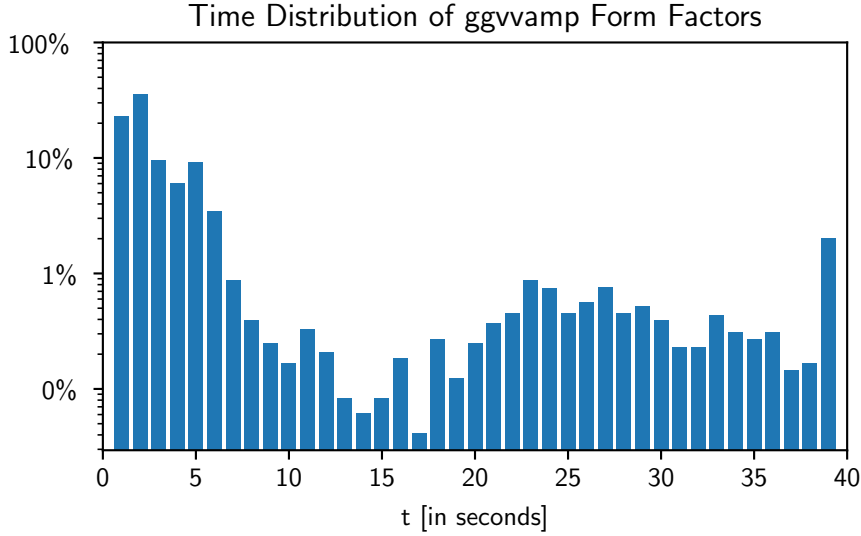
Figure 5.11: Time distribution of the evaluation of the `ggvvamp` form factors.

implemented in the development branch of SHERPA as part of the `ggvvamp` library add-on. This code is used to interpolate a pre-evaluated grid for the 72 form factors $E_i^{\lambda_1\lambda_2}(s, t, m_3^2, m_4^2)$ of the helicity amplitudes given in Eq. (5.3.18). It therefore actually builds 72 independent interpolators. In order to have a good interpolation performance, it is crucial to have a suitable parametrisation of the four kinematic variables s, t, M_3^2 and M_4^2 the helicity form factors depend on. A denser grid is needed in regions where the form factors have a larger derivative, *i.e.* for soft and/or collinear configurations of the two intermediate EW gauge bosons [8]. To this end each point of the four-dimensional kinematic space (s, t, m_3^2, m_4^2) is uniquely mapped to a four-dimensional unit hypercube $(x_1, x_2, x_3, x_4) = [0, 1]^4$ as follows:

$$M_{\{3,4\}}^2 = M_{\{3,4\},\text{min}}^2 + x_{\{3,4\}}^\alpha \left(M_{\{3,4\},\text{max}}^2 - M_{\{3,4\},\text{min}}^2\right),$$

$$\beta_3 = \frac{k\left(s, M_{V_1}^2, M_{V_2}^2\right)}{s + M_{V_1}^2 - M_{V_2}^2} = a_s(1 - x_3) + b_s x_3, \tag{5.3.24}$$

$$\cos\theta_3 = \frac{2t + s - M_{V_1}^2}{k\left(s, M_{V_1}^2, M_{V_2}^2\right)} = 1 - 2a_t(1 - x_4) - 2b_t x_4.$$

The range of the EW vector bosons masses mapped into the x_1 and x_2 variables goes from $M_{\{3,4\},\text{min}} = \sqrt{40}\,\text{GeV}$ to $M_{\{3,4\},\text{max}} = 1300\,\text{GeV}$. The lower boundary is chosen in order to avoid instability The exponent α in the first line of Eq. (5.3.24) is needed to have a finer binning in the small EW boson mass region. By testing this

value, it has been found that $\alpha = 5$ minimizes the interpolation error on the NLO total cross-section. Both smaller and larger values showed deviations from the exact total cross-section of a few percent. The s and t variables are mapped to the physical quantities β_3 and $\cos\theta_3$ that are respectively the relativistic velocity and cosine of the scattering angle of the EW boson with momentum p_3. These two variables are then mapped to the hypercube axes x_3 and x_4. However, since at the edges of the $(\beta_3, \cos\theta_3)$ plane the form factors have a very large derivative [8], the mapping to the x_3 and x_4 variables has been done adding four small cut-offs, a_s, b_s, a_t and b_t, to avoid numerical instabilities. To improve further the accuracy of the interpolation, it would be advantageous to reduce the grid binning in the highly relativistic $\beta_3 \to 1$ and highly collinear $|\cos\theta_3| \to 1$ regions. Alternatively, it is possible to divide the (x_3, x_4) plane into four regions and build a grid for each one of these separately. A similar grid splitting method has been used in Ref. [232]. In Fig. 5.12 it is shown how the four grids are mapped to cover the $(\beta_3, \cos\theta_3)$ plane. These four grids are all built as four-dimensional unit hypercubes with 50 grid points for each of the hypercube dimensions. Each grid uses the same parametrisation of Eq. (5.3.24), differing only by the choice of a_s, b_s, a_t and b_t. These are set in order to cover the entire $(\beta_3, \cos\theta_3)$ plane, excluding only the highly relativistic and collinear regions. The phase space points not covered by this grid are evaluated using a linear extrapolation method. The pre-evaluated grids implemented in SHERPA use the following cut-offs for the four regions:

$$
\begin{array}{llll}
\boxed{\text{Sector 1}} & & \boxed{\text{Sector 2}} & \\
a_s & = & 0.8, & a_s & = & 0.8, \\
b_s & = & 0.9999, & b_s & = & 0.9999, \\
a_t & = & 0.5, & a_t & = & 0.01, \\
b_t & = & 0.99, & b_t & = & 0.5, \\
\end{array}
$$

$$\text{(5.3.25)}$$

$$
\begin{array}{llll}
\boxed{\text{Sector 3}} & & \boxed{\text{Sector 4}} & \\
a_s & = & 0.0001, & a_s & = & 0.0001, \\
b_s & = & 0.8, & b_s & = & 0.8, \\
a_t & = & 0.5, & a_t & = & 0.01, \\
b_t & = & 0.99, & b_t & = & 0.5. \\
\end{array}
$$

With the settings just described, each grid needs to evaluate 50^4 phase space points, which with the `ggvvamp` average evaluation time of $2s$ per point would need about 20 months. Using standard parallelisation methods, the creation time of the grid can be easily brought down to a few days, using 500 jobs. A drawback of this method is that at run time the grids have to be loaded into RAM requiring about
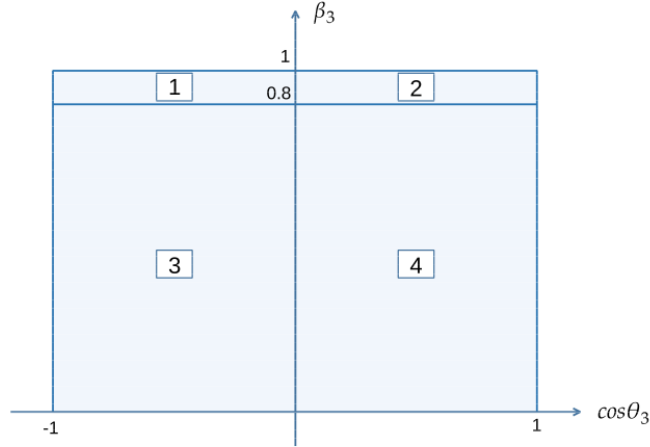
Figure 5.12: Sectors of the $(\beta_3, \cos\theta_3)$ plane corresponding to the four pre-evaluated (x_3, x_4) grids.

15 minutes on the same system used in the `ggvvamp` time distribution evaluation and 15 GB of RAM. However, once the grids are loaded their interpolation time takes $\mathcal{O}(ms)$, *i.e.* three orders of magnitude faster than the analytical result from `ggvvamp`, and slightly faster than the Born or real emission contributions.

The validation of the grid interpolation has been done by comparing only the BVI part of the $e^+e^-\mu^+\mu^-$ loop-induced production of the fixed order NLO calculation. The exact calculation is dubbed BVI_{ex}, and the interpolated calculation BVI_{int}. The two calculations have been performed using SHERPA's default SM parameters, a center-of-mass energy of $\sqrt{s} = 13\,\mathrm{TeV}$, the `NNPDF30_nnlo_as_0118` PDF set and setting the renormalisation and factorisation scales to $\mu_R = \mu_F = m_{4l}/2$. The analysis used is the standard RIVET [235] analysis for MC validation of the ZZ production, `MC_ZZINC`, which implements cuts on the lepton-pairs to avoid photon singularities, *i.e.* $66 < m_{2l} < 116\,\mathrm{GeV}$.

In this set-up, the total cross-sections for the BVI part of the NLO calculation agree:

$$\begin{aligned}
\sigma_{\mathrm{ex}} &= 1.438(2) \text{ fb,} \\
\sigma_{\mathrm{int}} &= 1.439(3) \text{ fb.}
\end{aligned} \tag{5.3.26}$$

Similarly, inclusive observables show a very good agreement between the two calculations as can be seen from Fig. 5.13. The plots show the four-lepton invariant mass, leading lepton pseudorapidity, single Z-boson pseudorapidity and leading lepton transverse momentum. In all these observables the exact calculation and the interpolated one are in very good agreement. Small deviations are only observed in the high energy region of the four-lepton invariant mass and leading lepton transverse momentum, but these can be attributed to statistical fluctuations. In Fig.
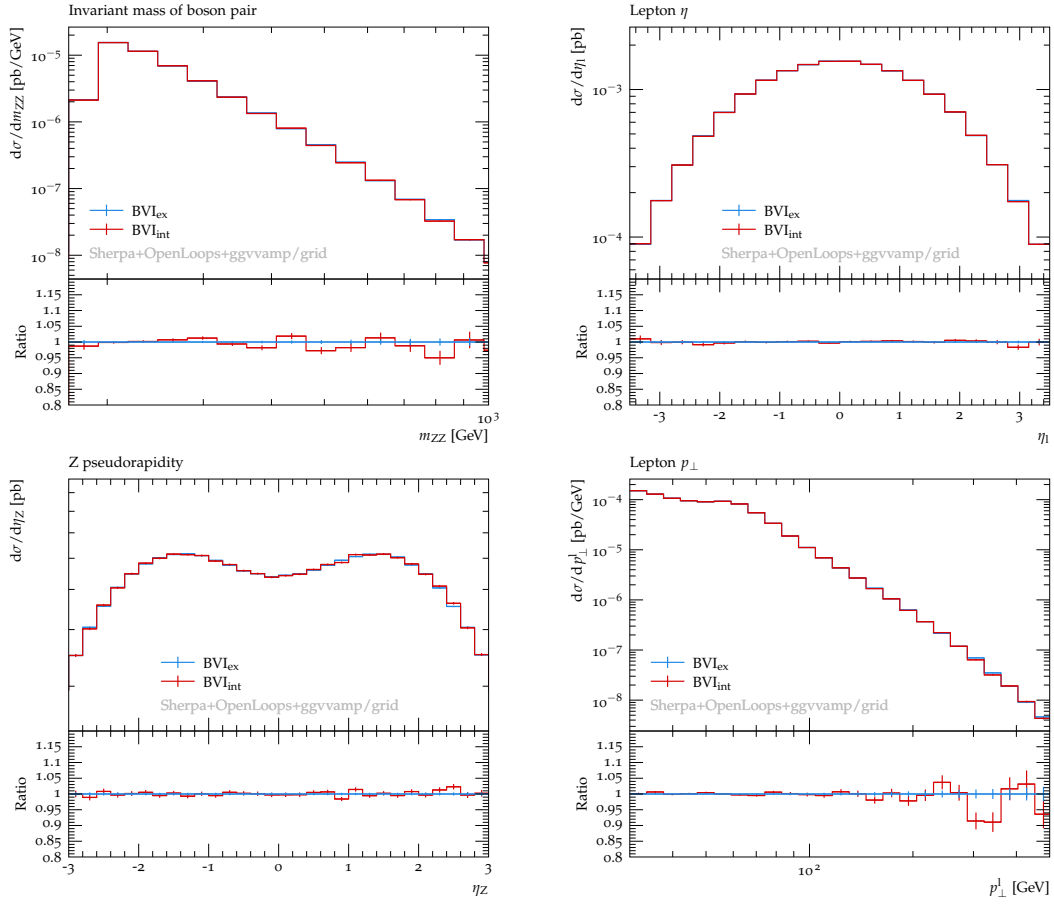
Figure 5.13: Comparison of the BVI part of the NLO fixed order $e^+e^-\mu^+\mu^-$ production in gluon fusion evaluated using the exact result from the `ggvvamp` code and the four-dimensional interpolation. The simulations have been done using SHERPA + OPENLOOPS.

5.14 the $\Delta\eta_{ZZ}$ and ΔR_{ZZ} observables are shown. In this case, large deviations of about 15% are in the tail of the distributions, *i.e.* $|\Delta\eta_{ZZ}| > 4.5$ and $\Delta R_{ZZ} > 5.5$. This is due to the fact that in that phase space region the interpolator switches to its extrapolation method due to the fact that those points are not covered by the pre-evaluated grid. Despite these differences, this interpolation framework is a very useful tool. For example, it can be used as a surrogate for the loop-induced virtual matrix element in unweighted event generation. Only when an event is accepted, a full evaluation using the analytical virtual matrix element from `ggvvamp` is required. Similarly to the technique described in Ref. [236].

The results in Sec. 5.4 for the MC@NLO calculation are all generated using the exact virtual matrix element after testing the simulation setup with the interpolated grid. In those tests there has been no statistically significant difference between the exact and interpolated calculation.
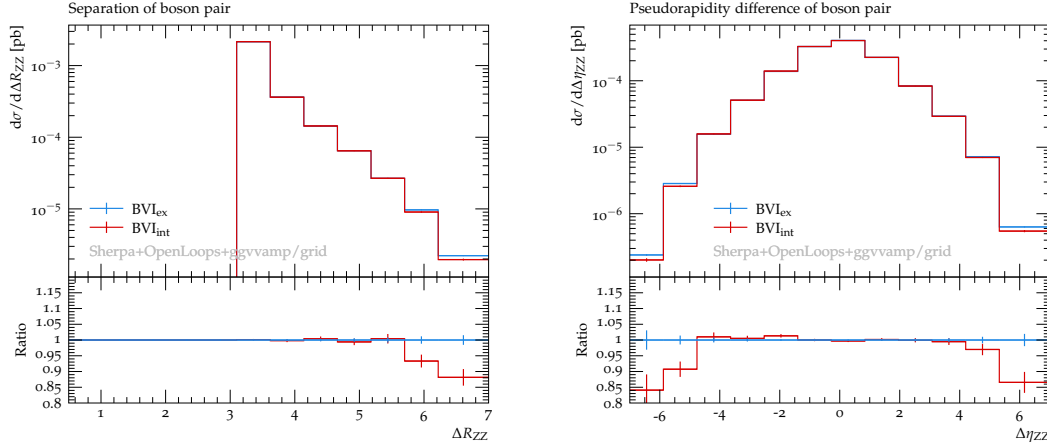
Figure 5.14: Comparison of the BVI part of the NLO fixed order $e^+e^-\mu^+\mu^-$ production in gluon fusion evaluated using the exact result form the `ggvvamp` code and the four-dimensional interpolation. The simulations have been done using SHERPA + OPENLOOPS.

5.4 NLO Di-Boson Production in Gluon Fusion Matched to Parton Shower

Sec. 5.1.3 has discussed the parton-shower matching to loop-induced gluon-initiated processes at leading order. In that case, it was shown that the parton-shower matching for loop-induced processes could produce non-trivial effects due to the large gluon initial state flux and splitting function. In observables sensitive to QCD emissions, such as the di-boson transverse momentum, the leading-order parton-shower matched calculation (Figs. 5.4 and 5.5a) produces a harder spectrum than the 0+1-jet merged matrix-element calculation in the transition region from soft/collinear to hard emissions. This is not observed in $q\bar{q}$ initiated processes, as shown in Fig. 5.5b for the $e^+e^-\mu^+\mu^-$ production at leading order, suggesting that the parton-shower matching to NLO loop-induced gluon-initiated processes has to be studied carefully before using it for phenomenological studies. The parton-shower matching to the NLO $gg \to e^+e^-\mu^+\mu^-$ loop-induced process is going to be studied by comparing the MC@NLO to the fixed order calculation. Due to the parton-shower unitarity, these two calculations are expected to coincide at least for inclusive observables, and especially they are expected to reproduce the same one-jet high transverse momentum spectrum. The fixed order calculation is supplemented by an uncertainty band defined as the envelope of the renormalisation (μ_R) and factorisation (μ_F) 7-point scale variations, *i.e.*

$$\left\{ \left(\tfrac{1}{2}\mu_\mathrm{R},\ \tfrac{1}{2}\mu_\mathrm{F}\right),\ \left(\tfrac{1}{2}\mu_\mathrm{R},\mu_\mathrm{F}\right),\ \left(\mu_\mathrm{R},\tfrac{1}{2}\mu_\mathrm{F}\right),\ \left(\mu_\mathrm{R},\mu_\mathrm{F}\right),\ \left(\mu_\mathrm{R},2\mu_\mathrm{F}\right),\ \left(2\mu_\mathrm{R},\mu_\mathrm{F}\right),\ \left(2\mu_\mathrm{R},2\mu_\mathrm{F}\right) \right\} \ .$$

The MC@NLO calculation features a scale-variation uncertainty band for the parton-

shower starting scale. This has been varied by a factor of 2 both upward and downward, *i.e.* $\{\frac{1}{2}\mu_{PS}, \mu_{PS}, 2\mu_{PS}\}$. Together with these samples, the MEPS 0+1-jet merged calculation is also included. This sample is added in order to highlight the role played by the significant virtual correction in the showered calculation. All these calculations have been performed using the same SM and PDF parameters used in the validation of SHERPA's `ggvvamp` implementation. The fixed order renormalisation and factorisation scales are instead set to the final-state lepton pairs' mean transverse energy, *i.e.*

$$\mu_R = \mu_F = \frac{1}{2}\left(E_{\text{T},ee} + E_{\text{T},\mu\mu}\right). \tag{5.4.1}$$

This is also used to set the renormalisation and factorisation scales of the core process in the MC@NLO and MEPS 0+1-jet calculations. In the merged calculation, the merging cut is set to $Q_{\text{cut}} = 30\,\text{GeV}$, while the renormalisation, factorisation, and resummation scales are set using the CKKW algorithm as for the results of Sec. 4.6.2. It is essential to note that each 1-jet process also includes the $q\bar{q}$ and gq initial-state channels. Finally, the phase space cuts used are,

$$p_{T,2l} > 25\text{ GeV}, \quad |\eta_Z| < 3.5, \quad \Delta R_{ee/\mu\mu} > 0.2,$$
$$66\text{ GeV} \leq m_{e^+e^-/\mu^+\mu^-} \leq 116\text{ GeV}.$$

These are general cuts for the standard MC validation analyses `MC_ZZINC` and `MC_ZZJETS` from the RIVET repository. In Tab. 5.4 the results for the total cross-sections from the three calculations are shown. The first thing to notice is that the fixed order and MC@NLO total cross-sections are in perfect agreement. This is expected due to the unitarity of the parton-shower, and it confirms that the MC@NLO method is working as it should also for NLO loop-induced processes. Instead, the comparison to the MEPS 0+1-jet total cross-section shows a very large NLO k-factor of about +75%, which is not covered by the still very large fixed order scale variation uncertainty which goes from -10% to +27%. The size of the fixed order scale uncertainty and the NLO correction agrees with other calculations [169, 207]. The parton-shower starting scale uncertainty of the MC@NLO result has not been reported because it was smaller than the statistical error of the nominal value. The large NLO k-factor and theoretical uncertainty indicate that for an accurate description of the $e^+e^-\mu^+\mu^-$ production, the NLO correction of loop-induced four-lepton production needs to be included.

The effects of the parton-shower matching are studied by looking at more exclusive observables. In Fig. 5.15 and Fig. 5.17 are shown respectively lepton and jet exclusive observables. Together with the comparison of the fixed order calculation against the MC@NLO and MEPS 0+1-jet calculations, a second ratio plot is added showing the contribution of the S- and H-type events in the MC@NLO sample.

Loop Ind. $pp \to e^+e^-\mu^+\mu^-$+jets	NLO	Mc@Nlo	MePs 0+1-jet
Total Cross Section [fb]	$1.7904(49)^{+27\%}_{-10\%}$	$1.793(7)$	$1.0184(6)$

Table 5.4: Total cross-sections for the $pp \to e^+e^-\mu^+\mu^-$ in gluon fusion evaluated at fixed order NLO, Mc@Nlo and MePs 0+1-jet.

    The lepton observables taken into consideration are the four-lepton invariant mass $m_{2e2\mu}$, di-boson transverse momentum $p_{T,2e2\mu}$, leading Z-boson transverse momentum $p_{T,Z}$ and pseudorapidity difference of the boson pair $\Delta\eta_{2e,2\mu}$. Except for the di-boson transverse momentum, for every other lepton observable the Mc@Nlo is in very good agreement with the fixed order calculation. The comparison with the MePs 0+1-jet calculation shows that the virtual correction has a more considerable impact in the low energy region in both the four-lepton invariant mass and the leading Z-boson transverse momentum. Indeed, in the four-lepton invariant mass distribution, both NLO calculations are about 75% bigger than the MePs 0+1-jet in the on-shell region, *i.e.* at about $m_{2e2\mu} = 2M_Z$, and only 45% bigger at $500\,\text{GeV}$. Very large deviations between the Mc@Nlo and fixed order calculations are instead displayed in the di-boson transverse momentum. Here, the nominal Mc@Nlo deviates from the fixed order by more than 100% for energies between $40\,\text{GeV}$ and $100\,\text{GeV}$. Furthermore, in this energy region, the Mc@Nlo displays a very large parton-shower starting scale uncertainty reaching 200% difference with the fixed order at about $150\,\text{GeV}$. At higher energies, the Mc@Nlo calculation converges to the fixed order calculation reproducing the right single hard QCD emission spectrum. However, despite this deviation being similar to the one observed in the leading order loop-induced parton-shower matching in Fig. 5.4 and Fig. 5.5a, they can not be traced back to the same origin. The reason why they are different is given by the fact that the MePs 0+1-jet line does not display any bump, and it is, on the contrary, in very good agreement with the fixed order result in the hard emission energy region. This means that it can not just be a large parton shower effect due to the size of the gluon splitting functions and their incoming luminosity. It has instead to be linked to the large virtual correction in the NLO calculation matched to the parton-shower since it is the only different piece between the MePs 0+1-jet and Mc@Nlo. Indeed, by looking at the second ratio panel of the di-boson transverse momentum it is clear that the large deviation of the Mc@Nlo calculation comes from S-type events that are dominant up until $100\,\text{GeV}$. At higher energies, the Mc@Nlo sample is dominated by the H-type events that correctly reproduce the hard emission spectrum of the fixed order calculation as expected.

    The large contribution to the S-type events comes from higher order terms included in the Mc@Nlo method. These terms can be understood by rearranging the Mc@Nlo formula from Eq. (2.2.6) for the case of an observable insensitive to Born configurations,

$$\langle\, O\,\rangle = \int d\Phi_B d\Phi_1 \bar{B}(\Phi_B)\Delta(t,\mu_{PS}^2)\frac{D(\Phi_B,\Phi_1)}{B(\Phi_B)}\Theta(\mu_{PS}^2-t)O(\Phi_R)$$
$$+ \int d\Phi_R H(\Phi_R)O(\Phi_R). \tag{5.4.2}$$

Taking this expression outside the Sudakov suppression region, *i.e.* $\Delta(t,\mu_{PS}^2) = 1$, and writing explicitly the real emission contribution, Eq. (5.4.2) becomes

$$\langle\, O\,\rangle_H = \int \mathrm{d}\Phi_B \mathrm{d}\Phi_1 \left(\bar{B}(\Phi_B) - B(\Phi_B)\right)\frac{D(\Phi_B,\Phi_1)}{B(\Phi_B)}\Theta(\mu_{PS}^2-t)O(\Phi_R)$$
$$+ \int \mathrm{d}\Phi_R R(\Phi_R)O(\Phi_R)$$
$$= \int \mathrm{d}\Phi_B \mathrm{d}\Phi_1 \left(V(\Phi_B) + I(\Phi_B)\right)\bar{K}(\Phi_B,\Phi_1)\Theta(\mu_{PS}^2-t)O(\Phi_R)$$
$$+ \int \mathrm{d}\Phi_R R(\Phi_R)O(\Phi_R). \tag{5.4.3}$$

From the last equivalence in Eq. (5.4.3) it is clear that the energy region that should be populated only by the real emission matrix elements also gets populated by S-type events of the form $[V(\Phi_B) + I(\Phi_B)] \cdot \bar{K}(\Phi_B,\Phi_1)\Theta(\mu_{PS}^2-t)$. This is formally a contribution at the order $\mathcal{O}(\alpha_s^4\alpha^4)$ that does not spoil the claimed accuracy of the Mc@Nlo calculation. Moreover, this term can be considered the soft and/or collinear approximation of the virtual correction for the real emission diagrams. In loop-induced processes the size of $[V(\Phi_B) + I(\Phi_B)] \cdot \bar{K}(\Phi_B,\Phi_1)$ can be comparable to the $R(\Phi_R)$ piece of the NLO calculation due to the very large virtual correction and gluon splitting function. Moreover, the presence of the $\Theta(\mu_{PS}^2-t)$ explains the very large parton-shower starting scale uncertainty in the Mc@Nlo sample. Indeed, for smaller choices of μ_{PS}, the activity of these higher order terms is reduced, improving the agreement between the fixed order and the Mc@Nlo as observed in the di-boson transverse momentum distribution in Fig. 5.15. On the contrary, larger values of the parton-shower starting scale would let these terms populate the higher energy region worsening the agreement with the fixed order. The same effect was observed in the NLO loop-induced di-Higgs production in Ref. [214]. It is important to point out that these higher order terms are not only present in the Mc@Nlo method but also in the Powheg method, as shown in Refs. [168, 207], leading to the very same kind of deviation. In quark-initiated processes, the higher order terms do not produce such a sizeable contribution due to the more modest size of the virtual correction and parton splitting functions, as shown in Fig. 5.16.

The jet observables studied in Fig. 5.17 are the leading jet transverse momentum $p_{T,j}$, the separation between the Z-boson and leading jet $\Delta R(2e2\mu, j)$, pseu-

dorapidity of the leading jet η_j and the inclusive jet multiplicity N_{jet}. The leading jet transverse momentum displays the same Mc@Nlo deviation as the four-lepton transverse momentum. In this case, its nominal value deviates from the leading order at most by 80% at about 65 GeV. It again covers the energy range from 40 GeV to 100 GeV with a very large parton-shower starting scale uncertainty that largely exceeds the fixed order renormalisation and factorisation scale uncertainty. The MePs 0+1-jet sample is again in good agreement with the fixed order calculation in the hard emission region. The separation of the di-boson system with the leading-jet shows a good agreement between the Mc@Nlo and the fixed order calculation for $\Delta R(2e2\mu, j) > \pi$. The small deviations displayed can be attributed entirely to parton-shower effects since the Mc@Nlo and the MePs 0+1-jet differ only by a constant factor. In this case, the parton-shower starting scale uncertainty is relatively small, especially for $\Delta R(2e2\mu, j) > \pi$. The region $\Delta R(2e2\mu, j) < \pi$ has a larger parton-shower uncertainty since it is entirely populated by it. The flat difference between the Mc@Nlo and MePs 0+1-jet of about 75% is again a confirmation of the correct behavior of the parton-shower matched to an NLO loop-induced process. The pseudorapidity of the leading jet and the inclusive jet multiplicity observables show a very interesting behavior. In this case, the Mc@Nlo is about 35% bigger than the fixed order and 75% than the MePs 0+1-jet calculations in both the one-jet inclusive cross-section and throughout the range of the leading jet pseudorapidity. It is very interesting to note that the difference between Mc@Nlo and MePs 0+1-jet is still of the same order as the 0-jet NLO correction despite these observables being formally at leading order. This is due to the fact that the Mc@Nlo sample is dominated by S-type events, meaning that these observables are populated mainly by soft/collinear emissions according to the first line of Eq. (5.4.2). In other words, in the leading-jet pseudorapidity and the one-jet inclusive cross-section, the Mc@Nlo sample is still about 70% bigger than the MePs 0+1-jet sample because the soft/collinear emissions in the Mc@Nlo are weighted by $\bar{B}(\Phi_B)$ while in the MePs 0+1-jet they are weighted by $B(\Phi_B)$, reproducing so the displayed 75% difference of the 0-jet NLO correction between the two samples. Moreover, the parton-shower starting scale uncertainty of the Mc@Nlo sample is not large enough to make up for this 75% difference. All these observations suggest that observables sensitive to jet configurations in loop-induced processes may still receive substantial corrections from higher orders terms.
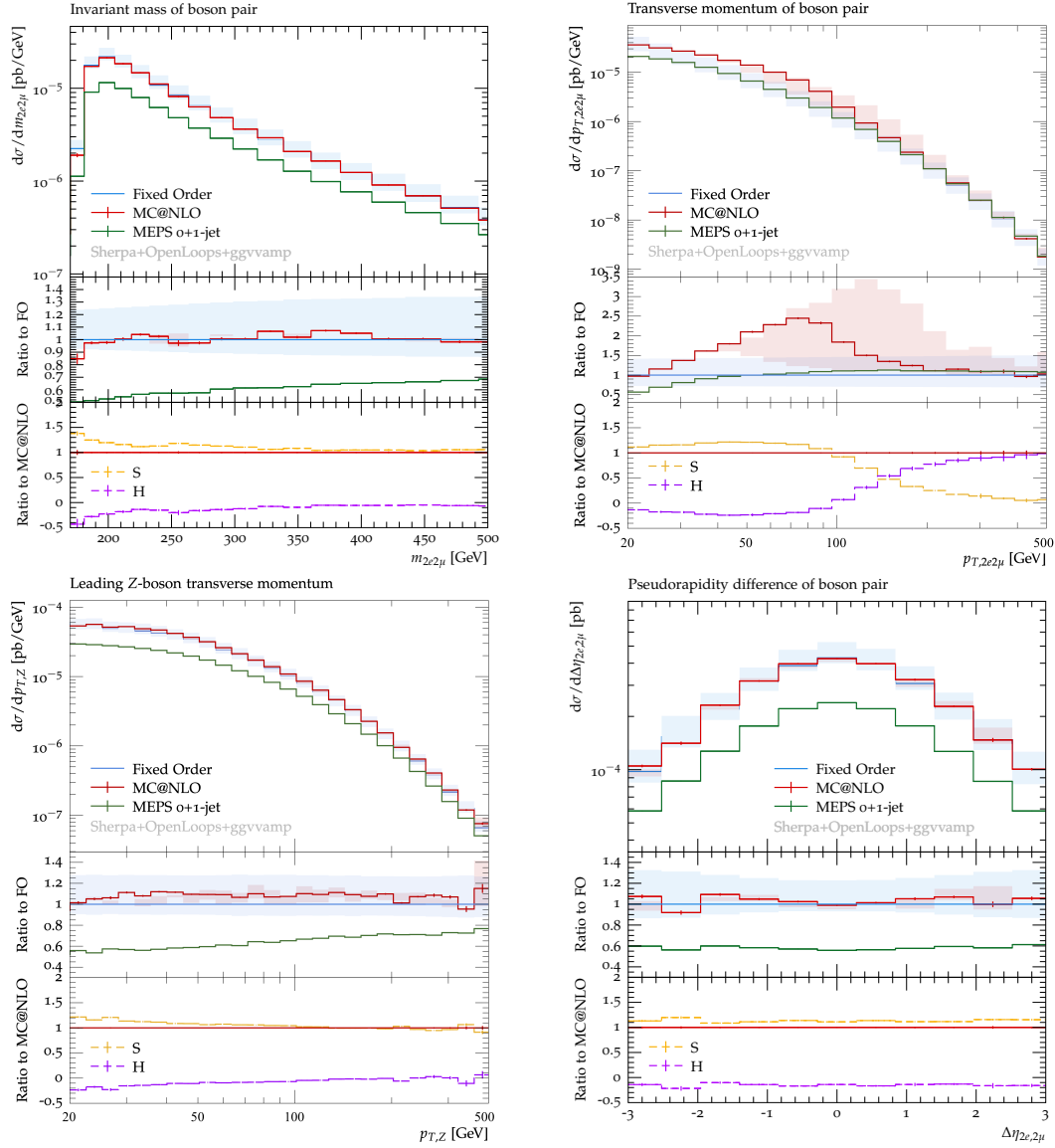
Figure 5.15: Distributions of leptonic observables for the loop-induced $e^+e^-\mu^+\mu^-$ + jets production. The Mc@Nlo calculation is compared against the fixed order. These two lines are supplemented with uncertainty bands for, respectively, the parton-shower starting scale and the renormalisation and factorisation scale 7-point variation. The MePs 0+1-jet is also included as extra reference. The four observables shown from top left to bottom right are: the invariant mass of the four-lepton system $m_{2e2\mu}$, the transverse momentum of the four-lepton system $p_{T,2e2\mu}$ the leading Z-boson transverse momentum $p_{T,Z}$, and the pseudorapidity difference of the Z-boson pair $\Delta\eta_{2e,2\mu}$. All predictions are calculated using Sherpa+OpenLoops +ggvvamp. The first ratio plot shows the showered samples relative to the fixed order, while the second one gives the relative size of the contributions to the Mc@Nlo prediction.
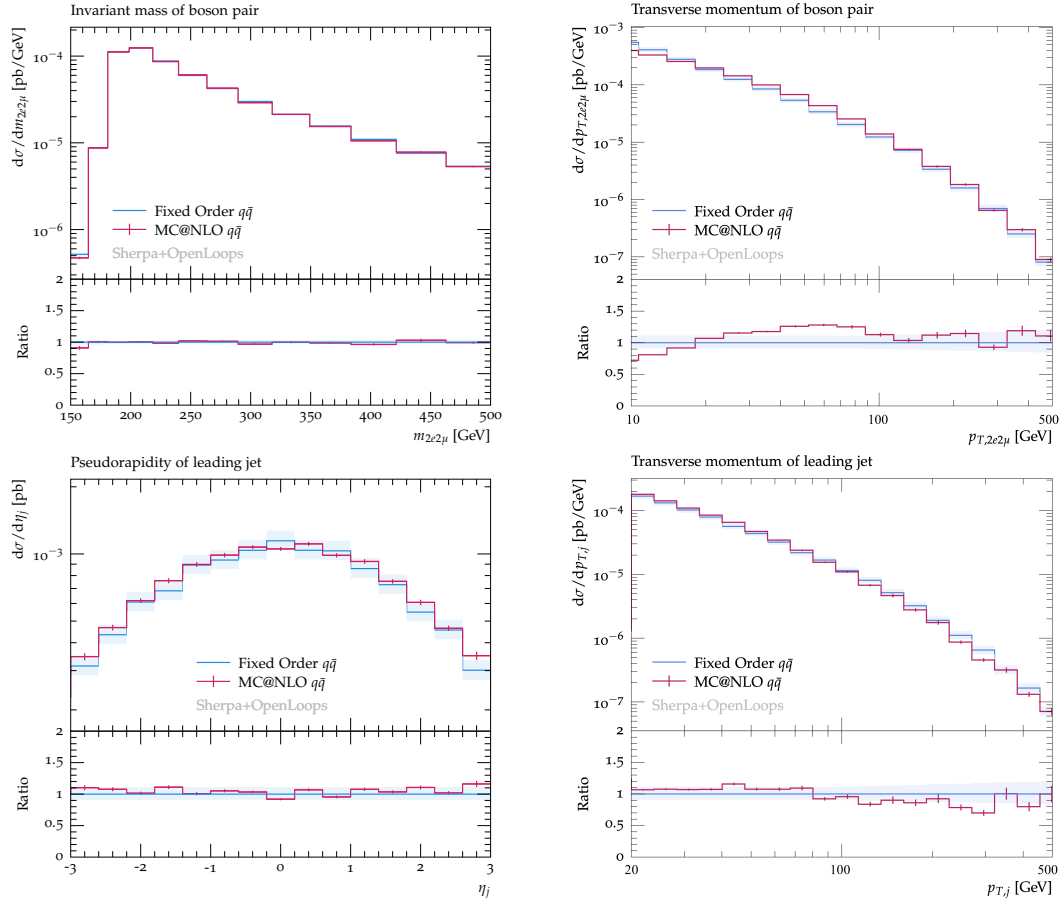
Figure 5.16: Distributions for the $pp \rightarrow e^+e^-\mu^+\mu^- +$ jets process at NLO QCD. The MC@NLO calculation is compared against the fixed order. The fixed order line is supplemented with the renormalisation and factorisation scale 7-point variation uncertainty band. The four observables shown from top left to bottom right are: the invariant mass of the four-lepton system $m_{2e2\mu}$, the transverse momentum of the four-lepton system $p_{T,2e2\mu}$ the leading-jet pseudorapidity η_j, and the leading-jet transverse momentum $p_{T,j}$. All predictions are calculated using SHERPA+OPENLOOPS.
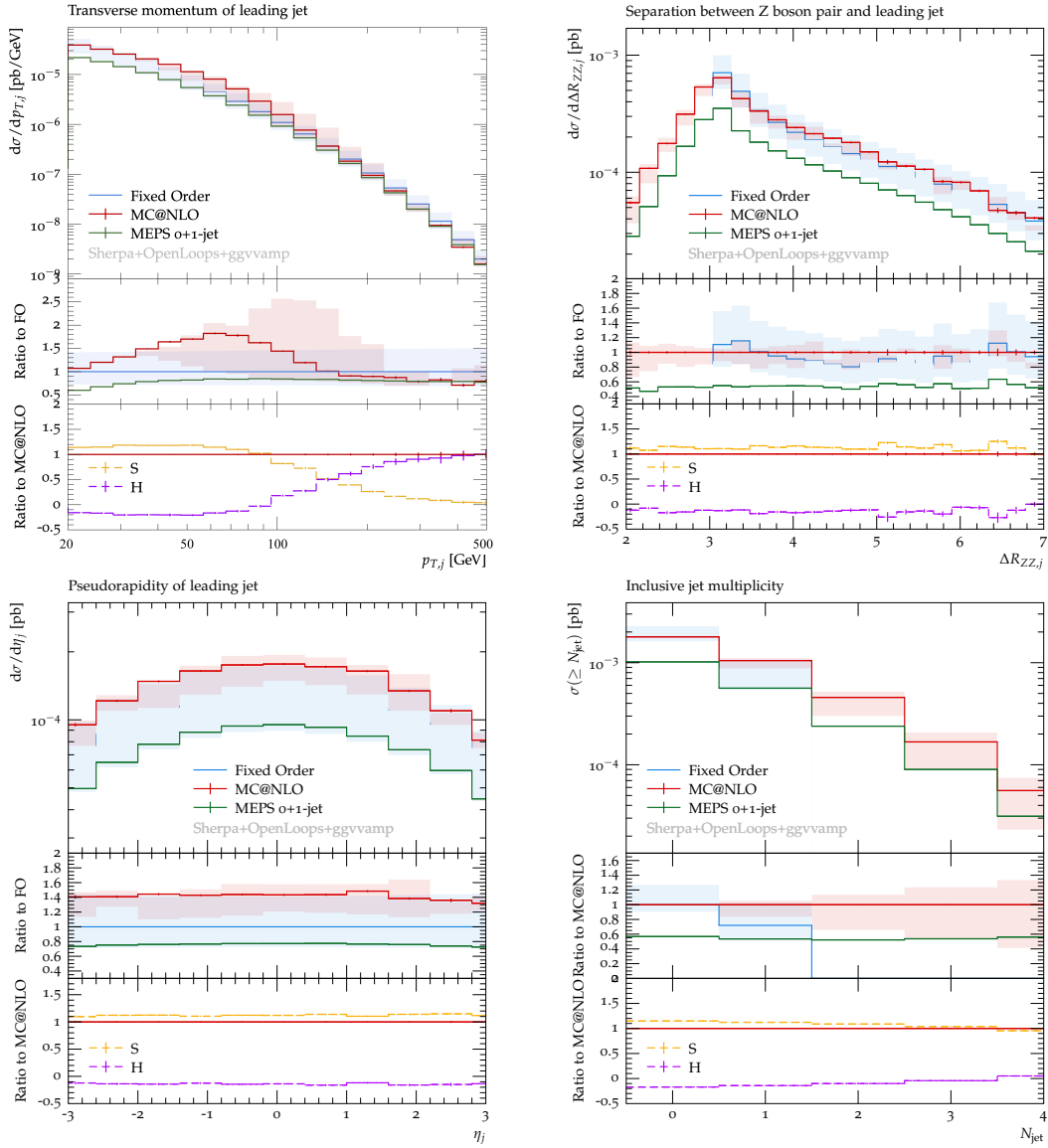
Figure 5.17: Distributions of jet observables for the loop-induced $e^+e^-\mu^+\mu^-$ + jets production. The MC@NLO calculation is compared against the fixed order. These two lines are supplemented with uncertainty bands for, respectively, the parton-shower starting scale and the renormalisation and factorisation scale 7-point variation. The MEPS 0+1-jet is also included as extra reference. The four observables shown from top left to bottom right are: the leading-jet transverse momentum $p_{T,j}$, the separation between the Z boson pair and the leading jet $\Delta R_{ZZ,j}$ the leading-jet pseudorapidity η_j, and the inclusive number of jets N_{jet}. All predictions are calculated using SHERPA+OPENLOOPS +ggvvamp. The first ratio plot shows the showered samples relative to the fixed order, while the second one gives the relative size of the contributions to the MC@NLO prediction.

Conclusion

With the upcoming Run III and the future high luminosity upgrade of the LHC, datasets will reach an unprecedented accuracy. In particular, the experimental uncertainty on di-boson measurements is expected to decrease to just a few percent on many differential observables, such as the four-lepton invariant mass and transverse momentum. Theoretical predictions are then required to match the experimental measurements' high precision level. Specifically, calculations based on perturbation theory need to be improved, including higher-order corrections.

High precision measurements for the di-boson production are crucial for testing the gauge invariance of the SM because they allow studying the effects of the EW gauge boson self-coupling dictated by the gauge symmetry. Moreover, many BSM models introduce terms in the SM Lagrangian that modify these couplings by breaking the SM gauge invariance. High precision measurements are crucial to set limits on the couplings and masses of possible new particles and further investigate the SM.

In this thesis the higher order corrections taken under consideration are the NLO EW to $pp \to e^+ e^- \mu^+ \mu^- +$ jets and NLO QCD to $gg \to e^+ e^- \mu^+ \mu^-$ in a general multiple QCD emission simulation.

Since a general framework to include the full NLO EW correction in a multi-jet merged calculation is not fully developed yet, in this thesis, EW corrections have been studied via two approximations, the high-energy virtual EW ($\mathrm{EW}_\mathrm{virt}$) and Sudakov ($\mathrm{EW}_\mathrm{sud}$) approximations, that were already implemented and automated in Sherpa. Both these approximations are based on the fact that in the high energy region of the phase space, the NLO EW correction is dominated by Sudakov logarithms from the virtual matrix element. In this thesis, these EW approximations have been in the first place compared to the full NLO EW correction to the $pp \to e^+ e^- \mu^+ \mu^-$ and $pp \to e^+ e^- \mu^+ \mu^- j$ processes, in order to check how well they capture the exact high energy behavior of the full NLO EW correction.

The EW virtual matrix elements have been evaluated for the 0- and 1-jet process, respectively with OpenLoops and Recola. Sherpa's interface to the Recola matrix element generator has required to be ported and validated to the new version of Sherpa (v3.0.0). The validation of the EW approximations has shown very good agreement with the fixed order NLO EW calculation. Only in the case of jet observables for the four-lepton production associated with one jet a significant discrepancy

with the fixed order calculation was observed. The cause for this discrepancy is found to be a QCD-EW interference finite contribution to the real emission that is not part of the EW approximations. However, the impact of this contribution is shown to be significantly reduced by including the NLO QCD correction, improving the agreement between the EW approximations and the fixed order calculation. The effects of matching the fixed order NLO EW calculations to the resummed EW Sudakov logarithms are studied in this validation. The effect of the resummation has been shown to reduce the negative correction of the fixed order NLO EW calculation in the very high-energy region. The overall good level of agreement of the EW approximations motivates their use in a MEPS@NLO calculation based on the NLO QCD 0- and 1-jet multiplicity and LO and 2- and 3-jet multiplicity matrix elements. Both the total cross-section and the differential observables studied here have shown a good agreement between the predictions with the two approximations. However, systematic deviations have been observed for phase space regions dominated by higher multiplicities' matrix elements. These deviations are explained by the different ways EW_{virt} and EW_{sud} approximations are applied to the pieces of the multi-jet merged calculation. Specifically, the EW_{virt} is applied to higher multiplicities only via a local k-factor using the EW virtual matrix elements of the lower multiplicities. Instead, in the EW_{sud} approximation, higher multiplicity matrix elements receive the correct NLL EW Sudakov factor. Finally, the phenomenology of EW effects in this setup has been studied, including the theoretical uncertainty for the reference calculation, *i.e.* MEPS@NLO. The impact of the EW Sudakov logarithms is observed to exceed the theoretical uncertainty for high energetic configurations reaching up to -40%.

The second higher order correction to the $pp \to e^+e^-\mu^+\mu^-$ process studied in this thesis is the NLO QCD of the loop-induced $gg \to e^+e^-\mu^+\mu^-$. The study of this process focuses on its parton-shower matching at both leading order and NLO. The leading order parton-shower matching highlights general features specific to loop-induced processes, such as the large initial state gluon luminosity and splitting functions. To give an idea of the generality of these features, the leading order ZH on-shell production in gluon fusion matched to parton-shower was discussed. In this study, two different parton-shower were considered, SHERPA and PYTHIA 8. Both these parton-showers have shown very similar behavior with differences covered by SHERPA's parton-shower starting scale uncertainty. These two calculations have also been compared to the MEPS@LO 0+1-jet merged matrix elements. In this comparison, the multi-jet merged calculation included the scale variation uncertainty. As expected, the LO+PS calculations failed to capture the hard emission spectrum of the MEPS@LO calculation. However, it was also observed that the parton-shower produces a harder spectrum that exceeds the scale uncertainty of the MEPS@LO calculation for energies between $40\,\mathrm{GeV}$ to $100\,\mathrm{GeV}$. This behavior is characteristic of loop-induced processes due to the large gluon splitting functions. This observation suggests that the NLO parton-shower matching has to be carefully checked to identify any possible parton-shower artifact. The evaluation of the NLO loop-induced $e^+e^-\mu^+\mu^-$ production used OPENLOOPS for the Born and real emission

matrix elements and `ggvvamp` for the virtual matrix elements. The interface to the `ggvvamp` code in SHERPA and its validation is part of the technical achievements of this thesis. Due to the highly complex structure of the virtual matrix element, its single phase-space point evaluation takes, on average, 2 seconds. The large evaluation time makes the NLO loop-induced four-lepton production quite impractical for unweighted event generation or simulations involving several weight variations. An interpolation framework has been developed for a fast evaluation of the virtual matrix elements in order to solve this problem. With this method, the average single phase-space point evaluation takes on the order of milliseconds. However, the main results of this thesis have been evaluated using the actual analytical matrix element. The interpolation is, instead, used for preliminary tests of the setup. Turning to the NLO parton-shower matching results. The NLO loop-induced has been matched to the parton-shower using the MC@NLO method, including the parton-shower starting scale uncertainty in the sample. This calculation has been compared to the NLO fixed order calculation that includes the renormalisation and factorisation scale uncertainty and the MEPS@LO merging the 0+1-jet multiplicity matrix elements at the leading order. From this analysis has been observed that in the total production rate and differential observables that are insensible to jet configurations, the fixed order and MC@NLO calculations are in perfect agreement. Instead, the comparison with the MEPS@LO displayed the very large NLO k-factor of about 75% featured by loop-induced processes. In observables sensible to jet configurations, such as the four-lepton transverse momentum, the MC@NLO displayed substantial deviations from the fixed order in the energy range from $40\,\mathrm{GeV}$ to $100\,\mathrm{GeV}$. Unlike the leading order matching, this discrepancy is due to higher order corrections introduced by the MC@NLO method, which are generally small. However, in the case of loop-induced processes, these are enhanced by the large NLO k-factor and gluon splitting functions. The significant effects of these higher order terms suggest that loop-induced processes may still receive significant contributions from their NNLO correction.

To give an outlook, the most immediate improvement to the results presented here concerns the NLO QCD correction to the loop-induced $e^+e^-\mu^+\mu^-$ production. The virtual matrix element implemented and studied in this thesis has top-quark mass effects included only via approximation. Analytical calculations, including the complete top-quark mass dependence, have started to appear only very recently [167]. The interface to the `ggvvamp` code developed in SHERPA is general enough for a simple implementation of the virtual matrix elements' form factors with full top quark mass dependence. Implementing such amplitudes will give us a complete description of the NLO QCD loop-induced four-lepton production. Moreover, the interpolation framework developed for the fast evaluation of the massless virtual matrix elements form-factors is expected to work as well, giving a fast alternative for phenomenological studies of the full NLO loop-induced correction.

Another important follow-up is to include matched EW corrections in a multi-jet merged calculation. This can be achieved by matching the $\mathrm{EW_{virt}}$ approximation

to the all-order resummation of the EW Sudakov logarithms at NLL logarithmic accuracy, using the exponentiated EW_{sud} approximation. The motivation to include the all-order resummed EW Sudakov logarithms with the EW_{virt} approximation is to improve the description of very energetic regions of the phase space that are where many BSM new elementary particle candidates should contribute the most.

The higher order corrections presented in this thesis are the state-of-the-art of the $pp \rightarrow e^+e^-\mu^+\mu^+$ process modelling in both fixed order and fully differential multijet-merged MC simulations. This work will be fundamental for the upcoming measurements of $e^+e^-\mu^+\mu^-$ four-lepton production at the LHC in Run III and the future HL-LHC.

Appendix A

OPENLOOPS and RECOLA Validation

In this appendix are reported some validation plots for the porting of SHERPA's interface to the RECOLA matrix element generator to its version 3.0.0, and the development and update of the new module, `EXTAMP`. Since this thesis focuses on the $e^+e^-\mu^+\mu^-$ production the plots in Fig. A.2 are all calculations of this process.

Each sub-figure in Fig. A.2 contains ratio plots with different calculations of the same observable, while different sub-figures show different observables. The calculations under consideration are:

- LO+PS. The reference calculation uses `AMEGIC`, and it is compared against `EXTAMP` using OPENLOOPS as matrix element generator. The parton-shower used is SHERPA's default Catani-Seymour shower.

- MC@NLO. The reference calculation uses `AMEGIC` and OPENLOOPS for the virtual amplitude. This is compared against `EXTAMP` using OPENLOOPS for every matrix element. The parton-shower used is SHERPA's default Catani-Seymour shower.

- NLO QCD. Both calculations use `AMEGIC` to evaluate the tree-like matrix elements, while the virtual correction is evaluated with OPENLOOPS in the reference line and with RECOLA in the compared calculation.

- NLO EW. Both calculations use `AMEGIC` to evaluate the tree-like matrix elements, while the virtual correction is evaluated with OPENLOOPS in the reference line and with RECOLA in the compared calculation. These calculations are done in the G_μ scheme.

The showered samples are reported for the four-lepton invariant mass, the separation of the Z-boson pair, the azimuthal angle difference of the Z-boson pair and the di-boson transverse momentum, while the fixed order calculations for the

(a) **Four-lepton invariant mass.**   (b) **Separation of the Z-boson pair.**
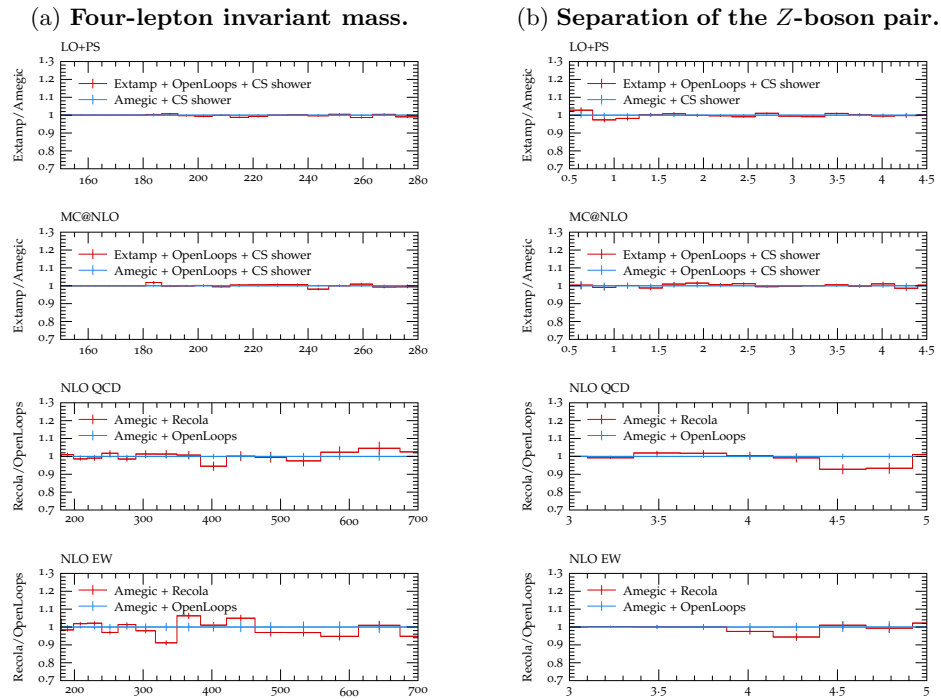
Figure A.1: Validation plots for the `EXTAMP` module and the update of Recola. Each sub-figure contains calculations for the same observable. The observables considered are, the four-lepton invariant mass Fig. A.2a, the separation of the Z-boson pair Fig. A.2b. The different calculations considered are: LO+PS, Mc@Nlo, fixed order NLO QCD and fixed order NLO EW.

four-lepton invariant mass, the separation of the Z-boson pair, the pseudorapidity difference and the leading Z-boson transverse momentum All calculations show a good level of agreement within the statistical uncertainty.

(a) **Azimuthal angle difference of the Z-boson pair.**
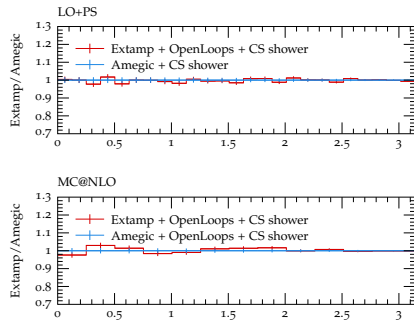
(b) **Four-lepton transverse momentum.**
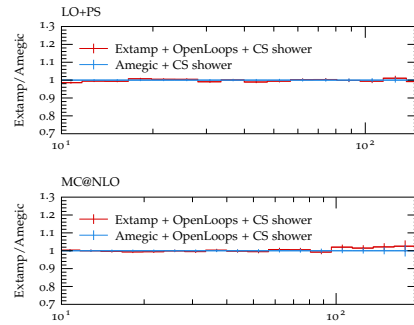
(c) **Pseudorapidity difference of the Z-boson pair.**
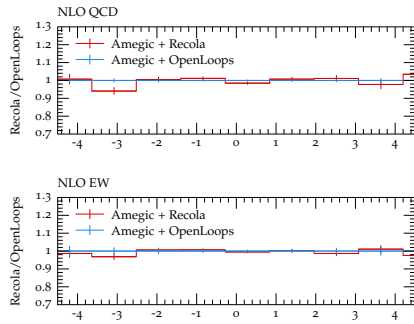
(d) **Leading Z-boson transverse momentum.**
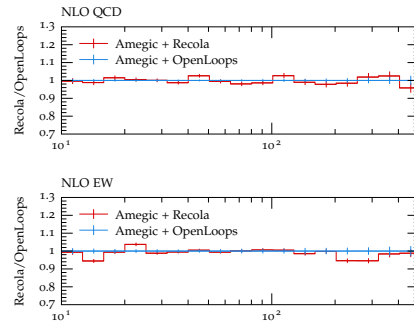
Figure A.2: Validation plots for the `EXTAMP` module and the update of RECOLA. Each sub-figure contains calculations for the same observable. The observables considered are, the azimuthal angle difference of the Z-boson pair Fig. A.2a, the di-boson transverse momentum Fig.A.2b, the pseudorapidity difference Fig. A.2c and the leading Z-boson transverse momentum Fig. A.2d. The different calculations considered are: LO+PS, MC@NLO, fixed order NLO QCD and fixed order NLO EW.

Bibliography

[1] Lyndon Evans and Philip Bryant. "LHC Machine". In: *Journal of Instrumentation* 3.08 (2008), S08001–S08001. DOI: 10.1088/1748-0221/3/08/s08001. URL: https://doi.org/10.1088/1748-0221/3/08/s08001.

[2] Georges Aad et al. "Observation of a new particle in the search for the Standard Model Higgs boson with the ATLAS detector at the LHC". In: *Phys. Lett. B* 716 (2012), pp. 1–29. DOI: 10.1016/j.physletb.2012.08.020. arXiv: 1207.7214 [hep-ex].

[3] Serguei Chatrchyan et al. "Observation of a New Boson at a Mass of 125 GeV with the CMS Experiment at the LHC". In: *Phys. Lett. B* 716 (2012), pp. 30–61. DOI: 10.1016/j.physletb.2012.08.021. arXiv: 1207.7235 [hep-ex].

[4] U. Baur and David L. Rainwater. "Probing neutral gauge boson selfinteractions in ZZ production at hadron colliders". In: *Phys. Rev. D* 62 (2000), p. 113011. DOI: 10.1103/PhysRevD.62.113011. arXiv: hep-ph/0008063.

[5] Georges Aad et al. "Measurements of differential cross-sections in four-lepton events in 13 TeV proton-proton collisions with the ATLAS detector". In: *JHEP* 07 (2021), p. 005. DOI: 10.1007/JHEP07(2021)005. arXiv: 2103.01918 [hep-ex].

[6] Enrico Bothmann et al. "Higher-order EW corrections in ZZ and ZZj production at the LHC". In: *JHEP* 06 (2022), p. 064. DOI: 10.1007/JHEP06(2022)064. arXiv: 2111.13453 [hep-ph].

[7] Massimiliano Grazzini et al. "Four lepton production in gluon fusion: Off-shell Higgs effects in NLO QCD". In: *Phys. Lett. B* 819 (2021), p. 136465. DOI: 10.1016/j.physletb.2021.136465. arXiv: 2102.08344 [hep-ph].

[8] Andreas von Manteuffel and Lorenzo Tancredi. "The two-loop helicity amplitudes for $gg \rightarrow V_1 V_2 \rightarrow 4$ leptons". In: *JHEP* 06 (2015), p. 197. DOI: 10.1007/JHEP06(2015)197. arXiv: 1503.08835 [hep-ph].

[9] E. D. Bloom et al. "High-Energy Inelastic $e - p$ Scattering at 6° and 10°". In: *Phys. Rev. Lett.* 23 (16 1969), pp. 930–934. DOI: 10.1103/PhysRevLett.23.930. URL: https://link.aps.org/doi/10.1103/PhysRevLett.23.930.

[10] M. Breidenbach et al. "Observed Behavior of Highly Inelastic Electron-Proton Scattering". In: *Phys. Rev. Lett.* 23 (16 1969), pp. 935–939. DOI: 10.1103/PhysRevLett.23.935. URL: https://link.aps.org/doi/10.1103/PhysRevLett.23.935.

[11] F. Englert and R. Brout. "Broken Symmetry and the Mass of Gauge Vector Mesons". In: *Phys. Rev. Lett.* 13 (1964). Ed. by J. C. Taylor, pp. 321–323. DOI: 10.1103/PhysRevLett.13.321.

[12] Peter W. Higgs. "Broken Symmetries and the Masses of Gauge Bosons". In: *Phys. Rev. Lett.* 13 (1964). Ed. by J. C. Taylor, pp. 508–509. DOI: 10.1103/PhysRevLett.13.508.

[13] Peter W. Higgs. "Broken symmetries, massless particles and gauge fields". In: *Phys. Lett.* 12 (1964), pp. 132–133. DOI: 10.1016/0031-9163(64)91136-9.

[14] G. S. Guralnik, C. R. Hagen, and T. W. B. Kibble. "Global Conservation Laws and Massless Particles". In: *Phys. Rev. Lett.* 13 (1964). Ed. by J. C. Taylor, pp. 585–587. DOI: 10.1103/PhysRevLett.13.585.

[15] Steven Weinberg. "A Model of Leptons". In: *Phys. Rev. Lett.* 19 (21 1967), pp. 1264–1266. DOI: 10.1103/PhysRevLett.19.1264. URL: https://link.aps.org/doi/10.1103/PhysRevLett.19.1264.

[16] A. Salam. "Elementary Particle Physics: Relativistic Groups and Analyticity". In: *N. Svartholm, Ed., Eighth Nobel Symposium, Almquvist and Wiksell, Stockholm* (1968).

[17] Murray Gell-Mann. "The Eightfold Way: A Theory of strong interaction symmetry". In: (Mar. 1961). DOI: 10.2172/4008239.

[18] Yuval Ne'eman. "Derivation of strong interactions from a gauge invariance". In: *Nucl. Phys.* 26 (1961). Ed. by R. Ruffini and Y. Verbin, pp. 222–229. DOI: 10.1016/0029-5582(61)90134-1.

[19] C. N. Yang and R. L. Mills. "Conservation of Isotopic Spin and Isotopic Gauge Invariance". In: *Phys. Rev.* 96 (1 1954), pp. 191–195. DOI: 10.1103/PhysRev.96.191. URL: https://link.aps.org/doi/10.1103/PhysRev.96.191.

[20] John C. Collins. *Renormalization: An Introduction to Renormalization, The Renormalization Group, and the Operator Product Expansion*. Vol. 26. Cambridge Monographs on Mathematical Physics. Cambridge: Cambridge University Press, 1986. ISBN: 978-0-521-31177-9, 978-0-511-86739-2. DOI: 10.1017/CBO9780511622656.

[21] W. Pauli and F. Villars. "On the Invariant regularization in relativistic quantum theory". In: *Rev. Mod. Phys.* 21 (1949), pp. 434–444. DOI: 10.1103/RevModPhys.21.434.

[22] Serguei Chatrchyan et al. "Measurement of the Ratio of the Inclusive 3-Jet Cross Section to the Inclusive 2-Jet Cross Section in pp Collisions at $\sqrt{s} = 7$ TeV and First Determination of the Strong Coupling Constant in the TeV Range". In: *Eur. Phys. J. C* 73.10 (2013), p. 2604. DOI: 10.1140/epjc/s10052-013-2604-6. arXiv: 1304.7498 [hep-ex].

[23] Serguei Chatrchyan et al. "Determination of the Top-Quark Pole Mass and Strong Coupling Constant from the $t\bar{t}$ Production Cross Section in pp Collisions at $\sqrt{s} = 7$ TeV". In: *Phys. Lett. B* 728 (2014). [Erratum: Phys.Lett.B 738, 526–528 (2014)], pp. 496–517. DOI: 10.1016/j.physletb.2013.12.009. arXiv: 1307.1907 [hep-ex].

[24] Vardan Khachatryan et al. "Measurement of the inclusive 3-jet production differential cross section in proton–proton collisions at 7 TeV and determination of the strong coupling constant in the TeV range". In: *Eur. Phys. J. C* 75.5 (2015), p. 186. DOI: 10.1140/epjc/s10052-015-3376-y. arXiv: 1412.1633 [hep-ex].

[25] V. M. Abazov et al. "Determination of the strong coupling constant from the inclusive jet cross section in $p\bar{p}$ collisions at sqrt(s)=1.96 TeV". In: *Phys. Rev. D* 80 (2009), p. 111107. DOI: 10.1103/PhysRevD.80.111107. arXiv: 0911.2710 [hep-ex].

[26] Victor Mukhamedovich Abazov et al. "Measurement of angular correlations of jets at $\sqrt{s} = 1.96$ TeV and determination of the strong coupling at high momentum transfers". In: *Phys. Lett. B* 718 (2012), pp. 56–63. DOI: 10.1016/j.physletb.2012.10.003. arXiv: 1207.4957 [hep-ex].

[27] V. Andreev et al. "Measurement of Jet Production Cross Sections in Deep-inelastic ep Scattering at HERA". In: *Eur. Phys. J. C* 77.4 (2017). [Erratum: Eur.Phys.J.C 81, 739 (2021)], p. 215. DOI: 10.1140/epjc/s10052-017-4717-9. arXiv: 1611.03421 [hep-ex].

[28] H. Abramowicz et al. "Inclusive-jet photoproduction at HERA and determination of alphas". In: *Nucl. Phys. B* 864 (2012), pp. 1–37. DOI: 10.1016/j.nuclphysb.2012.06.006. arXiv: 1205.6153 [hep-ex].

[29] Vardan Khachatryan et al. "Measurement and QCD analysis of double-differential inclusive jet cross sections in pp collisions at $\sqrt{s} = 8$ TeV and cross section ratios to 2.76 and 7 TeV". In: *JHEP* 03 (2017), p. 156. DOI: 10.1007/JHEP03(2017)156. arXiv: 1609.05331 [hep-ex].

[30] Murray Gell-Mann. "A Schematic Model of Baryons and Mesons". In: *Phys. Lett.* 8 (1964), pp. 214–215. DOI: 10.1016/S0031-9163(64)92001-3.

[31] G. Zweig. "An SU(3) model for strong interaction symmetry and its breaking. Version 1". In: (Jan. 1964).

[32] G. Zweig. "An SU(3) model for strong interaction symmetry and its breaking. Version 2". In: *DEVELOPMENTS IN THE QUARK THEORY OF HADRONS. VOL. 1. 1964 - 1978*. Ed. by D. B. Lichtenberg and Simon Peter Rosen. Feb. 1964, pp. 22–101.

[33] V. E. Barnes et al. "Observation of a Hyperon with Strangeness Minus Three". In: *Phys. Rev. Lett.* 12 (1964), pp. 204–206. DOI: 10.1103/PhysRevLett. 12.204.

[34] David J. Gross and Frank Wilczek. "Ultraviolet Behavior of Non-Abelian Gauge Theories". In: *Phys. Rev. Lett.* 30 (26 1973), pp. 1343–1346. DOI: 10.1103/PhysRevLett.30.1343. URL: https://link.aps.org/doi/10. 1103/PhysRevLett.30.1343.

[35] H. David Politzer. "Reliable Perturbative Results for Strong Interactions?" In: *Phys. Rev. Lett.* 30 (26 1973), pp. 1346–1349. DOI: 10.1103/PhysRevLett. 30.1346. URL: https://link.aps.org/doi/10.1103/PhysRevLett.30. 1346.

[36] Richard P. Feynman. "The Behavior of Hadron Collisions at Extreme Energies". In: *Special Relativity and Quantum Theory: A Collection of Papers on the Poincaré Group*. Ed. by M. E. Noz and Y. S. Kim. Dordrecht: Springer Netherlands, 1988, pp. 289–304. ISBN: 978-94-009-3051-3. DOI: 10.1007/978-94-009-3051-3_25. URL: https://doi.org/10.1007/978-94-009-3051-3_25.

[37] Enrico Fermi. "Tentativo di una teoria dell'emissione dei raggi beta". In: *Ric. Sci.* 4 (1933), pp. 491–495.

[38] R. P. Feynman and M. Gell-Mann. "Theory of the Fermi Interaction". In: *Phys. Rev.* 109 (1 1958), pp. 193–198. DOI: 10.1103/PhysRev.109.193. URL: https://link.aps.org/doi/10.1103/PhysRev.109.193.

[39] E. C. G. Sudarshan and R. E. Marshak. "Chirality Invariance and the Universal Fermi Interaction". In: *Phys. Rev.* 109 (5 1958), pp. 1860–1862. DOI: 10.1103/PhysRev.109.1860.2. URL: https://link.aps.org/doi/10. 1103/PhysRev.109.1860.2.

[40] J. J. Sakurai. "MASS REVERSAL AND WEAK INTERACTIONS". In: *Nuovo Cim.* 7 (1958), pp. 649–660. DOI: 10.1007/BF02781569.

[41] Nicola Cabibbo. "Unitary Symmetry and Leptonic Decays". In: *Phys. Rev. Lett.* 10 (1963), pp. 531–533. DOI: 10.1103/PhysRevLett.10.531.

[42] Sheldon L. Glashow. "The renormalizability of vector meson interactions". In: *Nucl. Phys.* 10 (1959), pp. 107–117. DOI: 10.1016/0029-5582(59)90196-8.

[43] Abdus Salam and John Clive Ward. "Weak and electromagnetic interactions". In: *Nuovo Cim.* 11 (1959), pp. 568–577. DOI: 10.1007/BF02726525.

[44] P. A. Zyla et al. "Review of Particle Physics". In: *PTEP* 2020.8 (2020), p. 083C01. DOI: 10.1093/ptep/ptaa104.

[45] Yoichiro Nambu. "Quasi-Particles and Gauge Invariance in the Theory of Superconductivity". In: *Phys. Rev.* 117 (3 1960), pp. 648–663. DOI: 10.1103/PhysRev.117.648. URL: https://link.aps.org/doi/10.1103/PhysRev.117.648.

[46] J. Goldstone. "Field Theories with Superconductor Solutions". In: *Nuovo Cim.* 19 (1961), pp. 154–164. DOI: 10.1007/BF02812722.

[47] Jeffrey Goldstone, Abdus Salam, and Steven Weinberg. "Broken Symmetries". In: *Phys. Rev.* 127 (3 1962), pp. 965–970. DOI: 10.1103/PhysRev.127.965. URL: https://link.aps.org/doi/10.1103/PhysRev.127.965.

[48] Makoto Kobayashi and Toshihide Maskawa. "CP Violation in the Renormalizable Theory of Weak Interaction". In: *Prog. Theor. Phys.* 49 (1973), pp. 652–657. DOI: 10.1143/PTP.49.652.

[49] D. DeCamp et al. "Determination of the number of light neutrino species". In: *Physics Letters B* 231.4 (1989), pp. 519–529. ISSN: 0370-2693. DOI: https://doi.org/10.1016/0370-2693(89)90704-1. URL: https://www.sciencedirect.com/science/article/pii/0370269389907041.

[50] J. H. Christenson et al. "Evidence for the 2π Decay of the K_2^0 Meson". In: *Phys. Rev. Lett.* 13 (4 1964), pp. 138–140. DOI: 10.1103/PhysRevLett.13.138. URL: https://link.aps.org/doi/10.1103/PhysRevLett.13.138.

[51] Michael E. Peskin and Daniel V. Schroeder. *An Introduction to quantum field theory.* Reading, USA: Addison-Wesley, 1995. ISBN: 978-0-201-50397-5.

[52] A. Banfi et al. "Optimisation of variables for studying dilepton transverse momentum distributions at hadron colliders". In: *Eur. Phys. J. C* 71 (2011), p. 1600. DOI: 10.1140/epjc/s10052-011-1600-y. arXiv: 1009.1580 [hep-ex].

[53] Morad Aaboud et al. "Measurement of the four-lepton invariant mass spectrum in 13 TeV proton-proton collisions with the ATLAS detector". In: *JHEP* 04 (2019), p. 048. DOI: 10.1007/JHEP04(2019)048. arXiv: 1902.05892 [hep-ex].

[54] S. Agostinelli et al. "Geant4—a simulation toolkit". In: *Nuclear Instruments and Methods in Physics Research Section A: Accelerators, Spectrometers, Detectors and Associated Equipment* 506.3 (2003), pp. 250–303. ISSN: 0168-9002. DOI: https://doi.org/10.1016/S0168-9002(03)01368-8. URL: https://www.sciencedirect.com/science/article/pii/S0168900203013688.

[55] J. Allison et al. "Geant4 developments and applications". In: *IEEE Transactions on Nuclear Science* 53.1 (2006), pp. 270–278. DOI: 10.1109/TNS.2006.869826.

[56] J. Allison et al. "Recent developments in Geant4". In: *Nuclear Instruments and Methods in Physics Research Section A: Accelerators, Spectrometers, Detectors and Associated Equipment* 835 (2016), pp. 186–225. ISSN: 0168-9002. DOI: https://doi.org/10.1016/j.nima.2016.06.125. URL: https://www.sciencedirect.com/science/article/pii/S0168900216306957.

[57] Enrico Bothmann et al. "Event Generation with Sherpa 2.2". In: *SciPost Phys.* 7.3 (2019), p. 034. DOI: 10.21468/SciPostPhys.7.3.034. arXiv: 1905.09127 [hep-ph].

[58] J. Bellm et al. "Herwig++ 2.7 Release Note". In: (Oct. 2013). arXiv: 1310.6877 [hep-ph].

[59] Johannes Bellm et al. "Herwig 7.0/Herwig++ 3.0 release note". In: *Eur. Phys. J. C* 76.4 (2016), p. 196. DOI: 10.1140/epjc/s10052-016-4018-8. arXiv: 1512.01178 [hep-ph].

[60] Christian Bierlich et al. "A comprehensive guide to the physics and usage of PYTHIA 8.3". In: (Mar. 2022). arXiv: 2203.11601 [hep-ph].

[61] V. V. Sudakov. "Vertex parts at very high-energies in quantum electrodynamics". In: *Sov. Phys. JETP* 3 (1956), pp. 65–71.

[62] Guido Altarelli and G. Parisi. "Asymptotic Freedom in Parton Language". In: *Nucl. Phys. B* 126 (1977), pp. 298–318. DOI: 10.1016/0550-3213(77)90384-4.

[63] Yuri L. Dokshitzer. "Calculation of the Structure Functions for Deep Inelastic Scattering and e+ e- Annihilation by Perturbation Theory in Quantum Chromodynamics." In: *Sov. Phys. JETP* 46 (1977), pp. 641–653.

[64] V. N. Gribov and L. N. Lipatov. "Deep inelastic e p scattering in perturbation theory". In: *Sov. J. Nucl. Phys.* 15 (1972), pp. 438–450.

[65] Torbjörn Sjöstrand. "A model for initial state parton showers". In: *Physics Letters B* 157.4 (1985), pp. 321–325. ISSN: 0370-2693. DOI: https://doi.org/10.1016/0370-2693(85)90674-4. URL: https://www.sciencedirect.com/science/article/pii/0370269385906744.

[66] G. Marchesini and B. R. Webber. "Monte Carlo Simulation of General Hard Processes with Coherent QCD Radiation". In: *Nucl. Phys. B* 310 (1988), pp. 461–526. DOI: 10.1016/0550-3213(88)90089-2.

[67] David A. Kosower. "Antenna factorization of gauge theory amplitudes". In: *Phys. Rev. D* 57 (1998), pp. 5410–5416. DOI: 10.1103/PhysRevD.57.5410. arXiv: hep-ph/9710213.

[68] A. Daleo, T. Gehrmann, and D. Maitre. "Antenna subtraction with hadronic initial states". In: *JHEP* 04 (2007), p. 016. DOI: 10.1088/1126-6708/2007/04/016. arXiv: hep-ph/0612257.

[69] S. Frixione, Z. Kunszt, and A. Signer. "Three-jet cross sections to next-to-leading order". In: *Nuclear Physics B* 467.3 (1996), pp. 399–442. ISSN: 0550-3213. DOI: https://doi.org/10.1016/0550-3213(96)00110-1. URL: https://www.sciencedirect.com/science/article/pii/0550321396001101.

[70] S. Catani and M.H. Seymour. "A general algorithm for calculating jet cross sections in NLO QCD". In: *Nuclear Physics B* 485.1 (1997), pp. 291–419. ISSN: 0550-3213. DOI: https://doi.org/10.1016/S0550-3213(96)00589-5. URL: https://www.sciencedirect.com/science/article/pii/S0550321396005895.

[71] Stefano Catani et al. "The Dipole formalism for next-to-leading order QCD calculations with massive partons". In: *Nucl. Phys. B* 627 (2002), pp. 189–265. DOI: 10.1016/S0550-3213(02)00098-6. arXiv: hep-ph/0201036.

[72] Tanju Gleisberg and Frank Krauss. "Automating dipole subtraction for QCD NLO calculations". In: *Eur. Phys. J. C* 53 (2008), pp. 501–523. DOI: 10.1140/epjc/s10052-007-0495-0. arXiv: 0709.2881 [hep-ph].

[73] Paolo Nason. "A New Method for Combining NLO QCD with Shower Monte Carlo Algorithms". In: *Journal of High Energy Physics* 2004.11 (2004), pp. 040–040. DOI: 10.1088/1126-6708/2004/11/040. URL: https://doi.org/10.1088/1126-6708/2004/11/040.

[74] Stefano Frixione, Paolo Nason, and Carlo Oleari. "Matching NLO QCD computations with parton shower simulations: the POWHEG method". In: *Journal of High Energy Physics* 2007.11 (2007), pp. 070–070. DOI: 10.1088/1126-6708/2007/11/070. URL: https://doi.org/10.1088/1126-6708/2007/11/070.

[75] Stefano Frixione and Bryan R Webber. "Matching NLO QCD computations and parton shower simulations". In: *Journal of High Energy Physics* 2002.06 (2002), pp. 029–029. DOI: 10.1088/1126-6708/2002/06/029. URL: https://doi.org/10.1088/1126-6708/2002/06/029.

[76] Simone Alioli et al. "NLO vector-boson production matched with shower in POWHEG". In: *JHEP* 07 (2008), p. 060. DOI: 10.1088/1126-6708/2008/07/060. arXiv: 0805.4802 [hep-ph].

[77] S Schumann and F Krauss. "A parton shower algorithm based on Catani-Seymour dipole factorisation". In: *Journal of High Energy Physics* 2008.03 (2008), pp. 038–038. DOI: 10.1088/1126-6708/2008/03/038. URL: https://doi.org/10.1088/1126-6708/2008/03/038.

[78] Stefan Hoeche et al. "A critical appraisal of NLO+PS matching methods". In: *JHEP* 09 (2012), p. 049. DOI: 10.1007/JHEP09(2012)049. arXiv: 1111.1220 [hep-ph].

[79]   Stefano Catani et al. "QCD Matrix Elements + Parton Showers". In: *Journal of High Energy Physics* 2001.11 (2001), pp. 063–063. DOI: 10.1088/1126-6708/2001/11/063. URL: https://doi.org/10.1088/1126-6708/2001/11/063.

[80]   F. Krauss. "Matrix elements and parton showers in hadronic interactions". In: *JHEP* 08 (2002), p. 015. DOI: 10.1088/1126-6708/2002/08/015. arXiv: hep-ph/0205283.

[81]   Leif Lonnblad. "Correcting the color dipole cascade model with fixed order matrix elements". In: *JHEP* 05 (2002), p. 046. DOI: 10.1088/1126-6708/2002/05/046. arXiv: hep-ph/0112284.

[82]   Nils Lavesson and Leif Lonnblad. "W+jets matrix elements and the dipole cascade". In: *JHEP* 07 (2005), p. 054. DOI: 10.1088/1126-6708/2005/07/054. arXiv: hep-ph/0503293.

[83]   Michelangelo L. Mangano, Mauro Moretti, and Roberto Pittau. "Multijet matrix elements and shower evolution in hadronic collisions: $Wb\bar{b}+n$ jets as a case study". In: *Nucl. Phys. B* 632 (2002), pp. 343–362. DOI: 10.1016/S0550-3213(02)00249-3. arXiv: hep-ph/0108069.

[84]   Stefan Hoeche et al. "QCD matrix elements + parton showers: The NLO case". In: *JHEP* 04 (2013), p. 027. DOI: 10.1007/JHEP04(2013)027. arXiv: 1207.5030 [hep-ph].

[85]   Thomas Gehrmann et al. "NLO QCD matrix elements + parton showers in $e^+e^- \longrightarrow$ hadrons". In: *JHEP* 01 (2013), p. 144. DOI: 10.1007/JHEP01(2013)144. arXiv: 1207.5031 [hep-ph].

[86]   Rikkert Frederix and Stefano Frixione. "Merging meets matching in MC@NLO". In: *JHEP* 12 (2012), p. 061. DOI: 10.1007/JHEP12(2012)061. arXiv: 1209.6215 [hep-ph].

[87]   Stefan Hoeche et al. "QCD matrix elements and truncated showers". In: *JHEP* 05 (2009), p. 053. DOI: 10.1088/1126-6708/2009/05/053. arXiv: 0903.1219 [hep-ph].

[88]   R. Hamberg, W.L. van Neerven, and T. Matsuura. "A complete calculation of the order α_s^2 correction to the Drell-Yan K-factor". In: *Nuclear Physics B* 359.2 (1991), pp. 343–405. ISSN: 0550-3213. DOI: https://doi.org/10.1016/0550-3213(91)90064-5. URL: https://www.sciencedirect.com/science/article/pii/0550321391900645.

[89]   Charalampos Anastasiou. "Differential cross-sections at next-to-next-to-leading-order in QCD". In: *Nuclear Physics B - Proceedings Supplements* 135 (2004). Loops and Legs in Quantum Field Theory. Proceedings of the 7th DESY Workshop on Elementary Particle Theory, pp. 124–128. ISSN: 0920-5632. DOI: https://doi.org/10.1016/j.nuclphysbps.2004.09.055. URL: https://www.sciencedirect.com/science/article/pii/S0920563204003561.

[90] Stefan Hoeche, Ye Li, and Stefan Prestel. "Drell-Yan Lepton pair production at NNLO QCD with parton showers". In: *Physical Review. D, Particles, Fields, Gravitation and Cosmology* 91.7 (Apr. 2015). DOI: `10.1103/PhysRevD.91.074015`.

[91] Radja Boughezal et al. "*Z*-Boson Production in Association with a Jet at Next-To-Next-To-Leading Order in Perturbative QCD". In: *Phys. Rev. Lett.* 116 (15 2016), p. 152001. DOI: `10.1103/PhysRevLett.116.152001`. URL: `https://link.aps.org/doi/10.1103/PhysRevLett.116.152001`.

[92] Radja Boughezal, Xiaohui Liu, and Frank Petriello. "W-boson plus jet differential distributions at NNLO in QCD". In: *Phys. Rev. D* 94.11 (2016), p. 113009. DOI: `10.1103/PhysRevD.94.113009`. arXiv: `1602.06965 [hep-ph]`.

[93] Aude Gehrmann-De Ridder et al. "The NNLO QCD corrections to Z boson production at large transverse momentum". In: *JHEP* 07 (2016), p. 133. DOI: `10.1007/JHEP07(2016)133`. arXiv: `1605.04295 [hep-ph]`.

[94] John M. Campbell et al. "Predictions for diphoton production at the LHC through NNLO in QCD". In: *JHEP* 07 (2016), p. 148. DOI: `10.1007/JHEP07(2016)148`. arXiv: `1603.02663 [hep-ph]`.

[95] Herschel A. Chawdhry et al. "NNLO QCD corrections to diphoton production with an additional jet at the LHC". In: *JHEP* 09 (2021), p. 093. DOI: `10.1007/JHEP09(2021)093`. arXiv: `2105.06940 [hep-ph]`.

[96] Edmond L. Berger et al. "NNLO QCD Corrections to t-channel Single Top-Quark Production and Decay". In: *Phys. Rev. D* 94.7 (2016), p. 071501. DOI: `10.1103/PhysRevD.94.071501`. arXiv: `1606.08463 [hep-ph]`.

[97] Massimiliano Grazzini et al. "W^+W^- production at the LHC: fiducial cross sections and distributions in NNLO QCD". In: *JHEP* 08 (2016), p. 140. DOI: `10.1007/JHEP08(2016)140`. arXiv: `1605.02716 [hep-ph]`.

[98] Massimiliano Grazzini, Stefan Kallweit, and Dirk Rathlev. "ZZ production at the LHC: fiducial cross sections and distributions in NNLO QCD". In: *Phys. Lett. B* 750 (2015), pp. 407–410. DOI: `10.1016/j.physletb.2015.09.055`. arXiv: `1507.06257 [hep-ph]`.

[99] Massimiliano Grazzini et al. "NNLO QCD + NLO EW with Matrix+OpenLoops: precise predictions for vector-boson pair production". In: *JHEP* 02 (2020), p. 087. DOI: `10.1007/JHEP02(2020)087`. arXiv: `1912.00068 [hep-ph]`.

[100] Charalampos Anastasiou, Kirill Melnikov, and Frank Petriello. "Higgs boson production at hadron colliders: Differential cross sections through next-to-next-to-leading order". In: *Phys. Rev. Lett.* 93 (2004), p. 262002. DOI: `10.1103/PhysRevLett.93.262002`. arXiv: `hep-ph/0409088`.

[101] Massimiliano Grazzini, Stefan Kallweit, and Marius Wiesemann. "Fully differential NNLO computations with MATRIX". In: *Eur. Phys. J. C* 78.7 (2018), p. 537. DOI: 10.1140/epjc/s10052-018-5771-7. arXiv: 1711.06631 [hep-ph].

[102] John Campbell and Tobias Neumann. "Precision Phenomenology with MCFM". In: *JHEP* 12 (2019), p. 034. DOI: 10.1007/JHEP12(2019)034. arXiv: 1909.09117 [hep-ph].

[103] John M. Campbell and R. Keith Ellis. "An Update on vector boson pair production at hadron colliders". In: *Phys. Rev. D* 60 (1999), p. 113006. DOI: 10.1103/PhysRevD.60.113006. arXiv: hep-ph/9905386.

[104] John M. Campbell, R. Keith Ellis, and Walter T. Giele. "A Multi-Threaded Version of MCFM". In: *Eur. Phys. J. C* 75.6 (2015), p. 246. DOI: 10.1140/epjc/s10052-015-3461-2. arXiv: 1503.06182 [physics.comp-ph].

[105] A. Gehrmann-De Ridder, T. Gehrmann, and E. W. Nigel Glover. "Antenna subtraction at NNLO". In: *JHEP* 09 (2005), p. 056. DOI: 10.1088/1126-6708/2005/09/056. arXiv: hep-ph/0505111.

[106] Fabrizio Caola, Kirill Melnikov, and Raoul Röntsch. "Nested soft-collinear subtractions in NNLO QCD computations". In: *Eur. Phys. J. C* 77.4 (2017), p. 248. DOI: 10.1140/epjc/s10052-017-4774-0. arXiv: 1702.01352 [hep-ph].

[107] Franz Herzog. "Geometric IR subtraction for final state real radiation". In: *JHEP* 08 (2018), p. 006. DOI: 10.1007/JHEP08(2018)006. arXiv: 1804.07949 [hep-ph].

[108] L. Magnea et al. "Local analytic sector subtraction at NNLO". In: *JHEP* 12 (2018). [Erratum: JHEP 06, 013 (2019)], p. 107. DOI: 10.1007/JHEP12(2018)107. arXiv: 1806.09570 [hep-ph].

[109] Keith Hamilton et al. "Merging H/W/Z + 0 and 1 jet at NLO with no merging scale: a path to parton shower + NNLO matching". In: *JHEP* 05 (2013), p. 082. DOI: 10.1007/JHEP05(2013)082. arXiv: 1212.4504 [hep-ph].

[110] Keith Hamilton et al. "NNLOPS simulation of Higgs boson production". In: *JHEP* 10 (2013), p. 222. DOI: 10.1007/JHEP10(2013)222. arXiv: 1309.0017 [hep-ph].

[111] Stefan Höche, Ye Li, and Stefan Prestel. "Drell-Yan lepton pair production at NNLO QCD with parton showers". In: *Phys. Rev. D* 91.7 (2015), p. 074015. DOI: 10.1103/PhysRevD.91.074015. arXiv: 1405.3607 [hep-ph].

[112] Pier Francesco Monni et al. "MiNNLO$_{PS}$: a new method to match NNLO QCD to parton showers". In: *JHEP* 05 (2020), p. 143. DOI: 10.1007/JHEP05(2020)143. arXiv: 1908.06987 [hep-ph].

[113] Pier Francesco Monni, Emanuele Re, and Marius Wiesemann. "MiNNLO$_{\text{PS}}$: optimizing $2 \rightarrow 1$ hadronic processes". In: *Eur. Phys. J. C* 80.11 (2020), p. 1075. DOI: 10.1140/epjc/s10052-020-08658-5. arXiv: 2006.04133 [hep-ph].

[114] John M. Campbell et al. "Towards NNLO+PS Matching with Sector Showers". In: (Aug. 2021). arXiv: 2108.07133 [hep-ph].

[115] Leif Lönnblad and Stefan Prestel. "Merging Multi-leg NLO Matrix Elements with Parton Showers". In: *JHEP* 03 (2013), p. 166. DOI: 10.1007/JHEP03(2013)166. arXiv: 1211.7278 [hep-ph].

[116] Stefan Höche et al. "Beyond Standard Model calculations with Sherpa". In: *Eur. Phys. J. C* 75.3 (2015), p. 135. DOI: 10.1140/epjc/s10052-015-3338-4. arXiv: 1412.6478 [hep-ph].

[117] Stefan Höche, Frank Krauss, and Stefan Prestel. "Implementing NLO DGLAP evolution in Parton Showers". In: *JHEP* 10 (2017), p. 093. DOI: 10.1007/JHEP10(2017)093. arXiv: 1705.00982 [hep-ph].

[118] John M. Campbell, Stefan Höche, and Christian T. Preuss. "Accelerating LHC phenomenology with analytic one-loop amplitudes: A C++ interface to MCFM". In: *Eur. Phys. J. C* 81.12 (2021), p. 1117. DOI: 10.1140/epjc/s10052-021-09885-0. arXiv: 2107.04472 [hep-ph].

[119] S. Actis et al. "Recursive generation of one-loop amplitudes in the Standard Model". In: *JHEP* 04 (2013), p. 037. DOI: 10.1007/JHEP04(2013)037. arXiv: 1211.6316 [hep-ph].

[120] Benedikt Biedermann et al. "Automation of NLO QCD and EW corrections with Sherpa and Recola". In: *Eur. Phys. J. C* 77 (2017), p. 492. DOI: 10.1140/epjc/s10052-017-5054-8. arXiv: 1704.05783 [hep-ph].

[121] Andy Buckley et al. "LHAPDF6: parton density access in the LHC precision era". In: *Eur. Phys. J. C* 75 (2015), p. 132. DOI: 10.1140/epjc/s10052-015-3318-8. arXiv: 1412.7420 [hep-ph].

[122] Frank Krauss, Ralf Kuhn, and Gerhard Soff. "AMEGIC++ 1.0, A Matrix Element Generator In C++". In: *Journal of High Energy Physics* 2002.02 (2002), pp. 044–044. DOI: 10.1088/1126-6708/2002/02/044. URL: https://doi.org/10.1088/1126-6708/2002/02/044.

[123] R. Kleiss and W.J. Stirling. "Spinor techniques for calculating $pp \rightarrow W/Z$ + jets". In: *Nuclear Physics B* 262.2 (1985), pp. 235–262. ISSN: 0550-3213. DOI: https://doi.org/10.1016/0550-3213(85)90285-8. URL: https://www.sciencedirect.com/science/article/pii/0550321385902858.

[124] Alessandro Ballestrero, Ezio Maina, and Stefano Moretti. "Heavy quarks and leptons at $e + e-$ colliders". In: *Nuclear Physics B* 415.2 (1994), pp. 265–292. ISSN: 0550-3213. DOI: https://doi.org/10.1016/0550-3213(94)90112-0. URL: https://www.sciencedirect.com/science/article/pii/055032139490112O.

[125] Claude Duhr, Stefan Hoeche, and Fabio Maltoni. "Color-dressed recursive relations for multi-parton amplitudes". In: *JHEP* 08 (2006), p. 062. DOI: 10.1088/1126-6708/2006/08/062. arXiv: hep-ph/0607057.

[126] G P Lepage. *VEGAS - an adaptive multi-dimensional integration program*. Tech. rep. Ithaca, NY: Cornell Univ. Lab. Nucl. Stud., 1980. URL: http://cds.cern.ch/record/123074.

[127] R. Kleiss, W. James Stirling, and S. D. Ellis. "A New Monte Carlo Treatment of Multiparticle Phase Space at High-energies". In: *Comput. Phys. Commun.* 40 (1986), p. 359. DOI: 10.1016/0010-4655(86)90119-0.

[128] D. R. Yennie, Steven C. Frautschi, and H. Suura. "The infrared divergence phenomena and high-energy processes". In: *Annals Phys.* 13 (1961), pp. 379–452. DOI: 10.1016/0003-4916(61)90151-8.

[129] Marek Schonherr and Frank Krauss. "Soft Photon Radiation in Particle Decays in SHERPA". In: *JHEP* 12 (2008), p. 018. DOI: 10.1088/1126-6708/2008/12/018. arXiv: 0810.5071 [hep-ph].

[130] Elisabetta Barberio and Zbigniew Was. "PHOTOS: A Universal Monte Carlo for QED radiative corrections. Version 2.0". In: *Comput. Phys. Commun.* 79 (1994), pp. 291–308. DOI: 10.1016/0010-4655(94)90074-4.

[131] Torbjörn Sjöstrand and Maria van Zijl. "A multiple-interaction model for the event structure in hadron collisions". In: *Phys. Rev. D* 36 (7 1987), pp. 2019–2041. DOI: 10.1103/PhysRevD.36.2019. URL: https://link.aps.org/doi/10.1103/PhysRevD.36.2019.

[132] Jan-Christopher Winter, Frank Krauss, and Gerhard Soff. "A Modified cluster hadronization model". In: *Eur. Phys. J. C* 36 (2004), pp. 381–395. DOI: 10.1140/epjc/s2004-01960-8. arXiv: hep-ph/0311085.

[133] Thomas D. Gottschalk and Duncan A. Morris. "A New Model for Hadronization and $e + e-$ Annihilation". In: *Nucl. Phys. B* 288 (1987), pp. 729–781. DOI: 10.1016/0550-3213(87)90236-7.

[134] B.R. Webber. "A QCD model for jet fragmentation including soft gluon interference". In: *Nuclear Physics B* 238.3 (1984), pp. 492–528. ISSN: 0550-3213. DOI: https://doi.org/10.1016/0550-3213(84)90333-X. URL: https://www.sciencedirect.com/science/article/pii/055032138490333X.

[135] V. L. Chernyak and I. R. Zhitnitsky. "B meson exclusive decays into baryons". In: *Nucl. Phys. B* 345 (1990), pp. 137–172. DOI: 10.1016/0550-3213(90)90612-H.

[136] Vladimir M. Braun and I. E. Filyanov. "QCD Sum Rules in Exclusive Kinematics and Pion Wave Function". In: *Z. Phys. C* 44 (1989), p. 157. DOI: 10.1007/BF01548594.

[137] Johann H. Kuhn and A. Santamaria. "Tau decays to pions". In: *Z. Phys. C* 48 (1990), pp. 445–452. DOI: 10.1007/BF01572024.

[138] G. Ecker et al. "The Role of Resonances in Chiral Perturbation Theory". In: *Nucl. Phys. B* 321 (1989), pp. 311–342. DOI: 10.1016/0550-3213(89)90346-5.

[139] G. J. Gounaris, J. Layssac, and F. M. Renard. "New and standard physics contributions to anomalous Z and gamma selfcouplings". In: *Phys. Rev. D* 62 (2000), p. 073013. DOI: 10.1103/PhysRevD.62.073013. arXiv: hep-ph/0003143.

[140] Georges Aad et al. "Search for an additional, heavy Higgs boson in the $H \to ZZ$ decay channel at $\sqrt{s} = 8$ TeV in pp collision data with the ATLAS detector". In: *Eur. Phys. J. C* 76.1 (2016), p. 45. DOI: 10.1140/epjc/s10052-015-3820-z. arXiv: 1507.05930 [hep-ex].

[141] Vardan Khachatryan et al. "Search for a Higgs boson in the mass range from 145 to 1000 GeV decaying to a pair of W or Z bosons". In: *JHEP* 10 (2015), p. 144. DOI: 10.1007/JHEP10(2015)144. arXiv: 1504.00936 [hep-ex].

[142] Morad Aaboud et al. "Searches for heavy diboson resonances in pp collisions at $\sqrt{s} = 13$ TeV with the ATLAS detector". In: *JHEP* 09 (2016), p. 173. DOI: 10.1007/JHEP09(2016)173. arXiv: 1606.04833 [hep-ex].

[143] Albert M Sirunyan et al. "Search for massive resonances decaying into WW, WZ or ZZ bosons in proton-proton collisions at $\sqrt{s} = 13$ TeV". In: *JHEP* 03 (2017), p. 162. DOI: 10.1007/JHEP03(2017)162. arXiv: 1612.09159 [hep-ex].

[144] Georges Aad et al. "Measurements of the Total and Differential Higgs Boson Production Cross Sections Combining the H→γγ and H→ZZ*→4ℓ Decay Channels at $\sqrt{s}$=8 TeV with the ATLAS Detector". In: *Phys. Rev. Lett.* 115.9 (2015), p. 091801. DOI: 10.1103/PhysRevLett.115.091801. arXiv: 1504.05833 [hep-ex].

[145] Georges Aad et al. "Constraints on the off-shell Higgs boson signal strength in the high-mass ZZ and WW final states with the ATLAS detector". In: *Eur. Phys. J. C* 75.7 (2015), p. 335. DOI: 10.1140/epjc/s10052-015-3542-2. arXiv: 1503.01060 [hep-ex].

[146] Vardan Khachatryan et al. "Limits on the Higgs boson lifetime and width from its decay to four charged leptons". In: *Phys. Rev. D* 92.7 (2015), p. 072010. DOI: 10.1103/PhysRevD.92.072010. arXiv: 1507.06656 [hep-ex].

[147] Vardan Khachatryan et al. "Measurement of differential and integrated fiducial cross sections for Higgs boson production in the four-lepton decay channel in pp collisions at $\sqrt{s} = 7$ and 8 TeV". In: *JHEP* 04 (2016), p. 005. DOI: 10.1007/JHEP04(2016)005. arXiv: 1512.08377 [hep-ex].

[148] A. M. Sirunyan et al. "Measurements of the Higgs boson width and anomalous *HVV* couplings from on-shell and off-shell production in the four-lepton final state". In: *Phys. Rev. D* 99 (11 2019), p. 112003. DOI: 10.1103/PhysRevD.99.112003. URL: https://link.aps.org/doi/10.1103/PhysRevD.99.112003.

[149] Vardan Khachatryan et al. "Search for Higgs boson off-shell production in proton-proton collisions at 7 and 8 TeV and derivation of constraints on its total decay width". In: *JHEP* 09 (2016), p. 051. DOI: 10.1007/JHEP09(2016)051. arXiv: 1605.02329 [hep-ex].

[150] Alexander Savin. "Electroweak measurements at High-Luminosity LHC". In: *PoS* LHCP2019 (2019). Ed. by Pablo Roig Garcés et al., p. 242. DOI: 10.22323/1.350.0242.

[151] Barbara Mele. "QCD corrections to Z pair hadronic production". In: *Ettore Majorana Int. Sci. Ser. Phys. Sci.* 60 (1992). Ed. by Luisa Cifarelli and Yuri Dokshitzer, pp. 237–251. DOI: 10.1007/978-1-4615-3440-2_15.

[152] J. Ohnemus. "Hadronic Z Z, W- W+, and W+- Z production with QCD corrections and leptonic decays". In: *Phys. Rev. D* 50 (1994), pp. 1931–1945. DOI: 10.1103/PhysRevD.50.1931. arXiv: hep-ph/9403331.

[153] J. Alwall et al. "The automated computation of tree-level and next-to-leading order differential cross sections, and their matching to parton shower simulations". In: *JHEP* 07 (2014), p. 079. DOI: 10.1007/JHEP07(2014)079. arXiv: 1405.0301 [hep-ph].

[154] Federico Buccioni et al. "OpenLoops 2". In: *Eur. Phys. J. C* 79.10 (2019), p. 866. DOI: 10.1140/epjc/s10052-019-7306-2. arXiv: 1907.13071 [hep-ph].

[155] Ansgar Denner, Jean-Nicolas Lang, and Sandro Uccirati. "NLO electroweak corrections in extended Higgs Sectors with RECOLA2". In: *JHEP* 07 (2017), p. 087. DOI: 10.1007/JHEP07(2017)087. arXiv: 1705.06053 [hep-ph].

[156] Gavin Cullen et al. "Automated One-Loop Calculations with GoSam". In: *Eur. Phys. J. C* 72 (2012), p. 1889. DOI: 10.1140/epjc/s10052-012-1889-1. arXiv: 1111.2034 [hep-ph].

[157] Valentin Hirschi et al. "Automation of one-loop QCD corrections". In: *JHEP* 05 (2011), p. 044. DOI: 10.1007/JHEP05(2011)044. arXiv: 1103.0621 [hep-ph].

[158] Anastasiya Bierweiler, Tobias Kasprzik, and Johann H. Kühn. "Vector-boson pair production at the LHC to $\mathcal{O}(\alpha^3)$ accuracy". In: *JHEP* 12 (2013), p. 071. DOI: 10.1007/JHEP12(2013)071. arXiv: 1305.5402 [hep-ph].

[159] Julien Baglio, Le Duc Ninh, and Marcus M. Weber. "Massive gauge boson pair production at the LHC: a next-to-leading order story". In: *Phys. Rev. D* 88 (2013). [Erratum: Phys.Rev.D 94, 099902 (2016)], p. 113005. DOI: 10.1103/PhysRevD.94.099902. arXiv: 1307.4331 [hep-ph].

[160] B. Biedermann et al. "Electroweak corrections to $pp \to \mu^+\mu^-e^+e^- + X$ at the LHC: a Higgs background study". In: *Phys. Rev. Lett.* 116.16 (2016), p. 161803. DOI: 10.1103/PhysRevLett.116.161803. arXiv: 1601.07787 [hep-ph].

[161] Benedikt Biedermann et al. "Next-to-leading-order electroweak corrections to the production of four charged leptons at the LHC". In: *JHEP* 01 (2017), p. 033. DOI: 10.1007/JHEP01(2017)033. arXiv: 1611.05338 [hep-ph].

[162] Mauro Chiesa, Ansgar Denner, and Jean-Nicolas Lang. "Anomalous triple-gauge-boson interactions in vector-boson pair production with RECOLA2". In: *Eur. Phys. J. C* 78.6 (2018), p. 467. DOI: 10.1140/epjc/s10052-018-5949-z. arXiv: 1804.01477 [hep-ph].

[163] Thomas Gehrmann, Andreas von Manteuffel, and Lorenzo Tancredi. "The two-loop helicity amplitudes for $q\bar{q}' \to V_1V_2 \to 4$ leptons". In: *JHEP* 09 (2015), p. 128. DOI: 10.1007/JHEP09(2015)128. arXiv: 1503.04812 [hep-ph].

[164] Stefan Kallweit and Marius Wiesemann. "ZZ production at the LHC: NNLO predictions for 2l2ν and 4l signatures". In: *Physics Letters B* 786 (2018), pp. 382–389. ISSN: 0370-2693. DOI: https://doi.org/10.1016/j.physletb.2018.10.016. URL: https://www.sciencedirect.com/science/article/pii/S0370269318307822.

[165] John M. Campbell, R. Keith Ellis, and Ciaran Williams. "Bounding the Higgs Width at the LHC Using Full Analytic Results for $gg-> e^-e^+\mu^-\mu^+$". In: *JHEP* 04 (2014), p. 060. DOI: 10.1007/JHEP04(2014)060. arXiv: 1311.3589 [hep-ph].

[166] Fabrizio Caola et al. "QCD corrections to ZZ production in gluon fusion at the LHC". In: *Phys. Rev. D* 92 (9 2015), p. 094028. DOI: 10.1103/PhysRevD.92.094028. URL: https://link.aps.org/doi/10.1103/PhysRevD.92.094028.

[167] Bakul Agarwal, Stephen P. Jones, and Andreas von Manteuffel. "Two-loop helicity amplitudes for $gg \to ZZ$ with full top-quark mass effects". In: *JHEP* 05 (2021), p. 256. DOI: 10.1007/JHEP05(2021)256. arXiv: 2011.15113 [hep-ph].

[168] Simone Alioli et al. "ZZ production in gluon fusion at NLO matched to parton-shower". In: *Phys. Rev. D* 95.3 (2017), p. 034042. DOI: 10.1103/PhysRevD.95.034042. arXiv: 1609.09719 [hep-ph].

[169] Massimiliano Grazzini et al. "*ZZ* production at the LHC: NLO QCD corrections to the loop-induced gluon fusion channel". In: *JHEP* 03 (2019), p. 070. DOI: 10.1007/JHEP03(2019)070. arXiv: 1811.09593 [hep-ph].

[170] Mauro Chiesa, Carlo Oleari, and Emanuele Re. "NLO QCD+NLO EW corrections to diboson production matched to parton shower". In: *Eur. Phys. J. C* 80.9 (2020), p. 849. DOI: 10.1140/epjc/s10052-020-8419-3. arXiv: 2005.12146 [hep-ph].

[171] Luca Buonocore et al. "ZZ production at nNNLO+PS with MiNNLO$_{PS}$". In: *JHEP* 01 (2022), p. 072. DOI: 10.1007/JHEP01(2022)072. arXiv: 2108.05337 [hep-ph].

[172] The ATLAS Collaboration et al. "The ATLAS Experiment at the CERN Large Hadron Collider". In: *Journal of Instrumentation* 3.08 (2008), S08003–S08003. DOI: 10.1088/1748-0221/3/08/s08003. URL: https://doi.org/10.1088/1748-0221/3/08/s08003.

[173] F. Cascioli et al. "ZZ production at hadron colliders in NNLO QCD". In: *Phys. Lett. B* 735 (2014), pp. 311–313. DOI: 10.1016/j.physletb.2014.06.056. arXiv: 1405.2219 [hep-ph].

[174] Georges Aad et al. "Measurement of the *ZZ* Production Cross Section in *pp* Collisions at $\sqrt{s} = 13$ TeV with the ATLAS Detector". In: *Phys. Rev. Lett.* 116.10 (2016), p. 101801. DOI: 10.1103/PhysRevLett.116.101801. arXiv: 1512.05314 [hep-ex].

[175] Morad Aaboud et al. "Measurement of the *ZZ* production cross section in proton-proton collisions at $\sqrt{s} = 8$ TeV using the $ZZ \to \ell^-\ell^+\ell'^-\ell'^+$ and $ZZ \to \ell^-\ell^+\nu\bar{\nu}$ channels with the ATLAS detector". In: *JHEP* 01 (2017), p. 099. DOI: 10.1007/JHEP01(2017)099. arXiv: 1610.07585 [hep-ex].

[176] Frank F. Deppisch, Wei Liu, and Manimala Mitra. "Long-lived Heavy Neutrinos from Higgs Decays". In: *JHEP* 08 (2018), p. 181. DOI: 10.1007/JHEP08(2018)181. arXiv: 1804.04075 [hep-ph].

[177] Borut Bajc et al. "Threshold corrections to dimension-six proton decay operators in non-minimal SUSY SU (5) GUTs". In: *Nucl. Phys. B* 910 (2016), pp. 1–22. DOI: 10.1016/j.nuclphysb.2016.06.017. arXiv: 1603.03568 [hep-ph].

[178] S. Amrith et al. "LHC Constraints on a $B - L$ Gauge Model using Contur". In: *JHEP* 05 (2019), p. 154. DOI: 10.1007/JHEP05(2019)154. arXiv: 1811.11452 [hep-ph].

[179] D. López-Val and T. Robens. "Δr and the W-boson mass in the singlet extension of the standard model". In: *Phys. Rev. D* 90 (2014), p. 114018. DOI: 10.1103/PhysRevD.90.114018. arXiv: 1406.1043 [hep-ph].

[180] Ansgar Denner and Stefano Pozzorini. "One loop leading logarithms in electroweak radiative corrections. 2. Factorization of collinear singularities". In: *Eur. Phys. J. C* 21 (2001), pp. 63–79. DOI: 10.1007/s100520100721. arXiv: hep-ph/0104127.

[181] Ansgar Denner, Michael Melles, and Stefano Pozzorini. "Two loop electroweak corrections at high-energies". In: *Nucl. Phys. B Proc. Suppl.* 116 (2003). Ed. by J. Blumlein et al., pp. 18–22. DOI: 10.1016/S0920-5632(03)80136-6. arXiv: hep-ph/0211196.

[182] Enrico Bothmann and Davide Napoletano. "Automated evaluation of electroweak Sudakov logarithms in Sherpa". In: *Eur. Phys. J. C* 80.11 (2020), p. 1024. DOI: 10.1140/epjc/s10052-020-08596-2. arXiv: 2006.14635 [hep-ph].

[183] Evgenii I. Khukhro. *p-Automorphisms of Finite p-Groups*. London Mathematical Society Lecture Note Series. Cambridge University Press, 1998. DOI: 10.1017/CBO9780511526008.

[184] Marek Schönherr. "An automated subtraction of NLO EW infrared divergences". In: *Eur. Phys. J. C* 78.2 (2018), p. 119. DOI: 10.1140/epjc/s10052-018-5600-z. arXiv: 1712.07975 [hep-ph].

[185] Frank Krauss, Alan Price, and Marek Schönherr. "YFS Resummation for Future Lepton-Lepton Colliders in SHERPA". In: (Mar. 2022). arXiv: 2203.10948 [hep-ph].

[186] Victor S. Fadin et al. "Resummation of double logarithms in electroweak high-energy processes". In: *Phys. Rev. D* 61 (2000), p. 094002. DOI: 10.1103/PhysRevD.61.094002. arXiv: hep-ph/9910338.

[187] Michael Melles. "Electroweak radiative corrections in high-energy processes". In: *Phys. Rept.* 375 (2003), pp. 219–326. DOI: 10.1016/S0370-1573(02)00550-1. arXiv: hep-ph/0104232.

[188] Michael Melles. "Resummation of angular dependent corrections in spontaneously broken gauge theories". In: *Eur. Phys. J. C* 24 (2002), pp. 193–204. DOI: 10.1007/s100520200942. arXiv: hep-ph/0108221.

[189] Jui-Yu Chiu et al. "Electroweak Sudakov corrections using effective field theory". In: *Phys. Rev. Lett.* 100 (2008), p. 021802. DOI: 10.1103/PhysRevLett.100.021802. arXiv: 0709.2377 [hep-ph].

[190] Jui-Yu Chiu et al. "Electroweak Corrections in High Energy Processes using Effective Field Theory". In: *Phys. Rev. D* 77 (2008), p. 053004. DOI: 10.1103/PhysRevD.77.053004. arXiv: 0712.0396 [hep-ph].

[191] Jui-Yu Chiu, Randall Kelley, and Aneesh V. Manohar. "Electroweak Corrections using Effective Field Theory: Applications to the LHC". In: *Phys. Rev. D* 78 (2008), p. 073006. DOI: 10.1103/PhysRevD.78.073006. arXiv: 0806.1240 [hep-ph].

[192] Jui-Yu Chiu et al. "Factorization Structure of Gauge Theory Amplitudes and Application to Hard Scattering Processes at the LHC". In: *Phys. Rev. D* 80 (2009), p. 094013. DOI: 10.1103/PhysRevD.80.094013. arXiv: 0909.0012 [hep-ph].

[193] Jui-Yu Chiu et al. "Soft and Collinear Functions for the Standard Model". In: *Phys. Rev. D* 81 (2010), p. 014023. DOI: 10.1103/PhysRevD.81.014023. arXiv: 0909.0947 [hep-ph].

[194] Andreas Fuhrer et al. "Radiative Corrections to Longitudinal and Transverse Gauge Boson and Higgs Production". In: *Phys. Rev. D* 81 (2010), p. 093005. DOI: 10.1103/PhysRevD.81.093005. arXiv: 1003.0025 [hep-ph].

[195] D. Yu. Bardin et al. "Energy Dependent Width Effects in e+ e- Annihilation Near the Z Boson Pole". In: *Phys. Lett. B* 206 (1988), pp. 539–542. DOI: 10.1016/0370-2693(88)91627-9.

[196] Matteo Cacciari, Gavin P. Salam, and Gregory Soyez. "The anti-k_t jet clustering algorithm". In: *JHEP* 04 (2008), p. 063. DOI: 10.1088/1126-6708/2008/04/063. arXiv: 0802.1189 [hep-ph].

[197] William J. Marciano. "The Weak Mixing Angle and Grand Unified Gauge Theories". In: *Phys. Rev. D* 20 (1979), p. 274. DOI: 10.1103/PhysRevD.20.274.

[198] A. Sirlin. "On the O(alpha**2) Corrections to tau (mu), m (W), m (Z) in the SU(2)-L x U(1) Theory". In: *Phys. Rev. D* 29 (1984), p. 89. DOI: 10.1103/PhysRevD.29.89.

[199] A. Sirlin. "Radiative Corrections in the SU(2)-L x U(1) Theory: A Simple Renormalization Framework". In: *Phys. Rev. D* 22 (1980), pp. 971–981. DOI: 10.1103/PhysRevD.22.971.

[200] Ansgar Denner. "Techniques for calculation of electroweak radiative corrections at the one loop level and results for W physics at LEP-200". In: *Fortsch. Phys.* 41 (1993), pp. 307–420. DOI: 10.1002/prop.2190410402. arXiv: 0709.1075 [hep-ph].

[201] M. Consoli, W. Hollik, and F. Jegerlehner. "The Effect of the Top Quark on the M(W)-M(Z) Interdependence and Possible Decoupling of Heavy Fermions from Low-Energy Physics". In: *Phys. Lett. B* 227 (1989), pp. 167–170. DOI: 10.1016/0370-2693(89)91301-4.

[202] Stephan Bräuer et al. "Fixed-order and merged parton-shower predictions for WW and WWj production at the LHC including NLO QCD and EW corrections". In: *JHEP* 10 (2020), p. 159. DOI: 10.1007/JHEP10(2020)159. arXiv: 2005.12128 [hep-ph].

[203] T. Binoth et al. "NLO QCD corrections to ZZ+ jet production at hadron colliders". In: *Phys. Lett. B* 683 (2010), pp. 154–159. DOI: 10.1016/j.physletb.2009.12.013. arXiv: 0911.3181 [hep-ph].

[204] M. Cacciari et al. "The t anti-t cross-section at 1.8-TeV and 1.96-TeV: A Study of the systematics due to parton densities and scale dependence". In: *JHEP* 04 (2004), p. 068. DOI: 10.1088/1126-6708/2004/04/068. arXiv: hep-ph/0303085.

[205] Enrico Bothmann, Marek Schönherr, and Steffen Schumann. "Reweighting QCD matrix-element and parton-shower calculations". In: *Eur. Phys. J. C* 76.11 (2016), p. 590. DOI: 10.1140/epjc/s10052-016-4430-0. arXiv: 1606.08753 [hep-ph].

[206] S. Amoroso et al. "Les Houches 2019: Physics at TeV Colliders: Standard Model Working Group Report". In: *11th Les Houches Workshop on Physics at TeV Colliders: PhysTeV Les Houches*. Mar. 2020. arXiv: 2003.01700 [hep-ph].

[207] Simone Alioli et al. "Four-lepton production in gluon fusion at NLO matched to parton showers". In: *Eur. Phys. J. C* 81.8 (2021), p. 687. DOI: 10.1140/epjc/s10052-021-09470-5. arXiv: 2102.07783 [hep-ph].

[208] Duane A. Dicus, Chung Kao, and W. W. Repko. "Gluon Production of Gauge Bosons". In: *Phys. Rev. D* 36 (1987), p. 1570. DOI: 10.1103/PhysRevD.36.1570.

[209] E. W. Nigel Glover and J. J. van der Bij. "Z BOSON PAIR PRODUCTION VIA GLUON FUSION". In: *Nucl. Phys. B* 321 (1989), pp. 561–590. DOI: 10.1016/0550-3213(89)90262-9.

[210] Valentin Hirschi and Olivier Mattelaer. "Automated event generation for loop-induced processes". In: *JHEP* 10 (2015), p. 146. DOI: 10.1007/JHEP10(2015)146. arXiv: 1507.00020 [hep-ph].

[211] Fabrizio Caola et al. "QCD corrections to ZZ production in gluon fusion at the LHC". In: *Phys. Rev. D* 92.9 (2015), p. 094028. DOI: 10.1103/PhysRevD.92.094028. arXiv: 1509.06734 [hep-ph].

[212] Fabrizio Caola et al. "QCD corrections to vector boson pair production in gluon fusion including interference effects with off-shell Higgs at the LHC". In: *JHEP* 07 (2016), p. 087. DOI: 10.1007/JHEP07(2016)087. arXiv: 1605.04610 [hep-ph].

[213] Christian Brønnum-Hansen and Chen-Yu Wang. "Top quark contribution to two-loop helicity amplitudes for *Z* boson pair production in gluon fusion". In: *JHEP* 05 (2021), p. 244. DOI: 10.1007/JHEP05(2021)244. arXiv: 2101.12095 [hep-ph].

[214] Stephen Jones and Silvan Kuttimalai. "Parton Shower and NLO-Matching uncertainties in Higgs Boson Pair Production". In: *JHEP* 02 (2018), p. 176. DOI: 10.1007/JHEP02(2018)176. arXiv: 1711.03319 [hep-ph].

[215] Fabrizio Caola and Kirill Melnikov. "Constraining the Higgs boson width with ZZ production at the LHC". In: *Phys. Rev. D* 88 (2013), p. 054024. DOI: 10.1103/PhysRevD.88.054024. arXiv: 1307.4935 [hep-ph].

[216] E. W. Nigel Glover and J. J. van der Bij. "VECTOR BOSON PAIR PRODUCTION VIA GLUON FUSION". In: *Phys. Lett. B* 219 (1989), pp. 488–492. DOI: 10.1016/0370-2693(89)91099-X.

[217] F. Cascioli et al. "Precise Higgs-background predictions: merging NLO QCD and squared quark-loop corrections to four-lepton + 0,1 jet production". In: *JHEP* 01 (2014), p. 046. DOI: 10.1007/JHEP01(2014)046. arXiv: 1309.0500 [hep-ph].

[218] Thomas Gehrmann, Lorenzo Tancredi, and Erich Weihs. "Two-loop master integrals for $q\bar{q} \to VV$: the planar topologies". In: *JHEP* 08 (2013), p. 070. DOI: 10.1007/JHEP08(2013)070. arXiv: 1306.6344 [hep-ph].

[219] Thomas Gehrmann et al. "The two-loop master integrals for $q\bar{q} \to VV$". In: *JHEP* 06 (2014), p. 032. DOI: 10.1007/JHEP06(2014)032. arXiv: 1404.4853 [hep-ph].

[220] Johannes M. Henn, Kirill Melnikov, and Vladimir A. Smirnov. "Two-loop planar master integrals for the production of off-shell vector bosons in hadron collisions". In: *JHEP* 05 (2014), p. 090. DOI: 10.1007/JHEP05(2014)090. arXiv: 1402.7078 [hep-ph].

[221] Fabrizio Caola et al. "Non-planar master integrals for the production of two off-shell vector bosons in collisions of massless partons". In: *JHEP* 09 (2014), p. 043. DOI: 10.1007/JHEP09(2014)043. arXiv: 1404.5590 [hep-ph].

[222] Costas G. Papadopoulos, Damiano Tommasini, and Christopher Wever. "Two-loop Master Integrals with the Simplified Differential Equations approach". In: *JHEP* 01 (2015), p. 072. DOI: 10.1007/JHEP01(2015)072. arXiv: 1409.6114 [hep-ph].

[223] Hiren H. Patel. "Package-X 2.0: A Mathematica package for the analytic calculation of one-loop integrals". In: *Comput. Phys. Commun.* 218 (2017), pp. 66–70. DOI: 10.1016/j.cpc.2017.04.015. arXiv: 1612.00009 [hep-ph].

[224] Lance J. Dixon. "A brief introduction to modern amplitude methods". In: *Theoretical Advanced Study Institute in Elementary Particle Physics: Particle Physics: The Higgs Boson and Beyond.* 2014, pp. 31–67. DOI: 10.5170/CERN-2014-008.31. arXiv: 1310.5353 [hep-ph].

[225] R. Gastmans and T. T. Wu. *The Ubiquitous photon: Helicity method for QED and QCD.* Vol. 80. 1990.

[226] Zhan Xu, Da-Hua Zhang, and Lee Chang. "Helicity Amplitudes for Multiple Bremsstrahlung in Massless Nonabelian Gauge Theories". In: *Nucl. Phys. B* 291 (1987), pp. 392–428. DOI: 10.1016/0550-3213(87)90479-2.

[227] P. De Causmaecker et al. "Multiple Bremsstrahlung in Gauge Theories at High-Energies. 1. General Formalism for Quantum Electrodynamics". In: *Nucl. Phys. B* 206 (1982), pp. 53–60. DOI: 10.1016/0550-3213(82)90488-6.

[228] Stefano Catani et al. "Universality of transverse-momentum resummation and hard factors at the NNLO". In: *Nucl. Phys. B* 881 (2014), pp. 414–443. DOI: 10.1016/j.nuclphysb.2014.02.011. arXiv: 1311.1654 [hep-ph].

[229] Stefano Catani. "The Singular behavior of QCD amplitudes at two loop order". In: *Phys. Lett. B* 427 (1998), pp. 161–171. DOI: 10.1016/S0370-2693(98)00332-3. arXiv: hep-ph/9802439.

[230] Joshua Davies et al. "$gg \to ZZ$: analytic two-loop results for the low- and high-energy regions". In: *JHEP* 04 (2020), p. 024. DOI: 10.1007/JHEP04(2020)024. arXiv: 2002.05558 [hep-ph].

[231] John M. Campbell et al. "Two loop correction to interference in $gg \to ZZ$". In: *JHEP* 08 (2016), p. 011. DOI: 10.1007/JHEP08(2016)011. arXiv: 1605.01380 [hep-ph].

[232] Daniele Lombardi, Marius Wiesemann, and Giulia Zanderighi. "W+W- production at NNLO+PS with MINNLO$_{PS}$". In: *JHEP* 11 (2021), p. 230. DOI: 10.1007/JHEP11(2021)230. arXiv: 2103.12077 [hep-ph].

[233] Garrett Birkhoff and Henry L. Garabedian. "Smooth Surface Interpolation". In: *Journal of Mathematics and Physics* 39.1-4 (1960), pp. 258–268. DOI: https://doi.org/10.1002/sapm1960391258. eprint: https://onlinelibrary.wiley.com/doi/pdf/10.1002/sapm1960391258. URL: https://onlinelibrary.wiley.com/doi/abs/10.1002/sapm1960391258.

[234] P. Sullivan N. Kruis T. Scimone. "The Btwxt general-purpose, N-dimensional interpolation library". In: (2020). URL: https://github.com/bigladder/btwxt.

[235] Andy Buckley et al. "Rivet user manual". In: *Comput. Phys. Commun.* 184 (2013), pp. 2803–2819. DOI: 10.1016/j.cpc.2013.05.021. arXiv: 1003.0694 [hep-ph].

[236] Katharina Danziger et al. "Accelerating Monte Carlo event generation – rejection sampling using neural network event-weight estimates". In: *SciPost Phys.* 12 (2022), p. 164. DOI: 10.21468/SciPostPhys.12.5.164. arXiv: 2109.11964 [hep-ph].

Curriculum Vitae

Simon Luca Villani

Nationality: Italian

PhD Student: University of Göttingen
Thesis: *Higher-order Electroweak and QCD Corrections
in $e^+e^-\mu^+\mu^-$ production at LHC*
Supervisor: Prof. Dr. Steffen Schumann
Date of Oral Examination: 2nd September 2022

Academic Education

2018   **M.Sc. in Theoretical Physics:**   University of Bologna
Thesis: *Comparison between two different
approaches to resum large threshold logarithms in
Drell-Yan rapidity distribution*
Supervisor: Prof. Dr. Roberto Soldati

2015   **B.Sc. in Physics:**   University of Bologna
Thesis: *Path Integral and Weyl Ordering*
Supervisor: Prof. Dr. Fiorenzo Sebastianelli

Publications and Preprints

- E. Bothmann, D. Napoletano, M. Schönherr, S. Schumann and S.L. Villani,
  Higher-order EW corrections in ZZ and ZZj production at the LHC. JHEP 06
  (2022) 064

- E. Bothmann, M. Calvetti, P. Francavilla, C. Pandini, E. Re and S. L. Villani *A study of loop-induced ZH production with up to one additional jet.*
  arXiv:2003.01700